

# UC Irvine

## UC Irvine Previously Published Works

**Title**

Mechanisms of pulsed laser ablation of biological tissues

**Permalink**

<https://escholarship.org/uc/item/5qb7v6qb>

**Journal**

Chemical Reviews, 103(2)

**ISSN**

0009-2665

**Authors**

Vogel, A  
Venugopalan, V

**Publication Date**

2003-02-01

**DOI**

10.1021/cr010379n

**License**

[CC BY 4.0](#)

Peer reviewed

# Mechanisms of Pulsed Laser Ablation of Biological Tissues

Alfred Vogel<sup>\*,†</sup> and Vasan Venugopalan<sup>‡</sup>

Medical Laser Center Lübeck, Peter-Monnik-Weg 4, D-23562 Lübeck, Germany, and Department of Chemical Engineering and Materials Science and Laser Microbeam and Medical Program, Beckman Laser Institute, University of California, Irvine, California 92697

Received September 12, 2002

## Contents

I. Introduction	578	2. Plume Dynamics for Microsecond Pulses	602
II. Properties of Soft Biological Tissues	579	3. Postpulse Ablation	604
A. Tissue Composition and Morphology	579	B. Recoil Stress	604
B. Mechanical Properties	582	1. Temporal Shape and Amplitude	604
C. Thermal Denaturation	583	2. Recoil-Induced Material Expulsion	605
III. Energy Deposition and Transport	584	3. Collateral Tissue Effects Induced by Recoil Stress	606
A. Optical Absorption Properties of Tissue	584	C. Flow-Induced Material Redeposition	607
1. Ultraviolet Radiation ( $\lambda = 180\text{--}400\text{ nm}$ )	584	D. Shielding by the Ablation Plume	608
2. Visible Radiation ( $\lambda = 400\text{--}780\text{ nm}$ )	585	VII. Ablation Models and Metrics	609
3. Near-Far-Infrared Radiation ( $\lambda = 780\text{ nm--}15\text{ }\mu\text{m}$ )	585	A. Heuristic Models	609
B. Optical Scattering Properties of Tissue	585	1. Blow-off Model	609
C. Dynamic Optical Properties in Tissue	586	2. Steady-State Models	610
IV. Linear Thermomechanical Response of Tissue to Pulsed Irradiation	588	3. Comparison of Blow-off and Steady-State Models	611
A. Temperature Rise and Thermal Diffusion	588	4. Applicability of Blow-off and Steady-State Models	611
B. Thermoelastic Stress Generation and Propagation	588	5. Unification of Blow-off and Steady-State Models	612
C. Implications for Precise Tissue Ablation	590	B. Ablation Metrics and Their Relationship to Heuristic Model Predictions	612
V. Thermodynamics and Kinetics of Phase Transitions	590	1. Ablation Threshold	612
A. Phase Diagrams	590	2. Ablation Enthalpy	613
B. Surface Vaporization	591	3. Ablation Efficiency	613
C. Normal Boiling	592	C. Mechanistic Models	613
D. Phase Explosions: Bubble Nucleation and Spinodal Decomposition	592	1. Steady-State Vaporization Models	614
E. Confined Boiling	595	2. Thermomechanical Models	614
F. Effects of the Tissue Matrix on the Interplay of Phase Explosions and Confined Boiling	596	D. Molecular Dynamics Simulations	615
G. Effect of Stress Confinement on the Ablation Process	596	VIII. UV and IR Ablation	615
1. Stress Confinement and Phase Transitions	597	A. Tissue Absorption Coefficients	615
2. Stress Confinement and Tissue Fracture	597	B. Ablation without Stress Confinement	617
3. Stress Confinement and Ablation Threshold	598	1. Temperature Rise and Thermal Diffusion	617
H. Photochemical Decomposition	598	2. Kinetics of Tissue Decomposition	618
I. Interplay of Photochemical Decomposition and Confined Boiling in Tissue	600	3. Material Ejection	618
VI. Ablation Plume Dynamics	600	C. Ablation with Stress Confinement	620
A. Plume Formation and Expansion	600	1. Reduction of the Ablation Threshold	621
1. Plume Dynamics for Nanosecond Pulses	601	2. Kinetics of Tissue Decomposition and Material Ejection	621
		3. Precision Achieved by Ablation under Stress-Confined Conditions	622
		D. Overall Picture	623
		IX. Ablation in a Liquid Environment	623
		A. Bubble Formation	623
		B. Amplification of Mechanical Effects by Liquid Confinement	625
		C. Influence of the Bubble Dynamics on Ablation Efficiency	626

\* To whom correspondence should be addressed. Phone: +49-451-500-6504. Fax: +49-451-505-486. E-mail: vogel@ml.mlu-luebeck.de.

<sup>†</sup> Medical Laser Center Lübeck.

<sup>‡</sup> University of California, Irvine. E-mail: vvenugop@uci.edu.

X. Plasma-Mediated Ablation	627
A. Kinetics of Plasma Formation in Biological Tissues	627
B. Threshold for Plasma Formation	629
C. Plasma Formation above the Breakdown Threshold	630
D. Plasma Absorption	631
E. Plasma Energy Density	632
F. Thermomechanical and Chemical Effects	632
G. Implications for Tissue Ablation	634
XI. Control of Precision, Thermal and Mechanical Damage, and Ablated Mass	636
A. Control of Precision	636
B. Control of Thermal Side Effects	636
C. Control of Mechanical Side Effects	637
D. Maximizing the Ablated Mass	637
E. Selective Ablation	637
XII. Outlook and Challenges	638
XIII. Acknowledgment	639
XIV. References	639

## I. Introduction

Soon after the invention of the pulsed ruby laser by Maiman in 1960, investigators were eager to examine the potential of pulsed laser radiation for medical applications. It was greatly anticipated that lasers would enable manipulation and destruction of biological tissue with unprecedented precision and selectivity.<sup>1,2</sup> Within a few years, reports of the use of pulsed lasers for precise tissue coagulation in patients along with the development of laser systems designed for clinical use appeared in the literature.<sup>3–6</sup> However, a clinically viable application of pulsed laser *ablation* was not reported until the early 1970s.<sup>7</sup> It was only at the beginning of the 1980s that lasers were routinely used for ophthalmic dissection and ablation procedures. In other medical subspecialties, routine laser use did not occur until the mid-1980s.<sup>8</sup> The delay between the invention of the laser and its successful clinical application was due largely to a lack of understanding of the fundamental mechanisms that govern laser–tissue interactions. Much progress has been made in this regard, and now, at the beginning of the 21st century, medical procedures that employ pulsed lasers are present in nearly every medical subspecialty; for many ophthalmologists and dermatologists, lasers are considered essential tools for medical practice.

As the understanding of laser–tissue interactions matured in the 1990s, three books became available and serve as a valuable resource for the field,<sup>9–11</sup> together with the books by Ready<sup>12</sup> and by Bäuerle<sup>13</sup> that address general aspects of laser ablation. Previous survey papers include the reviews on laser–tissue interactions by Hillenkamp<sup>14</sup> and by Jacques;<sup>15</sup> ultraviolet laser ablation of polymers and biological tissues by Srinivasan,<sup>16</sup> Srinivasan and Braren,<sup>17</sup> and Pettit;<sup>18</sup> photophysics of laser–tissue interactions by Boulnois;<sup>19</sup> thermal processes in laser–tissue interactions by McKenzie;<sup>20</sup> medical laser applications by Verdaasdonk;<sup>21</sup> and laser applications in the cornea and in ophthalmology by Marshall,<sup>22</sup> Krauss and Puliafito,<sup>8</sup> and by Krueger and co-workers.<sup>23</sup> Reviews



Alfred Vogel studied physics and sociology, receiving the University degree for high school teaching and the Ph.D. degree in physics from the Georg-August University of Göttingen, Germany. Later, he earned the degree of Habilitated Doctor of Physics from the University of Lübeck. In 1988, he joined the laser laboratory of the Eye Hospital of the Ludwig-Maximilians University Munich, and in 1992, he moved to the Medical Laser Center Lübeck, where he has been Vice-Chairman since 1999. His research interests include laser–tissue interactions in biomedical applications of photodisruption, pulsed laser ablation, and photocoagulation as well as laser-induced plasma formation, cavitation, and stress waves.



Vasan Venugopalan received his B.S. degree in mechanical engineering from the University of California, Berkeley, and S.M. and Sc.D. degrees in mechanical engineering from MIT. He held postdoctoral positions at the Wellman Laboratories of Photomedicine, Harvard Medical School, and the Departments of Molecular Biology and Physics, Princeton University. He joined the University of California, Irvine, in 1996, where he is currently Assistant Professor of Chemical Engineering, Biomedical Engineering, and Surgery. His research focuses on applications of laser-induced thermal, mechanical, and radiative transport processes in medical diagnostics, therapeutics, biotechnology, and micro-electromechanical systems.

on general aspects of tissue ablation include those of Müller,<sup>24</sup> Oraevsky,<sup>25</sup> van Leeuwen,<sup>26</sup> and Walsh.<sup>27</sup> Specific aspects of laser ablation processes have also been considered in comprehensive studies. Medical applications of laser-induced plasmas were reviewed by Gitomer and Jones,<sup>28</sup> while ablation processes resulting from nonlinear absorption have been considered in both a review paper<sup>29</sup> and a monograph<sup>30</sup> by Vogel.

Despite the increasing medical use of lasers, a comprehensive presentation of the fundamental mechanisms involved in pulsed laser tissue ablation has not appeared in the scientific literature. This is not surprising, as the elements required for an understanding of the relevant processes range from non-equilibrium thermodynamics to photochemistry to

plasma physics to tissue biomechanics. Consequently, researchers who investigate the mechanisms of pulsed laser tissue ablation originate from several disciplines. Moreover, the resulting scientific reports are often narrow in scope and scattered in journals whose foci range from the medical and biological sciences to the physical sciences and engineering. The purpose of this review is to collect the information to be gleaned from these studies and organize it into a logical structure that provides an improved mechanistic understanding of pulsed laser ablation of tissue.

We consider ablation to be any process of tissue incision or removal, regardless of the photophysical or photochemical processes involved. We restrict this review to *pulsed* ablation (pulse durations  $\lesssim 1$  ms) and will not treat processes in which either tissue carbonization or dehydration/diffusive mass transfer play important roles, as they typically result from the use of long exposure times or low peak powers. We further restrict the review to ablation processes performed on a tissue level. Thus, even though it shares the same fundamental principles and is an area of growing importance and active research, we do not consider explicitly pulsed microirradiation and microdissection of cellular and subcellular targets. However, as the fundamental principles of the laser–material interactions are the same, many of the insights regarding the mechanisms of pulsed laser ablation presented here also apply to pulsed laser microirradiation. From a phenomenological standpoint, we examine the laser ablation process on mesoscopic and macroscopic scales. The underlying molecular dynamics involved in pulsed laser ablation is treated by the review of Zhigilei and co-workers appearing in this issue. Finally, we focus attention on ablation of soft biological tissues (all tissues except bone and teeth) because the extracellular matrix of soft tissues resembles the molecular substrates that are the primary focus of this special issue of *Chemical Reviews*.

This review aims at providing a framework that yields an understanding of the mechanisms of pulsed laser tissue ablation which reaches beyond a mere compilation of previous studies. We first present a section regarding the material properties of soft biological tissues that summarizes tissue composition, structure, and mechanical properties. We further explore how these characteristics may change as a result of pulsed laser irradiation (section II). We then detail the mechanisms that govern radiative transport and energy deposition resulting from pulsed laser irradiation (section III) and consider the thermal and mechanical transients produced by pulsed laser heating (section IV). In the following section, we focus on the key processes that drive pulsed laser tissue ablation: the kinetics of phase transitions and photochemical decomposition (section V). The detailed consideration of these processes provides the necessary basis for understanding the crucial role of material ejection in tissue ablation. For ablation in an air environment, we examine both the dynamics of the ablation plume that consists of vaporized and ejected material and the role of the plume in modify-

ing the amount of energy reaching the tissue (section VI). Once the various steps constituting the ablation process have been analyzed, we survey the theoretical models that have been developed to describe this process as well as the use of metrics such as ablation threshold, ablation enthalpy, and ablation efficiency that are used to characterize its energetics (section VII). We end our discussion of pulsed laser ablation in air by analyzing the elements responsible for the observed differences between ablation produced by pulsed ultraviolet (UV) and infrared (IR) laser sources (section VIII). We then describe how the interplay of the various mechanisms is modified when ablation is performed in an aqueous environment (section IX) and consider those ablation processes that are mediated principally by nonlinear energy deposition and plasma formation (section X). Finally, once the various mechanisms of ablation and their range of applicability have been established, we use this knowledge to devise strategies to control ablative precision, thermal and mechanical injury, and total ablated mass (section XI) because the primary motivation for developing a mechanistic understanding of pulsed laser tissue ablation is to enable the rational selection of laser parameters. We end with a summary and outlook with regard to the challenges and opportunities that remain in the field (section XII).

## II. Properties of Soft Biological Tissues

Several properties of biological tissues are relevant to pulsed laser ablation. Tissue composition and morphology establish tissue optical properties that determine the internal volumetric energy distribution which drives the ablation process. Structure and morphology also affect the energy transport among tissue constituents and, together with tissue mechanical properties, mediate the thermomechanical response of tissue to pulsed laser heating and phase transformation. Here we consider the compositional, structural, and mechanical properties of tissue, together with their modification when subjected to the thermal and mechanical effects induced by pulsed laser irradiation.

### A. Tissue Composition and Morphology

Soft biological tissues can be viewed crudely as a material consisting of cells that reside in and attach to an extracellular matrix (ECM). By mass, most soft tissues are dominated by water (55–99%) and collagen (0–35%). The ECM is a complex composite material, the principal components of which include water, collagen, elastin, glycosaminoglycans, glycoproteins, and cell adhesion proteins.<sup>31–33</sup> The ratio of ECM components to the total tissue mass varies significantly among tissue types. In “cell-continuous” tissues such as liver and epithelia, the ECM fraction is quite small and consists mostly of cell adhesion proteins such as fibronectin. By contrast, “matrix-continuous” tissues that include the corneal stroma, dermis, cartilage, and tendon have a very small cellular fraction and are almost entirely ECM. In such matrix-continuous tissues, the collagen content can be as high as 35%.<sup>32</sup> A primary function of the ECM is to maintain the structural integrity of the



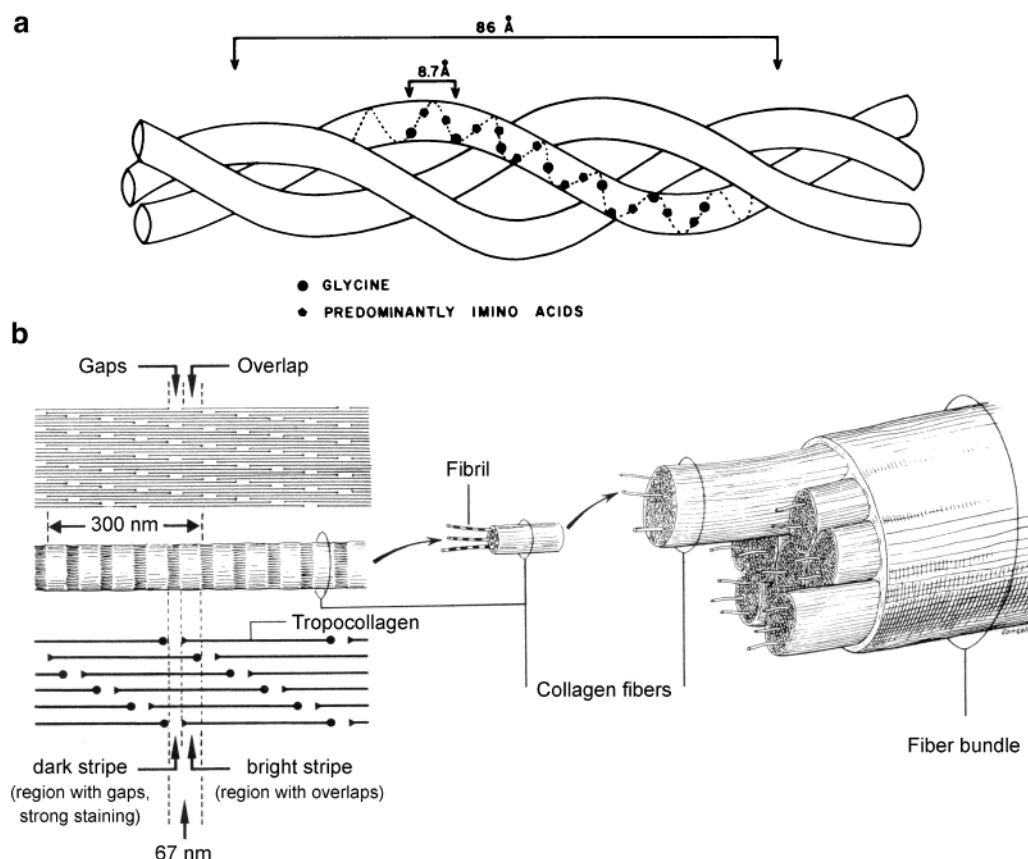


**Figure 1.** (a) Schematic drawing of the tropocollagen (TC) molecule. (Reprinted with permission from ref 35. Copyright 1988 CRC Press.) (b) Spatial organization of collagen from the molecular to the tissue level. (Reprinted with permission from ref 36. Copyright 1996 Springer). The staggering of the TC molecules in the collagen fibrils creates the banded structure that is visible in electron microscopy of stained native collagen.

tissue. Thus, the ECM inhibits tissue vaporization and material removal, which are the objectives of the ablation process.

Collagen is the single most abundant animal protein and accounts for approximately 25% of all protein in humans.<sup>31,32</sup> Collagen is a strongly hydrophilic protein as the amount of acidic, basic, and hydroxylated amino acid residues far exceeds the amount of lipophilic residues. As a result, in soft tissues, collagen exists in a highly swollen state.<sup>34</sup> Collagen is enormously complex and displays several levels of structural hierarchy. In fibril-forming collagens, over 95% of the molecule consists of three chains ( $\alpha$ -chains), each of which possesses a specific amino acid sequence. These  $\alpha$ -chains associate in a right-handed triple-helical structure, with each individual chain being a left-handed helix. This triple-helical structure forms the fundamental unit known as the tropocollagen (TC) molecule, a schematic of which is shown in Figure 1a. The TC molecule has a diameter of 1.51 nm, a length of 290 nm, and a helical repeat length of 8.6 nm.<sup>34,35</sup> The next level of structural hierarchy is related to the organization of neighboring TC molecules to form a larger unit, known as a microfibril. These microfibrils have a diameter of approximately 3.5 nm and consist of six TC molecules that organize around a common center and are stabilized by covalent cross-links.<sup>33,35</sup> These covalent cross-links are critical to the mechanical and thermal stability of collagen in vivo. The microfibrils

in turn associate with each other through lateral and end-to-end aggregation to form collagen fibrils, the diameters of which are specific to tissue type and can range from 10 to 300 nm,<sup>36</sup> as shown in Figure 1b. Moreover, the individual TC molecules within the microfibril are staggered by approximately one-quarter of their length, which gives rise to structural periodicity along the microfibrils and fibrils with a repeat distance of 64–68 nm. This periodicity results in a banding pattern that is apparent under transmission electron microscopy (TEM) and shown schematically in Figure 1b. The absence of this banding indicates a loss in the spatial organization within the collagen fibrils and is often used as a marker for the onset of thermal denaturation.<sup>37</sup>

In collagen-based tissues, the individual fibrils are embedded within a ground substance, as shown in Figure 2 for the case of skin. The ground substance consists largely of water, proteoglycans, glycosaminoglycans (GAGs), and, to a much smaller extent, nonfibrillar collagens (e.g., collagen type VI in cornea) and globular cell adhesion proteins such as fibronectin. Proteoglycans consist of sulfonated GAG side chains that are covalently linked to a core protein.<sup>38</sup> Although proteoglycans and GAG components are present in connective tissues in small quantities (typically ~1%), they are strongly hydrophilic and sequester water in amounts equivalent to 1000 times their own volume.<sup>32,39</sup> Thus, nearly all the water content of matrix-continuous tissues resides in the

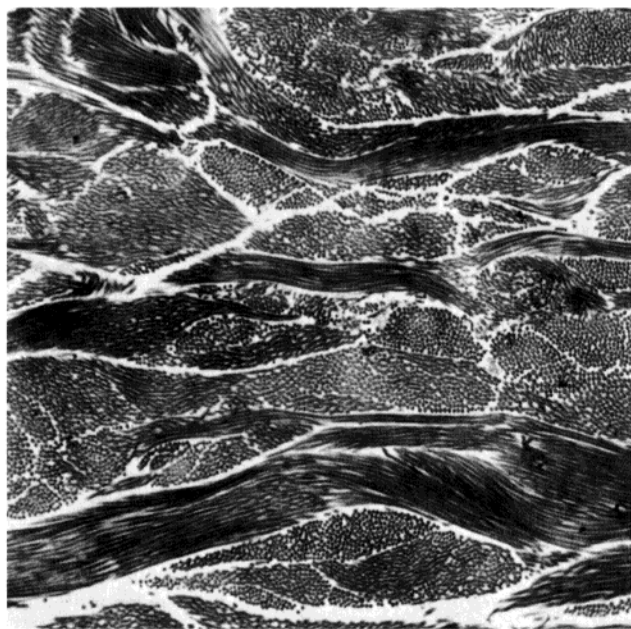


**Figure 2.** Transmission electron micrograph of human skin (dermis), showing collagen fibers sectioned both longitudinally and transversely. Magnification 4900 $\times$ . The fibers consist of individual fibrils that are embedded in a ground substance with high water content. (Reprinted with permission from ref 41. Copyright 1988 Blackwell Science.)

ground substance between the collagen fibrils. While the ground substance is not stiff, it is largely incompressible and provides resistance to compressive loading.

The individual collagen fibrils associate with each other to form sheets known as lamellae in the corneal stroma and collagen fibers in tissues such as tendon and dermis (Figure 1). The lamellae have characteristic thicknesses of 1–2  $\mu\text{m}$ , while collagen fibers in tendon and dermis possess characteristic diameters of 1–10  $\mu\text{m}$ . In tendon, bundles of collagen fibers form even larger units called fascicles. The cells in such tissue attach to and reside between the collagen lamellae or fibers.<sup>33</sup>

There are several types of collagen, each of which is defined by the sequence of amino acid residues that comprise the individual  $\alpha$ -chains within the TC molecule. The majority of collagen types found in the body form fibrils (types I, II, III, V, and XI), while other types form fibrillar networks (types IV, VII, X, and XVII), thin beaded filaments (type VI) or serve as links either between collagen fibrils or between collagen fibrils and other components of the ECM (Types IX, XII, XIV, XVI, and XIX).<sup>40,41</sup> In fibrillar collagens,  $\sim 25\%$  of the amino acids in the  $\alpha$ -chain are imino acid residues (proline or hydroxyproline) that effectively block rotation of the collagen chain at these sites and stabilize the triple-helical structure. This results in a fairly rigid polymer displaying a persistence length on the order of 160 nm, or nearly 100 times its diameter.<sup>42</sup> This rigid backbone of the TC molecule provides for high mechanical strength. While the spatial arrangement of amino acid residues within each collagen  $\alpha$ -chain precludes the formation of bonds between the chains within the TC molecule, hydrogen bonds and van der Waals interactions between the  $\alpha$ -chains are possible and further sta-

bilize the configuration and orientation of the TC molecule *in vivo*.<sup>35,40,43</sup>

The collagen amount, collagen type, macroscopic fibril size distribution and organization, and composition of the extrafibrillar space are all important in giving rise to specific tissue characteristics. For example, the primary mechanical function of the dermis is to protect underlying tissues and organs from injury. Thus, the dermis must provide both elastic deformability and high strength in response to compressive, tensile, and shear stresses. Collagen provides 75% of the dry weight and 18–30% of the volume of the dermis, which itself constitutes 15–20% of the weight of the human body.<sup>41</sup> Collagens I and III are fibrillar and the most prevalent collagen types in the dermis, constituting 70% and 15% of its dry weight, respectively. Collagen fibril diameters in the papillary (superficial) dermis range between 20 and 70 nm and reach up to 120 nm in the reticular (deep) dermis.<sup>39,41,44</sup> The collagen fibers form a loose, nonwoven, three-dimensional network.<sup>33</sup> The loose network enables the collagen fibers to spatially reconfigure and align in response to loading from a variety of directions. Moreover, collagen fibers in the dermis and other organs are “wavy” or “crimped”. This provides the dermis with significant extensibility at low stresses without loading the backbone of the TC molecule. However, once the collagen fibers are straightened and loaded, the dermis is stiff and can withstand high stresses before fracturing. The ground substance between collagen fibrils in the dermis does not contribute to more than 0.4% of the dry weight of the skin but comprises the majority of its volume due to its strongly hydrophilic nature.

Another important collagen-based tissue is the cornea. To serve its function of focusing and transmitting visible light to the lens and retina, it must retain its shape and be optically transparent to radiation in the visible spectrum. The corneal stroma consists primarily of fibrillar collagen types I (50–55% dry weight), III ( $\sim 10\%$  dry weight), and V (8–10% dry weight) as well as the beaded filament collagen type VI (25–30% dry weight) and proteoglycans.<sup>45</sup> The transparency of the cornea is facilitated by the high concentration of collagen type V that is believed to facilitate the assembly of collagen fibrils possessing a small and regular diameter.<sup>46</sup> Collagen type VI is a nonfibrillar collagen that resides in the ground substance and is important for establishing the regular spacing of the collagen fibrils.<sup>47</sup> Thus, corneal stroma, unlike dermis, has a high protein content in the ground substance itself. The interplay of these collagen constituents results in a tissue in which the collagen fibrils have a tightly controlled range of diameters between 29 and 34 nm that are spaced at a center-to-center distance of 64–67 nm.<sup>48</sup> These characteristics of regular size and spacing of collagen fibrils are the essential elements that provide the cornea with optical transparency at visible wavelengths.<sup>46,49,50</sup>

The interaction of collagen and the other extracellular matrix elements with water is important when considering energy transport processes within the tissue. As explained above, both collagen and the

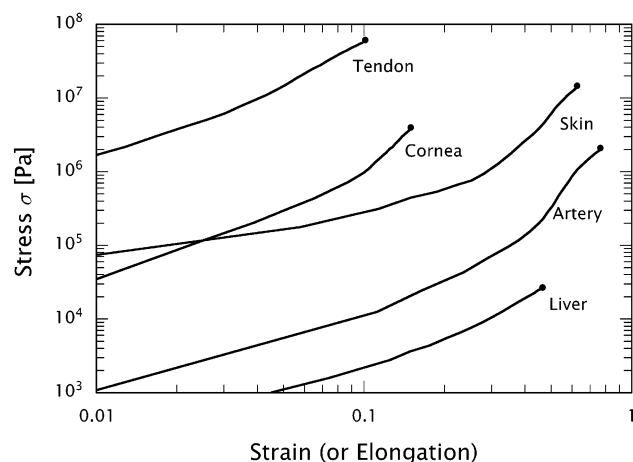


**Figure 3.** Stress–strain curves characterizing the mechanical properties of various biological tissues under uniaxial tension. The ● symbols represent the mechanical state at which tissue fracture occurs. Data compiled from ref 53.

ground substance are hydrophilic and display complex structural organization. At many laser wavelengths, only a single tissue constituent (e.g., water or collagen) absorbs the radiation. Thus, the spatial scales that characterize the collagen and water “domains” within tissue are vital to understanding potential energy-transfer mechanisms. Traditionally, the water associated with proteins *in vivo* is categorized as structural water, bound water, or free water. Structural water is directly associated with the protein and described stoichiometrically in a fashion similar to the hydrates of inorganic salts. Bound water is not directly associated with the protein but possesses properties that are measurably different than those of free water. For collagen, the amount of structural and bound water is typically 0.35 g of H<sub>2</sub>O/g of collagen.<sup>51</sup> Thus, for a hypothetical tissue comprising ~35% collagen and 65% water, only 10% of the tissue consists of structural/bound water. As a result, the vast majority of tissue water resides in the ground substance in which the collagen fibrils are embedded, and the spatial scale characterizing domains with different absorption properties is given by the diameter and spacing of the collagen fibrils.

## B. Mechanical Properties

The mechanical properties of biological tissues are of great importance to laser ablation, as both the elasticity and strength of the tissues modulate the kinetics and dynamics of the ablation process. Figure 3 provides stress–strain curves for a variety of collagen-based soft biological tissues. Although the mechanical characteristics vary considerably in terms of stiffness, extensibility at fracture, and ultimate tensile strength, one generalization can be made. When loaded in tension, nearly all soft biological tissues possess a nonlinear stress–strain characteristic with a “concave-up” shape. This is because small strains do not stretch the collagen fibers themselves but simply align the fibers and/or straighten them from their normally wavy or crimped configuration. However, once the collagen network is aligned and straightened at larger strains, the stresses act di-

rectly on the rigid collagen fiber backbone. As a result, biological tissues have a soft and elastic consistency under normal physiological conditions but become much stiffer when loaded in an extreme fashion. Both tissue extensibility and strength are relevant to pulsed ablation, as they provide a guide to the stresses and deformations that must be generated when material removal is achieved via fracture of the tissue matrix.

There is a positive correlation between tissue strength and collagen content.<sup>52</sup> Tissues that represent extremes of mechanical strength are the liver and tendon. Liver is a very soft and friable tissue possessing a very low ultimate tensile strength (UTS) of 23 kPa but a moderate extensibility at fracture of ~40%.<sup>33,53,54</sup> Tendon, by contrast, is both strong and stiff, with an UTS of  $\geq 100$  MPa and a fracture extensibility of ~10%. Liver is a cell-continuous tissue with little ECM and collagen content. Tendon is a matrix-continuous tissue that possesses high collagen content. Other matrix-continuous tissues, such as ligament and skin, have similarly high collagen content (25–33%) and similar, albeit lower, UTS (~40 and ~10 MPa, respectively) relative to tendon.

Tissue extensibility is related to both the architecture of the collagen fibrils and the content of another ECM protein, elastin. Elastin is a strongly hydrophobic and very extensible protein that forms a covalently cross-linked network of fibers within some collagen-based tissues, such as dermis.<sup>31,33</sup> Collagen-based tissues with high extensibility tend to have collagen fibrils that are wavy or crimped and can partially reorient to align with the direction of the applied stress. The waviness of the collagen fibrils provides tissue extensibility simply by straightening when loaded. The intercalation of elastin with the collagen fibril network provides these tissues with some additional stiffness as the collagen fibrils straighten. As a result of the waviness of the collagen fibrils, skin fractures at relatively large extensibilities between 30 and 100%.

One must exercise caution when relating published stress–strain data of biological tissue to pulsed laser ablation. The stresses reported are often calculated on the basis of the ratio of the applied load to the cross-sectional area of the *un-deformed* sample. In fact, the cross-sectional area of biological tissues reduces significantly when loaded under tension. Thus, to avoid an underestimation of the UTS, one must determine the “engineering stress”, which is obtained by dividing the applied load by the cross-sectional area of the sample when loaded.<sup>33</sup> A second issue warranting concern is that nearly all tissue mechanical data are acquired under “quasi-static” loading, i.e., conditions under which the tissue is deformed at very slow strain rates, typically on the order of 0.1% or  $10^{-3}$  s<sup>-1</sup>. However, during a pulsed laser ablation process, tissue is subjected to enormously high strain rates, on the order of  $10^5$ – $10^7$  s<sup>-1</sup>. Some studies have been performed to examine the variation of tissue properties with strain rate over the range 0.3–170 s<sup>-1</sup>.<sup>55–57</sup> These studies indicate that, while the tissue strain at fracture does not



change significantly with strain rate, the UTS increases. The increase in UTS is due to the fact that, under conditions of rapid deformation, there is significant viscous dissipation between the collagen fibrils and the adjacent ground substance. The available data demonstrate that the UTS increases in proportion to the logarithm of the strain rate. However, it is not known whether this dependence remains valid up to the extreme strain rates produced by pulsed laser ablation. Nevertheless, the available data suggest that the tissue UTS under ablative conditions can be considerably higher than that measured under 'quasi-static' loading conditions.

### C. Thermal Denaturation

Thermal denaturation of ECM proteins resulting from pulsed laser irradiation is of great importance, as it affects the dynamics of the ablation process and governs the extent of thermal injury produced in the remaining tissue. Here we limit our discussion to the denaturation kinetics of fibrillar collagen. Denaturation of fibrillar collagen begins when a rise in temperature increases the kinetic energy of the constituent molecules such that they overcome the weak hydrogen bonds and van der Waals interactions that are responsible for stabilizing the helical configuration of the  $\alpha$ -chains in the TC molecule.<sup>43</sup> If the collagen is free to deform, the denaturation results in a structural transformation of the TC molecule from a "native" triple-helical structure to a "denatured" random coil structure that is associated with a loss of the banding pattern of the native collagen fibrils in TEM.<sup>37</sup> When this helix-coil transition is accomplished, the fibrils shrink due to the presence of the covalent cross-links that connect and maintain the organization of the microfibrils.<sup>35</sup> The shrinkage occurs parallel to the longitudinal axis of the fibrils and results in a thickening in a direction perpendicular to the fibrils. However, when the collagen is under isometric conditions, this deformation is not allowed, and a tensile stress is developed along fibrils.<sup>58,59</sup> Studies of the helix-coil transition under quasi-static heating conditions using differential scanning calorimetry reveal that the transition has the characteristics of a first-order phase transformation with a well-defined "melting" temperature and enthalpy of denaturation.<sup>60,61</sup> The melting temperature and latent enthalpy increase with the relative amount proline and hydroxyproline residues in the primary amino acid sequence of the  $\alpha$ -chains. As noted in section II.A, these imino acid residues block rotation of the peptide backbone at these sites and apparently contribute to the thermal stability of the collagen triple helix.<sup>43,60,62</sup>

When the tissue is heated further, a second stage of denaturation occurs via the hydrolysis of initially the thermally labile and subsequently the thermally stable covalent cross-links between the TC molecules. This results in a stepwise disintegration of the collagen fibrils<sup>63</sup> and a relaxation of the stresses developed during shrinkage.<sup>58,59,64</sup> The dissolution of the cross-links is termed "gelatinization" or "hyalinization" and results in total mechanical failure and disintegration of the fibrillar structure of the tis-

sue.<sup>37,43</sup> The temperature for maximum shrinkage and the relaxation temperature are dependent on the density and type of covalent cross-links within the tissue. Older tissues possess a higher density of cross-links and thus display increased thermal stability with corresponding increases in the characteristic temperatures for maximum shrinkage and for stress relaxation.<sup>35,65,66</sup>

Thermal denaturation is a rate process, as the ability to transform a tissue from a native to a denatured state depends not only on temperature but also on the duration of the exposure to the elevated temperature.<sup>67-70</sup> If the heating time is reduced, considerably higher temperatures are required for denaturation.<sup>67,70-72</sup> Often the Arrhenius rate integral is applied to estimate the thermal injury. For a given thermal transient,  $T(t)$ , the accumulation of thermal injury can be expressed as

$$\Gamma(t) = \int_0^t A \exp\left(\frac{-\Delta E}{k_B T(t')}\right) dt' \quad (1)$$

where  $\Gamma(t)$  is a dimensionless measure of the degree of thermal injury accumulated at time  $t$ ,  $k_B$  is the Boltzmann constant,  $\Delta E$  is the activation energy barrier for the denaturation process, and  $A$  is a frequency factor.<sup>70</sup> For fibrillar collagens, this temperature-time relationship has been studied only for relatively long ( $\geq 1$  s) thermal exposures. With exposure times of several minutes, the onset of shrinking of dermal and corneal collagen occurs at approximately 60 °C, regardless of collagen type and cross-link density.<sup>58,73</sup> Relaxation of the tissue shrinkage, indicating gelatinization, begins at temperatures above 77 °C in 15-month-old rat skin, with a temperature of 100 °C being necessary to reduce tissue shrinkage to half its maximal value.<sup>58</sup> However, when heating 52-year-old human skin, which possesses a greater density of thermally stable covalent cross-links, no stress relaxation was observed upon exposure to temperatures up to 100 °C over several minutes.<sup>65</sup> These results indicate that the tissue matrix remains mechanically intact at temperatures of 100 °C or higher, even for long thermal exposures. For short thermal exposures in the nanosecond to millisecond range, characteristic of pulsed laser ablation, the temperatures required to affect mechanical stability are certainly far in excess of 100 °C. Moreover, it is known that the application of external tensile stresses to collagen fibrils stabilizes the helical architecture and results in a significant increase in the denaturation temperature.<sup>74,75</sup> Thus, the generation of internal tensile stresses resulting from pulsed laser heating is expected to further stabilize the collagen ECM with respect to possible collagen denaturation. Nevertheless, given that surface temperatures approaching 400–750 °C have been measured during tissue ablation using laser pulses of 100  $\mu$ s duration,<sup>76</sup> the possibility of a modification in the mechanical integrity of the tissue ECM during the nanosecond to millisecond time scales that we consider here remains likely. Moreover, when using nanosecond laser pulses, it is possible, even at moderate radiant exposures, to raise the temperature



in the superficial tissue layer to values exceeding 1000 °C at which point the constituent molecules of the ECM can be thermally dissociated into volatile fragments.

### III. Energy Deposition and Transport

The spatial distribution of volumetric energy density generated by laser irradiation drives all pulsed laser ablation processes. This distribution is controlled by the incident radiant exposure,  $\Phi_0$ , and the optical absorption and scattering properties of the tissue. A survey of the photophysical and photochemical determinants of tissue optical properties has been prepared by Hillenkamp,<sup>14</sup> and surveys restricted to the ultraviolet spectral region are provided by Pettit<sup>18</sup> and by Coohill.<sup>77</sup> A presentation of the numerous optical methods currently used for optical property determination can be found in the book by Welch and van Gemert.<sup>9</sup> Tissue optical properties have also been determined through measurement and analysis of laser-induced mechanical and thermal transients.<sup>78–82</sup> Here we shall provide an overview of the key components that govern tissue optical properties and discuss the implications for radiative transport and the resulting spatial scales for energy deposition within tissue. A compilation of tissue optical properties measured *in vitro* and *in vivo* has been prepared by Cheong.<sup>83</sup>

#### A. Optical Absorption Properties of Tissue

The optical absorption properties of tissue are governed by the electronic, vibrational, and rotational structures of the constituent biomolecules.<sup>14</sup> In non-turbid samples, optical transmission  $T$  is governed by Beer–Lambert's law according to

$$T = \left[ \frac{\Phi}{\Phi_0(1 - R_s)} \right] = 10^{-\epsilon cl} = \exp(-\mu_a l) \quad (2)$$

where  $R_s$  is the specular reflection of the sample and  $\Phi$  is the radiant exposure transmitted after travel through an optical path length  $l$  in a sample with molar extinction coefficient  $\epsilon$  ( $\text{M}^{-1} \text{cm}^{-1}$ ) and concentration  $c$  ( $\text{M}$ ). Alternatively, the absorption properties of the sample can be characterized by an absorption coefficient  $\mu_a$  ( $\text{cm}^{-1}$ ). Typically, in the biomedical optics community, the absorption coefficient  $\mu_a$  is used to express the optical absorption properties of tissue, while  $\epsilon$  is used in reference to the optical absorption properties of specific isolated biomolecules. In general, the optical absorption properties of tissue are dominated by the absorption of proteins, DNA, melanin, hemoglobin, and water. However, as shown in Figure 4, the variation of their optical activities with wavelength is quite different. In the following sub-sections, we examine the principal tissue chromophores in the ultraviolet, visible, and infrared spectral regions.

##### 1. Ultraviolet Radiation ( $\lambda = 180\text{--}400 \text{ nm}$ )

The ultraviolet (UV) region of the optical spectrum relevant for tissue ablation lies between the vacuum ultraviolet (VUV;  $\lambda < 180 \text{ nm}$ ) and visible regions.

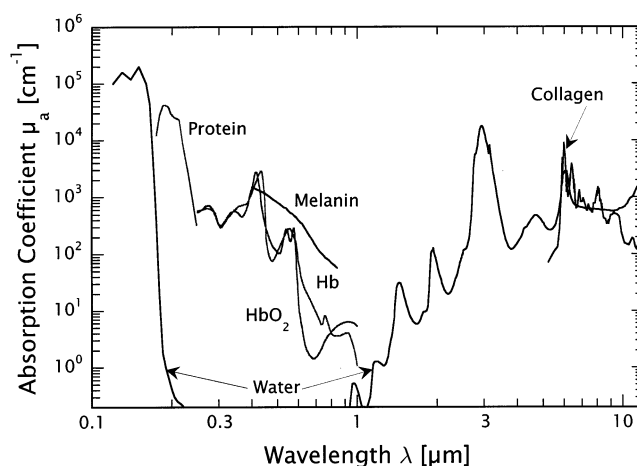


**Figure 4.** Optical absorption coefficients of principal tissue chromophores in the 0.1–12- $\mu\text{m}$  spectral region.

UV radiation represents light with very high photon energy (6.5–3.1 eV) and enables the excitation of  $n \rightarrow \sigma^*$  and  $\pi \rightarrow \pi^*$  molecular orbital transitions. UV absorption properties of tissues have long been of interest to the photobiology community.<sup>84</sup> While water displays significant absorption at  $\lambda \leq 170 \text{ nm}$ , its absorption throughout the UV at room temperature is negligible.<sup>85–87</sup> The dominant tissue chromophores in the UV are proteins, DNA, and melanin. In general, UV absorption by collagen-based soft tissues drops significantly with wavelength. Accordingly, the characteristic optical absorption depth ( $1/\mu_a$ ) of these tissues varies from  $\lesssim 0.5 \mu\text{m}$  at  $\lambda = 190 \text{ nm}$  to  $\sim 200\text{--}400 \mu\text{m}$  at  $\lambda = 400 \text{ nm}$ .

The most important chromophore at short UV wavelengths is the peptide bond ( $\text{O}=\text{C}-\text{N}-\text{H}$ ) present in the backbone of all proteins. This absorption peak is centered at roughly  $\lambda = 190 \text{ nm}$  and is accomplished through an  $n \rightarrow \sigma^*$  transition.<sup>77,88</sup> Given that, in human tissue, protein is the most abundant constituent next to water, the absorption coefficients of tissues containing large amounts of the protein collagen, (e.g., cornea, dermis) is very high in the wavelength region around  $\lambda = 190 \text{ nm}$  and has a value of  $\mu_a = (2\text{--}4) \times 10^4 \text{ cm}^{-1}$ .<sup>81,89</sup> Although the absorption of the peptide bond falls considerably at longer wavelengths, its contribution to overall tissue absorption remains significant to  $\lambda = 240 \text{ nm}$ .<sup>84</sup>

At longer UV wavelengths, deoxyribonucleic acid (DNA), the aromatic amino acid residues, and melanin become important chromophores. With respect to DNA, both the purine and pyrimidine bases are aromatic and responsible for the DNA absorption peak centered at  $\lambda = 260 \text{ nm}$ . Because of this absorption peak, DNA displays an optical absorption that is 10–20 times higher than that for an equal weight of protein in the  $\lambda = 240\text{--}290 \text{ nm}$  wavelength region.<sup>84</sup> Although DNA displays an even higher absorption at  $\lambda \leq 210 \text{ nm}$ , its contribution to tissue absorption is negligible when compared to the absorption cross section and the concentration of the peptide bond present in tissue protein. The aromatic amino acids tryptophan, tyrosine, and phenylalanine also exhibit broad absorption peaks centered in the  $\lambda = 250\text{--}280 \text{ nm}$  region that are accomplished via a  $\pi \rightarrow \pi^*$  molecular orbital transition.<sup>88</sup> It should be

noted, however, that connective tissues are relatively acellular and do not have much DNA content. Moreover, no more than 3% of the amino acid residues in collagen are aromatic.<sup>34,35</sup> Therefore, even within the spectral region where both aromatic amino acids and DNA absorb, the absorption of collagen-based tissues is at least 100 times lower for  $\lambda = 240\text{--}290\text{ nm}$  than in the  $\lambda = 190\text{ nm}$  region.

Melanin absorption is important when considering the optical absorption properties of pigmented tissues such as the skin, iris, and retinal pigment epithelium. Melanin refers to a large class of biological pigments whose color in the visible ranges from yellow and red-brown to brown and black. In human skin, the optical absorption of melanin becomes important at about  $\lambda = 300\text{ nm}$ , and after displaying an apparent absorption peak at  $\lambda = 335\text{ nm}$ , its absorption spectrum drops monotonically with wavelength from the UV to the IR.<sup>90–92</sup>

## 2. Visible Radiation ( $\lambda = 400\text{--}780\text{ nm}$ )

Optical absorption properties of tissue in the visible spectral region are dominated by the absorption of melanin and hemoglobin. Hemoglobin itself is present in tissue in both deoxygenated (Hb) and oxygenated (HbO<sub>2</sub>) forms. Although Hb and HbO<sub>2</sub> do display optical absorption in the UV, their absorption becomes significant relative to that of other tissue chromophores only in the visible spectral region. Hb and HbO<sub>2</sub> have their most prominent absorption peaks in the violet at  $\lambda = 433$  and  $414\text{ nm}$ , respectively.<sup>93</sup> Their absorption drops by more than an order of magnitude in the violet and blue and then increases again in the green, where HbO<sub>2</sub> presents absorption peaks at  $\lambda = 542$  and  $576\text{ nm}$  and Hb presents an absorption peak at  $\lambda = 556\text{ nm}$ . The absorption of both of these chromophores drops again by over an order of magnitude in the yellow/red. Despite this fact, as all biomolecules have little absorption in the red and near-infrared, both Hb and HbO<sub>2</sub> contribute significantly to the overall optical absorption of vascularized tissues into the near-infrared region.<sup>93,94</sup>

In pigmented tissues such as skin, hair, and ocular tissues, melanin plays a significant role in determining the optical absorption properties. The absorption spectrum of melanin is featureless in the visible spectrum, dropping monotonically with wavelength such that its absorption at  $\lambda = 780\text{ nm}$  is roughly 10% of that at  $\lambda = 400\text{ nm}$ .<sup>95,96</sup> This featureless characteristic of the absorption spectrum of melanin is somewhat surprising. A possible explanation may reside in the fact that melanin naturally exists in particulate form with a diameter of roughly  $160\text{ nm}$ .<sup>97</sup> Thus, the contribution of optical scattering to the measured extinction coefficient of melanin cannot easily be separated from the intrinsic absorption properties of melanin.<sup>96</sup> Recent work indicates that the extinction coefficient of melanin is primarily due to a large scattering coefficient that at visible wavelengths dominates absorption by as much as 100 times.<sup>98</sup>

## 3. Near-Far-Infrared Radiation ( $\lambda = 780\text{ nm}\text{--}15\text{ }\mu\text{m}$ )

Apart from hemoglobin, which contributes significantly to the optical absorption of vascularized tissues out to approximately  $\lambda = 1000\text{ nm}$ , water and protein are the principal tissue chromophores in the infrared (IR) spectral region. Water is the most important tissue chromophore in the infrared and begins to contribute significantly to tissue absorption at  $\lambda \gtrsim 900\text{ nm}$ . The absorption spectrum of water is governed by the resonance of its symmetric and asymmetric stretch modes that are located at  $\nu_1 = 3651.7\text{ cm}^{-1}$  ( $\lambda = 2.74\text{ }\mu\text{m}$ ) and  $\nu_3 = 3755.8\text{ cm}^{-1}$  ( $\lambda = 2.66\text{ }\mu\text{m}$ ), respectively, and the resonance of its symmetric bend mode at  $\nu_2 = 1595\text{ cm}^{-1}$  ( $\lambda = 6.27\text{ }\mu\text{m}$ ).<sup>99</sup> These vibrational modes and their combinations give rise to its absorption peaks, located at  $\lambda = 0.96, 1.44, 1.95, 2.94, 4.68,$  and  $6.1\text{ }\mu\text{m}$ .<sup>100</sup> The optical absorption of water in the near-infrared is initially quite weak but rises quite rapidly with wavelength. From the visible spectral region, the absorption of water increases by nearly 6 orders of magnitude and reaches a maximum at  $\lambda = 2.94\text{ }\mu\text{m}$ , where the absorption coefficient is  $\mu_a = 12\,000\text{ cm}^{-1}$ .<sup>101</sup> Although this absorption is high, it is nearly 3 times lower than the optical absorption of collagen-based tissues in the UV at  $\lambda \approx 190\text{ nm}$ . Optical absorption continues to be strong ( $\mu_a > 500\text{ cm}^{-1}$ ) in the far-infrared ( $6\text{--}15\text{ }\mu\text{m}$ ) and exhibits another maximum at  $\lambda = 6.1\text{ }\mu\text{m}$ , where  $\mu_a = 2740\text{ cm}^{-1}$ .

The other chief chromophore in the IR is protein. Infrared spectra of proteins in the IR are governed by various vibrational modes of the peptide bond (O=C–N–H). The most important of these are (1) the C=O stretch, also termed the amide I band, which for collagen is located at  $\nu_1 = 1640\text{--}1660\text{ cm}^{-1}$  ( $\lambda = 6.02\text{--}6.10\text{ }\mu\text{m}$ ); (2) the N–H in-plane deformation with C–N stretch, also termed the amide II band, located at  $\nu_2 = 1535\text{--}1550\text{ cm}^{-1}$  ( $\lambda = 6.45\text{--}6.51\text{ }\mu\text{m}$ ) for collagen; and (3) the C–N stretch with N–H in-plane deformation, also termed the amide III band, located at  $\nu_3 = 1230\text{--}1270\text{ cm}^{-1}$  ( $\lambda = 7.87\text{--}8.13\text{ }\mu\text{m}$ ) for collagen.<sup>34,102</sup> Collagen and water share an absorption peak at  $\lambda \approx 6.1\text{ }\mu\text{m}$ , where the absorption of collagen is larger than that of water by more than a factor of 2. For the amide II peak at  $\lambda \approx 6.45\text{ }\mu\text{m}$ , the absorption of water is roughly a factor of 6 lower than that of protein.

## B. Optical Scattering Properties of Tissue

Both optical absorption and scattering play important roles in determining the spatial distribution of volumetric energy density deposited by laser radiation in tissue. When scattering is negligible or absent, the optical penetration depth,  $\delta$ , of the incident radiation is given by the reciprocal of the absorption coefficient and defines the characteristic depth to which the tissue is heated. However, at wavelengths where optical scattering is significant,  $\delta$  is smaller than  $1/\mu_a$  and also is dependent on the diameter of the laser beam.<sup>103</sup>

Optical scattering arises from spatial variations in the refractive index within tissue. This variation is dependent on the composition, size, and morphology

of both cellular and extracellular tissue components.<sup>104–109</sup> The effect that any given scatterer has upon the light distribution is dependent not only on its scattering properties but also on its spatial location and orientation relative to neighboring scatterers. As a consequence, even in systems with large densities of optical scatterers, significant scattering results only when substantial variation in the refractive index is present over length scales that are comparable to or larger than half the wavelength of light.<sup>50,110</sup> For example, the microstructure of human cornea is very regular, such that the collagen fibrils have diameters of  $\sim 30$  nm and are spaced at center-to-center distances of  $\sim 65$  nm. Thus, the variation of refractive index over a spatial scale comparable to the wavelength of visible light is very small, even though individual collagen fibrils are strong scatterers. This feature provides the optical transparency of the cornea in the visible spectrum. Other collagen-based tissues, such as dermis and sclera, possess collagen fibrils with a significant variability in diameter (30–300 nm), orientation, and spacing. This variability produces significant refractive index variations over spatial scales comparable to half the wavelength of visible light, resulting in opacity.<sup>41,49,50</sup>

Typical reduced scattering coefficients for tissues in the green are of the order of  $10\text{--}40\text{ cm}^{-1}$ .<sup>83</sup> In addition, scattering data for tissue acquired over significant wavelength ranges indicate that the reduced scattering coefficient is well characterized by the scaling law  $\mu_s' \sim \lambda^{-b}$ , where  $b \approx 0.5\text{--}2$ .<sup>111,112</sup> Apart from the absolute values of the tissue optical properties, the magnitude of optical absorption relative to optical scattering is a key determinant of the spatial distribution of radiation generated by the laser exposure. When absorption is dominant over scattering, application of the Beer–Lambert law is appropriate to determine the spatial distribution of the absorbed radiation from a known absorption coefficient. However, when scattering is dominant over or comparable to optical absorption, one must resort to more detailed models of radiative transport (e.g., using Monte Carlo simulations or approximate solutions such as those provided by diffusion or random-walk models) to obtain the distribution of the absorbed radiation.<sup>103,113,114</sup>

Figure 5 presents the relative magnitudes of absorption and scattering in skin as a function of wavelength. For  $\lambda < 450$  nm, the optical activity of the peptide bond, aromatic amino acid residues, DNA, and hemoglobin provides for the domination of absorption over scattering. For  $\lambda = 450\text{--}1750$  nm, tissue scattering is, in general, more prevalent than absorption, although for  $\lambda = 450\text{--}600$  nm, melanin and hemoglobin provide significant absorption while water plays a similar role for  $\lambda > 1350$  nm. At longer wavelengths, water absorption picks up dramatically, and for  $\lambda > 1750$  nm, tissue absorption once again dominates over scattering. The optical scattering will reduce the optical penetration depth,  $\delta$ , of light relative to the absorption depth. Moreover, for scattering tissues,  $\delta$  becomes smaller as the laser beam diameter is reduced.<sup>15,103</sup> In addition, when scattering is dominant over absorption, backscattering and total

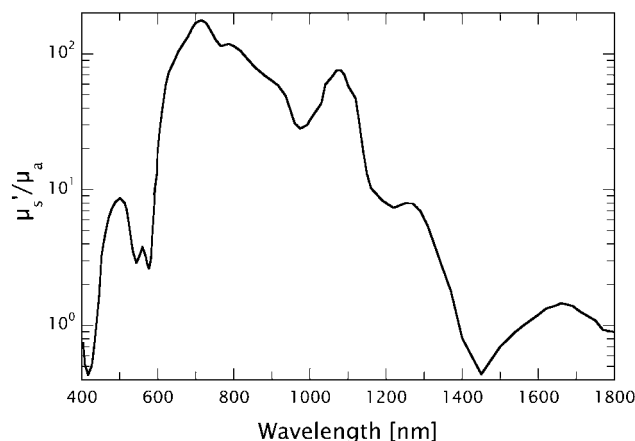


**Figure 5.** Ratio of the reduced scattering coefficient to the absorption coefficient of human skin. For wavelengths below 450 nm and above 1800 nm, optical absorption, provided by hemoglobin and protein in the UV and water in the mid- and far-IR, dominates the optical properties. Data compiled from refs 111 and 112.

internal reflection lead to a large fluence rate proximal to the tissue surface which can exceed by several times the delivered irradiance.<sup>15,103</sup> It should be noted, however, that using laser wavelengths where optical scattering is comparable to or dominant over tissue absorption is not conducive to precise ablation (see section IV.C).

### C. Dynamic Optical Properties in Tissue

Typically, measurement of tissue optical properties is done under room or physiological conditions. However, the thermal and mechanical transients generated by pulsed laser ablation processes are substantial and can result in a significant alteration of the tissue optical properties. While thermal denaturation can result in a significant increase (as much as 5 times) in the reduced scattering coefficient,<sup>115–117</sup> such changes are usually of minor importance, considering that ablation is typically performed at wavelengths where optical absorption dominates scattering. Changes in tissue absorption, however, are much more important. Walsh and co-workers<sup>118,119</sup> suggested in 1989 that tissue absorption may change significantly during laser irradiation to explain the unexpectedly large etch depths and zones of thermal injury produced by Q-switched Er:YAG ( $\lambda = 2.94\text{ }\mu\text{m}$ ) laser ablation of tissue. Subsequent studies that investigated the thermal injury and mass removal produced by pulsed IR laser ablation at other wavelengths also found results that were not fully consistent with the room-temperature absorption spectra of water.<sup>120–122</sup>

Motivated by spectroscopy literature indicating that the absorption peak of water at  $\lambda = 2.94\text{ }\mu\text{m}$  drops and shifts toward shorter wavelengths for increasing temperature,<sup>123,124</sup> various researchers investigated the reduction in the IR absorption coefficient of tissue upon heating of the tissue.<sup>26,125–130</sup> This reduction in optical absorption occurs due to the weakening of the hydrogen bonds between adjacent water molecules at higher temperature that results in a change in the length and strength of the OH bond. In the  $2\text{-}\mu\text{m}$  region, the absorption coeffi-



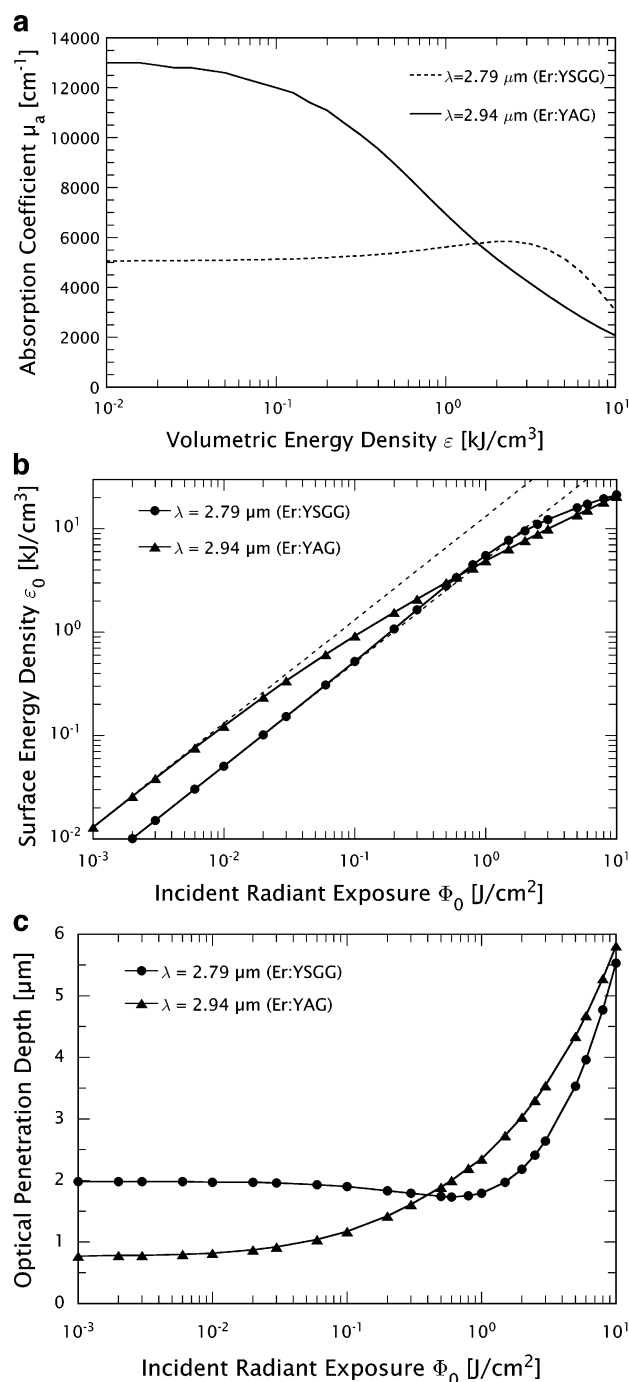


**Figure 6.** Effects of dynamic optical properties of a water target produced by Er:YSGG ( $\lambda = 2.79 \mu\text{m}$ ) and Er:YAG ( $\lambda = 2.94 \mu\text{m}$ ) laser irradiation. (a) Variation of optical absorption coefficient of water with volumetric energy density. Data compiled from refs 125 and 129. (b) Variation of volumetric energy density at the water surface with incident radiant exposure. Dashed lines indicate the expected variation if the absorption coefficient remained constant. (c) Variation of optical penetration depth with incident radiant exposure. Optical penetration depth is defined as the location at which the volumetric energy density drops to  $1/e$  of the surface value. Note that for incident radiant exposures  $\Phi_0 > 0.4 \text{ J}/\text{cm}^2$ , Er:YSGG laser irradiation offers more superficial energy deposition compared to Er:YAG laser irradiation.

cient drops by a factor of 2 at temperatures nearing  $100^\circ\text{C}$ .<sup>127,130</sup> The  $3\text{-}\mu\text{m}$  region offers the most dramatic change in absorption coefficient with temper-

ature. Results from a recent study by Shori and co-workers<sup>129</sup> for wavelengths of  $\lambda = 2.94 \mu\text{m}$ , along with data at  $\lambda = 2.79 \mu\text{m}$  obtained from an earlier study by Cummings and Walsh,<sup>125</sup> are shown in Figure 6a. At  $\lambda = 2.94 \mu\text{m}$ , the absorption coefficient remains nearly identical to the room-temperature value of  $\mu_a \approx 13000 \text{ cm}^{-1}$  until a volumetric energy density of  $0.02 \text{ kJ}/\text{cm}^3$  is reached; it then drops monotonically, reaching  $\mu_a \approx 2000 \text{ cm}^{-1}$  at  $20 \text{ kJ}/\text{cm}^3$ . For  $\lambda = 2.79 \mu\text{m}$ , the absorption coefficient remains at the room-temperature value of  $\mu_a \approx 5250 \text{ cm}^{-1}$  up to a volumetric energy density of  $\sim 1 \text{ kJ}/\text{cm}^3$ , when it begins to rise up to a maximum of approximately  $\mu_a \approx 6000 \text{ cm}^{-1}$  as a result of the  $\lambda = 2.94 \mu\text{m}$  absorption peak shifting to shorter wavelengths. When an energy density of  $4 \text{ kJ}/\text{cm}^3$  is reached, the absorption coefficient begins to fall and reaches  $\mu_a \approx 1000 \text{ cm}^{-1}$  at  $\sim 20 \text{ kJ}/\text{cm}^3$ .<sup>128</sup>

To appreciate the consequences of these findings, we performed finite difference calculations based on the absorption data shown in Figure 6a to determine the variation of the volumetric energy density absorbed at the tissue surface  $\varepsilon_0$  with incident radiant exposure,  $\Phi_0$ . The results are shown in Figure 6b. At  $\lambda = 2.94 \mu\text{m}$ , the increase of the volumetric energy deposition with radiant exposure reduces noticeably for  $\Phi_0 > 2 \times 10^{-2} \text{ J}/\text{cm}^2$ . This is due to the reduction in absorption coefficient at the surface that results in the deposition of laser energy to larger depths within the sample. By contrast, at  $\lambda = 2.79 \mu\text{m}$ , there is an enhancement of volumetric energy deposition at the surface over the radiant exposure interval of  $0.05\text{--}1.5 \text{ J}/\text{cm}^2$ . It is only for  $\Phi_0 > 1.5 \text{ J}/\text{cm}^2$  that we observe the effects of reduction of optical absorption on the volumetric energy density.

In Figure 6c, we present the variation in optical penetration depth as defined by the depth at which the volumetric energy density drops to  $1/e$  of that delivered to the tissue surface. It is evident that for  $\Phi_0 > 0.5 \text{ J}/\text{cm}^2$ , Er:YSGG radiation offers better spatial confinement of the laser energy than Er:YAG radiation. This is opposite to the behavior one would expect from the absorption coefficients measured at small radiant exposures.

The possibility of a variation in optical absorption with temperature in the UV has also been investigated. Ediger, Pettit, and co-workers reported that the absorption of collagen targets may be enhanced during laser irradiation at  $\lambda = 193 \text{ nm}$  and persists for a significant time ( $\sim 10^{-4} \text{ s}$ ) thereafter.<sup>131,132</sup> Moreover, in a paper by Staveteig and Walsh,<sup>133</sup> it is postulated that although the absorption of UV radiation by the peptide bond is a necessary first step in the UV ablation process, the heating of the surrounding water results in a change in hydrogen-bonding structure that leads to a shift of the water absorption band located at  $160 \text{ nm}$  to longer wavelengths. The paper provides data indicating that the absorption of water at  $\lambda = 193 \text{ nm}$  may be raised to as much as  $\mu_a \approx 10^4 \text{ cm}^{-1}$  at a volumetric energy density of  $2 \text{ kJ}/\text{cm}^3$ . This raises the possibility that UV laser ablation of tissue is driven by the optical absorption of both collagen and water.

#### IV. Linear Thermomechanical Response of Tissue to Pulsed Irradiation

The spatial distribution of volumetric energy density resulting from pulsed laser irradiation of tissue generates significant thermal and mechanical transients. These thermomechanical transients are the driving force for all laser ablation processes that are not photochemically mediated. In this section we describe the linear thermomechanical response of tissue as it is a precursor to the processes that follow. In section V, we then address the kinetics of phase transitions and photochemical processes that produce material removal in pulsed laser ablation.

##### A. Temperature Rise and Thermal Diffusion

In the absence of photochemical or phase transition processes, the energy absorbed by the tissue in response to pulsed laser irradiation is entirely converted to a temperature rise. Under adiabatic conditions, the local temperature rise at an arbitrary location  $r$ ,  $\Delta T(r)$ , is directly related to the local volumetric energy density,  $\epsilon(r)$ , as

$$\Delta T(r) = \frac{\epsilon(r)}{\rho c_v} \quad (3)$$

where  $\rho$  is the tissue density and  $c_v$  the specific heat capacity at constant volume. Once this energy is absorbed, it is subject to spatial redistribution by thermal diffusion.<sup>9,134</sup> In 1983, Anderson and Parrish<sup>135</sup> introduced the concept that spatially confined microsurgical effects (selective photothermolysis) can be achieved by the use of laser exposures that are shorter than the characteristic thermal diffusion time of the heated volume. For laser ablation, the heated volume is typically a layer of tissue of thickness  $1/\mu_a$ , and the characteristic thermal diffusion time,  $t_d$ , is given as<sup>15,103</sup>

$$t_d = \frac{1}{\kappa \mu_a^2} \quad (4)$$

where  $\kappa$  is the thermal diffusivity. "Thermal confinement" is achieved when the ratio of the laser pulse duration to the thermal diffusion time fulfills the condition  $(t_p/t_d) \lesssim 1$ . By defining a dimensionless measure of the laser pulse duration relative to the characteristic thermal diffusion time,  $t_d^* = (t_p/t_d)$  and using eq 4, the thermal confinement condition can be expressed as

$$t_d^* = \kappa \mu_a^2 t_p \lesssim 1 \quad (5)$$

The concept of thermal confinement can be appreciated by considering the temperature distribution within a water sample irradiated with a fixed radiant exposure using different pulse durations, as shown in Figure 7 for a planar semi-infinite target with  $\mu_a 10^4 \text{ cm}^{-1}$  (i.e., optical penetration depth of  $1 \mu\text{m}$ ). For this case, the characteristic thermal diffusion time given by eq 4 is  $t_d = 6.9 \mu\text{s}$ . At the end of laser exposures with duration  $t_p < 3 \mu\text{s}$ , the temperature profile is almost fully confined to the volume in which

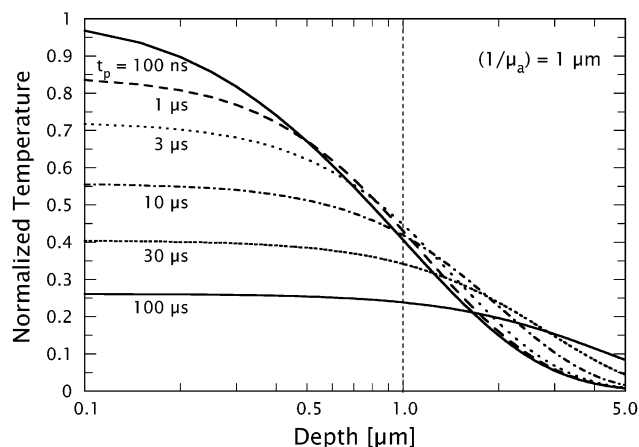


**Figure 7.** Normalized temperature profiles in water immediately following laser irradiation with a fixed radiant exposure and optical penetration depth ( $1 \mu\text{m}$ ) for various pulse durations,  $t_p$ .

the radiation is absorbed. However, for exposure durations of  $t_p \geq 10 \mu\text{s}$ , thermal diffusion has redistributed the energy over a larger volume and has reduced significantly the peak temperatures within the sample.

Water and collagen are most often the main chromophores for pulsed IR and UV ablation, respectively. When using a wavelength that is absorbed by water and not collagen (or vice versa), one must consider whether the concept of thermal confinement applies not only to the heated volume as a whole but also to the individual microscopic tissue structures that absorb the radiation.<sup>136,137</sup> As most matrix-continuous soft tissues consist of collagen fibrils embedded within a highly hydrated ground substance, microscale thermal confinement relates to length scales comparable to the collagen fibril diameter. Collagen fibrils in the corneal stroma and in dermis possess diameters of 30 and 100 nm, respectively, with corresponding characteristic thermal diffusion times  $t_d$  of 6.3 and 69 ns. These times are comparable in magnitude to the duration of UV excimer laser pulses when  $t_p \approx 20\text{--}30 \text{ ns}$  as well as Q-switched IR laser pulses when  $t_p \approx 100 \text{ ns}$ . Thus, while microscale thermal confinement may influence the ablation of skin, it is unlikely to play a strong role in the ablation of cornea unless laser pulses of picosecond or femtosecond duration are employed.

##### B. Thermoelastic Stress Generation and Propagation

Rapid heating of tissue by pulsed laser radiation also leads to the generation and propagation of thermoelastic stresses as the heated tissue volume reconfigures to its new equilibrium state. The magnitude and temporal structure of the thermoelastic stresses are governed by the longitudinal speed of sound in the medium,  $c_a$ , the laser pulse duration,  $t_p$ , the depth of the heated volume,  $1/\mu_a$ , and an intrinsic thermophysical property known as the Grüneisen coefficient.<sup>138–143</sup> The Grüneisen coefficient is simply the internal stress per unit energy density generated upon depositing energy into a target under constant volume (i.e., isochoric) conditions. Thus, its

definition is given by the thermodynamic derivative:<sup>144</sup>

$$\Gamma = \left( \frac{\partial \sigma}{\partial \epsilon} \right)_v = \frac{\alpha}{\rho c_v \kappa_T} \quad (6)$$

where  $\sigma$  is the internal stress,  $\epsilon$  the volumetric energy density,  $v$  the specific volume,  $\alpha$  the coefficient of thermal expansion,  $\rho$  the mass density,  $c_v$  the specific heat capacity at constant volume, and  $\kappa_T$  the isothermal compressibility.

Thermoelastic stresses are most prominent when the laser pulse duration  $t_p$  is smaller than or on the order of the characteristic time for a stress wave to propagate across the heated volume,  $t_m = (1/\mu_a c_a)$ . Thus, "stress confinement" is achieved when the ratio of the laser pulse duration to the stress propagation time,  $(t_p/t_m) \lesssim 1$ . When the stress confinement condition is expressed in terms of a dimensionless measure of the laser pulse duration relative to the stress propagation time,  $t_m^* = (t_p/t_m)$ , we obtain

$$t_m^* = \mu_a c_a t_p \lesssim 1 \quad (7)$$

In this case, heating of the laser-affected volume is achieved under isochoric conditions, and the internal stresses generated do not propagate outside the heated volume during the laser irradiation. The peak thermoelastic stress  $\sigma_p$  is given by

$$\sigma_p = A\Gamma\epsilon_0 = A\Gamma\mu_a\Phi_0 \quad (8)$$

where  $A = 1$  and the duration of the thermoelastic stress transient  $t_a$  scales with the stress propagation time (i.e. the acoustic transit time across the heated volume) and  $t_a \approx (4-6)/\mu_a c_a$ .<sup>142,145</sup> When the stress transient leaves the heated volume, the peak stress drops to  $0.5\sigma_p$  (Paltauf and Dyer, this issue).

For cases in which stress confinement is not achieved, i.e.,  $t_m^* = \mu_a c_a t_p \gtrsim 1$ , significant thermal expansion of the heated volume occurs during irradiation. This has the effect of reducing the magnitude of the peak stress, and thus  $A < 1$ . In the limit  $t_m^* \rightarrow \infty$ , where there is no stress confinement,  $A \rightarrow 0$ , and the duration of the stress transient approaches that of the laser pulse.<sup>145</sup> The variation of  $A$  with  $t_m^*$  has been discussed by various authors<sup>138-141,146</sup> and is shown for a biexponential temporal laser pulse shape in Figure 8. It is interesting to note that the pressure amplitudes produced by a laser pulse with a Gaussian temporal profile are slightly higher than those shown in Figure 8 (see Paltauf and Dyer, this issue).

Due to a strong variation in the thermal expansion coefficient with temperature, the Grüneisen coefficient of water is also strongly temperature dependent. A polynomial expression that approximates this temperature variation is given by Paltauf and Schmidt-Kloiber.<sup>143</sup> The effects of this temperature dependence on the magnitude and temporal structure of thermoelastic stress transients have been analyzed.<sup>147,148</sup> A temperature dependence of the stress amplitude has been recently reported for irradiation of the retinal pigment epithelium of the eye.<sup>149</sup>

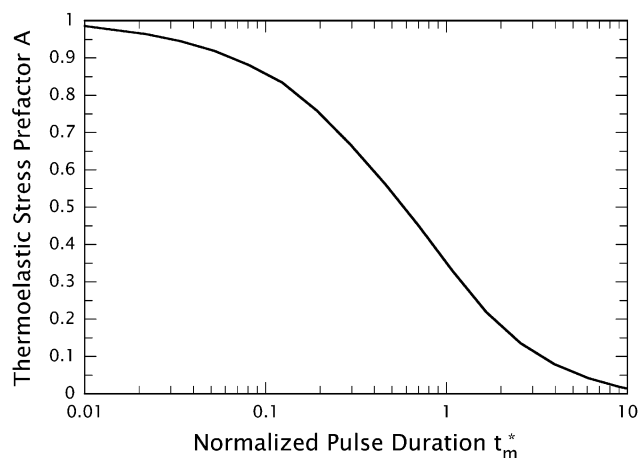


**Figure 8.** Variation of the thermoelastic stress prefactor  $A$  (see eq 8) with the dimensionless pulse duration relative to the stress propagation time across the heated volume  $t_m^*$ . Results are shown for a biexponential laser pulse shape and derived from the results of ref 139.

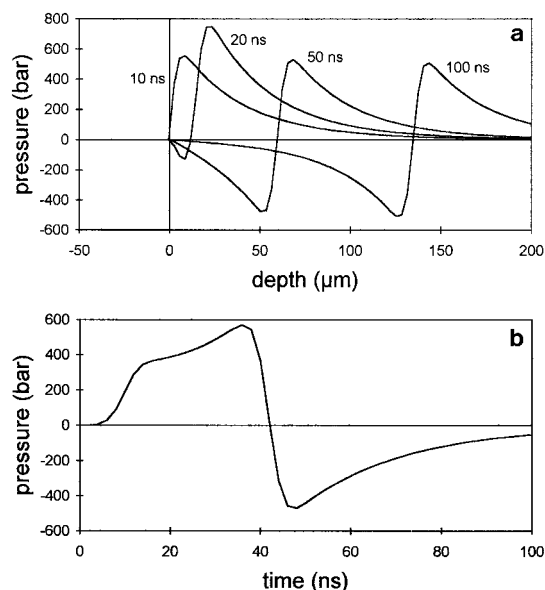


**Figure 9.** (a) Development of a thermoelastic stress wave in water calculated for  $\Phi_0 = 2 \text{ J/cm}^2$ ,  $\mu_a = 200 \text{ cm}^{-1}$ , and  $t_p = 8 \text{ ns}$ . (b) Pressure as a function of time at a depth of  $50 \text{ μm}$ . (Reprinted with permission from ref 143. Copyright 1996 Springer.)

Previous measurements of the variation of thermoelastic stress amplitude with radiant exposure in cornea, dermis, and aorta did not exhibit a strong nonlinearity for radiant exposures below the ablation threshold.<sup>78,137,150</sup>

While thermal expansion of a heated volume generates compressive thermoelastic stresses, subsequent propagation of these stresses result in transients that contain both compressive and tensile components. Tensile stresses arise from the reflection of the compressive stress waves at a boundary to a medium with lower acoustic impedance (tissue–air, tissue–water) or from the three-dimensional characteristics of acoustic wave propagation.<sup>140,143,151-153</sup> Tensile stress wave generation originating from acoustic impedance mismatch is shown in Figure 9. The compressive thermoelastic stress wave that originates from the heated volume at the target surface is almost completely reflected as a tensile



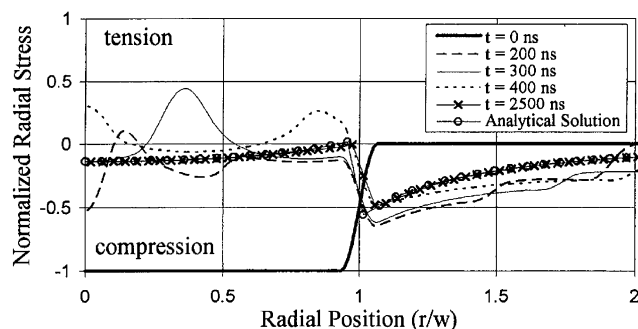


**Figure 10.** Time evolution of radial thermoelastic stresses on a tissue surface as a function of radial position at different times following the laser pulse. In the case shown, the laser beam diameter is  $1200\ \mu\text{m}$  and the optical penetration depth  $860\ \mu\text{m}$ . All stresses are normalized to the initial compressive stress at the surface. (Reprinted with permission from ref 156. Copyright 1995 National Academy of Sciences, U.S.A.)

stress wave at the air–target interface that propagates into the bulk medium. Dingus and Scammon first considered the possibility that tensile stress waves formed in this manner can lead to the fracture and “spallation” of the irradiated target.<sup>141</sup>

The second mechanism for tensile stress generation is connected with the three-dimensional character of stress wave propagation and arises when the condition for planar stress propagation is not satisfied. Conservation of momentum demands that the stress transient emitted from a heated tissue volume must contain both compressive and tensile components, such that the integral of the stress over time vanishes.<sup>153</sup> This phenomenon has also been described as an acoustic diffraction effect.<sup>140,142</sup> Tensile stresses related to the finite size of the heated volume are most pronounced when the laser beam diameter is comparable to the optical penetration depth. Detailed studies have been performed for the propagation of stress waves originating from the tip of an optical fiber immersed in an absorbing liquid<sup>151,152</sup> and from the heated volume in a solid sample that was irradiated in air.<sup>154–156</sup>

Studies in which optical fibers were used to irradiate targets within an absorbing aqueous medium produced significant tensile pressures with the ability to form voids near the fiber axis close to the fiber tip.<sup>151,152</sup> A similar effect has been observed for the ablation of porcine cornea in situ. Compressive recoil stresses produced by the ejection of ablated material from a disklike volume of finite size developed significant tensile stresses, approaching 4 MPa after propagation of a few millimeters into the ocular bulb.<sup>157</sup>

In studies that considered the generation of tensile stress by the irradiation of a solid target, attention was given to the full stress tensor rather than the hydrostatic pressure.<sup>82,154–156</sup> Thus, the three normal stress components, i.e., the axial ( $\sigma_{zz}$ ), radial ( $\sigma_{rr}$ ), and circumferential ( $\sigma_{\theta\theta}$ ) stresses, as well as the appropriate shear ( $\sigma_{rz}$ ,  $\sigma_{r\theta}$ ,  $\sigma_{\theta z}$ ) stress components were considered. As shown in Figure 10, these studies demonstrated that thermoelastic stress wave propagation produced strong transient variations in both

normal and shear stress components with significant tensile components at the target surface. Moreover, significant, albeit weaker, quasi-static stresses remain after the cessation of the thermal expansion and relax only after the sample has returned to a uniform temperature. A detailed description of these phenomena can be found in the article by Paltauf and Dyer in this issue.

### C. Implications for Precise Tissue Ablation

The achievement of precise tissue ablation requires the use of laser wavelengths possessing a small optical penetration depth in tissue that serves to confine the energy deposition to a small volume. However, this condition alone is not sufficient. Thermal confinement is also required for precise ablation in order to limit the spatial extent of thermal diffusion during irradiation and maximize the temperatures in the absorbed volume. Stress confinement may provide for a more efficient ablation process as there is ample evidence that it serves to reduce the volumetric energy density required for material removal. This results in an increase of the ablation efficiency and a reduction of the thermal injury in the tissue that remains. These issues will become clearer in the next section, where we consider the thermodynamics involved in phase transition and material removal processes.

## V. Thermodynamics and Kinetics of Phase Transitions

Ablative cutting or material removal requires the fracture of chemical bonds. The breakage of bonds leads either to the removal of molecules, molecular fragments, and molecular clusters or to the formation of voids within the bulk of the material. Void (i.e., bubble or crack) formation results in the ejection of non-decomposed material fragments upon mechanical failure of the material. Vaporization, molecular fragmentation, and void formation are all phase transitions and can be accomplished via photothermal, photomechanical, or photochemical mechanisms. Given the central role of phase transitions in the ablation process, this section is devoted to a systematic analysis of their thermodynamics and kinetics. In sections V.A–G, we consider the generation of phase transitions via photothermal and photomechanical phenomena and their modifications in the presence of a tissue matrix. We then treat photochemical mechanisms to achieve bond dissociation in section V.H and discuss their interplay with photothermal and photomechanical processes for tissue ablation in section V.I.

### A. Phase Diagrams

Consider a schematic of the pressure versus temperature projection of the phase diagram for liquid and gaseous water shown in Figure 11. The solid curve A–C represents those pressure/temperature pairs in which liquid and gaseous water are in equilibrium with one another and is known as the “binodal”.<sup>158–160</sup> The curve B–C–D in Figure 11 denotes a locus of states representing the intrinsic

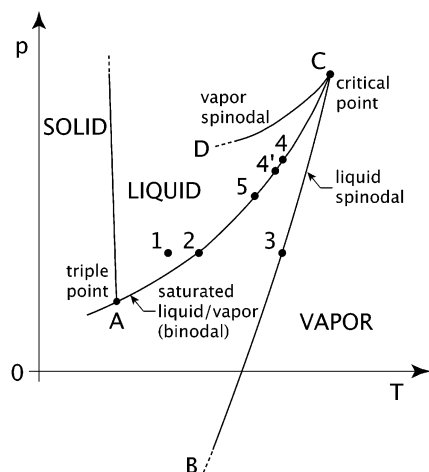


**Figure 11.** Pressure vs temperature projection of the thermodynamic phase diagram including the spinodal curve. Specific states of interest are (1) ambient temperature and pressure, (2) boiling temperature under ambient conditions, (3) spinodal temperature at ambient pressure, and (4) saturated conditions corresponding to the ambient spinodal temperature. The importance of points 4' and 5 are discussed in section V.D.

stability limit of the liquid or vapor phase (i.e.,  $(\partial T / \partial s)_p = 0$  and  $(\partial p / \partial v)_T = 0$ ) and is known as the "spinodal". At the spinodal, the superheated liquid phase or subcooled vapor phase is no longer stable with respect to the random density fluctuations that occur in all materials at nonzero temperatures. Thus, the segment of the spinodal denoted B–C represents the limit to which metastable liquids can be superheated, while the segment D–C represents the limit to which metastable vapor can be subcooled.<sup>158–163</sup>

The binodal and spinodal curves intersect at the critical point C, above which no thermodynamic distinction can be made between liquid and vapor phases. As ablation is often driven by a phase transition from the liquid to the vapor state, we focus our attention on segment B–C of the spinodal and future depictions of the  $p$  vs  $T$  phase diagram will omit segment D–C of the spinodal for clarity.

Figure 12 provides the pressure versus specific volume projection of the phase diagram with equilibrium and van der Waals isotherms shown. In this diagram, the liquid-, vapor-, and mixed-phase regions are clearly demarcated. The boundary of the mixed-phase region encloses the range of specific volumes in which liquid and gaseous phases coexist for a given pressure and temperature and is often referred to as the 'vapor dome'. The apex of the vapor dome (point C) denotes the critical point which for water is located at  $T_c = 374.14$  °C and  $p_c = 22.09$  MPa. The dashed curve within the mixed phase region represents the spinodal, where segment B–C specifies the stability limit of superheated liquid and segment D–C specifies the stability limit of subcooled vapor. In both Figures 11 and 12, additional locations have been indicated that are pertinent to the discussion that follows. Point 1 represents ambient conditions, i.e.,  $T_1 = 25$  °C and  $p_1 = 101$  kPa; point 2 denotes saturated liquid at atmospheric pressure, i.e., the "boiling temperature",  $T_2 = 100$  °C and  $p_2 = 101$  kPa; point 3 is the location of the spinodal at ambient pressure,  $T_3 = 305$  °C and  $p_3 = 101$  kPa; and point 4

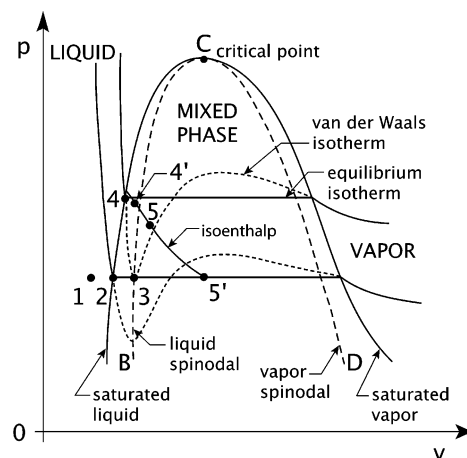


**Figure 12.** Pressure vs specific volume projection of the thermodynamic phase diagram including the spinodal curve along with equilibrium and van der Waals isotherms. Points 1–4 correspond to those shown in Figure 11. The importance of points 4', 5, 5' and that of the isoenthalp is discussed in section V.D.

provides the equilibrium vapor pressure and specific volume for saturated liquid corresponding to the spinodal temperature, i.e.,  $T_4 = 305$  °C and  $p_4 = 9.2$  MPa. Points 4', 5, and 5' lie on the binodal in the mixed phase region and possess the same specific enthalpy as liquid at ambient pressure heated to the spinodal limit. Their significance, along with the curve of constant enthalpy (isoenthalp) shown in Figure 12, is discussed in section V.D.

## B. Surface Vaporization

Equilibrium vaporization takes place at a liquid–vapor interface, where liquid water at a free surface is transformed to vapor at the saturation temperature and pressure.<sup>154,155</sup> Thus, equilibrium vaporization can occur when the liquid is in any thermodynamic state that lies on the binodal. As a result, vaporization does not occur at a predetermined temperature and all theoretical models that adopt a fixed "vaporization temperature" violate the basic physics of the process. The rate at which energy is supplied to the system dictates the vaporization rate. Many investigators have developed fluid dynamic models of surface vaporization driven by the absorption of laser radiation that are consistent with the thermodynamics of the process.<sup>166–171</sup>

Enhanced rates of vapor formation from the free surface of a liquid can be achieved at the start of pulsed laser radiation via the process of nonequilibrium interphase mass transfer.<sup>172</sup> Consider a liquid system located at point 1 in the phase diagram, where the surface of the liquid is in equilibrium with the ambient vapor at a temperature below the saturation temperature. An enhancement in the rate of vapor formation occurs when the liquid surface temperature is raised rapidly (to a value that may still be below the binodal), the liquid surface is no longer in equilibrium with the surrounding vapor. This results in a very high net mass flux from the liquid surface to the surroundings that persists until the ambient vapor pressure reaches the equilibrium vapor pressure corresponding to the new surface

liquid temperature. Once the vapor pressure returns to equilibrium, the balanced exchange of the evaporation of liquid molecules into the vapor phase and the condensation of vapor molecules back into the liquid phase is restored. Such a process also mediates the initial vapor flow from a liquid surface when rapidly heated to extreme temperatures; even those in excess of the critical point. The impact of nonequilibrium interphase mass transfer on pulsed infrared laser ablation has been considered by Yablon and co-workers.<sup>173</sup>

### C. Normal Boiling

Normal boiling refers to a process that, like surface vaporization, occurs at a thermodynamic state on the binodal, as indicated by point 2 in Figure 11. Thus, for a given pressure, the binodal defines the corresponding "boiling temperature", which is 100 °C for water at atmospheric pressure. Normal boiling relies on the presence of cavities of dissolved gas or other heterogeneities within the liquid that catalyze the nucleation and growth of vapor bubbles. The energy is deposited into the system at a rate sufficient to drive the growth of pre-existing vapor nuclei at such heterogeneous locations.<sup>158,160,164,165,174,175</sup> The rate of volumetric energy deposition provided by the laser irradiation is balanced by the energy of the vapor leaving the system. In a normal boiling process driven by laser irradiation of a free surface, the transition from saturated liquid to saturated vapor necessarily occurs in a finite layer of mixed phase at the sample surface. The thickness of this 'vapor-liquid' layer is comparable to the optical penetration depth of the incident radiation and its composition varies from that of saturated liquid at the base to saturated vapor at the surface.<sup>164,176</sup> As a result, the surface temperature is fixed to the saturation conditions corresponding to the pressure at the target surface and there is no temperature gradient within the vapor-liquid layer.

The temperature and pressure at which boiling occurs is influenced by the rate of mass removal from the target surface. The recoil associated with a rapid rate of mass removal increases the pressure at the target surface beyond ambient conditions. In such cases, if the ambient pressure is atmospheric, the boiling temperature of water will exceed 100 °C.

While normal boiling has provided the basis for models used to investigate the various aspects of laser ablation of tissue,<sup>176,177</sup> the density of heterogeneous bubble nucleation sites is likely insufficient to provide a boiling process sufficiently vigorous to balance the high rates of energy deposition achieved in most pulsed ablation processes.<sup>137,164,165</sup> Another factor limiting the role of normal boiling in pulsed laser ablation is the requirement that the bubbles move to the target surface on a time scale set by the propagation velocity of the ablation front. Miotello and Kelly<sup>165</sup> showed that this is not possible for irradiation of pure water with submicrosecond laser pulses. In tissue, the mobility of vapor bubbles is further inhibited by the presence of the ECM.

It is important to note that once a normal boiling process is established, the presence of volumetric

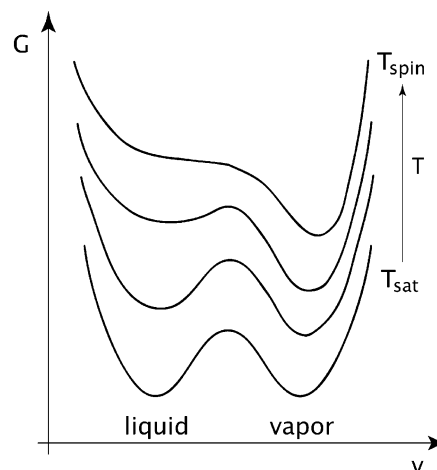


**Figure 13.** Gibbs free energy vs specific volume of a pure substance for several temperatures starting at the saturation temperature,  $T_{\text{sat}}$ , where the liquid and gaseous states are in equilibrium, up to the spinodal temperature,  $T_{\text{spin}}$ . Note that the local minimum corresponding to the liquid phase disappears at the spinodal temperature, effectively forcing conversion of the substance to the vapor phase.

energy densities infinitesimally higher than that corresponding to the saturation temperature results in the formation and growth of a vapor bubble. Thus, normal boiling always involves the *partial vaporization* of a liquid volume through the growth of vapor bubbles. In studies that consider the ablation of biological tissues, one sometimes finds the concept that vaporization occurs only once the entire latent heat of vaporization is deposited into a specified volume of water. This concept is not tenable, as it would lead to the superheating of liquid to temperatures far beyond the limit of stability.

### D. Phase Explosions: Bubble Nucleation and Spinodal Decomposition

When the rate of volumetric energy deposition provided by laser radiation is more rapid than the rate of energy consumed by vaporization and normal boiling, the tissue water is driven to a metastable superheated state. The liquid can remain metastable until the spinodal temperature is reached (point 3 in Figures 11 and 12). At the spinodal temperature, the stability limit is violated, and the liquid undergoes "spinodal decomposition", a spontaneous process by which a thermodynamically unstable liquid relaxes toward equilibrium.<sup>158,160</sup> Unique features of the spinodal temperature can be appreciated by viewing a plot of the Gibbs free energy versus specific volume at ambient pressure, such as that shown in Figure 13. For equilibrium saturation conditions ( $T = T_{\text{sat}}$ ), the Gibbs free energy displays two local minima of equal magnitude located at specific volumes corresponding to saturated liquid and saturated vapor states.<sup>144</sup> For temperatures greater than  $T_{\text{sat}}$ , the vapor state is favored, and thus the local minimum corresponding to the specific volume of the vapor is lower than the local minimum corresponding to the liquid state. However, the presence of the local minimum corresponding to the liquid state indicates



that the liquid, while not globally stable, resides in a *metastable* state. Accordingly, the transition from liquid to vapor requires that a free energy barrier be overcome. Larger temperature differences from saturation conditions result in a shallower local minimum for the liquid state and a reduction in the free energy barrier. At the spinodal temperature,  $T_{\text{spin}}$ , the Gibbs free energy minimum corresponding to the liquid phase disappears, the superheated liquid becomes unstable, and the transition to the vapor phase via spinodal decomposition is spontaneous.<sup>158</sup>

Thus, unlike bubble nucleation, spinodal decomposition is not an activated process and is not impeded by the presence of a free energy barrier. This results in a phase transition with a fundamentally different character. While bubble nucleation results in the formation of large density fluctuations of small spatial extent, spinodal decomposition involves the rapid spontaneous growth of small density fluctuations that extend over large spatial scales.<sup>158,178</sup> The result is a process of phase separation that encompasses the entire unstable liquid volume. The superheated, unstable water at atmospheric pressure spontaneously “relaxes” by separating into an equilibrium state of mixed phase composed of saturated liquid and vapor at pressures that can approach the saturation pressure corresponding to the spinodal temperature (i.e.,  $p = 9.2$  MPa; for water at atmospheric pressure). This “relaxation” process thus involves an impressive pressure rise.

For the phase diagram shown in Figure 11, the deposition of an amount of energy just sufficient to produce spinodal decomposition first produces a heating phase that corresponds to the path 1 → 3. The spinodal decomposition process initially results in an isochoric transition from point 3 on the spinodal to point 4' in the mixed phase region possessing the same enthalpy. If this pressure jump results in tissue fracture, the liquid-vapor mixture will be exposed to atmospheric pressure and be ejected as saturated vapor and saturated liquid droplets. As this mixture expands, its thermodynamic state will follow roughly the curve of constant enthalpy (isoenthalp) as shown on Figure 12 until it reaches atmospheric pressure at point 5'. However, if the pressure jump does not result in tissue fracture, the tissue will expand slightly and relax to an intermediate temperature and pressure represented by point 5. In this latter case, the precise location of point 5 depends on the stiffness of the tissue and additional energy deposition is required to further increase the internal temperature and pressure to produce ablation (see section V.F).

To provide a complete description of the phase transformation process, we must also consider the contribution of homogeneous nucleation as the liquid is heated to the spinodal limit.<sup>137,165,179–181</sup> For a superheated liquid, homogeneous nucleation refers to the spontaneous formation of vapor inclusions within the bulk liquid, solely from thermodynamic fluctuations and not catalyzed by the presence of impurities or dissolved gas. While the formation of such vapor “nuclei” is spontaneous, their growth is not ensured and depends strongly on superheat temperature. Thus, the transformation of super-

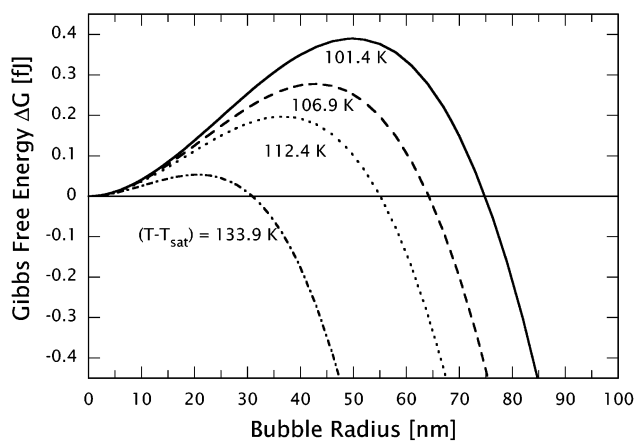


**Figure 14.** Schematic of the Gibbs free energy vs bubble radius required for the formation of a vapor inclusion coexisting with a superheated liquid phase for various superheat temperatures. The maximum of these curves is the critical Gibbs free energy,  $\Delta G_{\text{cr}}$ , and represents the energy barrier that impedes vapor bubble growth. The critical bubble radius,  $r_{\text{cr}}$ , is the bubble size corresponding to the critical Gibbs free energy. Note that both  $\Delta G_{\text{cr}}$  and  $r_{\text{cr}}$  decrease with increasing superheat temperature.

heated (metastable) liquid to an equilibrium state of mixed phase may involve both bubble nucleation and spinodal decomposition, and we refer to the collective phase transition processes as a “phase explosion”.

Let us consider the process of homogeneous bubble nucleation more closely. In the framework of classical nucleation theory initially formulated in the 1920s, the driving force for growth of vapor “nuclei” is supplied by the difference in chemical potential between the superheated liquid outside the bubble and the vapor inside, and it is necessary to overcome the surface tension separating the vapor from the liquid. Because the chemical potential difference that drives bubble growth scales with the bubble volume (i.e.,  $r^3$ ) while surface tension scales with the bubble surface area (i.e.,  $r^2$ ), small vapor nuclei that form due to thermodynamic fluctuations spontaneously collapse, while larger vapor nuclei will grow. The Gibbs free energy,  $\Delta G$ , that describes the thermodynamics of bubble formation is given by

$$\Delta G = \frac{4\pi r^3}{3}(\mu_v - \mu_l) + 4\pi r^2\sigma \quad (9)$$

where  $\mu_v$  and  $\mu_l$  are the chemical potentials of the vapor and liquid states, respectively,  $r$  is the size of the vapor nuclei, and  $\sigma$  is the surface tension of the surrounding liquid.<sup>160,175</sup> Nuclei grow only if they are larger than a critical radius,  $r_{\text{cr}}$ , such that the chemical potential difference exceeds the barrier posed by surface tension.<sup>160</sup> An increase in the superheat temperature increases the chemical potential difference between the superheated liquid and the vapor inside the bubble and results in a reduction in the critical embryo size that can spontaneously grow. Note that for bubble nucleation, the intrinsic stability of the superheated liquid phase is not at issue; instead, it is the difference in chemical potential of the superheated liquid relative to the vapor that drives the growth of vapor nuclei. This is illustrated in Figure 14, where the variation of the

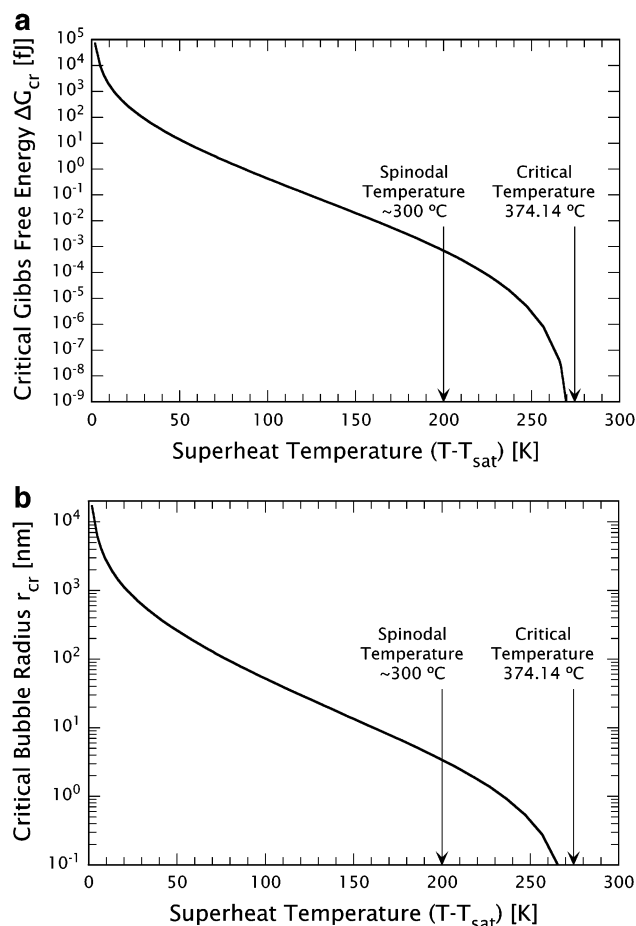


**Figure 15.** (a) Variation of the critical Gibbs free energy necessary for vapor bubble growth with superheat temperature. Note that the critical Gibbs free energy goes to zero at the critical temperature. (b) Variation of the critical bubble radius required for spontaneous vapor bubble growth with superheat temperature. Note that the critical bubble radius goes to zero at the critical temperature.

Gibbs free energy required for the formation of vapor nuclei with a given size within water is shown for different superheat temperatures. Vapor nuclei smaller than the size corresponding to the peak Gibbs free energy in these curves are called “embryos” and will spontaneously collapse because their growth is not favored energetically. However, vapor nuclei with size  $r_{cr}$  (or larger), corresponding to the maximum (or critical) Gibbs free energy,  $\Delta G_{cr}$ , are called bubbles and will grow spontaneously. Figure 15 shows the dependence of this critical Gibbs free energy and critical radius on superheat temperature for water. Note that although both  $\Delta G_{cr}$  and  $r_{cr}$  become very small for large superheat temperatures, they remain finite even at the spinodal temperature, and thus nucleation remains an activated process with a finite free energy barrier.<sup>158</sup> The strong reduction of  $\Delta G_{cr}$  and  $r_{cr}$  results in a dramatic rise in the nucleation rate,  $J$ , with the superheat temperature that attains a large, but finite, value at the spinodal temperature, as shown in Figure 16. The energy barrier that must be overcome for the conversion from the liquid to the vapor phase disappears only when surface tension disappears, and this occurs at the critical point.

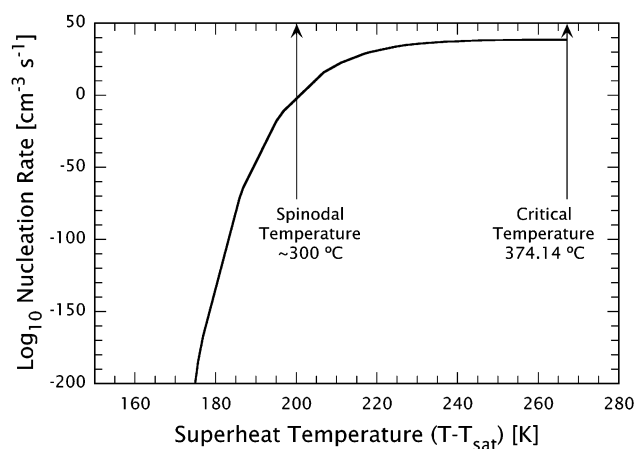


**Figure 16.** Variation of vapor bubble nucleation rate with superheat temperature.

At first glance, these results appear to be at odds with the expectation that the phase transition must occur once spinodal conditions are reached. However, we must recall that classical nucleation theory is not a general formalism that includes spinodal decomposition as a possible mechanism for phase separation. The first general formalism for phase separation, the van der Waals–Cahn–Hilliard theory of inhomogeneous fluids, was developed later in the 1950s. Using the theory of interfaces, this approach unifies the thermodynamics and kinetics of bubble nucleation and growth with those of spinodal decomposition and sharply distinguishes metastable states (from which phase separation occurs by the activated process of nucleation and growth) from unstable states (from which phase separation occurs spontaneously by spinodal decomposition). The analysis shows from first principles that the “expense” of free energy involved in the formation of a critical vapor “bubble” vanishes at the spinodal rather than at the critical point. It also provides a framework to describe the *kinetics* of the phase explosion once the spinodal is reached.<sup>158</sup>

Theoretical estimates for the spinodal temperature of water at atmospheric pressure are in the range  $T_{sp} = 305^\circ\text{C}$ .<sup>160</sup> When heating is done on time scales of several seconds to minutes, the superheat limit of water at ambient pressure has been measured as  $T = 279.5^\circ\text{C}$ ,<sup>181</sup> while for heating conditions on the microsecond time scale, superheat temperatures in excess of  $300^\circ\text{C}$  have been reported.<sup>182</sup> Taking  $T_{sp} = 305^\circ\text{C}$  and considering the strong temperature dependence of the specific heat capacity of superheated water,<sup>160,183</sup> one can determine that the volumetric energy density necessary to heat water from room temperature to the spinodal limit is  $1.27 \text{ kJ/g}$ , which comprises only 49.6% of the sum of the sensible and latent heat of vaporization for water. Thus, in cases where the phase explosion produces tissue fracture and material removal, less than half of the superheated liquid is transformed to saturated vapor, and the remaining saturated liquid is ejected in the form of liquid droplets.

Upon examination of Figure 11, one can infer that the spinodal limit can be reached through either a rapid increase in temperature or a rapid reduction

in pressure. The latter path is significant when considering the effect of tensile thermoelastic stresses on the ablation process (section V.G). In this context, it is important to know the tensile strength of water at room temperature, as this defines the onset of a tensile-stress-induced phase explosion. The tensile strength of macroscopic samples of water has been measured to be  $-27.7$  MPa at  $10^\circ\text{C}$ ,<sup>184</sup> while more recent measurements using microscopic samples of ultrapure water have been successful in obtaining metastable liquid water at pressures up to  $-140$  MPa at room temperature.<sup>185,186</sup> Theoretical considerations of the equation of state for water yield predictions for the spinodal limit of room-temperature water in the range from  $-110$  to  $-200$  MPa,<sup>186–188</sup> while classical nucleation theory and molecular dynamics approaches predict fracture limits of  $-140$  and  $-27$  MPa, respectively.<sup>186,189</sup>

Thus far, we have focused on processes tracing a path indicated by  $1 \rightarrow 2 \rightarrow 3 \rightarrow 4' \rightarrow 5$  or  $5'$  in Figure 11. This path corresponds to the extreme case in which no vapor nuclei are present in the liquid, or the heating occurs extremely rapidly. There are, however, instances in which heterogeneous nuclei are present prior to irradiation and/or a significant number of homogeneous nuclei form and grow during the laser heating, such that the rate of energy consumed by the formation and growth of the nuclei is comparable to, but does not match, the rate of energy deposition provided by the laser radiation. This results in a process that is intermediate between the path  $1 \rightarrow 3 \rightarrow 4' \rightarrow 5 \rightarrow 5'$  and normal boiling. The heating phase does not occur in an isobaric fashion but is accompanied by a finite pressure rise. Thus, spinodal conditions are reached somewhere between point 3 and the critical point C. The resulting phase explosion thus occurs at a higher temperature and pressure, but the pressure jump associated with the phase separation is less severe. Such intermediate processes will be referred to as “explosive boiling” and were first postulated as a driving mechanism for tissue ablation by Dmitriev and Furzikov.<sup>190–192</sup>

To assess the likelihood of a phase explosion versus normal boiling produced by laser irradiation, one must determine the rate of energy consumption by the growth of nucleation centers and compare it with the rate at which energy is deposited by the laser radiation. To determine the rate of energy consumption by the growing nucleation centers, one must consider that, for early times, the rate of bubble growth is limited by the inertia of the liquid mass that surrounds the bubbles, and for later times it is limited by diffusive heat transfer into the bubble.<sup>193</sup> By assuming that a certain volumetric density of heterogeneous vapor nuclei exist within the tissue and grow at the maximum rate possible, one can determine an upper bound for the volumetric power density that must be supplied by the laser radiation to superheat the tissue water to the spinodal limit.<sup>137</sup> Figure 17 presents the results of such an analysis that defines whether a phase transition proceeds as boiling or as phase explosion for a given laser pulse duration,  $t_p$ , and density of pre-existing heterogeneous nuclei,  $\Omega$ , in the tissue.<sup>194</sup>

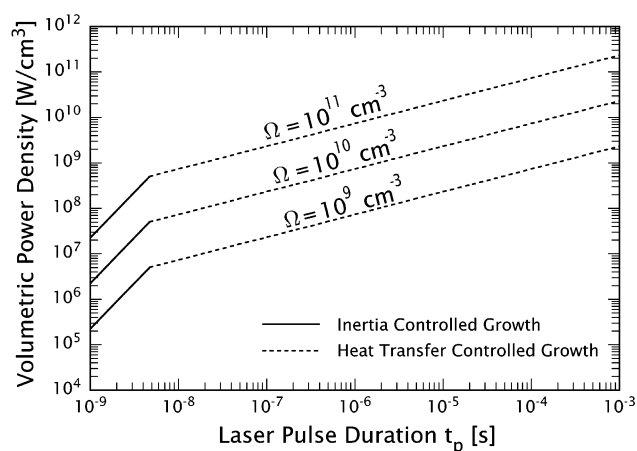


**Figure 17.** Minimum rate of volumetric energy deposition (power density) required for the generation of a phase explosion as a function of laser pulse duration. The results are shown for different number densities of heterogeneous vapor nuclei,  $\Omega$ . (Adapted with permission from ref 194. Copyright 1996 Biophysical Society.)

Before closing this discussion on phase explosions, it is important to note that water in tissue is associated with proteoglycans, collagen type VI, and other intracellular and extracellular proteins (section II.A). Therefore, it is possible, if not likely, that the spinodal limit of tissue water differs from that of pure water. Another point to be mindful of is that the presence of laser speckles may prevent the uniform heating of a liquid/tissue sample and lead to the production of phase explosion conditions at localized regions within the irradiated volume.<sup>195</sup>

### E. Confined Boiling

In pulsed laser ablation of tissues, the phase transition processes are altered by the presence of the ECM. Thus, for a boiling process within tissue, the chemical potential difference between the vapor and liquid phases necessary to drive bubble growth must exceed not only surface tension but also the elastic strain energy necessary to deform the tissue matrix surrounding the nucleation center. Therefore, bubble growth in tissue requires a higher internal pressure than in pure liquids, and the elevated pressure is coupled to an increase in the boiling (saturation) temperature. The pressure buildup that occurs during the boiling process continues until it exceeds the ultimate tensile strength of the ECM and results in explosive tissue ablation.<sup>118,119,136,196,197</sup> We term this process “confined boiling”. On the  $p$ – $T$  phase diagram in Figure 18, the evolution of the confined boiling process corresponds to a path that first proceeds as isobaric heating (e.g.,  $1 \rightarrow 2$ ) but then becomes coincident with the binodal and terminates when the saturated vapor pressure equals the ultimate tensile strength of the tissue (at point 6 for instance). In the presence of a tissue matrix, explosive material ejection will thus occur regardless of the rate of energy deposition. Therefore, it is not surprising that explosive material ejection due to confined boiling has also been reported to occur in continuous-wave laser ablation.<sup>198,199</sup>

In the above scenario, one can imagine that a stiff tissue matrix may suppress bubble growth to such a



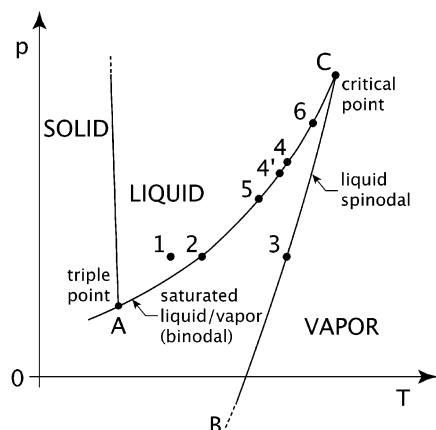


**Figure 18.** Path taken through the  $p$  vs  $T$  projection of the thermodynamic phase diagram for confined boiling ( $1 \rightarrow 2 \rightarrow 6$ ) and for tissue ablation involving a phase explosion ( $1 \rightarrow 2 \rightarrow 3 \rightarrow 4' \rightarrow 5 \rightarrow 6$ ). The actual path followed depends on the rate of energy deposition, number density of heterogeneous nuclei, and the mechanical strength of the tissue matrix relative to the saturation vapor pressure corresponding to the ambient spinodal temperature.

degree that little vaporization occurs prior to the onset of ablation. Thus, the volumetric energy density necessary for the initiation of the ablation process may not be much higher than that required for a temperature increase in pure water that produces a saturation vapor pressure equaling the ultimate tensile strength of the tissue. This raises the possibility that the ablation enthalpy can be considerably smaller than the vaporization enthalpy of water. A rigorous thermodynamic analysis of confined boiling has been developed by Majaron and co-workers and considers the effects of mechanical tissue properties on the process dynamics.<sup>197</sup>

## F. Effects of the Tissue Matrix on the Interplay of Phase Explosions and Confined Boiling

There are several factors that determine the role of confined boiling or phase explosions within the dynamics of an ablation process. Principal among these are the rate of volumetric energy deposition, the number density of heterogeneous nucleation sites within the tissue, and the strength and stiffness of the tissue matrix.

For cases in which the rate of volumetric energy deposition is slow and the number density of heterogeneous nuclei is high, the nature of the process is largely independent of the mechanical tissue properties. Initially, the tissue is heated under equilibrium conditions at constant pressure ( $1 \rightarrow 2$ ) and will then continue on the binodal until the ultimate tensile strength of the tissue is reached, resulting in explosive material removal. However, if the tissue is heated rapidly and/or a small number density of heterogeneous nuclei are present, the laser heating will result in metastable heating approaching the spinodal limit and induce a phase explosion ( $1 \rightarrow 2 \rightarrow 3 \rightarrow 4'$ ). The continuation of the process now depends on the mechanical properties of the tissue. Ablation will result for tissues that are unable to withstand the stresses and deformations associated

with the phase explosion and the process will continue along the isoenthalp and terminate at  $5'$ . However, for tissues possessing high collagen content, the tensile strength of the tissue matrix is higher than the stresses resulting from the phase explosion. In this case, ablation is not initiated by the phase explosion, and the process continues as confined boiling. The energy deposition following the phase explosion will drive the tissue water along the binodal ( $5 \rightarrow 6$ ), as indicated in Figure 18, until the tissue ruptures at higher vapor pressures, resulting in material removal. Once the high pressures in the tissue are relieved through mechanical failure of the ECM, the tissue water is again superheated relative to the atmospheric pressure to which it is exposed.

In instances when the tensile strength of the tissue matrix is higher than the pressure at the critical point, the tissue water must be heated to a supercritical state before material removal is achieved. In this case, the time evolution of the tissue state on the  $p$ - $T$  diagram under supercritical conditions is governed by both the equation of state of water and the elastic properties of the tissue. These views regarding the thermodynamics of the tissue ablation process are consistent with experimental data. Using  $\text{CO}_2$  laser ( $\lambda = 10.6 \mu\text{m}$ ) pulses of 100- $\mu\text{s}$  duration at radiant exposures of 3–14  $\text{J}/\text{cm}^2$ , Harris and co-workers measured skin surface temperatures of 400–750  $^\circ\text{C}$  during ablation of guinea pig skin.<sup>76</sup> The data indicate that the peak surface temperatures achieved during the ablation process are well above the spinodal and critical points of pure water and increase with radiant exposure.

We have yet to consider the possibility of a mechanical weakening of the ECM prior to tissue failure due to thermal processes driven by the high temperatures that accompany the laser ablation process. Mechanical weakening of the tissue matrix during laser irradiation will most likely play a more prominent role for microsecond laser pulse durations than for nanosecond laser exposures at radiant exposures close to the ablation threshold. When using nanosecond laser pulses of moderate to high radiant exposure, the volumetric energy densities are sufficiently high to result in rapid thermal dissociation of the ECM molecules into volatile products. In this case, the native mechanical strength of the ECM has a less prominent influence on the primary material ejection process but can still play a role in recoil-induced material expulsion (see section VI.B.2). It should also be noted that a potential reduction of the UTS due to denaturation (section II.C) may be compensated in part by the increase of UTS resulting from the high strain rates (section II.B). It is thus difficult to predict the effective UTS of tissue samples that are simultaneously heated and strained at very high rates from literature UTS values measured at room temperature and low strain rates.

## G. Effect of Stress Confinement on the Ablation Process

As discussed in section IV.B, significant tensile stresses result from the thermoelastic response of tissues to pulsed laser irradiation. The magnitude of

these stress transients is most prominent when irradiation takes place under conditions of stress confinement and when the laser beam diameter is comparable to the optical penetration depth of the incident radiation. The tensile stresses can significantly affect the ablation process by catalyzing the phase transition processes discussed in sections V.B–F or by causing direct tissue fracture and mechanical failure.

### 1. Stress Confinement and Phase Transitions

Traditionally, the “rupture” or “fracture” of a liquid achieved by tensile stress under isothermal conditions is called “cavitation”, while “bubble formation” due to heating under isobaric conditions is called “boiling”.<sup>174</sup> Such a distinction becomes obscure when targets are heated under conditions of stress confinement, as both the temperature rise and the negative stresses generated by the thermoelastic response are responsible for the phase transition processes that follow. For simplicity, we denote bubble formation accomplished at temperatures less than 100 °C as “cavitation” and use “explosive boiling” to refer to those processes that may be catalyzed by the presence of tensile stresses but nonetheless occur at temperatures above 100 °C. Depending on the temperature rise in the target, negative thermoelastic stresses can lead to the accelerated growth of pre-existing nucleation centers or initiate the nucleation and growth of vapor bubbles.<sup>200</sup> In fact, if the temperature of the tissue water is raised above 100 °C, any negative pressure results in a transient crossing of the binodal that results in a transient increase in the bubble nucleation rate. Once such tensile pressures reach magnitudes of 10–100 MPa, they may directly cause a phase explosion. Thus, the presence of tensile stresses offers the possibility of explosive boiling processes at temperatures much less than 300 °C. The thermodynamic path (1 → 2 → 3 → 4) that represents such a process is depicted in Figure 19.

### 2. Stress Confinement and Tissue Fracture

The use of tensile stresses that originate from the reflection of compressive thermoelastic stresses at a free surface to achieve tissue fracture at temperatures less than 100 °C was first considered for one-dimensional irradiation conditions in 1991 by Dingus and Scammon.<sup>141</sup> This process was termed “spallation” in reference to back-surface fracture processes known to result after the front surface of a solid experiences a high-velocity impact.<sup>201,202</sup> In the following years, it was realized that the achievement of material removal from tissues and tissue phantoms through tensile stress transients is a complex process involving cavitation bubble formation at heterogeneous nuclei, coalescence of these bubbles, and jet formation upon bubble collapse.<sup>143,203,204</sup> At room temperature, the threshold pressure required for bubble formation starting from heterogeneous nuclei via cavitation is about –1 MPa.<sup>205,206</sup> The physics governing the subsequent cavitation-induced material ejection process has been described by Paltauf and Schmidt-Kloiber.<sup>143</sup>

The range of radiant exposures over which “spallation” is the dominant mechanism for pulsed laser

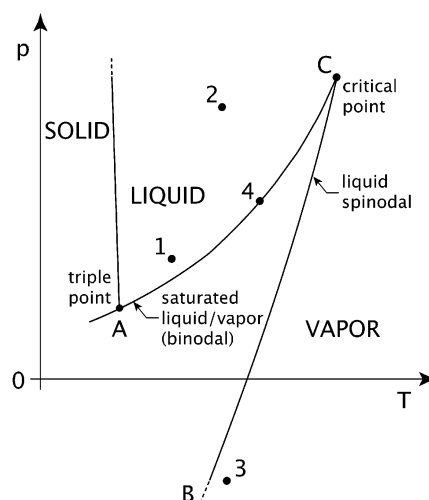


**Figure 19.** Path taken through the  $p$  vs  $T$  projection of the thermodynamic phase diagram for a temperature rise above 100 °C under stress confinement conditions. The transition 1 → 2 corresponds to the heating phase that is coupled with the generation of compressive stress. The transition 2 → 3 corresponds to the passage of the tensile stress wave that leads to a crossing of the spinodal limit, resulting in phase separation. After the passage of the stress wave, the system reaches point 4, that corresponds to explosive boiling into the large number of bubbles produced shortly before.

ablation of pure liquids is fairly small.<sup>143,205,206</sup> The efficiency of spallation is fairly low, and the amount of ejected material increases considerably when temperatures in excess of 100 °C are produced. In the latter case, the negative pressure facilitates an explosive boiling process that drives the ablation event.<sup>143,206,207</sup> In tissues and tissue phantoms, the possible role for spallation-induced ablation processes becomes narrower still. Oraevsky and co-workers<sup>204</sup> demonstrated material ejection from liver samples and tissue phantoms containing 5% dry gelatin and 95% water at radiant exposures that produce only a 30 °C temperature rise but emphasized that thermal explosion is more effective for tissue ablation compared with “cold” photomechanical ablation. This is consistent with calculations showing that less than 1% of the laser energy is converted to mechanical energy of the thermoelastic stress wave.<sup>206</sup> The tissues and tissue phantoms used by Oraevsky and co-workers had weak mechanical properties. Paltauf and Schmidt-Kloiber<sup>206</sup> observed that for mechanically stronger tissue phantoms composed of 25% dry gelatin and 75% water, material removal is achieved only at radiant exposures that result in vaporization. Venugopalan and co-workers<sup>137</sup> demonstrated that stress-confined ablation of a mechanically strong tissue such as dermis using IR laser pulses requires a temperature rise of at least 260 °C, i.e., a tissue temperature close to the spinodal limit. These observations indicate that, for most tissues, material removal using IR laser pulses cannot be achieved via a laser-induced spallation mechanism. However, Venugopalan and co-workers showed that the use of KrF excimer laser pulses under stress confined conditions can initiate ablation in porcine dermis at volumetric energy densities equivalent to a temperature rise of only 20 °C if the effects of microscale

stress confinement (section IV.A.) can be ignored.<sup>150</sup> These results suggest that stress confined irradiation conditions, combined with photochemical processes that weaken the tissue matrix may produce material removal via a spallation mechanism.

### 3. Stress Confinement and Ablation Threshold

The above considerations suggest that thermoelastic tensile stresses can reduce both the ablation threshold and the ablation enthalpy. This reduction is likely achieved by direct fracture of the tissue matrix or, even more importantly, by its catalytic effect on nucleation and explosive boiling. This reduction in ablation threshold has been observed or measured by many researchers.<sup>136,137,141,143,146,153,156,203–210</sup>

Albagli and co-workers<sup>210</sup> offered the first detailed examination of the variation of the ablation threshold with the degree of stress confinement. In 1994, they reported that for aortic tissues the volumetric energy densities at the ablation threshold displayed a strong correlation to the laser pulse duration normalized by the stress propagation time across the heated volume,  $t_m^*$  (section IV.B). Specifically, for values of  $t_m^* \lesssim 1$ , the volumetric energy density required for ablation was comparable to that required to raise water from room temperature to 100 °C. However, the transition to higher ablation thresholds was apparent only for values of  $t_m^* \geq 10$ . These results provide evidence that irradiation parameters with small  $t_m^*$  achieve ablation at volumetric energy densities much smaller than parameters which result in a large  $t_m^*$ , i.e., when using longer pulse durations or ablating very highly absorbing tissues. However, the data also show that the condition for stress confinement did not represent the proper metric to determine the conditions under which the threshold volumetric energy density is expected to rise.

To explain this latter finding, Albagli and co-workers<sup>210</sup> indicated that fracture of soft tissues differs considerably from that in brittle solids, hard calcified tissues, or liquids. In brittle materials and liquids, crack formation or cavitation will start promptly after the thermoelastic stress exceeds the mechanical strength of the material. In contrast, soft biological tissues must be strained significantly before fracture (see section II.B). In collagenous tissues, this is a consequence of the wavy/crimped arrangement of the collagen fibrils when the tissue is not subjected to stress.<sup>211</sup> Tissue tearing thus requires a significant straining of the tissue matrix that requires not only the development of a certain stress magnitude but the presence of this stress for a temporal duration sufficient to achieve the necessary tissue deformation.

These considerations suggest that one cannot simply use the stress confinement criterion to determine the conditions under which photomechanical effects cease to affect a reduction in the volumetric energy density needed to initiate the ablation process. While stress confinement will catalyze the inception of cavitation and the vaporization process as described above, Albagli and co-workers<sup>210</sup> suggested the use of an "inertial confinement" criterion instead of the stress confinement criterion to accommodate the

significant straining of the tissue matrix that must occur prior to the onset of material removal.

## H. Photochemical Decomposition

In 1982, two articles reported on the use of intense pulses of ultraviolet laser radiation to etch synthetic polymer surfaces with submicrometer precision and without evidence of thermal or mechanical damage to the remaining material.<sup>212,213</sup> Such clean and precise etching generated much interest in both materials processing and medical communities. Within one year, argon fluoride (ArF) excimer laser radiation ( $\lambda = 193$  nm) was being explored to cut or reshape the surface of the cornea for the correction of visual defects.<sup>214</sup>

To explain these unprecedented ablation characteristics, investigators invoked mechanisms unique to ultraviolet laser radiation. The dissociation energies of many organic molecular bonds (Table 1) are smaller than the substantial photon energies (4–6.5 eV) available from common UV laser sources (Table 2). Srinivasan and Leigh hypothesized that these UV photons cause direct "bond-breaking" of the absorbing molecular chains in the organic target, leading to ablative "photochemical decomposition".<sup>16,215</sup> The theory assumes that material is ablated above a certain threshold irradiance that provides a bond dissociation rate that exceeds the recombination rate of broken bonds.<sup>216,217</sup> The molecular fragments require a considerably larger volume than the native macromolecules, and this increase in volume results in a pressure rise and ejection of the decomposed material.<sup>17,218</sup>

Initially, it was believed that photochemical decomposition achieved using UV wavelengths involved characteristics that would easily distinguish it from thermal ablation processes. Moreover, it was thought that only a photochemical mechanism would provide the observed etching precision.<sup>218</sup> However, consideration of the reaction pathways following electronic excitation by the absorption of a UV photon reveals that other processes compete with photochemical dissociation.<sup>219–221</sup> Principal among these competing

**Table 1. Dissociation Energy of Selected Molecular Bonds**

molecular bond	dissociation energy (eV)	molecular bond	dissociation energy (eV)
C=O	7.5	C–O	3.6
C=C	6.4	C–C	3.6
O–H	4.8	S–H	3.5
C–H	4.3	C–N	3.0
N–H	4.1		

**Table 2. Wavelength and Photon Energy of Selected UV Laser Systems**

laser type	wavelength (nm)	photon energy (eV)
ArF excimer	193	6.4
Nd:YAG (5 $\nu$ )	213	5.8
KrF excimer	248	5.0
Nd:YAG (4 $\nu$ )	266	4.6
XeCl excimer	308	4.0
N <sub>2</sub>	337	3.7
Nd:YAG (3 $\nu$ )	355	3.5



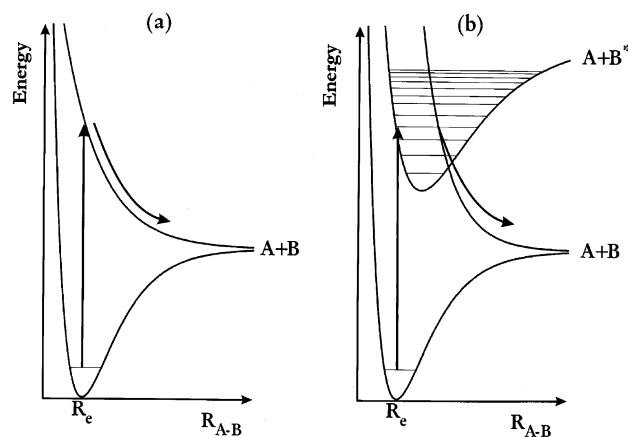


**Figure 20.** Energy level diagram illustrating various pathways for photochemical bond-breaking. See text for further details. (Reprinted with permission from ref 221. Copyright 2002 Academic Press.)

pathways is that of internal conversion of the absorbed photon energy to the vibrational modes of the molecule, which is the basis for possible photothermal ablation mechanisms. Two generic types of photochemical dissociation pathways of a diatomic molecule,  $A-B$ , are illustrated in Figure 20.<sup>221</sup> The first possibility, shown in Figure 20a, is that the electronic excitation promotes the molecule directly into an electronic state *with no net bonding* and results in a direct dissociation of the molecule into its constituent atoms  $A + B$ . The second possibility, shown in Figure 20b, represents the case in which the electronic excitation promotes the molecule into a *bound excited state* matching that of a second, dissociative electronic state  $A + B^*$ . Thus, while absorption of the UV photon promotes the molecule into a bound vibrational level within the excited electronic state, as the bond extends, the electronic configuration  $A + B^*$  can acquire the repulsive character of a dissociative state. Put another way, as the molecule reconfigures following electronic excitation, the vibrating nuclei sample the extended geometry and choose to follow either the bound or the repulsive potential; those that follow the former route execute another molecular vibration, but those taking the latter route continue to separate from one another, forming molecular fragments. The efficiency of this dissociation pathway depends on the coupling between the bound and repulsive state potentials. The dissociation pathways for polyatomic molecules are slightly more complex but exhibit the same principal features as those described above.<sup>219,221</sup> For both photochemical dissociation pathways, electronic energy exceeding the binding energy contributes to the kinetic energy of the dissociation products. The bond and repulsive energy potentials shown in Figure 20 imply that photon energies in significant excess of the bond energy are necessary to achieve photochemical dissociation.

Regardless of the specific photothermal or photo-dissociation pathway, if the ablation process occurs on time scales comparable to the laser pulse duration ( $\sim 20$  ns), thermal diffusion is minimal, and provided that the optical penetration depth of the laser radia-

tion is sufficiently small, thermal damage to the substrate would also be minimal.<sup>16,17,222</sup> Discrimination between photochemical and photothermal mechanisms for UV ablation has thus proven to be difficult. Investigations of the ablation mechanisms have focused on either determining the fraction of incident laser energy that results in thermal heating or characterizing the chemical reaction pathways via analysis of the reaction products. Davis and co-workers reported the measurement of rotational and vibrational temperatures of over 2900 °C in the ablation plume of poly(methyl methacrylate) (PMMA) ablation produced by nanosecond ArF excimer laser ( $\lambda = 193$  nm) pulses.<sup>223</sup> This finding revealed that, regardless of the specific ablation mechanism, the energy within the ablated fragments is quickly thermalized. Complementary to the plume studies were time-resolved thermal loading and colorimetric measurements of the polymer substrates that revealed that high temperatures between 800 and 2200 °C are reached on the polymer surfaces, resulting from ablative exposures of 193-, 248-, and 308-nm irradiation.<sup>224–226</sup>

The thermal loading experiments demonstrated that, for radiant exposures below the ablation threshold, all deposited energy is converted into heat.<sup>224–226</sup> Above the ablation threshold, the amount of thermal energy remaining in the substrate increased very slightly with radiant exposure, indicating that the majority of energy in excess of the threshold radiant exposure is contained in the ablation products.<sup>224–226</sup> Otis and co-workers performed an energy balance for UV ablation of polyimide and showed that the fraction of energy that does not manifest as heat in the remaining substrate was completely consumed for the radiation of a blast wave into the surrounding air.<sup>227</sup> While such studies provide strong evidence that the energy provided by the UV radiation is thermalized in the substrate and in the ablation plume, they do not exclude the possibility that the molecular dissociation process is driven by photochemical processes.<sup>228</sup> If this were in fact the case, then the laser energy deposited for subthreshold radiant exposures would eventually be dissipated via internal conversion and would manifest itself as thermal energy. Above the threshold, the energy necessary for photochemical bond breaking would be transformed into the kinetic and internal (thermal) energy of the ablated fragments.<sup>216,218</sup>

Further attempts to formulate criteria for the identification of photochemical process involved in UV ablation involved examining the reaction products and possible chemical reaction pathways leading to their generation.<sup>17,229</sup> Investigators expected that if photochemical processes were substantial, the prevalence of smaller molecular fragments would increase with shorter wavelengths, because high single-photon energy should be capable of breaking bonds of very high energy.<sup>17,18,228</sup> Unfortunately, these studies proved inconclusive because several researchers observed a similar composition of the photoproducts produced by UV and IR polymer ablation.<sup>230</sup> However, Küper and co-workers<sup>231</sup> conducted a de-

tailed analysis of the reaction pathways and products resulting from UV laser ablation of PMMA that provided evidence of a significant photochemical contribution for ArF ( $\lambda = 193$  nm) and KrF ( $\lambda = 248$  nm) excimer laser ablation. However, for XeCl ( $\lambda = 308$  nm) excimer laser ablation, no photochemical contribution was found. The primary photochemical process in the ablation of PMMA was the scission of side chains, forming gaseous and volatile fragments. Degradation of the main polymer chain was found to be a minor process relative to the amount of total photoproducts generated and was considered to be a photothermal process. Kitai and co-workers,<sup>232</sup> in developing a comprehensive model of the UV ablation process of PMMA, introduced the concept that splitting of main-chain bonds in the macromolecule arises from the production of volatile molecules by photochemical scission of side-chain bonds. The volatile products possess a larger specific volume than PMMA and fracture the bonds in the main polymer chain by placing them under stress. The authors argued that the quantum yield of purely photochemical processes is much too low to explain ablation at the experimentally observed threshold radiant exposure<sup>13,232–234</sup> and that the mechanical component of the decomposition will increase the efficiency of the ablation process. They transferred this concept to explain the physics of UV laser ablation of cornea by assuming that boiling of the water present in the biopolymer will provide the stresses necessary for the mechanical splitting of the bonds.<sup>232</sup>

As a result of these studies and model development, it is now generally accepted that UV laser ablation never exclusively involves photochemical dissociation but that thermal processes are also present.<sup>220</sup> The contribution of photochemical decomposition to the ablation process drops rapidly when longer wavelengths are used.<sup>222,235,236</sup> Oraevsky and co-workers<sup>236</sup> estimated that the value of absorbed XeCl laser energy ( $\lambda = 308$  nm) contributing to the photolysis of protein is only about 2%. We can conclude that photochemical decomposition plays a significant role in the ablation of tissues at wavelengths around  $\lambda = 200$  nm and, for some materials, is also important at  $\lambda = 248$  nm.

### I. Interplay of Photochemical Decomposition and Confined Boiling in Tissue

The assembly of a sequence of events to explain a photochemical ablation process in biological tissues is much more complex than that in an organic polymer due to its structural heterogeneity and large water content, as well as the greater diversity of molecules and molecular interactions. As elucidated in section III, the primary tissue chromophores in the UV are the proteins in the collagen fibrils and globular proteins that reside in the ground substance between the fibrils. Experimental evidence discussed in section V.H indicates that these chromophores are heated to high temperatures, even when photochemical decomposition of the proteins may be of major importance. The time for thermal diffusion from proteins interspersed in the ground substance to the tissue water is on the order of picoseconds, and the

thermal relaxation time of collagen fibrils is on the order of nanoseconds (section IV.C). The rapid heat transfer from the absorbing proteins to the tissue water implies that a potential phase change of water will interact strongly with any photochemical or photothermal decomposition processes of the UV-absorbing chromophores.<sup>232</sup> This interaction between the tissue water and tissue protein provides yet another thermal pathway for material removal that is relevant at temperatures considerably lower than those required for a direct thermal decomposition of homogeneous polymers ( $> 1000$  °C, section V.H). The phase change in the tissue water proceeds as confined boiling and results in a phase explosion for temperatures approaching the spinodal limit. The pressure rise that accompanies the phase change will contribute to the rupture of the tissue matrix. However, if the tissue matrix is already weakened by photochemical decomposition, it will offer less resistance to the vaporization process than in the situations described in sections V.D–H and will rupture at lower temperatures and pressures.

The presence of photochemical decomposition may also fundamentally alter the thermodynamics of the phase transition process. It is possible that volatile products produced by photochemical decomposition of the tissue proteins may serve as additional sites for heterogeneous nucleation and enhance the rate of vaporization of tissue water. The presence of a large number of growing vapor nuclei would reduce the superheat temperatures within the tissue water and would promote normal or explosive boiling at temperatures below the spinodal limit.

## VI. Ablation Plume Dynamics

The phase transitions described in the previous section drive the formation of an ablation plume that consists of material removed from the ablation site. The dynamics of plume formation and expansion is discussed in section VI.A. In addition, the characteristics of the ablation plume reflect the underlying ablation dynamics and influence the ablation process in various ways. The flow of ablation products perpendicular to the tissue surface induces a recoil pressure that may produce additional material expulsion and collateral effects in the bulk tissue (section VI.B). The flow components parallel to the tissue surface that develop at later times may also influence material removal and cause a redistribution of the ablated material (section VI.C). Scattering and absorption of the incident light by the ablation plume reduce the amount of energy deposited in the target and limit the ablation efficiency at high radiant exposures (section VI.D).

### A. Plume Formation and Expansion

The ablation process is typically characterized by a subablative phase followed by the development of a vapor plume and material ejection. The ablation plume consists of water vapor and gaseous organic products as well as water droplets and/or particulate tissue fragments. The expansion of the plume into the surrounding air is coupled with the generation

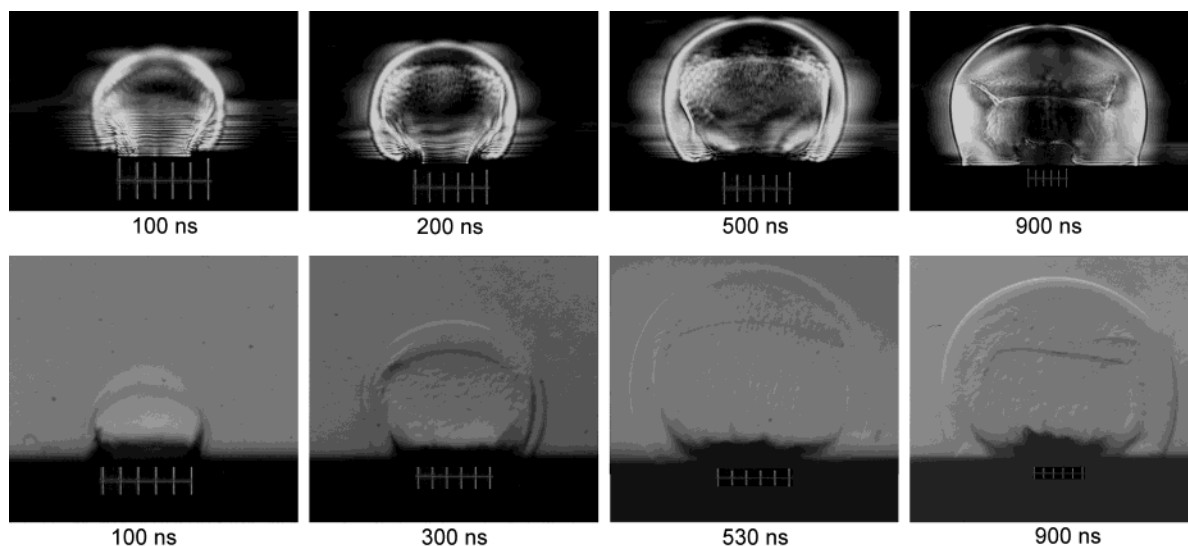


**Figure 21.** Early phase of Q-switched Er:YAG laser ablation of water characterized by vapor plume formation, shock wave emission, and droplet ejection. Pulse duration, 100 ns; radiant exposure, 5 J/cm<sup>2</sup>; spot size, 500  $\mu$ m. Upper row: Schlieren photographs. Lower row: bright-field photographs. Scale bars are 500  $\mu$ m.

of acoustic transients that, for high volumetric energy densities in the ablated material, evolve into shock waves.

To date, most investigations of the plume dynamics and acoustic phenomena associated with pulsed laser ablation of biological tissues have been performed experimentally. Particulate matter in the ablation plume has been visualized using bright-field photography<sup>237–241</sup> or photographic recording of scattered light.<sup>242,243</sup> Schlieren photography has enabled the visualization of vapor and gaseous ablation products in addition to the ejected particles.<sup>240,244,245</sup> Resonance absorption methods<sup>227,246</sup> have been used to detect specific ablation products and chemical reactions in the plume.<sup>246</sup> Other techniques employed to analyze the composition of the ablation products include mass spectrometry<sup>247</sup> and gas chromatography.<sup>248</sup> Specific data on the ablation dynamics, including the time delay between laser irradiation and the onset of tissue removal, the velocities of acoustic transients, vapor plume, and particulate matter, and the duration of postpulse material ejection, have been obtained by photographic techniques<sup>238–245,249,250</sup> or by use of a probe laser beam directed parallel to the target surface.<sup>238,240,244,249–251</sup> Probe beam techniques have also provided quantitative time-resolved information regarding plume transmission<sup>240</sup> and the shape and amplitude of acoustic transients.<sup>140,252–254</sup>

### 1. Plume Dynamics for Nanosecond Pulses

Ablation begins with the formation of a vapor plume that drives the propagation of a shock wave into the surrounding air. The ablation process continues with the ejection of condensed material mixed with vapor. This applies both to tissues, in which case the ejected material mostly consists of particulate fragments,<sup>238–243,245</sup> and to liquids, in which case small droplets are ejected.<sup>255,256</sup> The sequence of events in the early phase of Q-switched Er:YAG laser ( $\lambda = 2.94 \mu$ m) ablation of water is shown in Figure 21. The vapor plume and the external shock wave driven by the vapor expansion are both visible on the

Schlieren photographs in the upper row of the figure. Apart from the external shock wave, another shock wave within the plume that travels back toward the surface of the target becomes visible after 200 ns. This shock wave, like the external shock wave, originates at the contact front between plume and ambient air, where density and pressure rise due to the collision of the expanding vapor with the surrounding air. The vapor molecules propagating with the plume possess a nonzero average velocity. When they collide with air molecules that are, on average, at rest, they are partially reflected back into the plume. This reflection leads to the formation of the internal shock wave that begins to propagate toward the target surface when the rarefaction from the expansion of the vapor plume has reduced the pressure in the plume considerably below its initial value.<sup>257–259</sup> Material ejection commences after about 200 ns and is best visible in the bright-field pictures. The third and fourth pictures feature a fan-shaped cloud consisting of small droplets with sizes well below the resolution limit of the camera ( $<2 \mu$ m). Ejection of this cloud is driven by a phase explosion (section IV.D) and is followed by recoil-induced material expulsion that becomes visible after 900 ns. The continuation of the recoil-induced material ejection at later times is shown later in Figure 27.

The shock wave is often emitted after the end of the laser irradiation. However, at high radiant exposures shock wave emission begins during the laser pulse.<sup>251</sup> Ablation of water and soft tissue is, furthermore, characterized by a time difference of 100–200 ns between shock wave emission and particle ejection, as is visible in Figure 21. This time difference indicates that at moderate to high radiant exposures, the large volumetric energy densities produced in the superficial tissue layers drives the tissue water to a supercritical state and also enables the thermal dissociation of the molecules of the ECM. Therefore at the early stage of the ablation, the plume consists only of gaseous products and is driven by a volumetric process akin to non-equilibrium



interphase mass transfer (section V.B.). At later times, particulate fragments are ejected as the ablation proceeds to deeper tissue layers where the energy density is only sufficient to drive phase explosion and confined boiling processes. It should be noted that normal boiling does not provide a significant pathway for material removal on the nanosecond time scale, as even in pure liquids the bubbles do not have time to travel to the target surface.<sup>165</sup> In tissue, the mobility of vapor bubbles is even further inhibited by the presence of the ECM.

The delay between laser irradiation and the onset of particle ejection was measured between 90 and 280 ns for Q-switched Er:YAG laser ( $\lambda = 2.94 \mu\text{m}$ ) ablation of skin, liver, and agar and decreased with increasing radiant exposure.<sup>238,251</sup> A delay of 70 ns was observed for ArF excimer laser ( $\lambda = 193 \text{ nm}$ ) ablation of corneal tissue.<sup>239</sup> Processes contributing to these delays include the spinodal decomposition underlying the phase explosion, the straining of the tissue matrix required to achieve tissue fracture, and the acceleration of the plume material. At radiant exposures close to the ablation threshold, where thermal denaturation processes may be necessary to initiate ablation, the time required for thermal degradation and weakening of the tissue matrix further contributes to the delay of material ejection.<sup>233</sup>

Walsh and Deutsch<sup>238</sup> reported that particles ejected at early times after Q-switched Er:YAG laser irradiation of skin were quite small ( $<20 \mu\text{m}$ ) but became as large as  $20\text{--}50 \mu\text{m}$  in diameter after  $2\text{--}3 \mu\text{s}$ . This increase of particle diameter with time is consistent with the results of molecular dynamics simulations.<sup>260</sup> The particle size also depends on optical penetration depth: considerably larger particles are produced by KrF excimer laser irradiation ( $\lambda = 248 \text{ nm}$ ) of cornea than by ArF excimer laser irradiation ( $\lambda = 193 \text{ nm}$ )<sup>242</sup> because the optical penetration depth is about 100 times larger at  $\lambda = 248 \text{ nm}$  (Figure 4).

Shock front velocities are usually on the order of  $2000\text{--}4000 \text{ m/s}$  for both IR and UV wavelengths.<sup>239,251,261</sup> Particle velocities range from about  $500$  to about  $2000 \text{ m/s}$  but can approach  $5000 \text{ m/s}$  for very large radiant exposures.<sup>238,239,245,251</sup> Particle velocities increase markedly with increasing tissue strength and radiant exposure, consistent with the concept of confined boiling (sections V.E,F). The increase with radiant exposure is related to the delayed onset of particle ejection after the laser pulse. As a result, larger radiant exposures will lead to larger volumetric energy densities in the target and thus to higher pressures and velocities for plume expansion and shock wave emission. The volumetric energy density can become sufficiently high to initiate pyrolysis or plasma formation resulting in the creation of a luminous plume.<sup>251</sup>

A shock wave originating from a strong explosion in a homogeneous atmosphere is called a blast wave. The propagation of the shock front with time was first described by Taylor,<sup>262</sup> Sedov,<sup>263–265</sup> and, through the use of a higher order approximation, Sakurai.<sup>266,267</sup> This theory neglects the mass of the gas and debris

driving the shock wave and is thus valid only once the shock wave has swept over a mass of atmospheric gas much greater than the mass in which the energy was initially concentrated. Various authors have since obtained solutions for the mass-dependent flow regime.<sup>171,268–273</sup> Simple analytical solutions are available for some limiting cases. When the mass of the gas encompassed by the shock wave is much greater than the initial ablated mass and the pressure driving the shock is much greater than the atmospheric pressure ahead of the shock front, the position,  $R(t)$ , of a spherical shock wave is governed by<sup>273</sup>

$$R(t) = \xi(E_0/\rho_0)^{1/5} t^{2/5} \quad (10)$$

and that of a planar shock wave by

$$R(t) = \xi(E_0/\rho_0)^{1/3} t^{2/3} \quad (11)$$

where  $E_0$  is the energy driving the explosion,  $\rho_0$  the density of the undisturbed gas, and  $\xi$  a constant that is a function of the specific heat capacity ratio,  $\gamma$ , of the gas. The peak pressure scales with  $E^{2/5}$ .<sup>265</sup> Once the shock wave pressure becomes comparable to the ambient pressure, its propagation is better described by the Jones approximation.<sup>274,275</sup> When the mass of the material removed is very large or the background pressure very low (including vacuum), the motion of a planar shock wave can be described by<sup>268</sup>

$$R(t) = \xi(E_0/\rho_0)^{1/2} t \quad (12)$$

More refined numerical simulations by Brode<sup>258</sup> and the analytical treatment by Arnold and co-workers<sup>257</sup> include the movements of the external shock front, the contact front between plume and ambient gas, and the internal shock front within the plume.

A comparison of experimental  $R(t)$  data with eqs 10–12 allows the assessment of the transduction of laser pulse energy into blast wave energy  $E_0$ .<sup>227,275</sup> A comparison of these relations with experimental data for pulsed laser tissue ablation has been presented by Walsh and Deutsch.<sup>238</sup> However, the validity of their study is limited by the fact that the examination was performed for the particle velocity instead of the shock front velocity.

## 2. Plume Dynamics for Microsecond Pulses

Pulses from free-running lasers usually possess durations of more than  $100 \mu\text{s}$ . Thus, unlike nanosecond ablation, plume formation and expansion occurs largely during the laser irradiation. The ablation plume influences the energy deposition of the laser radiation into the tissue target, and the plume dynamics itself is also influenced by the interaction of the laser beam with the ejected material. Nevertheless, the succession of a subablative phase, development of a vapor plume, and material ejection is similar to the case with nanosecond pulses, even though it occurs on a much longer time scale.<sup>240,241</sup> However, the heating rates available from microsecond laser pulses are generally much smaller

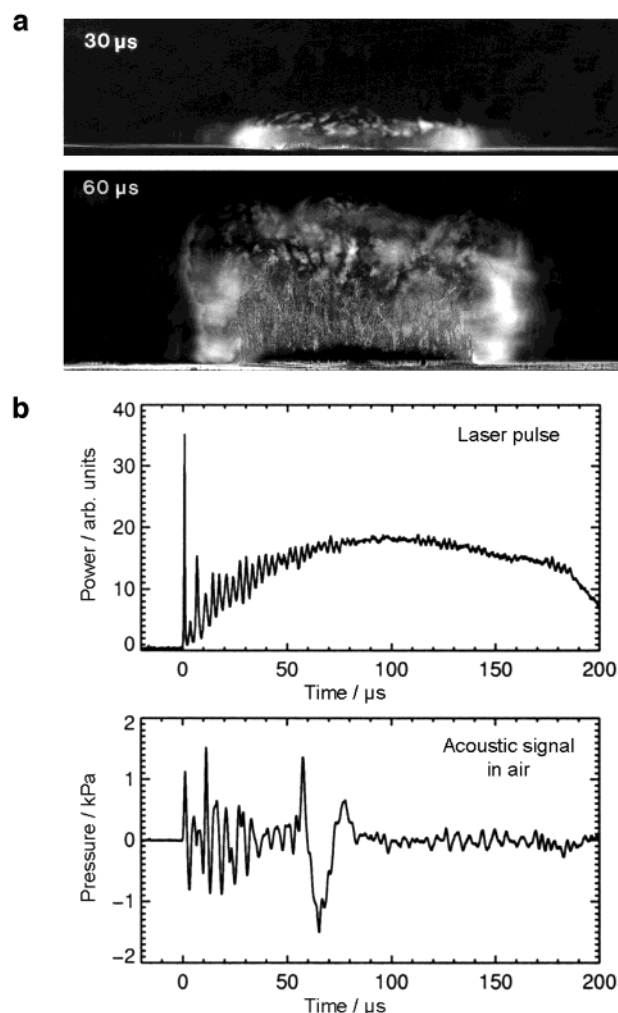


**Figure 22.** (a) Plume dynamics and (b) corresponding acoustic signal in air for free-running Er:YAG ablation of gelatin with 90% water content. Pulse duration, 200  $\mu\text{s}$ ; radiant exposure, 4.6 J/cm<sup>2</sup>; spot size, 5 mm. Only a vapor plume is produced during the first 30  $\mu\text{s}$ , after which material ejection commences. Prior to material ejection, various short acoustic transients are generated that are correlated with the temporal intensity modulation of the laser pulse. The onset of material ejection leads to a much longer bipolar signal containing a major part of the acoustic energy.<sup>241</sup> (Reprinted with permission from ref 279. Copyright 2000 SPIE.)

than those available from nanosecond laser pulses of moderate to high radiant exposure. These lower heating rates are typically insufficient to produce the volumetric energy densities necessary for supercritical water or direct thermal dissociation of ECM molecules. Free-running laser emission is usually characterized by intensity fluctuations during the laser pulse ("spiking" behavior). These intensity peaks modulate the rates of vaporization and material ejection.<sup>238,244,245,276</sup>

Acoustic transients are generated before and during material ejection. During the subablative phase, the air adjacent to the ablation site is heated by conduction, and its expansion creates an acoustic transient by the so-called thermal piston effect.<sup>277</sup> The intensity spikes of the laser pulse are coupled with the generation of several individual transients, as shown in Figure 22. Later, during the vaporization

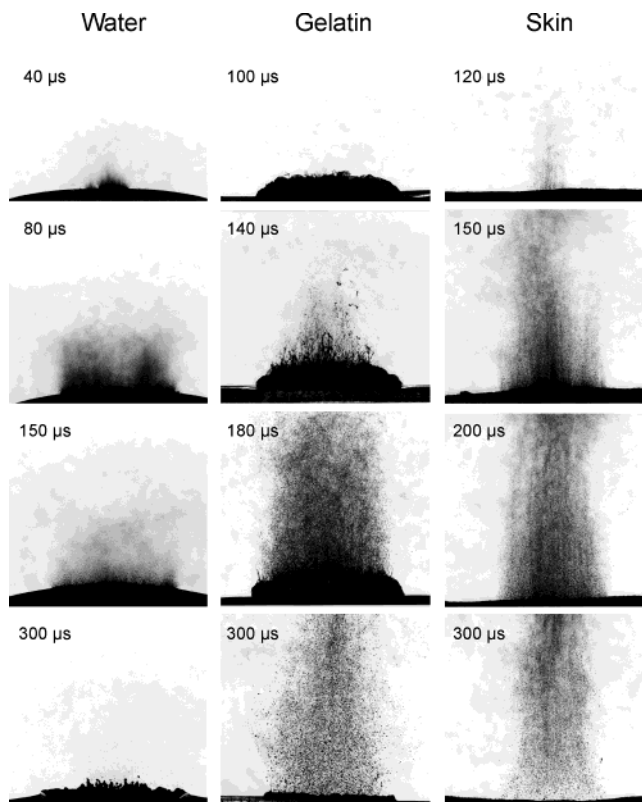


**Figure 23.** Dynamics of Er:YAG laser ablation of water, gelatin with 70% water content, and skin using a radiant exposure of 4.6 J/cm<sup>2</sup>, 5-mm spot size, and 200- $\mu\text{s}$  pulse duration. The times after the beginning of the laser pulse when the photographs were taken are indicated on the individual frames. Note the increasing delay in the ejection of particulate matter with increasing mechanical strength of the target. (Reprinted with permission from refs 240 and 241. Copyright 2002 SPIE and 2002 Andere Verlag.)

phase, the expanding vapor plume acts as a piston and produces acoustic transients that are again correlated to the intensity spikes of the laser pulse.<sup>276</sup> The onset of material ejection produces another piston-like movement that generates a strong bipolar acoustic signal.<sup>241,278,279</sup> The continued material ejection during later phases of the laser irradiation leads to smaller, irregular fluctuations of the acoustic signal amplitude.

The mechanisms leading to material ejection are the same as those for nanosecond pulses: a phase explosion for mechanically weak materials and a succession of phase explosion and confined boiling events for mechanically stronger tissues. Previously, it was believed that the generation of a phase explosion requires pulse durations in the nanosecond range.<sup>137</sup> However, using time-resolved photography, Nahen and Vogel<sup>240,241</sup> recently demonstrated that a phase explosion can also be produced by Er:YAG laser irradiation of water, gelatin, and skin with pulse durations on the order of 200  $\mu\text{s}$ . This is shown in Figure 23. The rapid droplet ejection during Er:YAG laser ablation of water can be explained only by the occurrence of a phase explosion, because in the absence of stress confinement, no other mechanism will lead to a material ejection perpendicular to the water surface. In gelatin, a phase explosion presumably occurs at the same time as in water.

**Table 3. Starting Time,  $t_0$ , of Material Ejection with Respect to the Beginning of the Laser Pulse, and Initial Velocity,  $v_0$ , of Ejected Particles for Water and Skin Ablation Using 200- $\mu$ s Er:YAG Laser Pulses Irradiating a Spot of 5 mm Diameter (Compiled from Ref 241)**

material	radiant exposure 4.6 J/cm <sup>2</sup>		radiant exposure 7.8 J/cm <sup>2</sup>	
	$t_0$ ( $\mu$ s)	$v_0$ (m/s)	$t_0$ ( $\mu$ s)	$v_0$ (m/s)
water	28	123	24	216
skin	117	188	49	360

However, it only deforms the gelatin surface without rupturing it. Fracture of the gelatin surface and rapid particle ejection are observed only after a further pressure buildup through confined boiling (section V.F). The material ejection during skin ablation is characterized also by the succession of a phase explosion followed by confined boiling. However, material ejection occurs even later than for gelatin because of the higher mechanical strength of skin. It is important to note that both skin and gelatin fragments are ejected in the form of solid particles. The absence of droplet-like ejecta indicates that gelatin exposed to temperatures near the spinodal limit does not melt within a time of 200  $\mu$ s, even though it melts at 60 °C for sufficiently long heat exposures. This finding is related to a strong increase in denaturation temperature for very short exposures, as discussed in section II.C.

The time delay to the onset of particle ejection increases with increasing mechanical strength and decreasing radiant exposure, as shown in Table 3.<sup>240</sup> At moderate radiant exposures, the time delay amounts to tens of microseconds. However, for high radiant exposures, particle ejection is already initiated during the first intensity spike of the laser pulse.<sup>238,244,245</sup> Table 3 shows that the initial velocity of tissue fragments ejected during skin ablation is higher than the initial droplet velocity in water ablation. The higher velocity for skin is due to the confinement by the tissue matrix that results in buildup of larger pressures and a more violent material ejection process.

Initial particle velocities observed for microsecond laser pulses are about 1 order of magnitude lower than those reported for nanosecond pulses.<sup>241,245</sup> For free-running pulses with durations in the range of hundreds of microseconds, an increase of the radiant exposure results in an earlier start of the material ejection but hardly changes the volumetric energy density required to initiate ejection. As a result, the ejection velocity shows minimal change with the incident dose, except for very large radiant exposures, in which case a dose in excess of the ablation threshold is already provided by the first intensity spike. The dynamics is fundamentally different for nanosecond exposures, in which case the ablation commences only towards the end of the laser pulse. In this case, an increase of the radiant exposure is coupled with an increase of the volumetric energy density prior to the onset of material removal and thus translates directly into higher temperature, pressure, and ejection velocity.

### 3. Postpulse Ablation

In both Q-switched and free-running laser ablation of soft tissues, material ejection continues for a considerable time after the end of the laser irradiation. The time period during which particles were detected close to the target surface after application of nanosecond pulses ranges from a few microseconds to several milliseconds for both UV and IR wavelengths.<sup>203,204,238,239,242,243,249,251</sup> Thus, postpulse ablation can last 3–5 orders of magnitude longer than the laser pulse duration. Similar durations for postpulse ablation were reported for microsecond laser exposures.<sup>238,240,250</sup> Postpulse ablation generally lasts longer for mechanically weaker tissues, larger radiant exposures, and larger laser beam diameters.

One possible driving force for the continuation of the ablation process after the end of the laser pulse is the heat retained in the tissue. A progressive weakening of the tissue matrix through thermal denaturation enables a propagation of the ablation front until the vapor pressure in the residual tissue drops below the UTS of the weakened tissue matrix. The lengthening of the ablation process by the combined action of thermal diffusion and denaturation is most pronounced for laser wavelengths with large optical penetration depth, i.e., long thermal relaxation times, and for mechanically weak tissues or tissue phantoms.<sup>176</sup>

Another very important source of postpulse ablation are hydrodynamic phenomena. These phenomena include recoil stress-induced material expulsion and jetting from collapsing bubbles in the target that were produced by thermoelastic tensile stress.<sup>203,204</sup> Recoil-induced material expulsion will be described in section VI.B.2. Another possible cause of the persistence of a particle cloud close to the tissue surface is the cessation of the movement of plume constituents ejected at late times.<sup>271,272</sup>

## B. Recoil Stress

### 1. Temporal Shape and Amplitude

Both the rapidly expanding vapor plume and the ejected particles generate recoil stresses that impart momentum to the tissue. The linear momentum per unit area of the ablated material,  $I$ , is the time integral of the recoil stress,  $\sigma_{\text{rec}}$ , at the target surface:

$$I = \int_0^{\infty} \sigma_{\text{rec}}(t) dt \quad (13)$$

A derivation of the peak recoil stress requires assumptions to be made on the nature and duration of the ablation process. Various authors have presented solutions for the peak stress amplitude produced by a continuous vaporization process<sup>13,150,280,281</sup> and by explosive ablation, in which the entire laser pulse is deposited prior to the onset of material removal.<sup>137,282</sup> The derivations are usually made by assuming that the duration of the ablation process scales with the laser pulse duration. This assumption neglects potential postpulse ablation processes (section VI.A.3) and may thus lead to an overestimation of the recoil stress.



Experimental investigations of the recoil stress produced by nanosecond laser ablation have been performed mostly through direct pressure measurements using piezoelectric transducers.<sup>78,137,146,150,207,283</sup> Peak pressure amplitudes range from a few MPa at the ablation threshold up to several hundred MPa for radiant exposures well above threshold. Recoil stresses produced by free-running microsecond laser pulses have been determined primarily by measurement of the recoil momentum using the ballistic pendulum method. The average axial stress was then calculated from the recoil momentum, the spot size, and the laser pulse duration.<sup>281,284</sup> Note that the peak recoil stress produced by the intensity maxima of the free-running pulses, which is considerably higher than the average axial stress, cannot be determined by this method. Direct transducer measurements of the recoil stress produced during cornea ablation using free-running Er:YSSG laser irradiation at a radiant exposure of 50 J/cm<sup>2</sup> revealed peak pressures of 2 MPa,<sup>283</sup> while the average pressure value for skin ablation at the same radiant exposure was only 0.3 MPa.<sup>281</sup>

The recoil momentum increases monotonically with radiant exposure. However, it is interesting to note that this is not always the case for the impulse coupling coefficient,  $I/\Phi$ , that describes the efficiency with which the deposited energy generates momentum.<sup>282,284</sup> For nanosecond ablation, in which the material ejection process starts after the laser irradiation, the impulse coupling coefficient exhibits a maximum value at 6.4 times the ablation threshold and decreases for higher radiant exposures.<sup>284</sup> This phenomenon is related to the decrease of the ablation efficiency at high radiant exposures, as described in section VII.A.3.

Experimental data for the variation of recoil stress with radiant exposure has been collected at various UV and IR laser wavelengths and compared to model predictions for different types of ablation processes in order to analyze the character of these ablation processes at various UV and IR laser wavelengths. These comparisons have allowed differentiation between continuous and explosive ablation processes<sup>137,150</sup> (section VIII.B.2).

In stress-confined tissue ablation, the compressive recoil stress transient is superimposed on a bipolar thermoelastic transient.<sup>208</sup> Figure 24 demonstrates the transition from a bipolar thermoelastic stress transient for radiant exposures below the ablation threshold to a monopolar compressive transient when the ablation threshold is exceeded. This transition and the corresponding increase in peak pressure is a sensitive method for the determination of the ablation threshold<sup>78,137,146,150,207</sup> (section VII.B.1).

## 2. Recoil-Induced Material Expulsion

The recoil stress produced by both vaporization and material ejection through phase explosion and confined boiling can induce a secondary material expulsion process that provides a strong increase of the ablation efficiency.<sup>13,280</sup> Recoil-induced material expulsion is most pronounced during ablation of liquids and of materials for which a molten layer is formed

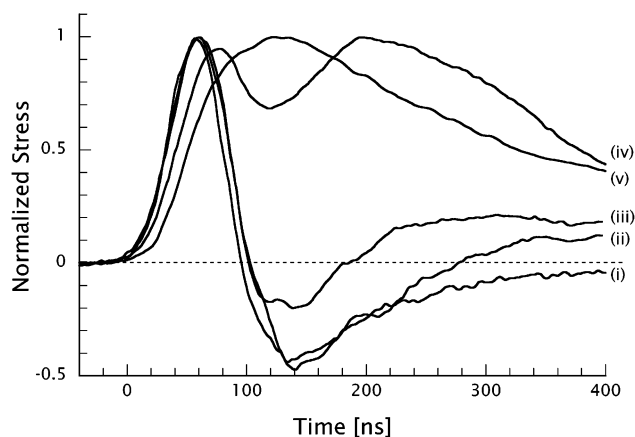


**Figure 24.** Stress transients resulting from TEA-CO<sub>2</sub> laser ( $t_p = 30$  ns) irradiation of porcine dermis for radiant exposures below the ablation threshold (i), at the threshold (ii), and above the threshold (iii–v). Radiant exposure below the ablation threshold produce bipolar thermoelastic stress transients. Radiant exposures equal to and above the ablation threshold result in a compressive pulse produced by the ablative recoil that is delayed relative to the laser pulse and the peak compressive thermoelastic stress. The time delay decreases with increasing radiant exposure until the tensile stress component vanishes, and both compressive peaks combine to form a single compressive stress pulse. This is the case in (v) at  $4.3\times$  threshold radiant exposure. (Adapted with permission from ref 137. Copyright 1996 Biophysical Society.)

during the ablation process. Variations of the recoil stress amplitude in the radial direction result in a force driving the liquid toward the edges of the ablation crater and out of the crater, as illustrated schematically in Figure 25. Note, however, that formation of a molten layer of tissue is not a necessary condition for recoil-induced material expulsion. Material will be ejected whenever the recoil stress component in the radial direction exceeds the mechanical strength of the tissue.

The sequence of primary material ejection and recoil-induced material expulsion is shown in Figures 26 and 27 for free-running and Q-switched Er:YAG laser ablation of water. While the primary material ejection visible at short delay times takes place across the entire ablation area, recoil-induced expulsion

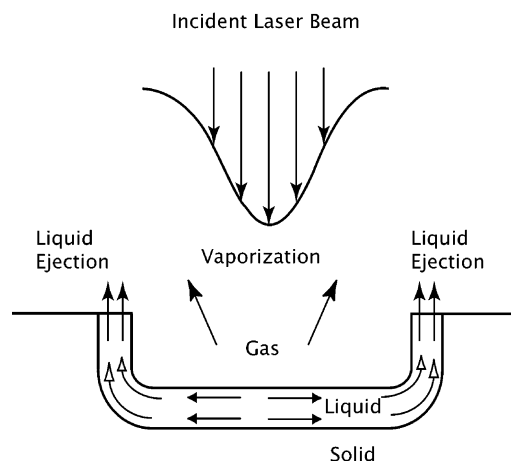


**Figure 25.** Illustration of recoil-induced material expulsion. (Adapted with permission from ref 284. Copyright 1989 American Institute of Physics.)

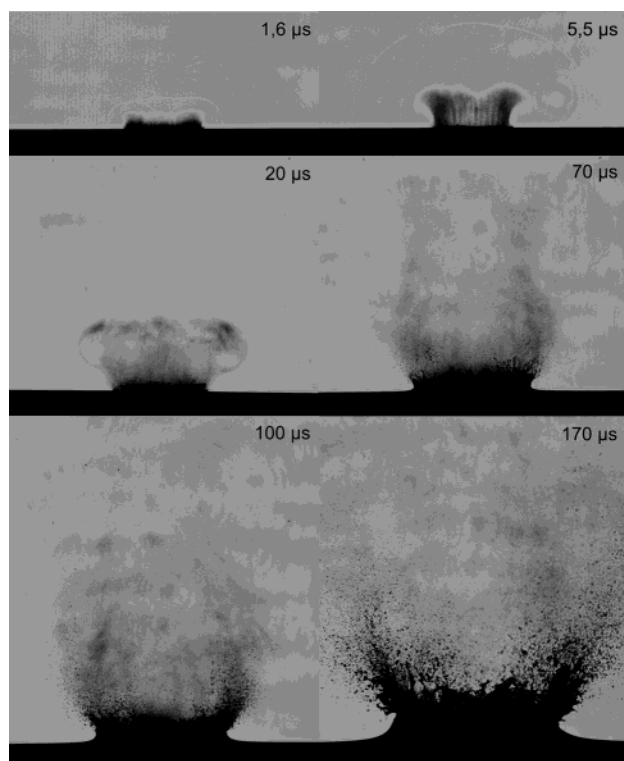


**Figure 26.** Photographs of water ablation by 200- $\mu$ s Er:YAG laser pulses at a radiant exposure of 32 J/cm<sup>2</sup> and 1.9-mm spot size. The ejection of a droplet cloud due to a phase explosion is followed by recoil-induced expulsion of a large mass of liquid water.

occurs preferentially at the ablation crater rim and includes the ejection of droplets much larger than those ejected during the initial phase explosion. For microsecond pulses irradiating a large ablation spot, as in Figure 26, the initial material ejection is directed perpendicular to the surface, while the recoil-induced expulsion exhibits a lateral component of motion. The mass expelled at later times far exceeds the mass ejected during the phase explosion. However, the velocity of the ejecta is considerably slower.

The recoil stress leads to a transient indentation of the surface.<sup>245,249,286</sup> The material displacement initiates the formation of a surface wave that is further enhanced by the vapor pressure in the expanding ablation crater.<sup>239,286</sup> For soft tissues, the recoil-induced material expulsion is less violent than that shown in Figures 26 and 27 for water, but it still plays an important role when the tissue is mechanically weak.<sup>249,280,284</sup>

A comparison of Figures 23 and 27 shows that recoil-induced droplet expulsion is present only during pulses of high radiant exposure and commences much later than the primary ejection process. Recoil-induced expulsion thus exhibits a threshold well above the ablation threshold. The threshold for recoil-induced material expulsion during soft-tissue ablation is even higher than that for water ablation, because the recoil stress component in the lateral direction must exceed the ultimate tensile strength of the tissue, i.e.,  $\sigma_{\text{rec}} > \sigma_{\text{UTS}}$ . Photographic evidence for the ejection of large tissue fragments with considerable lateral spread during liver ablation has

been presented by Domankevitz and Nishioka<sup>287</sup> and by Apitz and Vogel.<sup>249</sup> Cummings and Walsh<sup>281</sup> also detected large liver fragments in their ablation plumes. Further evidence for the appearance of a secondary material ejection process during tissue ablation is provided by an increase of the ablation efficiency above a certain radiant exposure. Such an increase has been observed for weak tissues, such as liver and myocardium, as well as for gelatin with high water content. However, this increase is not observed for tissues with greater mechanical strength, such as skin.<sup>119,241</sup>

Zweig and co-workers were the first to postulate and model the possible contribution of recoil-induced stresses to soft-tissue ablation.<sup>280,284,288–290</sup> However, they considered only surface vaporization as a primary ablation process, neglecting explosive mechanisms such as phase explosion and confined boiling. Since these processes contribute to material ejection both directly and indirectly by generation of a recoil momentum, their neglect leads to an underestimation of the importance of material ejection to the entire ablation process.

Cummings and Walsh<sup>251</sup> argued that tissue is elastically deformed by the ablative recoil stress (see section VI.D, below) and that the rebound of this deformation may contribute to material ejection. Evidence for the possibility of jetlike material ejection by the rebound of an elastically deformed surface was, for materials with moderate mechanical strength, later provided through numerical simulations<sup>291</sup> and photographic investigations.<sup>292,293</sup>

For mechanically strong tissues, the recoil stress does not lead to material expulsion. However, it can result in tissue tearing at the sides of the ablation crater, as can be seen in Figure 28. The origin of the cracks and the tearing patterns depend on the location and orientation of mechanical flaws in the tissue.<sup>281</sup> Examples of such flaws include the transitions between corneal lamellae, sinusoid spaces holding blood between plates of cells in liver tissue, and the weakness of the longitudinal strength of blood vessels compared to their circumferential strength.<sup>281</sup> Tissue tearing was not observed for skin, because here the collagen fibrils are not layered as in cornea but rather are interwoven (Figure 2). Tearing is most pronounced for deep ablation craters, where the confinement of ablation products by the crater walls creates higher pressures in the ablation plume as compared to ablation over a broad area.

### 3. Collateral Tissue Effects Induced by Recoil Stress

Apart from tears in the crater walls, recoil-induced stress transients can produce more subtle forms of collateral tissue damage. Tissue is more susceptible to damage from tensile and shear stress than to compressive stress.<sup>53,54,294</sup> To identify potential sources of tissue damage, it is thus useful to look for the production of shear and tensile stress by ablative recoil. The compressive recoil stress at the tissue surface causes radial tension across the periphery of the area under pressure and across the front of the expanding pressure wave below the irradiated spot.<sup>295</sup> Tensile stress can also be generated when the compressive recoil stresses are partially reflected at

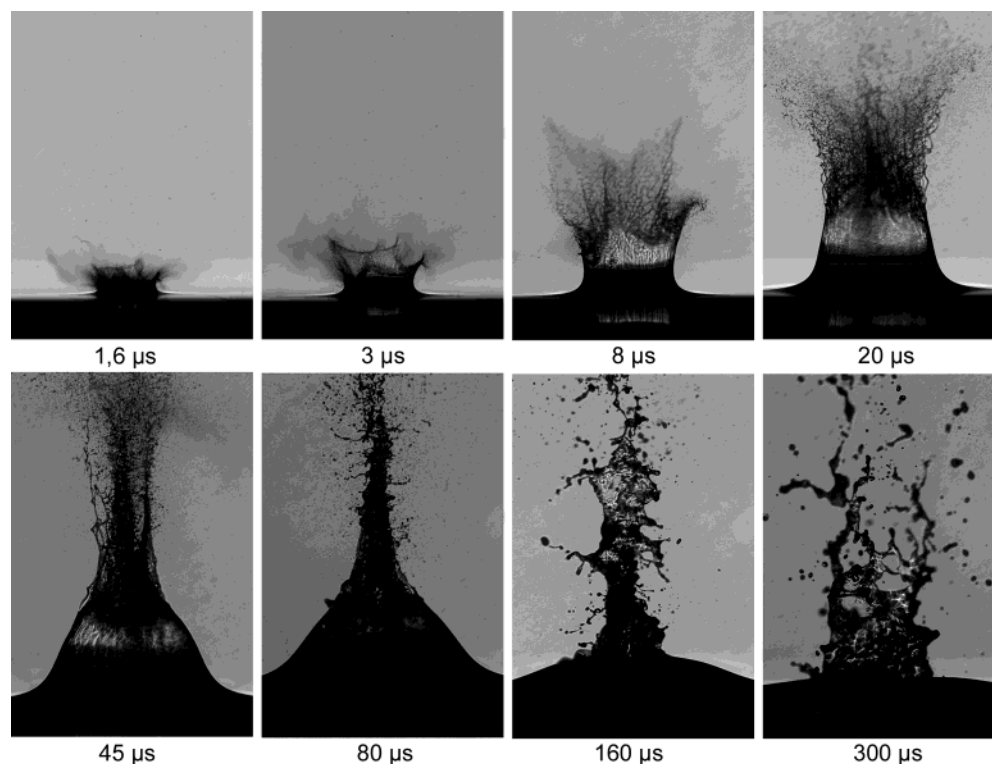


**Figure 27.** Late phase of the ablation dynamics for water ablation by 100-ns Er:YAG laser pulses at 5 J/cm<sup>2</sup> radiant exposure and 0.5-mm spot size. The laser parameters used were the same as in Figure 21, where the early phase of the ablation dynamics is presented. During the first 20  $\mu$ s, the plume dynamics is characterized by a powerful recoil-induced expulsion of liquid water. The flow in the vapor plume (section VI.C) then leads to a focusing of the hollow water column into a jetlike structure (20–80  $\mu$ s) that finally disintegrates (80–300  $\mu$ s).

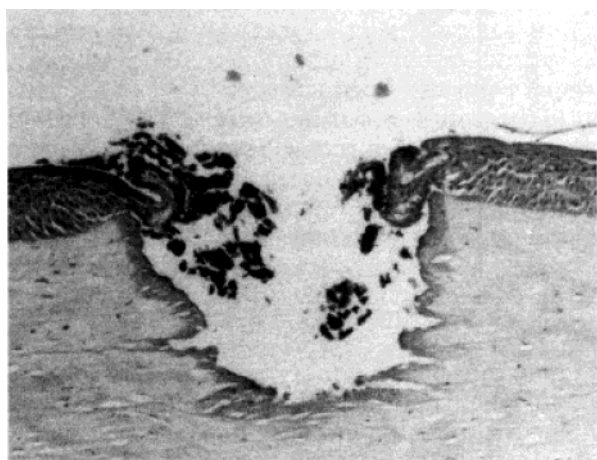


**Figure 28.** Histologic slide showing an ablation crater in bovine cornea produced by an Er:YSGG laser pulse with  $t_p = 250 \mu$ s and  $\Phi_0 = 100 \text{ J/cm}^2$ . The tissue around the ablation crater exhibits a 25–50- $\mu$ m zone of thermal damage (dark) and mechanical tearing between the corneal lamellae. (Reprinted with permission from ref 281. Copyright 1993 Optical Society of America.)

interfaces with materials of lower acoustic impedance, and due to acoustic diffraction associated with the propagation of stress waves emanating from a finite source (section IV.B).

Putative photoacoustic damage produced during ArF excimer ( $\lambda = 193 \text{ nm}$ ) laser ablation of skin was described by Watanabe and co-workers<sup>296</sup> and by Yashima and co-workers.<sup>297,298</sup> Doukas and co-workers found that unipolar laser-induced pulses of compressive pressure cause cell damage at ampli-

tudes exceeding 50–100 MPa<sup>299</sup> and pressure gradients exceeding 2 MPa/ $\mu$ m.<sup>300</sup> The formation of tensile stress with an amplitude of 3.5 MPa inside the eyeball through diffraction of the recoil stress wave produced during ArF excimer laser ablation of the cornea was demonstrated by Pini and co-workers.<sup>157</sup> Könz and co-workers demonstrated recoil-induced damage of the corneal endothelium after mid-IR laser ablation of the corneal stroma.<sup>283</sup>

Thermoelastic stress transients below and slightly above the ablation threshold contain a tensile stress component (Figure 24) that may contribute to tissue damage. We are not aware of studies investigating the effects of tensile thermoelastic stress transients in nonablated tissue. However, it is known that bipolar stress transients with an amplitude of 9.5 MPa can induce breakage of viruses.<sup>301–303</sup>

### C. Flow-Induced Material Redeposition

The flow in the ablation plume originates from the entire area of the irradiated spot. However, as the plume expands it acquires a mushroom-like shape, exhibiting a ring vortex at its top, a thin stem with a diameter smaller than the ablation spot, and a radial flow component parallel to the surface at the foot of the plume.<sup>242,243,279</sup> The evolution of this shape is illustrated in Figure 29 for ArF excimer laser ablation of PMMA and cornea.

The formation of the ring vortex is due to the viscous interaction between the flow of the ablated material and the stagnant ambient gas that leads to a Rayleigh–Taylor instability.<sup>13,259</sup> The thinning of



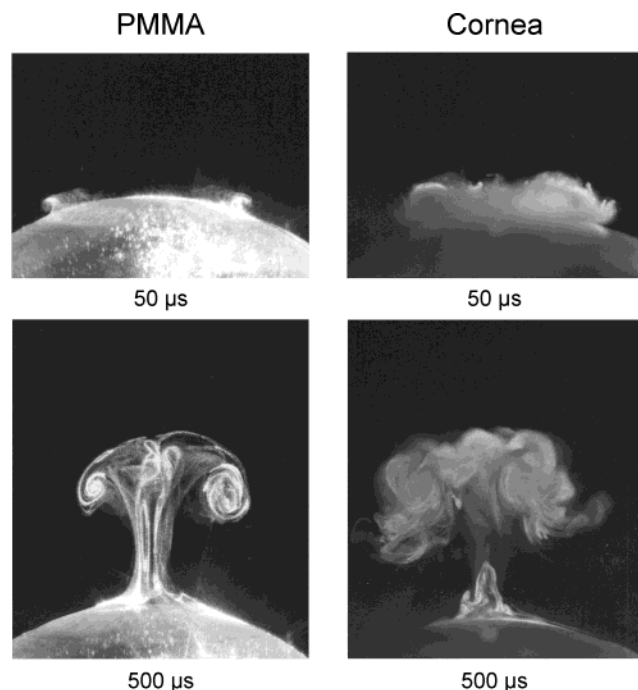


**Figure 29.** Photographs of plumes for PMMA and cornea ablation using ArF excimer laser irradiation ( $\lambda = 193$  nm) at a radiant exposure of  $120 \text{ mJ/cm}^2$ . The diameter of the ablated area was 7 mm. The flow pattern exhibits a mushroom-like shape with a ring vortex at the top, a thin stem, and a radial flow parallel to the target surface that turns in a direction perpendicular to the surface when it approaches the center of the ablation spot. (Reprinted with permission from ref 243. Copyright 1997 American Academy of Ophthalmology, Inc.)

the mushroom stem can be understood by considering Bernoulli's law, which states that the sum of static pressure and dynamic pressure in an inviscid, isothermal, irrotational flow is constant:<sup>265</sup>

$$p + \frac{\rho}{2}v^2 = p_0 = \text{constant} \quad (14)$$

Here,  $p$  is the static flow pressure,  $\rho$  the fluid density,  $v$  the flow velocity, and  $p_0$  the static pressure at  $v = 0$ . Large flow velocities, such as those encountered in the expanding plume, are coupled with large dynamic pressures and thus with small values of the static pressure inside the flow. The underpressure relative to the ambient air leads to the thinning of the stem of the ablation plume and induces a radial flow along the target surface toward the center of the ablation spot.

The radial flow parallel to the tissue surface can result in a redistribution of ablation products across the ablation spot. When corneal refractive surgery was performed using large ablation spots  $\geq 6$  mm, it was noticed that the ablation rates were smaller in the center of the ablation zone than in its periphery, even though the irradiance was spatially homogeneous. As a result, "central islands" remained that distorted the intended refractive correction.<sup>23,304–306</sup> A similar dependence of the ablation rate on the radial coordinate had previously been observed for polymer ablation.<sup>307</sup> Photographic investigations of the plume dynamics revealed that the "central islands" are the result of a redeposition of ablated

material after the end of the laser pulse that preferentially occurs near the stagnation point of the flow at the center of the ablated area,<sup>243</sup> as shown in Figure 29. A second factor contributing to the non-uniformity of the ablation rate is the attenuation of subsequent laser pulses in the center region of the ablated area by remnants of the plume from previous pulses that preferentially stay in the vicinity of the stagnation point. The "central islands" are most pronounced, with large spot sizes because the movement of the particle plume slows with increasing diameter of the irradiated spot.<sup>243</sup> This facilitates the redeposition of ablated material and increases the amount of debris that contributes to the spatially inhomogeneous attenuation of subsequent pulses.

#### D. Shielding by the Ablation Plume

Absorption, scattering, and diffuse reflection of incident laser light by the ablation plume lead to a reduction of the energy delivered to the target tissue and thus to a reduction of the ablation efficiency. Two approaches have been taken to estimate the shielding properties of the ablation plume. The first approach relies on a comparison of measured etch depth versus radiant exposure data with predictions of simple theoretical models (section VII) in which the extinction coefficient of the plume serves as a fit parameter.<sup>245,308,309</sup> The second approach consists of a direct measurement of the diffuse reflectance of the plume<sup>120</sup> and of the entire transmission reduction by the plume.<sup>240</sup>

In all studies comparing the predictions of ablation models with etch depth versus radiant exposure data, the interaction length between the laser beam and debris was assumed to be equal to the ablation crater depth.<sup>245,308,309</sup> However, this is reasonable only when no sample material is ejected during the laser pulse, which applies for nanosecond pulses (section VI.A.1) but not for microsecond pulses (section VI.A.2). For pulse durations between  $100 \mu\text{s}$  and  $1 \text{ ms}$ , the ablation plume reaches a height of several millimeters during the laser pulse, and the interaction length between the incident laser pulse and the plume is 2 orders of magnitude larger than the depth of the ablation crater.<sup>240</sup> The values for the extinction coefficient ranging between  $36$  and  $288 \text{ cm}^{-1}$ , obtained by various authors<sup>245,308,309</sup> under the assumption of an interaction length equal to the crater depth, are thus much larger than the actual values. Direct transmission measurements for soft-tissue ablation using Er:YAG laser irradiation ( $\lambda = 2.94 \mu\text{m}$ ) yield results on the order of  $1 \text{ cm}^{-1}$ .<sup>240</sup>

Hibst and Kaufmann<sup>310,311</sup> stated that ablation of skin using a free-running Er:YAG laser is not influenced by debris screening, because they observed a linear increase in the ablation rate with radiant exposure. The linear dependence was thought to be consistent with a simple steady-state ablation process without shielding (section VII.A.2). The apparent consistency was further interpreted as an indication that skin ablation relies on vaporization without particle ejection, because it is known that water vapor hardly absorbs at the Er:YAG laser wavelength.<sup>312</sup> Nahen and Vogel<sup>240</sup> showed later that such

conclusions regarding the mechanisms of laser ablation, drawn solely from ablation rate measurements, can be very misleading. Using photographic investigations, they demonstrated that Er:YAG laser ablation of water, gelatin, and skin is always accompanied by material ejection. The ejected debris attenuated the incident laser energy by up to 40%, even at moderate radiant exposures. Nevertheless, the etch depth showed a linear dependence on radiant exposure due to the combination of two nonlinear effects: the increasing attenuation of the incident laser beam by the ablation plume was compensated by an equally strong increase of the efficiency of material ejection.

Plume reflectance measurements by Nishioka and Domankevitz<sup>120</sup> showed that shielding is strongly enhanced when a series of pulses is delivered as opposed to single pulses. Kaufmann and Hibst<sup>313</sup> investigated the Er:YAG laser ablation of skin at different repetition rates and observed a decrease of the etch depth per pulse from 40 to 10  $\mu\text{m}$  when the pulse repetition rate was increased from 1 to 10 Hz. The significant reduction of the ablation efficiency at the higher repetition rate was attributed to increased shielding by the ablation plume. Kaufmann and Hibst used a spot size of 2 mm for ablation. When a considerably smaller spot size was used, in which case the lateral spread of the plume removes a larger fraction of the ablation products out of the beam path, the etch depth did not decrease with increasing repetition rate.<sup>314</sup>

At very high radiant exposures, plasma formation in front of the target may lead to a further decrease of the optical transmission to the target.<sup>12,315–317</sup> The plasma formation is initiated by heating of the plume and/or the target through linear absorption and thermionic emission of free electrons that then seed an ionization avalanche (section X). Plasma shielding was reported for ArF excimer ( $\lambda = 193$  nm) laser ablation of skin with radiant exposures larger than 0.25 J/cm<sup>2</sup>,<sup>150</sup> and for TEA-CO<sub>2</sub> ( $\lambda = 10.6$   $\mu\text{m}$ ) laser ablation of skin with radiant exposures larger than 12–18 J/cm<sup>2</sup>.<sup>315,318</sup> The ratio of the radiant exposures necessary for plasma formation using 10.6- $\mu\text{m}$  irradiation compared to 193-nm irradiation scales directly with the ratio of the optical penetration depths (18  $\mu\text{m}$  vs 330 nm). In all cases, the plasma originated from the tissue surface rather than the ablation plume because the durations of the intensity peaks responsible for plasma ignition were shorter ( $\leq 100$  ns) than the time commonly required for material ejection. Once plasma formation begins, it extends rapidly into the space in front of the tissue surface and thus reduces the ablation efficiency.<sup>315,316,318</sup>

## VII. Ablation Models and Metrics

In the previous sections we have discussed the role of phase transitions and plume dynamics in pulsed laser ablation processes. Considering the complexity of the phenomena involved, and the variety of laser and tissue parameters that influence them, it is quite difficult to devise a single model that faithfully represents the physics of the processes involved and

yields predictions for quantities such as the amount of material removed, the threshold radiant exposure for material removal, and the zone of residual thermal injury within the tissue bulk. In this section, we will first examine early ablation models that were heuristic in nature and not designed with a particular ablation mechanism in mind (section VII.A). The goal of these models was to provide rough predictions for the amount of material removal based on knowledge of the laser parameters. Predictions for specific laser parameters rely on empirically determined metrics, such as ablation threshold, ablation enthalpy, and ablation efficiency, that characterize the energetics of the ablation process. In section VII.B, we examine the characteristics of these metrics and relate them to predictions made by the heuristic models as well as available data. As experimental studies started providing greater insight into the ablation process, investigators also developed more sophisticated models to relate the ablation outcome to the underlying mechanisms. A description of these models, as well as their utility, limitations, and relationship to empirical findings, is the subject of section VII.C. Finally, in section VII.D, we briefly describe the molecular dynamics approach that has the potential to provide a microscopic and dynamic view of the ablation of complex materials such as tissue.

### A. Heuristic Models

#### 1. Blow-off Model

The blow-off model was first developed to predict the etch depth resulting from pulsed UV laser ablation of polymers<sup>213,230,319</sup> and has also been applied to tissue ablation data. Proper application of this model requires four conditions to be satisfied. First, the Lambert–Beer law must accurately describe the spatial distribution of absorbed laser energy in the tissue. Second, a finite threshold radiant exposure  $\Phi_{th}$  is required to initiate ablation and radiant exposures below the threshold result only in heating of the target. Third, material removal is assumed to commence only after the end of the laser irradiation. Fourth, the conditions for thermal confinement are satisfied. As discussed in sections IV.A and VI.A.1, these conditions are nearly always satisfied when performing laser ablation using pulse durations on the time scale of 100 ns or less. Under these conditions, the distribution of the volumetric energy density within the target immediately after the end of the laser pulse has the characteristics shown in Figure 30. For an incident radiant exposure,  $\Phi_0$ , larger than the threshold radiant exposure,  $\Phi_{th}$ , all

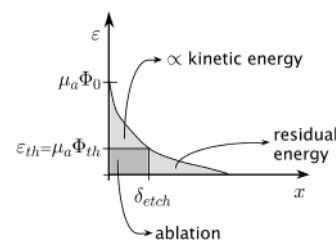


**Figure 30.** Illustration of the blow-off model.

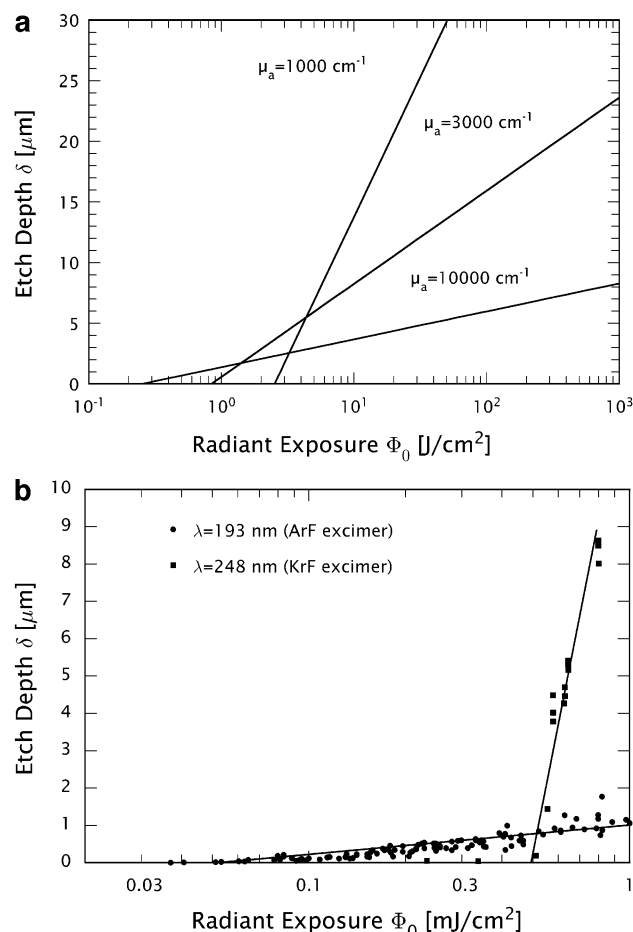


**Figure 31.** (a) Predictions for etch depth vs radiant exposure given by the blow-off ablation model for three different absorption coefficients and constant volumetric threshold energy density  $\epsilon_{\text{th}} = 2580 \text{ J}/\text{cm}^3$  which is the sum of the sensible and latent heats of the vaporization of water. (b) Etch depth vs radiant exposure data for ArF and KrF excimer laser ablation of cornea when  $\mu_a = 29\,000$  and  $290 \text{ cm}^{-1}$ , respectively. Data compiled from refs 89 and 345.

material receiving a radiant exposure in excess of  $\Phi_{\text{th}}$  is removed. This results in the following semilogarithmic relationship between the etch depth,  $\delta$ , and the incident radiant exposure:

$$\delta = \frac{1}{\mu_a} \ln\left(\frac{\Phi_0}{\Phi_{\text{th}}}\right) \quad (15)$$

The use of laser wavelengths at which the tissue absorption coefficient is large results in a low-threshold radiant exposure. As illustrated in Figure 31a, the superficial penetration of the laser radiation results in small etch depths that increase slowly with radiant exposure and thus display a shallow slope when the data are plotted on a semilog graph. By contrast, small tissue absorption coefficients result in a much higher threshold radiant exposure, and the deeper penetration of the laser radiation produces a much steeper slope of the etch depth versus radiant exposure curve. These predictions made by using the blow-off model are illustrated in Figure 31 and are corroborated by a comparison with experimental data for the variation of etch depth with incident radiant

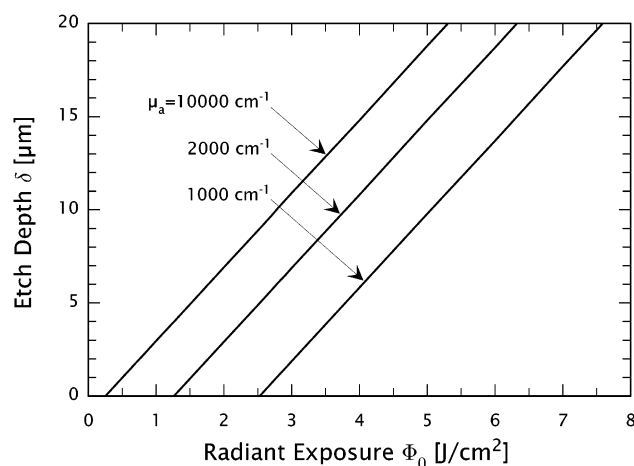


**Figure 32.** Variation of etch depth with radiant exposure as predicted by a steady-state ablation model for three different absorption coefficients and constant ablation enthalpy  $h_{\text{abl}} = 2580 \text{ J/g}$ .

exposure for 193- and 248-nm pulsed excimer laser ablation of cornea shown in Figure 31b.<sup>242</sup>

## 2. Steady-State Models

For laser pulses in the microsecond domain, material removal typically occurs concurrently with the irradiation of the target (section VI.A.2). A generic description of such processes is provided by models that assume that a fixed energy density,  $h_{\text{abl}}$ , is required for the removal of a unit mass of tissue. This assumption is adequate to describe a continuous ablation process because it results in a rate of material removal that balances the irradiance delivered to the tissue. It is also assumed that material removal begins soon after the beginning of laser irradiation and proceeds during the entire laser pulse. Similar to the blow-off models these “steady-state” models require the delivery of a threshold radiant exposure to the target to initiate material removal. Once this threshold is exceeded, such models predict a linear dependence between the etch depth and incident radiant exposure. The slope of the etch depth versus radiant exposure curve depends solely on the assumed value for the ablation enthalpy,  $h_{\text{abl}}$ , as

$$\delta = \frac{\Phi_0 - \Phi_{\text{th}}}{\rho h_{\text{abl}}} \quad (16)$$

Note that in the steady-state model, there is no explicit dependence of the etch depth on absorption coefficient and there is a direct relationship between the threshold radiant exposure and ablation enthalpy, namely,  $\Phi_{\text{th}} = \rho h_{\text{abl}}/\mu_a$ . This is illustrated in Figure 32, where the variation of etch depth with radiant exposure is plotted for three different absorption coefficients but identical ablation enthalpy.

The assumption that material removal commences early in the laser pulse implies that steady-state models are valid only for microsecond (or longer) pulse-durations at radiant exposures well above the threshold. This is because the application of radiant exposures close to the threshold often results in the



onset of material removal toward the end of the laser pulse, with the ablation exhibiting an unsteady character (section VI.A.2). The models also fail if the ablation process is characterized by a succession of stages with different ablation enthalpies. An example could be a process that begins initially as a surface vaporization but later takes on characteristics of bulk material ejection.

### 3. Comparison of Blow-off and Steady-State Models

To predict material removal, heuristic models require knowledge of either the threshold radiant exposure (blow-off model) or the ablation enthalpy (steady-state model). These values are sometimes chosen on the basis of theoretical considerations but are often inferred from empirical measurement. It is instructive to compare predictions of both models with respect to the ablation efficiency. The ablation efficiency,  $\eta_{abl}$ , is defined as the amount of mass removed per unit energy delivered to the tissue and given by

$$\eta_{abl} = \frac{\rho \delta}{\Phi_0} \quad (17)$$

Substituting eq 15 or 16 into eq 17 provides expressions for the ablation efficiency predicted by the blow-off and steady-state models, respectively:

$$\eta_{abl} = \frac{\rho}{\mu_a \Phi_0} \ln \left( \frac{\Phi_0}{\Phi_{th}} \right) \quad (\text{blow-off}) \quad (18)$$

$$\eta_{abl} = \frac{\Phi_0 - \Phi_{th}}{h_{abl} \Phi_0} \quad (\text{steady-state}) \quad (19)$$

Figure 33 displays the variation of ablation efficiency with radiant exposure for both blow-off and steady-state models for two different values of the absorption coefficient. In both cases, the ablation efficiency is zero at the threshold radiant exposure because a finite amount of energy is delivered to the target without any material removal. In the blow-off model, the ablation efficiency reaches a maximum at an incident radiant exposure approximately 2.7 times the threshold radiant exposure and decreases monotonically at larger radiant exposures. If the threshold energy density for ablation,  $\mu_a \Phi_{th}$ , is constant, then the maximum ablation efficiency is independent of the tissue absorption coefficient.<sup>24</sup> The decrease in ablation efficiency at large radiant exposures is due to the lack of material removal during irradiation, which limits the penetration of the incident radiation into the target. Thus, much of the laser energy is poorly utilized by “overheating” superficial tissue layers far in excess of the specific energy required for their removal. As discussed in section VI.A.1 and indicated in Figure 30, this excess energy typically contributes to the kinetic energy of the ablated fragments. In the steady-state model, the ablation efficiency increases continuously and asymptotically approaches a value  $\eta_{abl} = 1/h_{abl}$  for incident radiant exposures much larger than the threshold. As with the blow-off model, the maximum

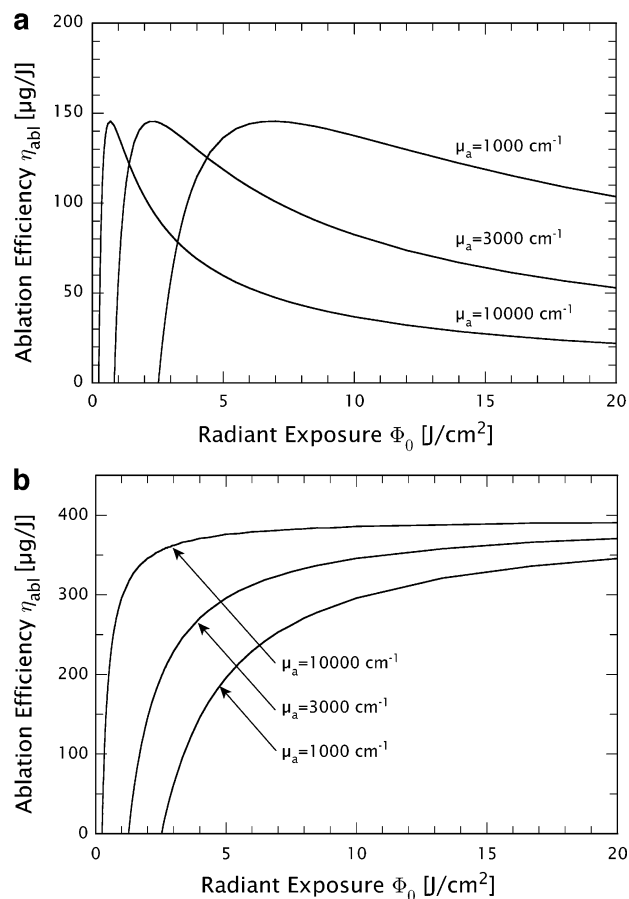


**Figure 33.** Variation of ablation efficiency with radiant exposure as predicted by (a) a blow-off ablation model and (b) a steady-state ablation model for three different absorption coefficients and constant ablation enthalpy. In both cases  $h_{abl} = 2580$  J/g.

ablation efficiency is also independent of the absorption coefficient.

### 4. Applicability of Blow-off and Steady-State Models

The applicability of blow-off versus steady-state models to ablation data is often not evident. Walsh and Deutsch demonstrated that, even with the availability of material removal data over a large range of radiant exposures, the discrimination between blow-off and steady-state processes remains difficult.<sup>315</sup> This arises because the assumptions made in the heuristic models are often not satisfied for the entire range of radiant exposures over which the mass removal data are collected. For example, although steady-state models are expected to be valid at high radiant exposures, it is at these radiant exposures that recoil-induced material expulsion (section VI.B.2) and shielding effects by the ablation plume (section VI.D) or by plasma formation become most prominent and are not accounted for by the simple assumption of a constant ablation enthalpy. Another characteristic limiting the applicability of steady-state models is that at low radiant exposures, material removal may consist of various distinct phases and thus possesses an unsteady character.<sup>240</sup> There is also evidence that, while ablation of strongly absorbing materials can be considered to be a blow-

off process at low radiant exposures, at higher radiant exposures the ablation exhibits a steady-state character.<sup>228</sup> We mention these possibilities to emphasize that conclusions drawn regarding the ablation process based merely on material removal data can be misleading. To be sound, such conclusions need to be supported by time-resolved investigations of the ablation process to confirm the assumptions required for the validity of the heuristic model used.

The caveats regarding the application of heuristic models notwithstanding, much can be inferred from careful application of these models to empirical data. For a blow-off ablation process, the slope of a line that fits the variation of etch depth with incident radiant exposure when plotted on a semilogarithmic graph (see eq 15) provides the absorption depth of the incident laser radiation. A comparison of the threshold radiant exposure,  $\Phi_{th}$ , or the ablation enthalpy,  $h_{abl}$ , with the numbers specific to water provides indirect information regarding the underlying ablation mechanisms. For example, ablation enthalpies significantly below the vaporization enthalpy of water,  $h_{vap} = [c_p \Delta T + h_{fg}] = 2580 \text{ J/g}$  ( $h_{fg}$  being the latent enthalpy required for the transformation from the fluid to the gaseous state), indicate that a significant mechanical or explosive component must be associated with material ejection. However, ablation enthalpies equal to or above the vaporization enthalpy of water do not exclude explosive material ejection, given that significant energy may be required to overcome the mechanical resistance posed by the tissue matrix.

### 5. Unification of Blow-off and Steady-State Models

Hibst unified blow-off and steady-state ablation models within a single heuristic framework to accommodate the effects of plume absorption on the ablation process.<sup>245</sup> Within this framework, predictions of a standard steady-state model are recovered for cases in which the ablation plume is transparent to the incident radiation. On the other hand, predictions of a blow-off ablation model are recovered for a steady-state process, in which the ablation plume possesses an absorption coefficient identical to that of the tissue. Defining  $\gamma = (\mu_{a,p}/\mu_a)$ , where  $\mu_{a,p}$  and  $\mu_a$  are the optical absorption coefficients of the plume and the tissue, respectively, Hibst showed that the etch depth,  $\delta$ , is given by

$$\delta = \frac{1}{\mu_a \gamma} \ln \left( \gamma \frac{\Phi_0}{\Phi_{th}} - \gamma + 1 \right) \quad (20)$$

Predictions equivalent to those provided by steady-state and blow-off models are recovered when  $\gamma \rightarrow 0$  and  $\gamma \rightarrow 1$ , respectively, and are shown in Figure 34, together with predictions for intermediate  $\gamma$  values.

### B. Ablation Metrics and Their Relationship to Heuristic Model Predictions

Proper application of the heuristic models to material removal data requires an understanding of the metrics of ablation threshold, ablation enthalpy, and ablation efficiency. The mechanistic models of tissue

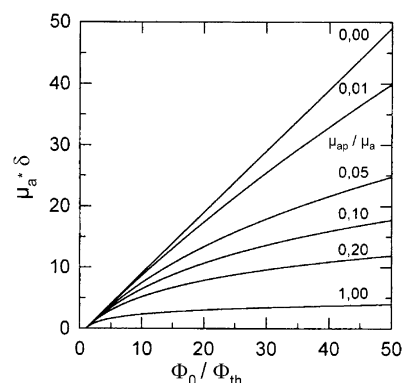


**Figure 34.** Variation of normalized etch depth with normalized radiant exposure as predicted by an ablation model that considers optical absorption by the ablation plume. Results are shown for various ratios for the optical absorption coefficient of the plume relative to the tissue. (Reprinted with permission from ref 245. Copyright 1996 Ecomed.)

ablation reviewed in section VII.C also render predictions for one or more of these metrics. Hence, we shall first provide definitions for these quantities and then describe the empirical evidence for the variation of these ablation metrics on laser parameters and tissue properties.

#### 1. Ablation Threshold

As mentioned earlier, the ablation threshold,  $\Phi_{th}$ , represents the minimum radiant exposure required to achieve effective ablative material removal. Thus, while we consider processes relying solely on surface vaporization to occur below the ablation threshold, any material ejection process, whether accomplished via a phase explosion or confined boiling, is considered to occur at radiant exposures above the ablation threshold. Other investigators have made a similar distinction for the ablation of nonbiological organic solids. Molecular dynamics simulations and experiments show the existence of a regime below the ablation threshold characterized by thermal desorption processes that display an Arrhenius-type dependence relative to the incident radiant exposure.<sup>233</sup> However, irradiation of material above the ablation threshold produces a collective volumetric ejection of large molecular clusters.<sup>233,320,321</sup> Thus, we define the ablation threshold as the radiant exposure necessary to achieve volumetric material ejection of tissue. This emphasizes that pulsed laser ablation of tissue requires destruction of the ECM and cannot be considered to have occurred by mere dehydration of the tissue.

Several methods have been applied to determine the threshold radiant exposure for ablation. The most basic, as indicated in Figure 35, is given by the intersection with the abscissa of an extrapolation of experimental data for material removal or etch depth versus incident radiant exposure.<sup>315</sup> However, such a determination is not very accurate due to a lack of sensitivity of the mass removal measurement. A more sensitive, albeit indirect, measurement of ablation threshold has been obtained using piezoelectric transducers to measure the appearance of recoil stresses connected with material removal.<sup>78,137,143,146,150</sup> For

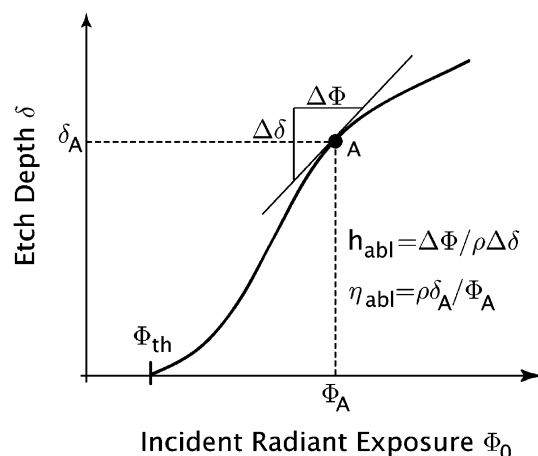


**Figure 35.** Graph depicting the relationship between etch depth and radiant exposure for a hypothetical tissue ablation process to illustrate the concepts of ablation threshold,  $\Phi_{th}$ , ablation enthalpy,  $h_{abl}$ , and ablation efficiency,  $\eta_{abl}$ .

laser pulse durations on the microsecond time scale, high-speed photography has provided sensitive and direct determination for the onset of material removal during pulsed laser irradiation,<sup>240,287,322</sup> as shown in Figure 22. When such measurements are combined with the time-resolved recording of the laser irradiance, temporal integration of the laser irradiance until the onset of material ejection provides an accurate measurement of the threshold radiant exposure.

Few empirical studies have systematically examined the dependence of ablation threshold on laser parameters and tissue properties.<sup>119,122,210,245</sup> In general, when ablating mechanically weak tissues, the ablation threshold is typically less than the sum of the sensible ( $c_p\Delta T$ ) and latent enthalpies ( $h_{fg}$ ) for the vaporization of water. As described in sections V.D,E, this occurs because the pressures generated via phase explosion or confined boiling are sufficient to produce mechanical failure of the tissue ECM and result in explosive ejection without complete vaporization of the target material. However, for mechanically strong tissues, very high temperatures are required to produce the stresses necessary to achieve the failure of the ECM. For such tissues, threshold volumetric energy densities similar to or in excess of the vaporization enthalpy of water are common.<sup>52,119,241,313</sup>

As discussed in section V.G, Albagli and co-workers<sup>210</sup> have shown a significant dependence of the threshold volumetric energy density,  $\epsilon_{th}$ , on the dimensionless stress confinement time,  $t_m^*$ , that for aorta varies from less than  $\epsilon_{th} = 0.3 \text{ kJ/cm}^3$  for  $t_m^* \lesssim 1$  to  $\epsilon_{th} = 2.2 \text{ kJ/cm}^3$  for  $t_m^* \geq 20$ , the latter value approaching the volumetric vaporization enthalpy of water [ $\rho(c_p\Delta T + h_{fg}) = 2.58 \text{ kJ/cm}^3$ ].

## 2. Ablation Enthalpy

The ablation enthalpy,  $h_{abl}$ , or heat of ablation is often used to describe the energetics of the ablation process.<sup>119,245,315,323</sup> As illustrated in Figure 35, ablation enthalpy is a differential quantity that varies with the incident radiant exposure and represents the additional tissue mass ablated when an ad-

ditional amount of laser energy is delivered. In the steady-state model, ablation enthalpy is constant and can be determined by fitting a line to etch depth versus incident radiant exposure and finding the reciprocal of the slope of this line. However, in the blow-off model, the ablation enthalpy increases monotonically with radiant exposure.

It is useful to distinguish this traditional definition for the ablation enthalpy, in which all the energy emitted by the laser is considered, from a definition that considers only the energy which is actually deposited into the tissue. To accomplish this, we must account for absorption losses in the ablation plume and diffuse and specular reflection by the tissue surface. The latter definition provides much better insight into the energetics of the phase transition processes leading to ablation. However, in most studies only the incident radiant exposure is used, because it is difficult to determine the actual energy deposition into the tissue. Calculation of the ablation enthalpy on the basis of the incident, rather than the absorbed, radiant exposure may explain, in part, the reported ablation enthalpies that are comparable to or in excess of the vaporization enthalpy for water, even in the presence of an explosive ablative process.<sup>52,119,241,315,323</sup>

## 3. Ablation Efficiency

Ablation efficiency,  $\eta_{abl}$ , is a metric for the total energy necessary to remove a given mass of tissue (Figure 35). As described in section VII.A.3,  $\eta_{abl}$  is zero at the ablation threshold. For steady ablation processes, the ablation efficiency increases monotonically and asymptotically approaches  $1/h_{abl}$  for large radiant exposures (Figure 33). By contrast, for blow-off processes, the ablation efficiency reaches a maximum at moderate radiant exposures and decreases at high radiant exposures, where energy is wasted in "overheating" the superficial layers of the tissue sample.

Walsh and Deutsch<sup>52</sup> showed a direct correspondence between ablation efficiency and the ultimate tensile strength of the tissue. Working with a TEA- $\text{CO}_2$  laser ( $\lambda = 10.6 \mu\text{m}$ ), they observed, for radiant exposures well above the ablation threshold, that the ablation efficiencies for liver, myocardium, and aorta were 6, 2.5, and 1.5 times higher than those for skin, in inverse correspondence to the ultimate tensile strengths of these tissues. Another interesting observation is that, for tissues possessing high UTS, the ablation efficiency reaches a maximum for radiant exposures approximately 4 times the ablation threshold and remains roughly constant at higher radiant exposures. By contrast, for the much weaker tissue of liver, the ablation efficiency continues to increase for radiant exposures up to 14 times the ablation threshold.<sup>52</sup> The increase of material removal with larger radiant exposures is likely due to the increased susceptibility of mechanically weak targets to recoil-induced material removal, as described in section VI.B.2.

## C. Mechanistic Models

Considering the significant limitations of the heuristic models discussed in section VII.A, many inves-



tigators sought to develop models that explicitly link laser and tissue parameters with the end effects of ablation (material removal and residual injury) by considering the mechanisms underlying the ablation process. However, given the complexity of phase transition processes involved in ablation and the significant dynamic changes of optical and mechanical tissue properties accompanying the process, this has proved to be a significant challenge. For simplicity, the first generation of these models ignored the explosive characteristics of the material removal process and instead treated ablation as a rapid laser "vaporization" or "boiling" of tissue. Soon thereafter, models were developed to consider the dynamics of the ablation process and as well as the impact of mechanical tissue properties.

### 1. Steady-State Vaporization Models

Early models for the laser ablation process in tissue were inspired by treatments developed to describe the ablation of metals.<sup>12,324,325</sup> These models treated ablation as a rapid vaporization process and reduced the process to a moving boundary problem, during which the metal surface possessed a fixed vaporization temperature. However, the assumption of a fixed vaporization temperature cannot be justified on thermodynamic grounds, as it violates the Clausius–Clapeyron relation that expresses the inter-relationship between the rate of vaporization and the surface temperature.<sup>164</sup> This erroneous assumption resulted in the prediction of a subsurface temperature peak necessary to supply the surface with the latent heat required for the vaporization of the metal.<sup>324,325</sup> The magnitude of this subsurface temperature peak increased with radiant exposure to support the higher rates of material removal. It was argued that the explosive character of ablation observed at high irradiances results from high internal pressures associated with subsurface vaporization produced by the subsurface temperature peak. While this modeling approach is wrong on thermodynamic grounds and the explosive ablation of metals is due to a phase explosion rather than to the existence of a subsurface temperature peak,<sup>164,326</sup> the moving boundary approach proved to be very useful and was taken by many investigators to model various aspects of the tissue ablation process.<sup>176,177,327–333</sup>

The first comprehensive model developed specifically for tissue ablation was presented by McKenzie in a series of papers starting in the early 1980s.<sup>328–330</sup> He developed a general relationship between the laser parameters used to create a laser excision and both the temperature profile developed inside the tissue and the resulting extent of thermal injury. McKenzie discovered that the thermal injury can be reduced by the use of high laser irradiances because tissue removal at a speed faster than that associated with thermal diffusion results in a thinner heat-affected zone. However, the model predictions were presented in a framework that required significant calculation to predict the zone of thermal injury for an arbitrary optical absorption coefficient. Moreover, the thermal diffusion that occurs after the end of the laser radiation and contributes significantly to the

propagation of the thermal injury zone was either neglected or not treated in a rigorous fashion. This motivated Venugopalan and co-workers<sup>176</sup> to develop a model to rigorously treat the thermal diffusion following the laser pulse. They presented results in a dimensionless framework that allowed the zone of thermal injury to be determined easily, regardless of laser wavelength and other laser parameters.

Similar approaches by other authors<sup>177,327,331–333</sup> typically provided predictions for threshold radiant exposure and material removal consistent with the vaporization enthalpy of water modified by losses associated with thermal diffusion. These predictions typically do not fare very well when compared to experimental measurements. This is not surprising, given the prominence of phase explosions (section V.D), confined boiling (section V.E), and the effects of photomechanical transients and the tissue matrix (sections V.F,G) on the ablation process. These limitations stimulated the construction of models that integrate the effects of photomechanical processes and tissue mechanical properties on the material removal process.

### 2. Thermomechanical Models

Like the steady-state vaporization models, the first comprehensive attempt at integrating mechanical effects into a steady-state model of the tissue ablation process drew upon models developed for the ablation of metals.<sup>334–338</sup> This approach for tissue ablation was pioneered by Zweig, Frenz, and co-workers, starting in the late 1980s.<sup>244,280,284,288–290</sup> In this model, tissue is considered to be capable of undergoing two phase-change processes: (a) a transition from a solid to a liquid phase and (b) a transition from a liquid to a vapor phase. The solid–liquid phase transition is postulated to occur upon thermal denaturation, at which point the tissue is thought to lack mechanical integrity and "flows" under the action of a shear stress or pressure gradient. This opens the possibility that recoil pressures produced by tissue vaporization would provide for the ejection of denatured tissue "liquid", as illustrated in Figure 25, and enables material removal with ablation enthalpies lower than the vaporization enthalpy for water. The model treated the thermodynamics of the vaporization process rigorously to describe the relationship between the recoil pressure and temperature at the tissue surface. The dynamics associated with the liquid ejection was modeled using the Navier–Stokes equations. However, the model does not consider phase explosions or confined boiling as driving the ablation process, and thus liquid or material ejection does not arise as a primary material removal process but only as a byproduct of the recoil forces produced by surface vaporization. Furthermore, as shown in section VI.A.2, the development of a liquid denatured tissue state during laser irradiation is a realistic approximation only for gelatin with a very high water content,<sup>241</sup> but not for tissue with an intact ECM. Zweig later noted that recoil-induced expulsion does not require tissue liquefaction if the recoil stress exceeds the UTS of the tissue.<sup>290</sup>

A more realistic approach was taken by Majaron and co-workers.<sup>197</sup> In this approach, the process of

confined boiling (section V.E) is modeled by considering the thermodynamic behavior of tissue water when it is heated within an elastic tissue ECM. This was the first attempt at modeling explosive material removal as the primary process of tissue ablation. The model accurately predicts that explosive material removal can be initiated without supplying the entire enthalpy of vaporization. Moreover, it predicts, in agreement with experimental observation, that the threshold radiant exposure is weakly dependent on tissue stiffness but varies significantly with the ultimate tensile strength.<sup>52</sup> However, the model examines only the initiation of explosive material removal and does not consider the ablation process at radiant exposures larger than the ablation threshold.

These advances notwithstanding, significant work remains for the development of a mechanistic ablation model that integrates the present conceptual and empirical understanding of the complex phenomena that play principal roles in the initiation and sustenance of the material removal process. As a result, assessment of the ablation threshold, enthalpy, and efficiency, within the context of the heuristic models presented in section VII.A, is still valuable and remains in prevalent use.

#### D. Molecular Dynamics Simulations

With conceptual developments in modeling the dynamics of groups of molecules, as well as advances in computational power, molecular dynamic simulations is becoming a viable complementary approach to model and understand ablation processes.<sup>218,235,260,338–341</sup> Computation of molecular dynamics offers predictions of the motion of molecular units produced by the deposition of laser energy. In these computations, macroscopic thermodynamic constraints are not imposed explicitly. Instead, ablation arises as a natural consequence of molecular interactions governed by the implementation of the equations of motion, intermolecular interactions, energy transfer, and molecular excitation within the model system.

The molecular dynamics approach yields a wealth of information regarding the time evolution of both the size and velocity distributions of the ablation products that is difficult to obtain by other means. As an example, Figure 36 provides the time evolution of a 2D system following the delivery of a 15-ps laser pulse with an incident radiant exposure 2 times the ablation threshold. These simulations reveal the volumetric nature of the ablative material removal process, in which small and large clusters leave the material bulk from locations not limited to those on the material surface. This is quite distinct from evaporative and desorption processes, in which material removal tends to occur strictly from the surface of the bulk material and consists predominantly of single molecules. The molecular dynamics approach has already provided valuable insight into the microscopic dynamics of desorption/ablation of both homogeneous and heterogeneous materials and is thus well suited to provide insight into the ablation dynamics of biological tissues. The topic is reviewed by Zhigilei and co-workers in this issue.

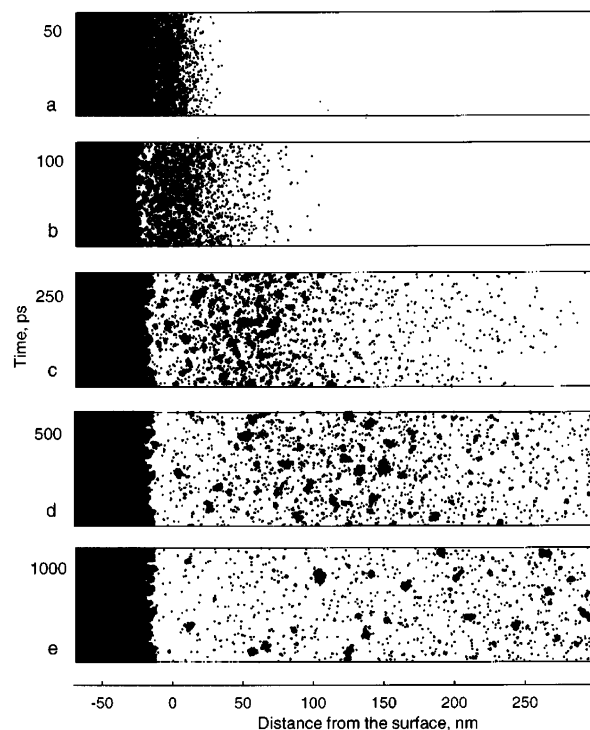


**Figure 36.** Time development of an ablation plume for a 2D molecular dynamics simulation. The radiant exposure is roughly 2 times the ablation threshold. The average energy deposited is 0.30 eV per particle in the irradiated region, whereas the cohesive energy is 0.31 eV. The laser pulse width is 15 ps. (Reprinted with permission from ref 340. Copyright 1998 American Chemical Society.)

#### VIII. UV and IR Ablation

The most common clinical application of pulsed laser tissue ablation is corneal refractive surgery using ArF excimer laser pulses ( $t_p = 20\text{--}30$  ns) at  $\lambda = 193$  nm. When ArF excimer laser pulses were first applied for the ablation of biological tissue, the smooth, precise, and nearly damage-free character of the ablation,<sup>8,23,214,342–346</sup> as shown in Figure 37a, was remarkable. This result was also enigmatic when compared with the much less precise and clean ablation produced by Q-switched (Q-sw) pulses from the Er:YAG ( $\lambda = 2.94\text{ }\mu\text{m}$ ) or Er:YSGG ( $\lambda = 2.79\text{ }\mu\text{m}$ ) lasers,<sup>348–350</sup> as shown in Figure 37b, because it appeared that the optical absorption coefficients at the two wavelength regions (190 nm vs  $2.8\text{--}3.0\text{ }\mu\text{m}$ ) were comparable.<sup>351</sup> The common argument advanced to explain the different quality of ablation achieved at UV vs IR wavelengths is that the tissue fragmentation and material removal produced by  $\lambda = 193$  nm radiation are mediated by photochemical processes that enable direct scission of chemical bonds in the cornea, while IR laser ablation is governed solely by thermal processes. Given the prominence of this issue within the tissue ablation community, we devote the following section to a recounting and analysis of the debate concerning the differences between UV and IR laser ablation using the fundamental principles we have developed in the previous sections.

##### A. Tissue Absorption Coefficients

The spatial scale in which the laser energy is deposited is determined by the tissue absorption



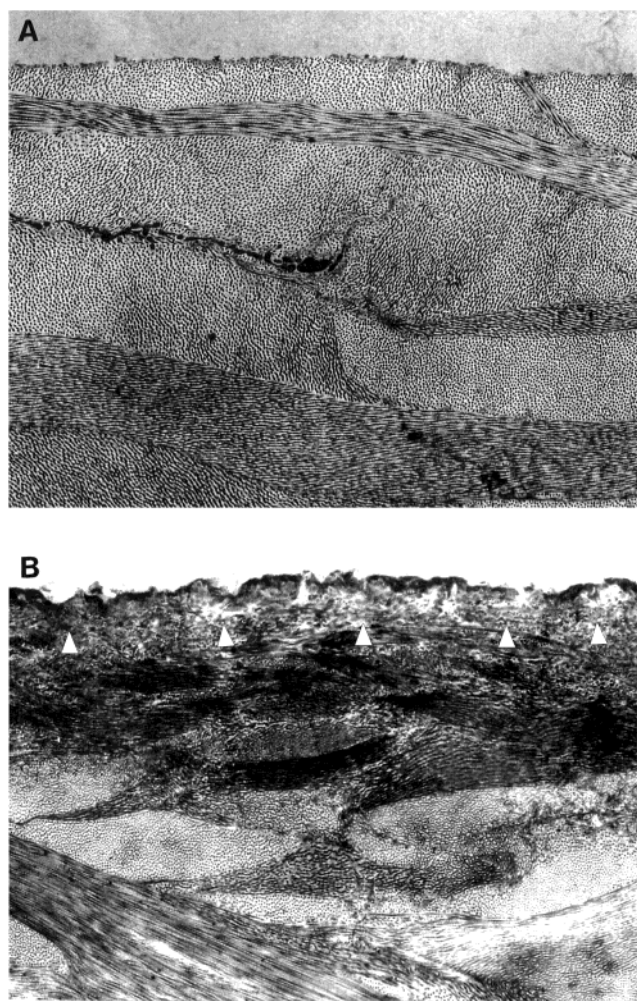


**Figure 37.** Transmission electron micrographs of corneal ablation with (a) 193-nm ArF excimer laser irradiation ( $\lambda = 193$  nm) and (b) Q-switched Er:YAG laser irradiation ( $\lambda = 2940$  nm). Magnification 10000 $\times$ . The damaged surface zone is visible as thin dark line in (a) and demarcated by arrowheads in (b). The damage zones have thicknesses of (a)  $\leq 0.2$   $\mu\text{m}$  and (b) 1–2  $\mu\text{m}$ . (Reprinted with permission from ref 367. Copyright 2000 International Society of Refractive Surgery.)

coefficient at the relevant wavelength. In the 1980s and -90s, the characteristic absorption depth of Er:YAG laser radiation ( $\lambda = 2.94$   $\mu\text{m}$ ) in corneal tissue was assumed to be approximately 1  $\mu\text{m}$ , given the optical absorption properties of water ( $1/\mu_a = 0.7$   $\mu\text{m}$ ) and the fact that the corneal stroma is composed of 70% water. The absorption depth of Er:YAG laser radiation was thought to be smaller than that of ArF excimer laser radiation, which was estimated to be 3.7  $\mu\text{m}$  from corneal transmission measurements performed by Puliafito and co-workers<sup>343</sup> that were later verified using the same technique by Lembares and co-workers.<sup>352</sup> This measured absorption depth at  $\lambda = 193$  nm did not seem to agree with the submicrometer precision obtained by measurement of the etch depth for ArF excimer laser ablation of tissues such as cornea.<sup>345</sup>

In the mid-1990s, the group led by Ediger and Pettit conducted detailed studies to examine the optical properties of collagen films and corneal tissue at the UV wavelengths used for laser ablation. They found a decrease of the transmission of thin dehy-

drated and rehydrated collagen films during irradiation by ablative ArF excimer laser pulses.<sup>131</sup> The magnitude of this decrease of transmission displayed a nonlinear dependence on radiant exposure.<sup>132</sup> Several factors were postulated to be the cause of this decrease in transmission. First, optical scattering by the ablation plume formed during irradiation was thought to reduce radiant exposure incident on the collagen target.<sup>353</sup> Second, the kinetics of the recovery in corneal transmission after the laser irradiation seemed to implicate the formation of highly absorbing free radicals that strongly absorb UV radiation.<sup>232,354,355</sup> Third, the characteristics of the dynamic transmission changes in hydrated versus dehydrated collagen films seemed to open the possibility that water may provide additional optical absorption at high temperatures. The latter two hypotheses represented an effective increase of the absorption coefficient of collagenous tissue and provided a possible explanation for the small etch depths. Staveteig and Walsh confirmed the suspicion that water absorption may play an important role for ArF excimer laser ablation of tissue.<sup>133</sup> In 1996, they reported in *Applied Optics* a 5 orders of magnitude increase in the absorption coefficient of water at  $\lambda = 193$  nm to  $\mu_a = 10^4$   $\text{cm}^{-1}$  when the sample was heated by a Q-sw Er:YAG laser pulse to a volumetric energy density of 2 kJ/cm<sup>3</sup>.<sup>133</sup> On the basis of this result, Staveteig and Walsh postulated that, while tissue protein is likely the principal chromophore for tissue ablation during the early portion of the ArF excimer laser pulse, rapid heat transfer from tissue protein to the neighboring water molecules may lead to a sufficient increase in water temperature to enable the water itself to become a potent chromophore at  $\lambda = 193$  nm during the ArF excimer laser irradiation.

In the very same issue of *Applied Optics*, Pettit and Ediger reported a measurement of the angular dependence of Fresnel reflection in samples of corneal stroma to determine the absorption coefficient for subablative radiant exposures of  $\lambda = 193$  nm radiation.<sup>89</sup> This measurement provided the result that corneal stroma tissue has an absorption coefficient  $\mu_a = 40\,000 \pm 10\,000$   $\text{cm}^{-1}$  at  $\lambda = 193$  nm and was in stunning disagreement with the earlier measurements reported by Puliafito and co-workers<sup>343</sup> ( $\mu_a = 3700$   $\text{cm}^{-1}$ ) that had served as a benchmark value. However, there is much evidence indicating that the Pettit and Ediger result is more accurate. First, the higher absorption coefficient value represents an optical penetration depth of 250 nm and is consistent with the submicrometer precision obtainable in etching collagenous tissue with 193-nm radiation. Second, the result largely agrees with a rough calculation, based on the known absorption cross section of the peptide bond, that provides an estimated absorption coefficient of  $\mu_a = 20\,000$   $\text{cm}^{-1}$  for collagenous tissue at  $\lambda = 193$  nm.<sup>89</sup> Third, the result of Pettit and Ediger was later confirmed by measurements reported by Yablon and co-workers, who obtained a value of  $\mu_a = 19\,000 \pm 4000$   $\text{cm}^{-1}$  for corneal stroma at  $\lambda = 193$  nm using an independent technique called interferometric photothermal spectroscopy.<sup>81</sup>



**Table 4. Laser Source, Wavelength  $\lambda$ , Photon Energy  $E_\lambda$ , Pulse Duration  $t_p$ , Optical Absorption Depth  $\mu_a^{-1}$ , Dimensionless Pulse Durations  $t_m^*$  and  $t_d^*$ , Radiant Exposure at Ablation Threshold  $\Phi_{th}$ , and Volumetric Energy Density at Ablation Threshold  $\epsilon_{th}$  for IR and UV Laser Ablation of Tissue<sup>a</sup> (Compiled from Refs 137 and 150)**

laser	$\lambda$ (nm)	$E_\lambda$ (eV)	$t_p$ (ns)	$\mu_a^{-1}$ ( $\mu\text{m}$ )	$t_m^*$ ( $=\mu_a c_a t_p$ )	$t_d^*$ ( $=\kappa \mu_a^2 t_p$ )	$\Phi_{th}$ (J/cm <sup>2</sup> )	$\epsilon_{th}$ (J/cm <sup>3</sup> )
TEA-CO <sub>2</sub>	10 600	0.12	30	18	2.5	$1.2 \times 10^{-5}$	1.3	720
OPO	2 940	0.42	6	1.5	6	$3.5 \times 10^{-3}$	0.035	230
Q-sw Er:YSGG	2 790	0.44	40	3	20	$5.8 \times 10^{-4}$	0.24	800
KrF excimer	248	5.0	24	30	1.2	$3.5 \times 10^{-6}$	0.21	70
ArF excimer	193	6.4	22	0.35	94	$3.2 \times 10^{-2}$	0.050	1 400

<sup>a</sup> For comparison, the volumetric energy densities corresponding to the sensible ( $c\delta T$ ) and latent ( $h_{fg}$ ) heats of water are 330 and 2255 J/cm<sup>3</sup>, respectively.

Given this spectroscopic evidence, the perceived disparity in the characteristics of UV and IR ablation may be partly due to measurement error of the UV absorption coefficient obtained by the earlier transmission measurements of corneal slices and thin collagen layers. In the measurements reported by the Puliafito<sup>343</sup> and Lembares<sup>352</sup> groups, no monochromator was used to eliminate fluorescence emission from the transmitted light. Since irradiation of collagen at  $\lambda = 193$  nm results in fluorescent emission at wavelengths between 250 and 500 nm<sup>356–358</sup> that is less strongly absorbed in corneal tissue, the fluorescent emission may have contributed to the measured transmittance. It is also possible that light was transmitted through microcracks in the frozen corneal sections used in the measurements.

At roughly the same time, the group headed by Walsh embarked on a detailed investigation of the temperature dependence of the optical absorption properties of tissue in the  $\lambda = 3$   $\mu\text{m}$  region,<sup>125,128,129</sup> based on midinfrared spectroscopic studies of the temperature dependence of the optical absorption of water.<sup>124</sup> As described in section III.C, these studies revealed that the optical absorption of water drops significantly with temperature at both  $\lambda = 2.94$  and 2.79  $\mu\text{m}$ . Thus, while the optical absorption depth of water is 0.7  $\mu\text{m}$  at room temperature, it exceeds 5  $\mu\text{m}$  at incident radiant exposures  $\Phi_0 > 10$  J/cm<sup>2</sup>, as shown in Figure 6c.

Taken together, these recent studies reveal that, under ablative conditions, the optical absorption coefficient of tissue at  $\lambda = 193$  nm is not similar to but instead is roughly an order of magnitude larger than that in the  $\lambda = 3$   $\mu\text{m}$  region. While this difference in tissue optical properties is sufficient to explain the smaller etch depths and zones of thermal injury achieved by UV excimer lasers, it is not sufficient to explain the much superior surface quality and the different ablation dynamics produced by UV and IR radiation. Thus, an examination of the interplay of thermomechanical and photochemical mechanisms for selected UV and IR lasers wavelengths is warranted. We focus our discussion on five different laser sources, as shown in Table 4. As a representative of cases in which stress confinement plays a minimal role in the ablation process, we first consider ablation using ArF excimer laser ( $\lambda = 193$  nm) and Q-sw Er:YSSG laser ( $\lambda = 2.79$   $\mu\text{m}$ ) sources in section VIII.B. In section VIII.C, we examine three cases in which stress-confined irradiation conditions may significantly influence the ablation process. These are provided by the KrF excimer

laser ( $\lambda = 248$  nm), the TEA-CO<sub>2</sub> laser ( $\lambda = 10.6$   $\mu\text{m}$ ), and an optical parametric oscillator (OPO) emitting radiation at  $\lambda = 2.94$   $\mu\text{m}$ . Table 4 provides the pulse duration and appropriate tissue optical penetration depth for each laser source, as well as the dimensionless pulse durations  $t_d^*$  and  $t_m^*$  that are normalized by the characteristic thermal diffusion and stress propagation times across the heated volume, respectively. Note that thermally confined conditions ( $t_d^* \lesssim 1$ ) are achieved in all of these cases.

## B. Ablation without Stress Confinement

### 1. Temperature Rise and Thermal Diffusion

Ablation using either the ArF excimer or Q-sw Er:YSGG laser results in volumetric energy densities that are sufficient to consider photothermal processes as playing a prominent if not dominant role in the ablation process.<sup>137,150,359</sup> Clearly, this is the case for irradiation by the Q-sw Er:YSGG laser, as the single-photon energies are inadequate to drive photochemistry. The prominence of thermal processes in the case of ArF excimer laser ablation depends on the fraction of absorbed energy that undergoes internal conversion into a vibrationally excited ground state without effecting direct scission of chemical bonds (section V.H). Moreover, the viability of a thermal phase transition process to drive material removal may be enhanced by energy transfer from the absorbing proteins to the tissue water. As discussed in section IV.A, significant thermal diffusion between collagen fibrils and the surrounding water is expected during the time scales of the irradiation processes considered here. Additionally, in the case of corneal stroma, the presence of significant amounts of collagen VI in the interfibrillar ground substance<sup>45</sup> provides for the direct absorption of UV radiation by the ground substance and rapid energy transfer to the water that resides in the interfibrillar space. Moreover, as discussed in section VIII.A, once heated to volumetric energy densities on the order of 0.5 kJ/cm<sup>3</sup>, water itself becomes a chromophore,<sup>133</sup> albeit not the dominant one, considering the optical absorption of the native tissue protein. Thus, rapid heating of tissue water is possible, even for ArF excimer laser irradiation, and may contribute to material removal by surface vaporization or confined boiling (sections V.B,E).

Empirical evidence implicating the presence of significant thermal effects during ArF excimer laser ablation of the cornea was provided in a recent report by Ishihara and co-workers.<sup>360</sup> Time-resolved tem-

perature measurements detected corneal surface temperatures exceeding 100 °C for a radiant exposure of  $\Phi_0 = 80 \text{ mJ/cm}^2$ , just above the ablation threshold, and exceeding 240 °C for  $\Phi_0 = 180 \text{ mJ/cm}^2$ . The HgCdTe detector used to make the radiometric measurements effectively integrates the sample temperature to a depth of approximately  $3 \mu\text{m}$ .<sup>361</sup> Given that the optical absorption depth of the incident radiation is roughly an order of magnitude smaller, the actual surface temperatures are much larger than those reported. These temperatures are likely comparable to those produced by Q-sw Er:YSGG laser ablation, in which the surface temperature was estimated to be 290 °C at the ablation threshold,<sup>137</sup> as well as to those produced by CO<sub>2</sub> laser ablation of skin using 100- $\mu\text{s}$  pulses, in which surface temperatures of 400 °C have been measured at the threshold radiant exposure and 750 °C for radiant exposures 3 times the ablation threshold.<sup>76</sup>

## 2. Kinetics of Tissue Decomposition

The time necessary for the onset of material removal effectively represents the time scale required for tissue decomposition and can be inferred from measurements of the acoustic transients generated by recoil of the ablation products. For Q-sw erbium laser ablation, these measurements indicate that the onset of material removal occurs after the end of the laser irradiation.<sup>137</sup> As shown in Figure 38, this result stands in stark contrast to ArF excimer laser ablation, in which case stress transients due to ablative recoil begin promptly after the start of the irradiation.<sup>78,150,224,359,362</sup>

The different onset of material removal appears to be linked with the different kinetics of the decomposition of the tissue matrix. For IR laser irradiation at radiant exposures proximal to the ablation threshold, the mechanical integrity of the tissue matrix is essentially maintained during the laser pulse. This applies even for IR laser irradiation occurring on the microsecond time scale, as shown in Figure 23.<sup>240</sup> The more rapid onset of the recoil stress in UV ablation strongly suggests that the mechanical integrity of the tissue matrix is destroyed on a more rapid time scale than in IR ablation. Thermal denaturation is not a viable mechanism to explain the early degradation of the tissue matrix in UV ablation. The thermal diffusion time between the tissue water contained in the ground substance and the collagen fibrils is on the nanosecond time scale. Thus, if thermal denaturation of the tissue matrix were responsible for the fast onset of material removal in UV irradiation, a similarly rapid onset should also be produced by IR exposures.

Photochemical decomposition is much more likely to be the mechanism causing the early degradation of the tissue matrix during UV laser irradiation (section V.H). In ArF excimer laser ablation, the peptide bond linking the amino acids serves as the primary chromophore. Several authors have shown that a considerable fraction of the chemical bonds present in the tissue matrix is affected by photochemical decomposition,<sup>18,234,359</sup> even though not enough to cause ablation by purely photochemical

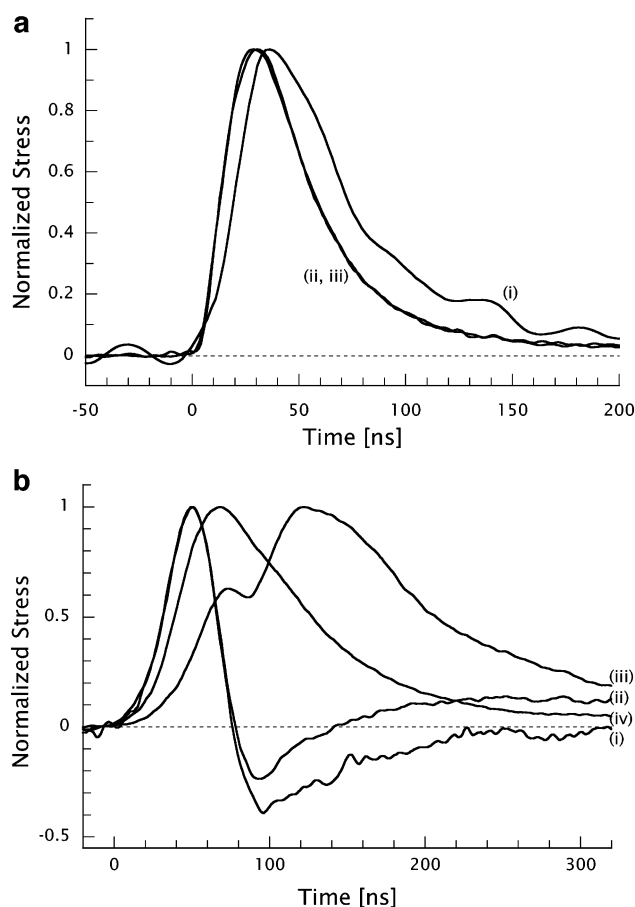


**Figure 38.** (a) Stress transients resulting from ArF excimer laser ( $t_p = 22 \text{ ns}$ ) irradiation of porcine dermis for radiant exposures at the ablation threshold (i) and above the ablation threshold (ii, iii). Thermoelastic stress transients are not observed at radiant exposures below the ablation threshold and the measured ablative recoil occurs on times scales similar to that of the laser pulse. (Adapted with permission from ref 150. Copyright 1995 Biophysical Society.) (b) Stress transients resulting from Q-switched Er:YSGG laser ( $t_p = 40 \text{ ns}$ ) irradiation of porcine dermis for radiant exposures below the ablation threshold (i), at the threshold (ii), and above the threshold (iii, iv). Radiant exposures below the ablation threshold produce bipolar thermoelastic stress transients. For radiant exposures equal to and above the ablation threshold, the ablative recoil produces a compressive pulse that is delayed with respect to the laser pulse and the peak of the compressive thermoelastic stress. The time delay decreases with increasing radiant exposure until the tensile stress component vanishes and both compressive peaks merge into one. This is the case in (iv) at  $2.3\times$  threshold radiant exposure. (Adapted with permission from ref 137. Copyright 1996 Biophysical Society.)

dissociation.<sup>232,233</sup> Nikogosyan and Görner<sup>234</sup> estimated that ArF excimer laser irradiation using  $\Phi_0 = 300 \text{ mJ/cm}^2$  (about 6 times the threshold and 2 times the dose used clinically) results in photochemical dissociation of up to 60% of the peptide bonds in corneal tissue.

## 3. Material Ejection

The mechanism and kinetics of the decomposition of the tissue matrix directly affects the material removal process. For UV laser ablation, significant photochemical decomposition of the tissue matrix likely occurs prior to the heating of the tissue water

to a high temperature. This greatly reduces the explosive character of the ablation process that for IR irradiation occurs as a phase explosion or confined boiling process (sections V.D,E). It is quite remarkable that ArF excimer laser ablation of tissue is not only less violent than IR laser ablation of tissue but also less violent than IR laser ablation of pure water, a sample that possesses no structural matrix. In IR laser ablation of both water and tissue, a phase explosion (sections V.D and VI.B) plays a prominent role in the sample fragmentation and material ejection process. By contrast, in ArF excimer laser ablation, it is likely that the volatile gaseous products of the photodecomposition process serve to avert a phase explosion of the tissue water. Specifically, these volatile photodecomposition products provide a large number of boiling nuclei that would promote a vaporization process and lower the degree of superheating in a way that prevents the spinodal limit from being reached (section V.I). This hypothesis is supported by the results of Kermani and co-workers,<sup>247</sup> who found a variety of organic gases including  $\text{NH}_2$ ,  $\text{C}_2\text{H}_2$ ,  $\text{CH}_2\text{NH}_2$ , and  $\text{CO}_2$  in addition to water vapor in the ablation products resulting from the ablation of corneal tissue using 193- and 248-nm laser radiation. Thus, the ArF excimer laser ablation process may be initiated by the formation of nucleation centers generated by photochemical decomposition combined with thermal energy to drive the growth of these nucleation centers. In analogy to a confined boiling process, ablation will probably occur when the pressure from the volatile dissociation products, together with the vapor pressure from the heated tissue water, exceeds the tensile strength of the ECM. However, this strength will be reduced by photochemical processes, and the ablation process is thus less explosive than that in IR ablation.

It is interesting to note that the volumetric energy density at the ablation threshold is higher when using the ArF excimer than when using the Er:YSSG laser (Table 4). This indicates that, while the photochemical contribution to UV ablation changes the dynamics of the ablation process, it does not lead to a marked reduction of the ablation threshold. The reason for this observation is not yet fully understood.

The picture of ArF excimer laser ablation as a continuous rather than explosive process is consistent with quantitative measurements of the time-resolved stress transients generated by the recoil of the ablation products. Venugopalan and co-workers demonstrated that a model which treats UV ablation as a continuous, surface-mediated process and provides predictions of the peak recoil stress amplitude as a function of radiant exposure in remarkable agreement with experimental measurements of both ArF and KrF excimer ablation of dermis.<sup>150</sup> By contrast, such a model did not correctly predict the recoil stresses produced by nanosecond IR laser ablation of skin. Instead, a quantitative model that described the IR laser ablation process as an explosion occurring after the end of the laser radiation provides good agreement with the measurements.<sup>137</sup> Plots of the variation of the peak stress amplitude with radiant exposure for ArF excimer and Q-sw Er:YSSG laser

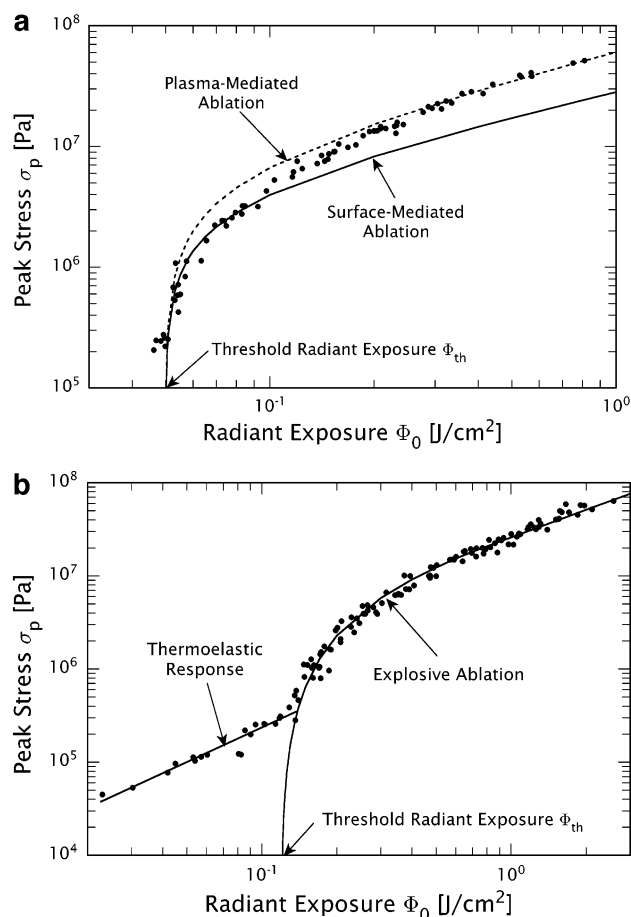


**Figure 39.** (a) Variation of the peak compressive stress with incident radiant exposure resulting from ArF excimer laser irradiation of porcine dermis. Solid and dashed curves represent theoretical model predictions for the compressive recoil stress produced by surface- and plasma-mediated ablation processes, respectively. (Adapted with permission from ref 150. Copyright 1995 Biophysical Society.) (b) Variation of the peak compressive stress with incident radiant exposure resulting from Q-switched Er:YSSG laser irradiation of porcine dermis. Solid curve represents a theoretical model prediction for the compressive recoil stress produced by an explosive ablation process. (Adapted with permission from ref 137. Copyright 1996 Biophysical Society.)

ablation of dermis are shown, along with the model predictions, in Figure 39.

Although models that describe pulsed ArF and KrF excimer laser ablation of tissue as a continuous, surface-mediated process can be successfully applied to quantitative measurements of the ablation-induced recoil stress, UV laser ablation of tissue is similar to IR tissue ablation in that fast-frame photography records ablation plumes that consist of material fragments, as shown in Figure 29.<sup>239,242,243,363</sup> Thus, the processes operative in ArF and KrF excimer laser ablation do not result in complete decomposition of the tissue.

The initial ejection velocity of plume material produced by ArF excimer laser ablation of cornea was found to be over  $v = 600$  m/s for  $\Phi_0 = 0.3\text{--}1$  J/cm<sup>2</sup>, slowing to  $v \approx 350$  m/s for times 500 ns after the laser irradiation for  $\Phi_0 = 0.4\text{--}0.9$  J/cm<sup>2</sup>.<sup>239,345</sup> For Q-sw Er:YAG ablation of skin, Walsh and Deutsch measured a maximum ejecta velocity of  $v \approx 1400$  m/s for  $\Phi_0 \approx$



25 J/cm<sup>2</sup>.<sup>238</sup> Note that if one considers the temperature dependence of optical properties at the Er:YAG laser wavelength (see Figure 6a), one finds that the volumetric energy density achieved by  $\Phi_0 = 0.5$  J/cm<sup>2</sup> of  $\lambda = 193$  nm radiation is roughly equivalent to that produced by  $\Phi_0 = 25$  J/cm<sup>2</sup> of  $\lambda = 2.94$   $\mu$ m radiation. Despite this, the characteristic velocities of the material ejection are significantly larger for the IR laser ablation process. While the mechanical properties of the different tissues (cornea versus dermis) may play a role in affecting this difference, the lower plume velocities at the UV wavelengths would be consistent with the notion that the energy consumed by bond scission would result in a lower kinetic energy of the tissue fragments produced. Interestingly, the initial shock wave velocities are similar for Q-switched Er:YAG and ArF excimer laser ablation when the above laser parameters are used.<sup>23,239,251</sup> The larger difference between shock wave and particle velocities for UV laser ablation indicates a more rapid release of volatile ablation products that drives the shock wave emission. The more prominent role of volatile ablation products is likely related to photochemical processes.

Although photomechanical signals resulting from the ablation recoil are detected *during* laser irradiation for ArF excimer laser ablation of tissue,<sup>150,359</sup> particulate material ejection becomes visible only after cessation of the laser irradiation. This holds for nanosecond laser ablation using *either* UV or IR wavelengths. The delay between laser irradiation and the onset of material ejection was measured to be  $\sim 70$  ns for ArF excimer laser ablation of cornea for  $\Phi_0 > 0.3$  J/cm<sup>2</sup> and 94 or 280 ns (depending on the measurement technique) for the Q-sw Er:YAG laser ablation of skin.<sup>238,239</sup> The phenomenon of delayed material ejection is not limited to tissue but has also been observed for UV ablation of polymers.<sup>237</sup>

For ArF excimer laser ablation, the photographic observations of an onset of material removal after the end of the laser pulse appear to contradict the stress transient measurements that show the presence of compressive stresses *during* the laser irradiation. A possible explanation is that the early part of this compressive stress transient is produced by the photochemical production of volatile products that results primarily from the scission of the amino acid residues of the collagen molecule during the laser irradiation.<sup>231,232</sup> The volatile gaseous products produced at the tissue surface would be ejected at high velocities, causing a recoil stress early during the laser pulse. Moreover, the gaseous and condensed products produced below the tissue surface results in a rapid internal pressure buildup that manifests as a compressive stress early during the laser irradiation. Ejection of particulate fragments occurs once the temperature and the pressure from the photochemical decomposition and vaporization reach values sufficiently high to rupture the collagen fibrils via degradation of the backbone of the collagen molecules and/or breakage of cross-links between the molecules.<sup>232</sup> The later parts of the stress transient would thus be indicative of the recoil produced by the ejected tissue fragments. This interpretation is con-

sistent with the observation that the duration of the stress transients for ArF excimer laser ablation decreases for higher radiant exposures (see Figure 38a), at which the temperature and pressure buildup is expected to occur faster and produces a more rapid onset and cessation of material ejection.

Hahn and co-workers found evidence that the particulate ejecta produced by ArF excimer ablation of cornea consists mainly of water droplets.<sup>363</sup> From this finding, they argued that the tissue matrix is transformed into gaseous products through photochemical decomposition and that these gaseous products drive the droplet ejection.<sup>359,363</sup> This view is consistent with the scenario described above but neglects the possible heating of the tissue water by heat diffusion from the absorbing biomolecules and the volatile products of the photochemical decomposition that are at elevated temperatures, as they possess an energy in excess of that required for bond dissociation. Considering the volumetric energy density in the ablated tissue layer (Table 4) and the measured surface temperatures in excess of 100 °C, as reported by Ishihara and co-workers,<sup>360</sup> it is unlikely that vaporization of tissue water plays no role in ArF excimer laser ablation of tissue. Thus, the observation of Hahn and co-workers<sup>363</sup> is compatible not only with a purely photochemical ablation process but also with a process that involves the interplay of photochemical and photothermal processes.

The ablation depth versus radiant exposure curve for ArF excimer laser ablation<sup>18,355</sup> resembles the curves typical for a simple blow-off process (Figure 31). This ablation depth characteristic is consistent with the observation that material ejection starts after the end of the laser pulse. This is in contradiction with the view of ArF excimer ablation as a continuous process proceeding during the laser pulse and for which a different etch depth characteristic would be expected (Figure 32). However, as shown in Figure 34, it is possible that a continuous ablation process, characterized by strong shielding during the laser pulse, could lead to an etch depth curve similar to that shown in Figure 31. There is evidence that this occurs, as Pettit and Ediger have implicated scattering by the ablation plume as a primary factor responsible for a drop in optical transmission of collagen samples during irradiation with an ablative ArF excimer laser pulse.<sup>353,364</sup>

In summary, the empirical studies that have been performed thus far provide a rough picture of the overall dynamics of the UV laser ablation process. However, these studies are not sufficient to draw an unequivocal picture of the UV laser ablation process that explains both the early onset of the photoacoustic signal and the late ejection of particulate material. Some clarification may be provided by a visualization of the emission of volatile gaseous ablation products. Further insight would be gained from a thorough comparative examination of UV vs IR ablation plume dynamics at equal volumetric energy density.

### C. Ablation with Stress Confinement

Before discussing the UV and IR ablation dynamics under stress-confined irradiation conditions, we shall

examine the characteristics of the thermoelastic stress transients produced by laser exposures below the ablation threshold. Such signals are observed not only for stress-confined irradiation using KrF excimer and TEA-CO<sub>2</sub> laser pulses, where  $\ell_m^*$  is close to unity, but also for Q-sw Er:YSGG irradiation, where  $\ell_m^* = 20$  (Table 4). It is only for ArF excimer laser irradiation that a thermoelastic stress signal could be detected.<sup>78,150</sup> This is due to the much smaller thermoelastic stress amplitude, as the much higher absorption coefficient at  $\lambda = 193$  nm results in a significantly larger degree of stress relaxation, with  $\ell_m^* \approx 90$ . The lack of a detectable thermoelastic stress transient provides additional evidence that the optical penetration depth at  $\lambda = 193$  nm is very small, even at radiant exposure values well below the ablation threshold.

### 1. Reduction of the Ablation Threshold

As mentioned in section V.G, stress-confined irradiation conditions promote failure of the tissue matrix because the tensile component of the thermoelastic stresses enhances bubble formation and vaporization and may also contribute to the direct fracture of the tissue matrix. This leads to a reduction of the threshold volumetric energy density for ablation at both IR and UV wavelengths (see Table 4). Venugopalan and co-workers<sup>137</sup> showed that the volumetric energy density at the ablation threshold is slightly lower for ablation using a TEA-CO<sub>2</sub> laser, with which a small degree of stress confinement is achieved, as compared to a Q-sw Er:YSGG laser, with which significant stress confinement is absent. In spite of the different degrees of stress confinement, the energy density values are fairly similar resulting in maximum tissue surface temperatures at the threshold of 260 and 294 °C for TEA-CO<sub>2</sub> and Q-sw Er:YSGG laser ablation, respectively.

For KrF excimer laser ablation, Venugopalan and co-workers<sup>150</sup> reported a threshold radiant exposure of  $\Phi_{th} = 210$  mJ/cm<sup>2</sup> that corresponds to a particularly low threshold volumetric energy density (Table 4) and is equivalent to a temperature rise at the tissue surface of only 20 °C if the effects of microscale thermal confinement (section IV.A.) are negligible. This result is consistent with the findings of Ishihara and co-workers,<sup>361</sup> who reported that the temperature rise for KrF excimer laser irradiation at the ablation threshold is less than half of that measured for ArF excimer laser irradiation. The data in Table 4 show that a much larger reduction in ablation threshold is achieved by mechanical confinement in the UV (KrF excimer laser compared to ArF excimer laser) than in the IR (TEA-CO<sub>2</sub> laser compared to Q-sw Er:YSGG laser). The thermoelastic stresses produced by the KrF excimer laser radiation interact with a tissue matrix that is weakened by photochemical processes and offers little resistance to the tensile component of the stress transient. By contrast, in IR laser ablation, the thermoelastic stresses interact with a fully intact matrix due to the absence of thermal damage on these time scales. Thus, a reduction of the ablation threshold similar to that for UV wavelengths is thus not possible.

The comparatively large value for the volumetric energy density at the ablation threshold for ArF excimer laser irradiation is probably related to the fact that, although photochemical processes are operative, no significant thermoelastic stresses are generated. Even if photochemical processes produce the scission of molecular bonds and impair the mechanical integrity of the tissue matrix, the forces necessary to effect material removal must be provided by a sufficient amount of volatile, energetic photoproducts and vaporization of tissue water.

Even though the degree of stress confinement is less for OPO irradiation at  $\lambda = 2.94$   $\mu$ m compared to TEA-CO<sub>2</sub> laser ablation, the threshold volumetric energy density for OPO ablation of corneal tissue was found to be smaller than that for TEA-CO<sub>2</sub> laser ablation of skin. This discrepancy may be due to the fact that collagen fibrils in the corneal stroma are oriented parallel to the tissue surface in a layered, lamellar structure. This structure offers less resistance to the tensile thermoelastic stresses oriented perpendicular to the tissue surface than the interwoven collagen network in dermis exhibiting fibers perpendicular to the tissue surface.

The peak stresses generated at the ablation threshold are 4 and 9 MPa for KrF excimer and TEA-CO<sub>2</sub> laser ablation of dermis, respectively.<sup>137,150</sup> This difference is consistent with a weakening of the tissue matrix by photochemical processes induced by KrF excimer laser irradiation. The ultimate tensile strength of dermis lies in the range 13.5–24 MPa<sup>33,56</sup> and is expected to be even larger at the high strain rates associated with the laser ablation process. The apparent contradiction between the stress values measured at the ablation threshold for TEA-CO<sub>2</sub> laser irradiation and the higher reported values of the UTS of skin is likely due to the fact that the mechanical testing of the skin samples is done under uniaxial conditions with loading parallel to the skin surface. However, under ablative conditions, the tissue may be loaded in a geometrical configuration that produces mechanical failure at lower stresses. Moreover, effects of thermal denaturation processes may counteract gains in UTS due to the high strain rates.

### 2. Kinetics of Tissue Decomposition and Material Ejection

The onset of material removal for ablation generated under stress-confined irradiation conditions occurs toward the end of the pulse for both the TEA-CO<sub>2</sub> and KrF excimer laser ablation, as can be seen in the time-resolved stress transients shown in Figures 24 and 40 for TEA-CO<sub>2</sub> and KrF excimer laser irradiation, respectively.<sup>137,150</sup>

The late start of the compressive recoil stress is not surprising, because the thermoelastic stresses that facilitate the material removal are generated on time scales longer than the laser irradiation as demonstrated in Figure 9. However, it is remarkable that, and not completely understood why, the experimental data for the peak recoil stresses generated by KrF excimer laser ablation are well predicted by the model of a continuous surface-mediated ablation process that commences during the laser irradiation,

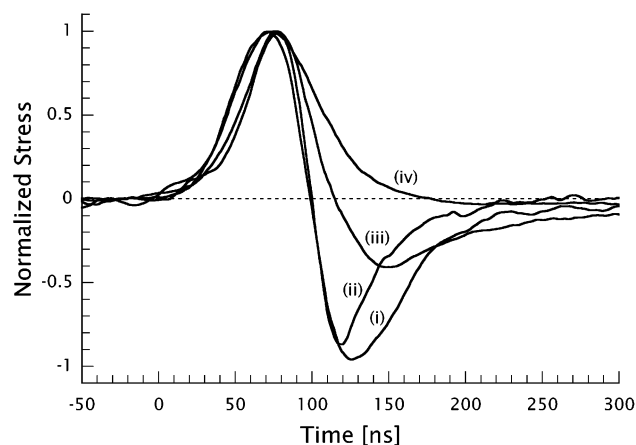


**Figure 40.** Stress transients resulting from KrF-excimer laser ( $t_p = 24$  ns) irradiation of porcine dermis for radiant exposures below the ablation threshold (i), at the threshold (ii), and above the threshold (iii, iv). Radiant exposures below the ablation threshold produce bipolar thermoelastic stress transients. Radiant exposures only slightly above the ablation threshold, result in a compressive pulse produced by the ablative recoil that is roughly concurrent with the tensile thermoelastic stress. At radiant exposures significantly above the threshold, the ablative recoil stress dominates the stresses generated by thermoelastic mechanisms, and only a single compressive stress pulse is observed. This is the case in (iv) at  $5.2\times$  threshold radiant exposure. (Reprinted with permission from ref 137. Copyright 1996 Biophysical Society.)

while the measured recoil stress amplitudes generated by TEA- $\text{CO}_2$  laser ablation are well characterized by a blow-off model for explosive ablation occurring after the irradiation. These data, along with the model fits, are shown in Figure 41.

The particulate fragments produced by KrF excimer laser ablation of cornea are of a much larger size than those produced by ArF excimer laser ablation and are easily identified in photographs of the ablation plume.<sup>242</sup> The ejection of large tissue fragments in KrF excimer laser ablation may be due to the combination of both the tensile thermoelastic stresses and photochemical weakening of the tissue matrix. The larger volumetric energy densities required to generate the forces necessary for material removal in ArF excimer laser ablation will lead to a greater degree of photochemical decomposition of the tissue ECM and result in smaller tissue fragments. Another factor that may explain the difference in particle sizes is the difference in optical penetration depths at the two laser wavelengths ( $0.4\ \mu\text{m}$  at  $\lambda = 193\ \text{nm}$  and  $30\ \mu\text{m}$  at  $\lambda = 248\ \text{nm}$ ), as it would be surprising for a laser ablation process to produce particles significantly larger than the optical penetration depth.

### 3. Precision Achieved by Ablation under Stress-Confined Conditions

Telfair and co-workers recently demonstrated that the use of an optical parametric oscillator (OPO) system producing 6-ns pulses of  $\lambda = 2.94\ \mu\text{m}$  radiation near the ablation threshold enables the ablation of corneal tissue with a precision comparable to that achieved with an ArF excimer laser.<sup>365–368</sup> Figure 42 provides a TEM micrograph of the cornea ablated

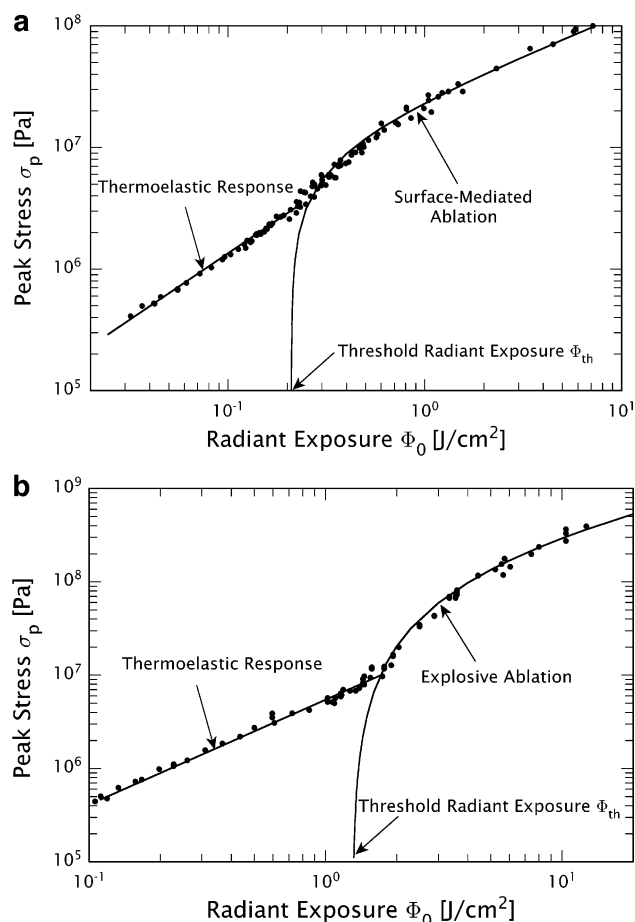


**Figure 41.** (a) Variation of the peak compressive stress with incident radiant exposure resulting from KrF excimer laser irradiation of porcine dermis. Solid curve represents a theoretical model prediction for the compressive recoil stress produced by a surface-mediated ablation process. (Adapted with permission from ref 150. Copyright 1995 Biophysical Society.) (b) Variation of the peak compressive stress with incident radiant exposure resulting from TEA- $\text{CO}_2$  laser irradiation of porcine dermis. Solid curve represents a theoretical model prediction for the compressive recoil stress produced by an explosive ablation process. (Adapted with permission from ref 137. Copyright 1996 Biophysical Society.)

using this OPO system. Stern and co-workers<sup>369</sup> also reported a near absence of thermal injury at the bottom of deep incisions produced by 6-ns pulses of  $\lambda = 2.8\ \mu\text{m}$  radiation. However, this finding was not fully appreciated due to the presence of a  $1.5\text{--}10\text{-}\mu\text{m}$  zone of thermal injury at the sides of the deep incision.

The small thermal damage zone produced in the study reported by Telfair and co-workers<sup>367</sup> is likely a consequence of the significant degree of stress confinement achieved by the laser parameters employed (Table 4). Under these conditions, the thermoelastic response of the tissue lowers both the ablation threshold and the residual heat in the tissue, thus resulting in a smaller zone of thermal injury. A similar phenomenon is observed for KrF excimer laser ablation, in which the thermal damage zone ( $\sim 2\ \mu\text{m}$ ) is only 1/20th of the optical penetration depth ( $\sim 37\ \mu\text{m}$ ).<sup>242</sup> The remarkably small extent of thermal injury corresponds to the particularly low volumetric energy density at the ablation threshold of  $0.07\ \text{kJ/}$





**Figure 42.** TEM picture of corneal ablation with 6-ns pulses from an optical parametric oscillator (OPO) emitting at 2.94  $\mu\text{m}$ . Magnification 10000 $\times$ . The damaged surface zone is  $\leq 0.3 \mu\text{m}$  thick and is visible as dark line. This damage zone is similar to that produced by ArF excimer laser irradiation shown as Figure 36a. (Reprinted with permission from ref 367. Copyright 2000 International Society of Refractive Surgery.)

$\text{cm}^3$ . However, the stress-confined irradiation at  $\lambda = 2.94 \mu\text{m}$ , offered by the OPO, provides a much higher ablation precision when compared to that at  $\lambda = 248 \text{ nm}$ , due to the much smaller optical penetration depth.

#### D. Overall Picture

Tissue ablation using IR radiation under thermally confined conditions has an explosive character that is produced via a process of phase explosion or confined boiling. The explosive character of the ablation, together with the bleaching of water at high volumetric energy densities, explains the relatively large ablation depth achieved, even at the threshold, and the rough surface of the ablation crater.

Ablation using ArF excimer laser pulses is likely driven by a combination of photochemical and photothermal mechanisms. The former is primarily responsible for the decomposition of the tissue matrix, while the latter is likely involved in the ejection of the fragments. Primary absorption occurs in the biomolecules, but the tissue water will likely be heated to temperatures  $\gg 100^\circ\text{C}$  via thermal diffusion that is supported by direct water absorption once high temperatures are reached. Photodecomposition reduces the ultimate tensile strength of the tissue matrix and thus weakens the degree of confinement for the vaporization of interfibrillar water. The gaseous and volatile photodecomposition products provide a large number of nuclei for vaporization of the tissue water. Therefore, the explosive character of ablation is reduced compared to that of IR ablation, but material ejection is not eliminated. Under stress-confined irradiation conditions, both IR and UV laser ablation can be considerably refined, and for energies near the ablation threshold, the zone of thermal injury is much smaller than the optical penetration depth.

### IX. Ablation in a Liquid Environment

Ablation in a liquid environment is most often encountered when delivering laser radiation through optical fibers for medical applications inside the human body. Current technology places significant limits on the use of optical fibers to transmit the laser wavelengths most suitable for precise tissue ablation in air, 193 nm (ArF excimer), 248 nm (KrF excimer), 2.79  $\mu\text{m}$  (Er:YSSG), 2.94  $\mu\text{m}$  (Er:YAG), and 10.6  $\mu\text{m}$  ( $\text{CO}_2$ ). Therefore, other wavelengths are commonly used that are well transmitted through low-OH quartz fibers:  $\lambda = 308 \text{ nm}$  (XeCl excimer), 2.01  $\mu\text{m}$  (Cr:Tm:YAG), and 2.12  $\mu\text{m}$  (Cr:Tm:Ho:YAG). While these wavelengths are not as highly absorbed by protein or water (see Figure 4), their optical penetration depth is still fairly small:  $\sim 50 \mu\text{m}$  for  $\lambda = 308 \text{ nm}$ ,<sup>370</sup>  $\sim 170 \mu\text{m}$  for  $\lambda = 2.01 \mu\text{m}$  (thulium laser), and  $\sim 350 \mu\text{m}$  for  $\lambda = 2.12 \mu\text{m}$  (holmium laser).<sup>371</sup>

In a liquid environment, a layer of aqueous fluid is usually present between the tip of the optical fiber and the tissue surface. This fluid absorbs all the IR laser wavelengths listed above and thus needs to be ablated or displaced before tissue ablation can start. A similar problem is encountered during UV ablation if the fluid is blood, because hemoglobin absorbs strongly in the UV (see Figure 4). However, once the radiation is delivered to the tissue, the kinetics of the phase transitions in the liquid environment are similar to those at a tissue surface in a gaseous environment, except that surface vaporization plays no role. As a result, the ablation thresholds with respect to the volumetric energy density deposited in the tissue are almost the same as those observed in air.<sup>78,210</sup>

The most important difference between ablation in air and ablation in a liquid environment is that the liquid confines the movement of the ablation products. Therefore, ablation in a liquid environment is accompanied by bubble formation and by mechanical effects much stronger than those observed in a gaseous environment. These effects are discussed in the present section, together with their consequences for the ablation efficiency and precision.

#### A. Bubble Formation

The expansion of gaseous products produced during tissue ablation creates a bubble in the liquid surrounding the ablation site. When the optical fiber is not in contact with tissue, a bubble is also formed by absorption of laser radiation in the liquid separating the fiber tip and the tissue surface, as shown in Figure 43. This bubble is essential for the transmission of optical energy to the target, and the mechanisms governing its formation and subsequent dynamics have thus received attention by various researchers.<sup>26,151,152,372–375</sup>

Experiments have demonstrated bubble formation at the tip of an optical fiber immersed in water at volumetric energy densities smaller than the vaporization enthalpy of water at constant pressure.<sup>26,373–375</sup> This observation of "partial vaporization" has puzzled some researchers but can be easily explained by examining the kinetics of phase transitions, as

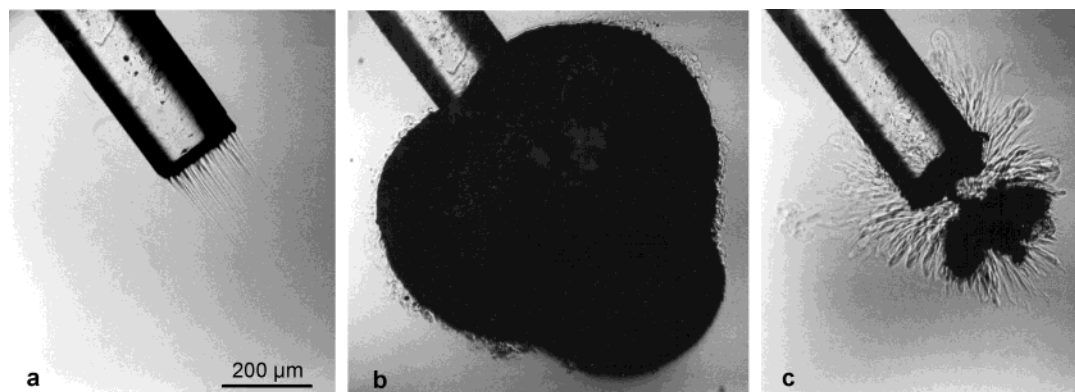


**Figure 43.** Bubble formation in water with free-running thulium laser pulse of 500-mJ pulse energy and 300- $\mu$ s duration applied through a 200- $\mu$ m-diameter optical fiber. (a) Thermal Schlieren marking the optical penetration depth during the initial phase of energy deposition. (b) Maximally expanded bubble 200  $\mu$ s after the beginning of the laser pulse. (c) Collapsed bubble shortly after the end of the laser pulse, with thermal Schlieren in the surrounding liquid.

described in section V. When the rate of energy deposition is low and heterogeneous vaporization nuclei are present, the phase transition is governed by normal boiling and starts once a temperature slightly exceeding 100 °C has been reached (a temperature exceeding 100 °C is required to overcome the surface tension of the vaporization nuclei). Due to the large specific volume of water vapor, bubbles of considerable size are formed, even when only a small fraction of the water within the optical penetration depth is vaporized. When the rate of energy deposition is high and the stress confinement condition is not fulfilled, a phase explosion occurs once the spinodal limit is reached.<sup>372,375</sup> The separation of the metastable liquid into saturated vapor and saturated liquid corresponds again to a partial vaporization. The fraction vaporized is below 50% and depends on the volumetric energy density in a way described by the theory of metastable liquids<sup>158,376,377</sup> (section V.D). For intermediate rates of energy deposition and in the presence of heterogeneous nuclei, the liquid is overheated only to a certain degree, and the phase transition occurs as explosive boiling. Jansen and co-workers<sup>373</sup> addressed this phenomenon empirically without considering the actual kinetics of the phase transition. When applying very large radiant exposures and nanosecond pulse durations, it is possible to produce supercritical conditions. In this case, the heated volume is completely transformed to vapor as it expands to pressures below the critical point.

With stress confinement, a thermoelastic stress wave is launched from a liquid volume directly adjacent to the fiber tip, and tensile stress waves are created due to the finite size of the absorbing volume (section IV.C). The tensile stress distribution can be described as a consequence of diffraction of the thermoelastic stress wave at the circular boundary of the acoustic source in front of the fiber tip. Depending on the ratio of the optical penetration depth,  $1/\mu_a$ , of the laser radiation and the diameter,  $d$ , of the fiber tip, cavitation-induced bubble formation occurs inside (for  $\mu_a d \approx 1$ ) or outside (for  $\mu_a d \ll 1$ ) the volume of energy deposition. An example of the latter case is shown in Figure 44.<sup>151,152</sup> Using nanosecond pulses delivered through a 400- $\mu$ m fiber into a medium with an optical penetration depth of 380  $\mu\text{m}^{-1}$ , cavitation could be created by a temper-

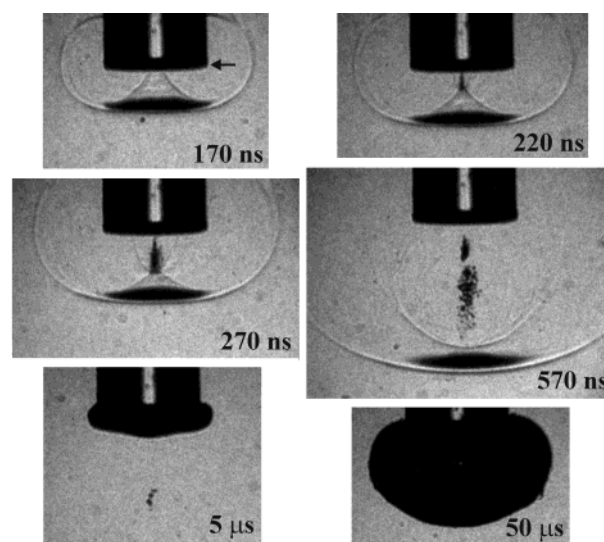


**Figure 44.** Laser-induced bubble formation at a fiber tip produced by 6-ns pulses under stress confinement conditions. The fiber tip was submerged in an aqueous solution of Orange G dye with an optical penetration depth of 11  $\mu$ m at the wavelength of 490 nm used for the experiment. Tensile stress waves originating from diffraction at the edges of the fiber produce cavitation bubbles at the fiber axis where they overlap. At 5  $\mu$ s, a vapor bubble appears directly at the fiber surface that reaches its maximum size at 50  $\mu$ s. (Reprinted with permission from ref 151. Copyright 1996 American Physical Society.)

ature rise as small as 33 °C.<sup>152</sup> Similar absorption and stress confinement conditions are achieved with a Q-switched holmium laser in an aqueous (water or blood) environment. A certain degree of stress confinement is also present during the individual intensity spikes of free-running holmium laser pulses. The tensile portion of the thermoelastic stress transients produced by these spikes leads to a transient lowering of the boiling temperature and to bubble formation from heterogeneous nuclei at temperatures well below 100 °C.<sup>375</sup>

The dynamics of bubble formation and growth depends on the number density and size of heterogeneous nuclei as well as on the specific path taken in the phase diagram, as discussed in sections V.B–F. Therefore, no general temperature threshold for bubble formation can be defined. The conditions leading to bubble formation must be determined in



each individual case by establishing the dynamics of temperature and pressure produced by the laser irradiation.

## B. Amplification of Mechanical Effects by Liquid Confinement

In a liquid environment, the expansion of the hot vapor generated by the laser radiation is inhibited. This applies to both the gaseous products generated during tissue ablation and the products of vaporization of liquid between the fiber tip and tissue surface. In cases in which the fiber tip is placed in contact with the tissue surface, the ablation products are even more strongly confined than when they are surrounded by liquid alone. For a given radiant exposure, the confining effect of the liquid or solid results in considerably higher temperatures and pressures within the target than ablation in a gaseous environment, because the expansion of the ablation products and the adiabatic cooling of the ablation products proceed more slowly. Therefore, in a liquid environment, there is generally a more effective transduction of the laser energy into mechanical energy.<sup>285,378,379</sup> As a result, the potential for mechanical collateral damage is much larger than that for ablation in air.<sup>24,26,78,207,292,293,378,380–388</sup>

When the laser-induced stress transients possess a sufficiently short rise time, their propagation results in the formation of a shock wave.<sup>387,389</sup> The large pressure in the laser-induced vapor bubble leads to a very rapid expansion that overshoots the equilibrium state, in which the internal bubble pressure equals the hydrostatic pressure. The increasing difference between the hydrostatic pressure and the falling internal bubble pressure then decelerates the expansion and brings it to a halt. At this point, the kinetic energy of the liquid during bubble expansion has been transformed into the potential energy of the expanded bubble. The bubble energy is related to the radius of the bubble at its maximum expansion,  $R_{\max}$ , and the difference between the hydrostatic pressure,  $p_0$ , and the vapor pressure,  $p_v$ , inside the bubble by<sup>174,389</sup>

$$E_B = \frac{4\pi}{3}(p_0 - p_v)R_{\max}^3 \quad (21)$$

The details of shock wave emission and bubble generation depend not on the mechanism of energy deposition (e.g., linear absorption versus optical breakdown) but rather on its time scale and the degree of stress confinement. A detailed description for the case of spherical bubble dynamics can be found in several references.<sup>379,387,389,390</sup>

The expanded bubble collapses again due to the static background fluid pressure. The collapse compresses the bubble content into a very small volume, thus generating a very high pressure that can exceed 1 GPa for an approximately spherical bubble collapse.<sup>391</sup> The rebound of the compressed bubble interior leads to the emission of a strong pressure transient into the surrounding liquid that can evolve into a shock wave.<sup>375,380,391–394</sup>

While the events during bubble generation are strongly influenced by the laser parameters, the subsequent bubble dynamics is primarily influenced by the properties of the fluid and the boundary conditions in the neighborhood of the laser focus. A spherical bubble produced in an unconfined liquid retains its spherical shape while oscillating, and the bubble collapse takes place at the site of bubble formation. However, when the bubble is formed near a material boundary, the collapse is asymmetric and associated with the formation of one or two high-speed water jets that concentrate the bubble energy at some distance from the locus of bubble generation.<sup>292,293,391,395</sup> When the bubble collapses in the vicinity of a rigid boundary, the jet is directed toward this boundary. The bubble collapse near an elastic, tissue-like boundary is characterized by the formation of two liquid jets that are directed one away from and one toward the boundary and reach velocities as high as 960 m/s.<sup>292</sup> Jet formation is also induced by the fiber tip itself, whereby the jet is usually directed away from the tip in the direction of the fiber axis.<sup>392,396</sup> The jets have been shown to cause collateral damage of ablation<sup>381</sup> and to increase the material removal (section IX.C).

The fraction of laser energy converted into the mechanical energy of the cavitation bubble depends on the laser pulse duration.<sup>393,394</sup> Bubbles produced by free-running laser pulses with durations on the order of several hundred microseconds expand during the laser pulse, and vaporization and condensation occur simultaneously in different parts of the bubble. Material is ablated at the bubble wall opposite to the fiber tip, while vapor condenses in those regions of the bubble that are not exposed to the laser radiation.<sup>374,394</sup> The bubble formation during the laser pulse limits the maximum energy density reached in the ablated liquid or tissue. The energy flow and condensation within the bubble further limit the maximum bubble size. By contrast, when nanosecond pulses are used for ablation, the bubble formation starts only at the end of the laser irradiation.<sup>374,375</sup> This leads to extremely high volumetric energy densities and temperatures in the liquid or tissue adjacent to the fiber tip at superthreshold radiant exposures. As a result, the cavitation bubble expands to a much larger size than that produced by a free-running pulse with equal energy.

Dramatic consequences of the cavitation bubble dynamics were observed in laser angioplasty, a procedure that aims to recanalize vessels that are obstructed by fatty or atherosclerotic plaque. Laser angioplasty was performed mostly using  $\lambda = 308$  nm laser excimer laser pulses, providing a high precision of the primary tissue effect.<sup>370</sup> However, it was realized after several years of clinical practice that the bubble expansion induced by the explosive vaporization in a liquid environment led to a rapid dilatation of the vessel on a microsecond time scale that often caused ruptures within the vessel wall. Moreover, the subsequent bubble collapse caused an invagination of the vessel that further added to the mechanical trauma.<sup>26,385,397</sup> These dynamics are shown in Figure 45. The mechanical trauma of the vessel



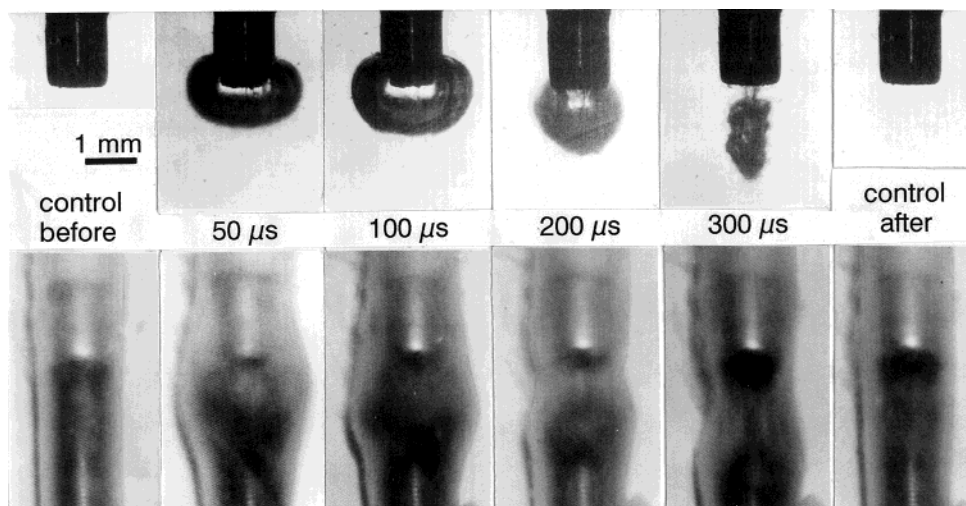


**Figure 45.** Cavitation bubble expansion and collapse produced by XeCl excimer laser pulses ( $\lambda = 308$  nm,  $t_p = 115$  ns,  $\Phi_0 = 6$  J/cm<sup>2</sup>) in a hemoglobin solution (top row) or within a rabbit femoral artery (bottom row). The dilatation and invagination of the artery walls by the oscillating bubble produces mechanical trauma to the vessel wall during laser angioplasty procedures. (Reprinted with permission from ref 385. Copyright 1993 American Heart Association.)

wall in turn led to an overactive and dysfunctional healing response that contributed to the high rate of restenosis that was clinically observed after laser angioplasty.<sup>370</sup> Cavitation can thus lead to a structural deformation of the tissue adjacent to the ablation site that is much more pronounced than the ablative tissue effect itself and compromises the high precision of the original ablation. After this was realized, laser angioplasty was abandoned by most clinicians. Alternative irradiation strategies to reduce the effects of inertial confinement are discussed in section XI.C.

Placement of an optical fiber tip in contact with the tissue further enhances the level of inertial confinement. In this case, the pressure induced by a free-running holmium:YAG laser pulse ( $\lambda = 2.1$   $\mu$ m) was found to be 2–6 times higher than that for noncontact ablation in air,<sup>398</sup> and violent material ejection and tissue dissection were reported by several authors.<sup>24,26,383,384,388,399,400</sup> Furthermore, the confinement of the ablation products by the ablation channel leads to an increase of the collateral thermal damage because the heat contained in the ablation products is conducted back into the residual tissue.<sup>388,399,401</sup> This effect is clearly visible in the histologic section of an Er:YAG laser sclerostomy presented in Figure 46. Thermomechanical injury of the tissue extends as much as 500  $\mu$ m into the walls, even though the optical penetration depth is only a few micrometers.

### C. Influence of the Bubble Dynamics on Ablation Efficiency

The cavitation bubble dynamic influences the ablation efficiency in two ways. First, the bubble creates a transmission channel for the laser radiation from the fiber tip to the tissue.<sup>382,392,397,402–406</sup> Second, the forces exerted on the tissue as a consequence of the bubble dynamics may contribute to material removal.<sup>291–293,407</sup>

The shape and lifetime of the transmission channel depend on the laser pulse duration and the optical

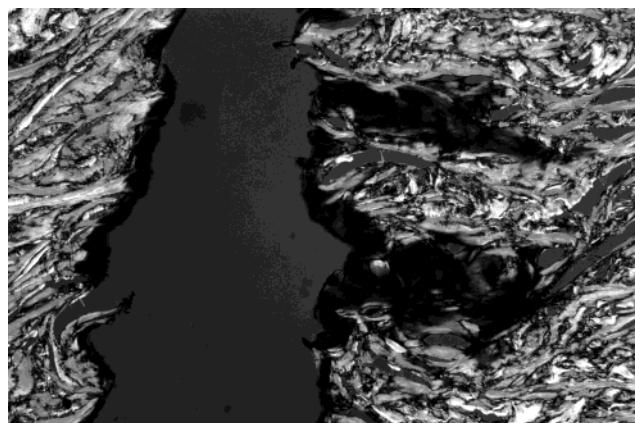


**Figure 46.** Histologic section of a fistula through porcine sclera produced by a sequence of Er:YAG laser pulses of 15-mJ energy and 500- $\mu$ s duration in a procedure used for glaucoma treatment. The photograph illustrates the large spatial extent of the thermomechanical effects produced when the ablation products are confined by an optical fiber. The high pressure in the ablation products leads to dissections of the fistula walls. The thermally damaged zone (dark) along these dissections extends up to 500  $\mu$ m into the sclera, while it is only 10–40  $\mu$ m wide in normal wall sections (Reprinted with permission from ref 388. Copyright 1997 Slack Inc.)

penetration depth. Nearly spherical bubbles are produced by nanosecond pulses, and pear-shaped bubbles are produced by 200- $\mu$ s free-running holmium and thulium laser pulses.<sup>374,384,394,403</sup> By contrast, 200- $\mu$ s pulses of the highly absorbed erbium laser radiation create thin, elongated bubbles that partially collapse during the laser pulse, such that the light path from the fiber to the target is again blocked.<sup>394,404</sup> Sequential application of holmium and erbium pulses allows for both efficient transmission and precise ablation with few thermal side effects,<sup>404</sup> as illustrated in Figure 47. The dynamics of channel formation *within* tissue has been studied in the context of transmyocardial and endomyocardial laser revascularisation (ELR) and sclerostomy.<sup>388,400,408</sup>

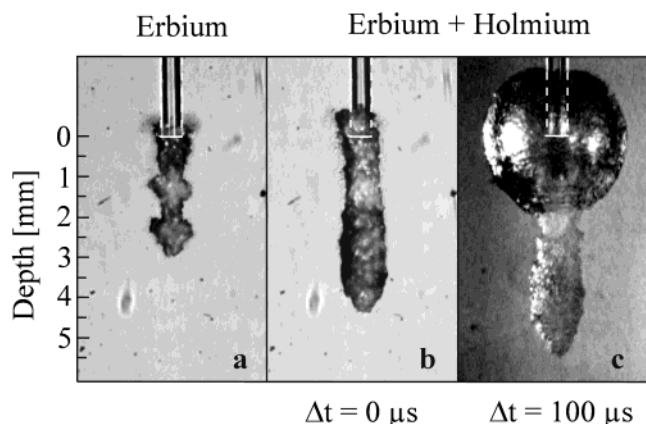


**Figure 47.** Bubble formation produced by the delivery of a erbium laser pulse and the sequential delivery of holmium + erbium laser pulses photographed 200  $\mu$ s after the beginning of the erbium laser pulse: (a) single erbium laser pulse, (b) erbium and holmium laser pulses delivered simultaneously, and (c) holmium laser prepulse followed by an erbium pulse after a delay of 100  $\mu$ s. Erbium pulse:  $E = 100$  mJ,  $t_p = 200$   $\mu$ s. Holmium pulse:  $E = 100$  mJ,  $t_p = 200$   $\mu$ s. The channel created by the single erbium laser pulse starts to collapse 200  $\mu$ s after the onset of irradiation and blocks the light transmission to a target located at a distance from the fiber tip. The use of a holmium prepulse results in a deeper channel that remains open for a considerably longer time. (Reprinted with permission from ref 404. Copyright 1996 Optical Society of America.)

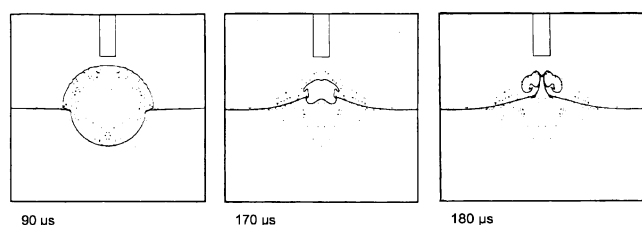


**Figure 48.** Numerical simulations showing the dynamics of the cavitation bubble generated during pulsed laser ablation of an elastic tissue-like material together with the bubble-induced material response. The elapsed time after the instantaneous energy deposition is indicated below each frame. Ablation is enhanced by jetlike material ejection during bubble collapse. (Reprinted with permission from ref 291. Copyright 1999 SPIE.)

Three aspects of the cavitation bubble dynamics can contribute to tissue ablation in a liquid environment: (a) the material erosion by the elastic rebound of the tissue that is deformed during bubble expansion, (b) the suction force exerted by the collapsing bubble, and (c) the impact of the high-velocity jet generated during bubble collapse.<sup>291–293,407</sup> Figure 48 presents results of numerical simulations of the bubble dynamics proximal to an elastic boundary which shows the material ejection upon bubble collapse.<sup>291</sup> While the suction force enhances the material removal only for very soft tissues, the elastic rebound plays a role also for tissues with moderate strength, and the jet impact can erode even hard materials with high mechanical strength.<sup>292,293,407</sup>

The influence of the cavitation bubble dynamics on ablation in a liquid environment is equivalent to the role played by the hydrodynamics of the ablation plume in a gaseous environment (sections VI.B–D). In both cases, the precision and efficiency of ablation are substantially influenced by events occurring long

after the direct interaction between laser radiation and tissue.

## X. Plasma-Mediated Ablation

Laser-induced plasma-mediated ablation, also known as laser-induced breakdown, relies on non-linear absorption in the target that is achieved when a material-specific irradiance threshold is exceeded.<sup>29,30,409</sup> Plasma formation thus plays an important role in interactions of high-power laser irradiation with matter.<sup>12</sup> In materials that are strongly heated through linear absorption of the laser radiation, plasma formation is either initiated or supported by thermionic emission of free electrons. In this case, the plasma formed at the target surface usually “shields” the target and impedes further energy deposition by linear absorption, as discussed in section VI.D. However, a plasma can also be formed in materials that are normally transparent. This occurs at high irradiances when multiphoton processes provide seed electrons for an ionization avalanche. Plasma formation then progresses through an interplay of multiphoton ionization and avalanche ionization of target molecules.

Plasma formation provides a unique possibility for localized energy deposition in transparent or low-absorbing materials.<sup>28,30,317,410</sup> The volume in which the energy deposition occurs can be controlled by focusing the laser radiation, because plasma formation occurs only at locations where the irradiance threshold for laser-induced breakdown is exceeded. Laser-induced breakdown in transparent media enables noninvasive surgery inside of cells, tissues, or even a whole organ of the human body, such as the eye. Main applications are intraocular surgery,<sup>30,411</sup> intrastromal corneal refractive surgery,<sup>410,412–414</sup> and intracellular surgery.<sup>415–417</sup>

In this section, we first describe the kinetics of plasma formation in biological tissues and its implications for three key parameters that characterize laser-induced breakdown: (a) the breakdown threshold, (b) plasma absorption, and (c) plasma energy density. We then discuss the thermomechanical and chemical effects induced by plasma formation and their consequences for ablation precision and efficiency.

### A. Kinetics of Plasma Formation in Biological Tissues

Experimental studies have demonstrated that the optical breakdown threshold in water is similar to that in transparent ocular and other biological media (cornea, vitreous fluid, and saline).<sup>418,419</sup> For convenience, we shall therefore focus attention on plasma formation in pure water. Whereas optical breakdown in gases leads to the generation of free electrons and ions, the electrons in liquid are either bound to a particular molecule or “quasi-free” when they possess sufficient kinetic energy to move without being captured by local molecular energy potentials. To describe the breakdown process in water, we adopt the approach followed by Sacchi and treat water as an amorphous semiconductor with an excitation

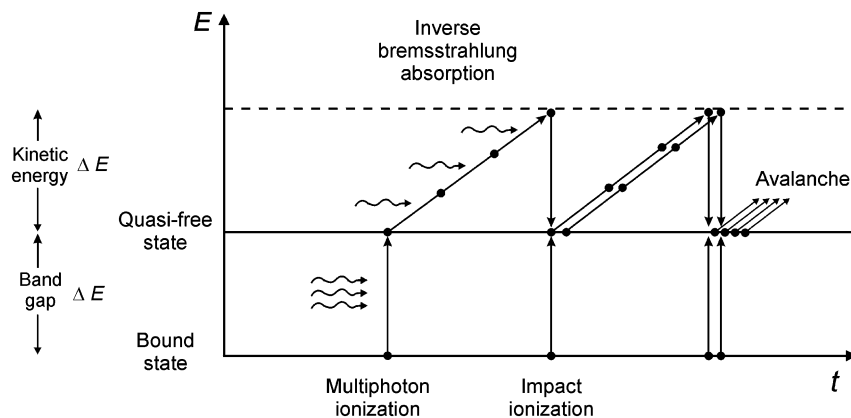


**Figure 49.** Interplay of multiphoton and avalanche ionization in the process of plasma formation. Avalanche ionization consists of a series of multiple inverse bremsstrahlung absorption events followed by impact ionization. (Reprinted with permission from ref 428. Copyright 2002 SPIE.)

energy of  $\Delta E = 6.5$  eV, corresponding to the transition from the  $1b_1$  molecular orbital into an excitation band.<sup>87,420</sup> For simplicity, we use the terms “free electrons” and “ionization” as abbreviations for “quasi-free electrons” and “excitation into the conduction band”, respectively.

Free electrons form via an interplay between multiphoton and avalanche ionization processes, as depicted schematically in Figure 49. The promotion of an electron from the ground state to the valence band requires the energy of two photons for UV wavelengths longer than  $\lambda = 191$  nm, three photons for wavelengths longer than 383 nm, and four, five, and six photons for wavelengths longer than 574, 766, and 958 nm, respectively. In pure water, this energy can be provided only when several photons interact simultaneously with a bound electron. The multiphoton ionization rate is proportional to  $I^k$ , where  $I$  is the laser irradiance and  $k$  the number of photons required for ionization.

Once a free electron is produced in the medium, it can absorb photons via a nonresonant process called “inverse Bremsstrahlung absorption” (IBA) in the course of collisions with other charged particles (ions or atomic nuclei).<sup>12</sup> IBA requires an interaction of the free electron with a third particle to conserve energy and momentum during optical absorption. Absorption of the photon increases the kinetic energy of the free electron. After  $k$  IBA events, the kinetic energy of the electron exceeds the band gap energy,  $\Delta E$ , and the electron can produce another free electron via impact ionization. After impact ionization, two free electrons with low kinetic energies are available which can again gain energy through IBA. The recurring sequences of IBA events and subsequent impact ionization lead to a rapid growth in the number of free electrons if the irradiance is sufficient to overcome the losses of free electrons through diffusion out of the focal volume and recombination. Moreover, the rate of energy gain through inverse Bremsstrahlung must be more rapid than energy losses through collisions with heavy particles. The process involving both IBA and impact ionization is called “avalanche” or “cascade” ionization. At high irradiances, the losses play a minor role, and the cascade ionization rate for a given number density of free electrons is proportional to the irradiance.<sup>409</sup>

Multiphoton ionization occurs on a time scale of a few femtoseconds, and its rate is independent of the number density of free electrons. By contrast, cascade ionization depends on the number density of free electrons in the focal volume and requires a longer time because several consecutive IBA events are necessary for a free electron to acquire the kinetic energy for impact ionization. For example, with an ionization energy of 6.5 eV and a photon energy of 1.56 eV (corresponding to  $\lambda = 800$  nm), an electron must undergo at least five IBA events before it can produce another free electron through impact ionization. As mentioned above, IBA can occur only during collisions of the electrons with heavy particles. In condensed matter, the time,  $\tau$ , between collisions is roughly 1 fs.<sup>421</sup> Thus, even at extremely high irradiance, in which case most collisions involve IBA, every doubling of the number of free electrons requires at least 5 fs. Due to this time constraint, avalanche ionization can contribute significantly to plasma formation for laser pulse durations in the femtosecond range only after a large number density of free electrons has been provided by multiphoton ionization.

Several authors have used rate equations based on the Drude model to describe the temporal evolution of the volumetric density of free electrons,  $\rho$ , and to calculate breakdown thresholds for various laser parameters.<sup>409,422–427</sup> The generic form of such a rate equation is

$$\frac{d\rho}{dt} = \eta_{\text{mp}} + \eta_{\text{casc}}\rho - g\rho - \eta_{\text{rec}}\rho^2 \quad (22)$$

The first two terms on the right-hand side of eq 22 represent the production of free electrons through multiphoton and cascade ionization, respectively. The last two terms describe electron losses through diffusion out of the focal volume and recombination, respectively. The cascade ionization rate,  $\eta_{\text{casc}}$ , and the diffusion loss rate,  $g$ , are proportional to the density of free electrons, while the recombination rate,  $\eta_{\text{rec}}$ , is proportional to  $\rho^2$ , as it involves an interaction between two charged particles (an electron–hole pair). A detailed description of the individual terms of eq 22 was given by Kennedy<sup>422</sup> and Noack and Vogel.<sup>427</sup>



Several investigations based on the above rate equation have neglected either multiphoton ionization,<sup>409,423</sup> recombination,<sup>422,426</sup> or diffusion,<sup>425</sup> and only in a few studies were all four terms of the rate equation considered.<sup>424,427,428</sup> While many of the early studies were focused on calculation of the breakdown thresholds, recent numerical simulations also include an analysis of the time evolution of the electron density during the laser pulse, the irradiance dependence of the free-electron density, the plasma absorption, and the volumetric energy density in the plasma.<sup>427,428</sup>

The description of plasma formation is complicated by the nonlinear variation of the refractive index with irradiance. This variation leads to a spatial phase modulation of the wave front in the laser beam that depends on the intensity distribution across the beam. The phase modulation changes the intensity distribution, causing self-focusing or defocusing of the laser beam, depending on the sign of the nonlinear refractive index.<sup>429</sup> The local increase in irradiance achieved by self-focusing enhances the nonlinear absorption process involved in plasma formation. The degree of self-focusing increases with reductions in either focusing angle or laser pulse duration.<sup>425,430–432</sup> Self-focusing is more prominent under these conditions, as it requires a critical power to be exceeded that is largely independent of the focusing angle or pulse duration used.<sup>30</sup> By contrast, optical breakdown requires an irradiance threshold to be surpassed. The power necessary to provide this irradiance becomes larger with larger spot size (i.e., decreasing focusing angle) and with decreasing laser pulse duration. Therefore, at sufficiently small focusing angles and short pulse durations, the optical breakdown threshold is larger than the critical power for self-focusing, and the breakdown process is thus influenced by self-focusing. Once plasma formation has started, a reduction of the nonlinear refractive index by free electrons comes into play that produces self-defocusing.<sup>429,433</sup> The interplay of self-focusing and -defocusing leads to the formation of plasma filaments.<sup>430,434,435</sup>

## B. Threshold for Plasma Formation

The threshold radiant exposure for breakdown determines the possible precision of the laser effects used for ablation or dissection. From an experimental perspective, the threshold for nanosecond and picosecond laser-induced breakdown in aqueous media is defined by the irradiance or radiant exposure leading to the observation of a luminescent plasma at the laser focus.<sup>436</sup> With shorter laser pulses, there is no plasma luminescence in the visible region of the spectrum, and breakdown is detected experimentally by the observation of a cavitation bubble in the liquid that is produced by the expanding plasma.<sup>427,437</sup> From a theoretical point of view, optical breakdown is identified by the generation of a critical free-electron density,  $\rho_{\text{cr}}$ , between  $10^{18}$  and  $10^{21} \text{ cm}^{-3}$ .<sup>422,424,427,436</sup> Good correspondence between experimental threshold values and theoretical predictions for optical breakdown in water is obtained when critical electron densities of  $\rho_{\text{cr}} = 10^{20} \text{ cm}^{-3}$  for nanosecond pulses and  $\rho_{\text{cr}} = 10^{21} \text{ cm}^{-3}$  for picosecond and femtosecond pulses are assumed.<sup>427</sup>

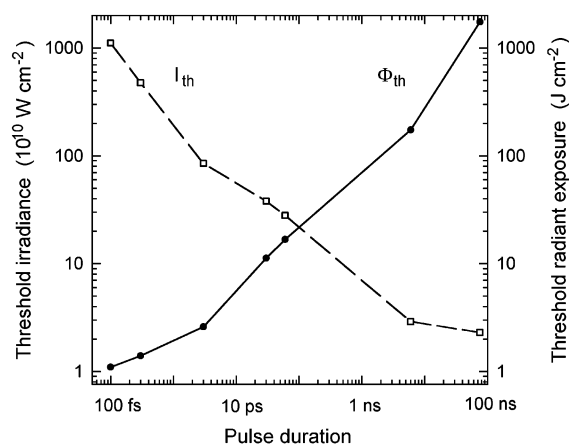


**Figure 50.** Threshold irradiance and radiant exposure for optical breakdown in water vs laser pulse duration. Data compiled from refs 427 and 379.

The irradiance threshold for plasma generation increases by 3 orders of magnitude when the laser pulse duration is decreased by 6 orders of magnitude from the nanosecond to femtosecond range, as shown in Figure 50. The increase in irradiance is required to compensate for the reduced time available to reach the critical electron density. Remarkably, the threshold radiant exposure decreases by 3 orders of magnitude for the same decrease of pulse duration. This decrease arises due to the scaling of the multiphoton ionization rate with  $I^k$  and the decrease of the plasma energy density with shorter laser pulse durations (section X.E).

For pulse durations in the nanosecond and picosecond ranges, the plasma formation threshold is reduced considerably when the target has a high linear absorption coefficient, because the seed electrons for avalanche ionization are provided by thermionic emission of free electrons. The threshold for plasma formation in transparent media (water or cornea) using pulses of a few nanoseconds is of the order  $100\text{--}400 \text{ J/cm}^2$ .<sup>430,438</sup> For TEA- $\text{CO}_2$  laser ablation of skin ( $\lambda = 10.6 \mu\text{m}$ ,  $t_L = 100 \text{ ns}$ ), where the optical penetration depth is  $\sim 20 \mu\text{m}$ , the plasma formation threshold is  $12\text{--}18 \text{ J/cm}^2$ .<sup>315,318</sup> and for ArF excimer laser ablation of skin ( $\lambda = 193 \text{ nm}$ ,  $t_L = 20 \text{ ns}$ ), where the optical penetration depth is only  $\sim 0.25 \mu\text{m}$ , plasma is formed at radiant exposures as small as  $0.25 \text{ J/cm}^2$ .<sup>150</sup> Thus, the threshold for nanosecond optical breakdown is reduced by a factor of  $\sim 1000$  when the target exhibits very high linear absorption. By contrast, linear absorption of the target was found to have no impact on the plasma threshold when ultrashort pulses with durations of  $\sim 100 \text{ fs}$  were used.<sup>438</sup> This is because the irradiance necessary to complete the ionization avalanche during the femtosecond pulses is so high that seed electrons are readily created by multiphoton ionization, and linear absorption does not serve to lower the threshold.

As shown in Figures 51 and 52, the laser pulse duration affects not only the threshold irradiance also but the entire dynamics of plasma formation and the irradiance dependence of the free-electron density. With nanosecond pulses in the IR (Figure 51), no free electrons are formed by impact ionization for irradiance values below the breakdown threshold, because

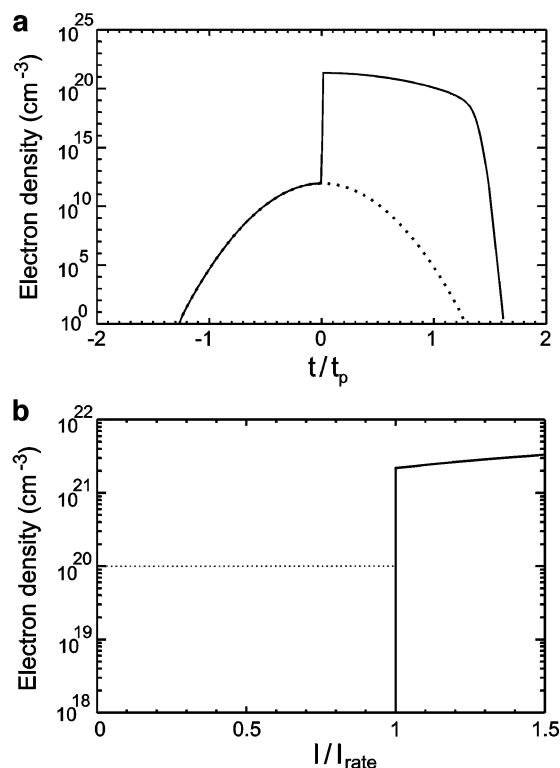


**Figure 51.** (a) Temporal evolution of free-electron density during laser irradiation for  $\lambda = 1064$  nm and  $t_p = 6$  ns. The temporal shape of the laser pulse is assumed to be Gaussian. The time,  $t$ , is normalized with respect to the laser pulse duration (FWHM)  $t_p$ . The contribution of multiphoton ionization to the total free-electron density is plotted as a dotted line. (b) Irradiance dependence of the maximal free-electron density,  $\rho_{\max}$ , for the same laser parameters. The irradiance is normalized with respect to the calculated threshold irradiance,  $I_{\text{rate}}$ . The threshold  $I_{\text{rate}}$  and the corresponding value of  $\rho_{\max}$  are marked with dotted lines. (Reprinted with permission from ref 428. Copyright 2002 SPIE.)

no seed electrons are created by multiphoton ionization. Once the irradiance is sufficiently high to provide a seed electron, the ionization cascade proceeds very rapidly due to the high irradiance. The electron density increases by 9 orders of magnitude within a small fraction of the laser pulse duration and actually overshoots the critical electron density of  $\rho_{\text{cr}} = 10^{20} \text{ cm}^{-3}$  (Figure 51a). This results in an extremely sharp breakdown threshold, because either a highly ionized plasma is produced or no plasma at all (Figure 51b). It is important to note that this “sharpness” does not exclude the possibility of pulse-to-pulse variations of the threshold irradiance. These variations are due to the probabilistic nature of the multiphoton-induced generation of seed electrons. With femtosecond pulses, there is no lack of multiphoton-induced seed electrons for avalanche ionization, and the onset of plasma formation is therefore deterministic. An avalanche is initiated at irradiance values considerably lower than the breakdown threshold, and the free-electron density varies continuously with irradiance (Figure 52b). Therefore, it is possible to generate any desired free-electron density through the application of an appropriate laser irradiance.<sup>428</sup>

It is interesting to note that, even for femtosecond plasmas, avalanche ionization is the mechanism that

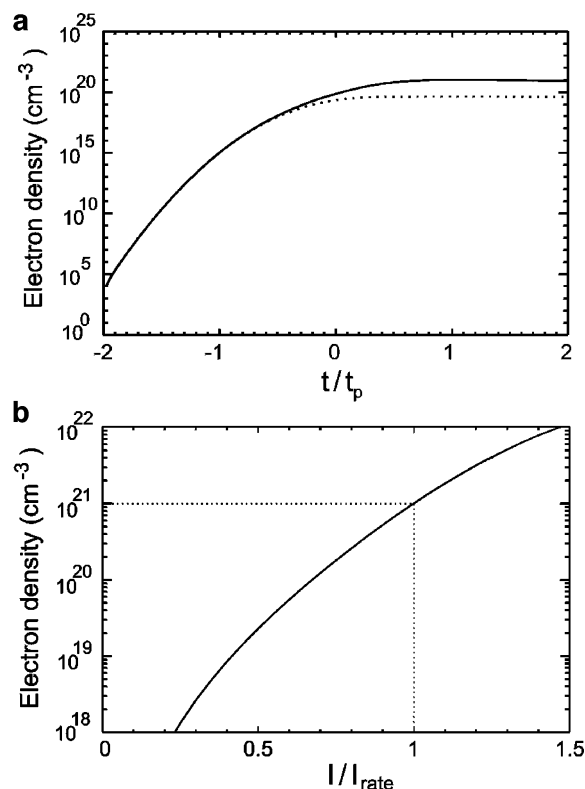


**Figure 52.** (a) Temporal evolution of free-electron density during laser irradiation and (b) irradiance dependence of the maximal free-electron density for  $\lambda = 532$  nm and  $t_p = 100$  fs. (Reprinted with permission from ref 428. Copyright 2002 SPIE.)

produces the majority of the free electrons during the laser pulse (Figure 52a). Multiphoton ionization dominates during the initial part of the pulse, but avalanche ionization takes over at later times, as its rate depends on both the irradiance and the free-electron density, whereas the multiphoton ionization rate depends only on irradiance (eq 22).

### C. Plasma Formation above the Breakdown Threshold

At the breakdown threshold, plasma formation is restricted to the focal region of the laser beam. By contrast, when the pulse energy exceeds the breakdown threshold and is focused within a transparent medium, the plasma formation is characterized by a growth of the plasma from the beam waist toward the incoming laser beam. Almost no plasma develops behind the laser focus, as most of the laser light is already absorbed prior to and in the beam waist. Thus, the region behind the focus is “shielded” by the plasma absorption.<sup>30,430,439–441</sup>

A realistic explanation for the plasma expansion is provided by the “moving breakdown” model originally proposed by Raizer<sup>442</sup> and further refined by Docchio and co-workers.<sup>439,440</sup> As depicted in Figure 53, this model assumes that optical breakdown is independent of the preceding plasma formation and occurs at all locations where the irradiance exceeds the breakdown threshold. As the power increases during the laser pulse, the plasma front moves along the optical axis at the same velocity as the location where the irradiance threshold for breakdown is

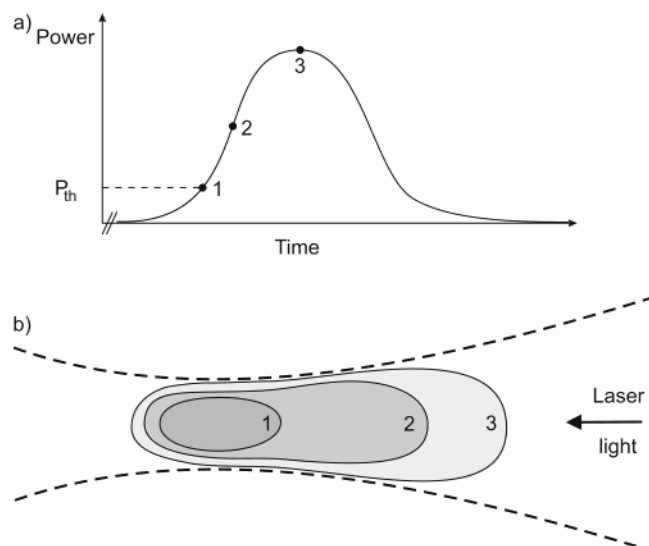


**Figure 53.** Temporal evolution of the laser power (a) and the plasma contours (b) during the optical breakdown process at pulse energies above threshold ("moving breakdown"). (1) When the laser power exceeds the optical breakdown threshold,  $P_{th}$ , a plasma is formed in the focal volume. (2) As the laser power increases during the pulse, the threshold irradiance is exceeded further upstream of the focal volume. (3) The maximum plasma extension is reached when the laser power reaches its maximum. While upstream of the focal volume the plasma contours at times (1)–(3) correspond to iso-irradiance lines, this does not hold for the region 'downstream' of the focal volume because of light absorption by the plasma ("plasma shielding").

exceeded. This results in a plasma that reaches its maximum length at the intensity peak of the laser pulse. The laser radiation delivered following the intensity peak serves only to heat the plasma but does not elongate it further. For a Gaussian beam, Docchio and co-workers derived the following prediction for the plasma length,  $z_{max}$ , from the beam waist toward the incoming laser beam:<sup>439</sup>

$$z_{max} = z_R \sqrt{\beta - 1} \quad (23)$$

where  $z_R$  is the Rayleigh range and  $\beta$  is the ratio between the peak irradiance of the laser pulse and the threshold irradiance for laser-induced breakdown, i.e.,  $\beta = I/I_{th}$ .

The validity of the moving breakdown model was shown experimentally for Nd:YAG laser pulses ( $\lambda = 1064$  nm) with pulse durations in the nanosecond and picosecond ranges.<sup>439,440</sup> The quantitative predictions are very good for picosecond pulses but degrade for pulse durations in the nanosecond range, as the assumption of a spatially and temporally constant breakdown threshold during the laser pulse is incorrect for longer pulses.<sup>30,430</sup> The reason for this is that the UV emission of the plasma contributes to the formation of additional free electrons in the plasma vicinity that act as seed electrons for cascade ionization. For nanosecond pulses, this leads to a lowering of the breakdown threshold during the laser pulse below the value required to create the first seed electron via multiphoton ionization. As a result optical breakdown produced by nanosecond pulses results in a much larger plasma size than that

predicted by the moving breakdown model.<sup>430</sup> For shorter pulses in the picosecond or femtosecond range, a higher irradiance is required to achieve the critical free-electron density at the end of the ionization avalanche, and the creation of seed electrons for the avalanche through multiphoton ionization does not provide an additional barrier. Therefore, at superthreshold energy, the breakdown threshold remains constant throughout the laser pulse, and the predictions of the moving breakdown model hold.

For breakdown produced using femtosecond pulses focused at moderate angles, the plasma length observed above the breakdown threshold is considerably longer than the spatial length of the laser pulse ( $30 \mu\text{m}$  for a 100-fs pulse). This indicates that plasma formation begins before the pulse reaches the laser focus. The plasma front moves with the laser pulse toward the focus, so that free electrons remain in its wake.<sup>443</sup> This is in contrast to picosecond and nanosecond breakdown, in which the physical length of the pulse is much longer than that of the plasma and the plasma front moves from the focus toward the incoming laser beam. Nevertheless, the plasma length for femtosecond pulses is proportional to  $\sqrt{\beta - 1}$ , as for picosecond pulses, even though the plasma front moves in the opposite direction.<sup>30</sup> In both cases, the extent of the plasma on the laser side is simply determined by the maximum axial distance from the beam waist at which the breakdown threshold is exceeded.

So far, we have considered plasma formation within transparent biological media. The situation is quite different when a plasma is formed at a tissue surface in air. Here, plasma formation is initially restricted to the tissue target, even when the irradiance has exceeded the breakdown threshold to a certain degree, because the breakdown threshold in air is higher than that in tissue.<sup>30</sup> However, when the electron density becomes sufficiently large for the plasma frequency to exceed the frequency of the light (the critical value is  $10^{21} \text{ cm}^{-3}$  for  $\lambda = 1064 \text{ nm}$ <sup>30</sup>), the plasma absorption coefficient increases dramatically, and the plasma becomes highly reflective up to a value of  $R = 0.9$ .<sup>444–446</sup> This change has two consequences: (a) the plasma electron and energy densities in the target continue to increase very rapidly,<sup>447</sup> and (b) plasma formation extends into the surrounding air because the hot electrons ejected from the target begin to ionize the air. The latter process leads to the development of a plasma plume that largely reduces the amount of laser light reaching the target.<sup>316</sup> It is only for femtosecond laser pulses that the coupling of optical energy into the target is not impaired by plasma shielding, as the laser pulse is too short to allow the formation of a plasma plume during the laser pulse.<sup>447</sup>

## D. Plasma Absorption

The plasma absorption determines the amounts of energy coupled into the target medium and transmitted past the target volume. Apart from influencing the efficiency of the laser surgical process, plasma absorption is important for its safety if surgery is performed near sensitive, strongly absorbing biologi-



cal structures such as the retina. Absorption coefficients of plasmas produced in bulk water have been determined by measuring the plasma transmission, scattering, and reflection together with the plasma length.<sup>30,441</sup> The experimental investigations covered a range of radiant exposures up to 50 times threshold and yielded values between 100 and 400 cm<sup>-1</sup>, depending on pulse duration (6 ns and 30 ps), wavelength, and radiant exposure. Slightly higher values, between 100 and ~1000 cm<sup>-1</sup>, were obtained by numerical calculations of the plasma absorption coefficients for pulse durations between 100 fs and 100 ns that considered the time evolution of the free-electron density and the absorption cross section of free electrons for IBA.<sup>427</sup>

For plasma formation at tissue surfaces in air, no experimental data for plasma absorption coefficients and the spatial distribution of energy deposition are available to date. Once the electron density at the surface exceeds the critical value of ~10<sup>21</sup> cm<sup>-3</sup>, the absorption coefficients will certainly be higher than the values for bulk media. Feit and co-workers assumed that plasma is formed in a layer with a thickness of only a few nanometers but did not discuss how the plasma electron and energy densities corresponding to such a small absorption depth are related to the ablation thresholds of soft and hard tissues.<sup>447</sup>

## E. Plasma Energy Density

The plasma energy density is closely linked to the strength of the mechanical effects (shock waves and cavitation) associated with breakdown. The energy density determines the degree of disruption created by the breakdown event and the amount of mechanical damage produced in the vicinity of the laser focus. The deposition of optical energy into the medium is mediated by the generation and subsequent acceleration of free electrons. Energy gained by the electrons is transferred to heavy plasma particles through collisions and recombination, and this results in a heating of the atomic and ionic plasma constituents. At constant electron density, the number of collisions and recombination events and the resulting energy transfer to the medium are proportional to the laser pulse duration. The plasma energy density must therefore increase with increasing laser pulse duration. Theoretical predictions of the variation of plasma energy density in bulk transparent media with laser pulse duration, based on eq 22, are shown in Figure 54.<sup>427</sup> For femtosecond exposures, the laser pulse duration is shorter than the electron-cooling and recombination times. Thus, minimal energy is transferred during the pulse, and the energy density deposited into the breakdown region is simply given by the number of free electrons produced, multiplied by the mean energy gain of each electron. For pulse durations longer than the electron-cooling time (several picoseconds) and recombination time (several tens of picoseconds), a dynamic equilibrium is established between the energy transfer through collision and recombination on one hand and the generation of free electrons by the incident radiation on the other hand. Therefore, the energy

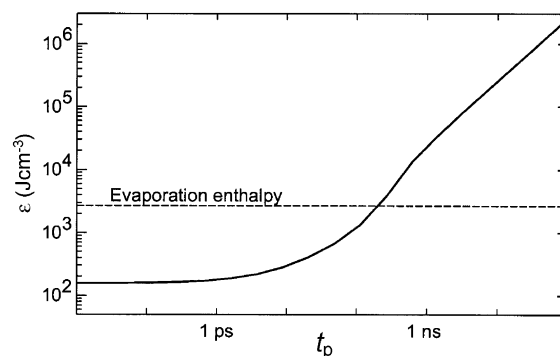


**Figure 54.** Calculated plasma energy density at the optical breakdown threshold versus laser pulse duration. The calculations were performed for a wavelength of 580 nm and a critical electron density of 10<sup>20</sup> cm<sup>-3</sup> which is realistic for nanosecond optical breakdown (see text). For picosecond and femtosecond pulses, the critical electron density is approximately 10<sup>21</sup> cm<sup>-3</sup>, and the corresponding plasma energy density is thus approximately 10 times higher than that plotted. (Reprinted with permission from ref 427. Copyright 1999 IEEE.)

density is larger than that for femtosecond pulses. For pulse durations in the nanosecond range, the calculated energy density is even larger and is proportional to the laser pulse duration.

Experimental values of the plasma energy density are 33–40 kJ/cm<sup>3</sup> for 6-ns pulses, ~10 kJ/cm<sup>3</sup> for 30-ps pulses, and less than 1 kJ/cm<sup>3</sup> for 100-fs pulses.<sup>387,448</sup> The model predictions in Figure 54 agree qualitatively with these experimental data. However, the calculated value for the 6-ns pulse duration (150 kJ/cm<sup>3</sup>) is approximately 4 times larger than the experimental value, because the model does not account for the plasma expansion during the laser pulse. The energy density values predicted for 100-fs and 30-ps pulses (150 and 550 J/cm<sup>3</sup>, respectively) are, on the other hand, about 1 order of magnitude smaller than the experimental values. This is because all energy density values were calculated assuming an electron density of 10<sup>20</sup> cm<sup>-3</sup>. Much better agreement with the experimental data is obtained assuming an electron density of 10<sup>21</sup> cm<sup>-3</sup> for picosecond and femtosecond breakdown, which also yields the best match between calculated and experimental values for the breakdown thresholds.<sup>427</sup> The above data indicate that, while the threshold energy density for optical breakdown and plasma-mediated ablation using nanosecond pulses is extremely high, for femtosecond pulses it is smaller than the vaporization enthalpy of water at constant pressure and resembles the volumetric energy density threshold for ablation based on linear absorption. The drop of plasma energy density with pulse duration is also responsible for the decrease in plasma luminescence, which is no longer visible for pulse durations ≤ 3 ps.<sup>443,448</sup>

## F. Thermomechanical and Chemical Effects

Plasma formation in a liquid environment or within biological tissue is coupled with shock wave emission, cavitation bubble generation, and jet formation upon bubble collapse in a way similar to that of pulsed laser ablation based on linear absorption (sections IX.A,B). However, the mechanical effects

induced by plasma formation are usually much stronger than those arising from ablation based on linear absorption because the volumetric plasma energy density is extremely high, particularly for nanosecond and picosecond pulses, for which it corresponds to plasma temperatures of several thousand Kelvin, even at threshold radiant exposure.<sup>379–381,387,430,436,449–454</sup> Mechanical effects produced in water are illustrated in Figure 55, and a summary of peak shock pressure amplitudes and transduction efficiencies of absorbed optical energy into cavitation bubble energy for different pulse durations is given in Table 5. Vogel and co-workers presented a complete energy balance for plasma formation in bulk water on nanosecond to femtosecond time scales.<sup>30,379</sup> They found that the transduction of laser energy into mechanical energy (shock wave and cavitation bubble energy) is as high as 90% for nanosecond pulses, more than for any other laser–tissue interaction. The ratio of shock wave energy (not included in the table) to cavitation bubble energy was ~2:1 for nanosecond pulses and ~3:2 for picosecond pulses.

The explosive expansion of the plasma produces disruptive tissue effects that extends spatially far beyond the vaporization and disintegration of tissue that occurs within the plasma volume. In the immediate vicinity of the plasma, the effects of the shock wave and cavitation bubble expansion can hardly be distinguished, but at a somewhat larger distance, cavitation effects are undoubtedly responsible for the creation of morphologically identifiable tissue alterations.<sup>381,387,419,452–456</sup>

The effects of the plasma and bubble expansion depend strongly on the location of the plasma in the tissue. When the plasma is formed in the bulk of the tissue, all deposited energy in excess of the vaporization threshold acts to deform the surrounding tissue. However, when the laser pulse is focused on a tissue surface in a liquid environment, a large fraction of the deposited energy is imparted to the surrounding fluid, and the hole created in the tissue is only slightly larger than the diameter of the laser focus.<sup>30,381</sup> Nevertheless, the inertial confinement of the vaporized material by the surrounding fluid causes a distinct indentation of the tissue surface during the expansion of the cavitation bubble.<sup>381,419</sup> Collateral mechanical effects are much less severe when the plasma is produced at a tissue surface in air, where the plasma expansion is not mechanically confined.<sup>457–459</sup>

The reduction of plasma energy density with decreasing pulse duration (section X.E) explains the strong reduction of mechanical effects produced with ultrashort as opposed to nanosecond laser pulses (Table 5). The ratio of mechanical energy,  $E_{\text{mech}}$ , to the energy fraction consumed for vaporization of the fluid within the plasma volume,  $E_{\text{vap}}$ , can serve as a metric for the strength of the disruptive effects that accompany plasma-mediated ablation. The ratio  $E_{\text{mech}}/E_{\text{vap}}$  for breakdown in water was found to decrease from 12:1 to 1:2 when the pulse duration was reduced from 6 ns to 100 fs.<sup>379</sup>

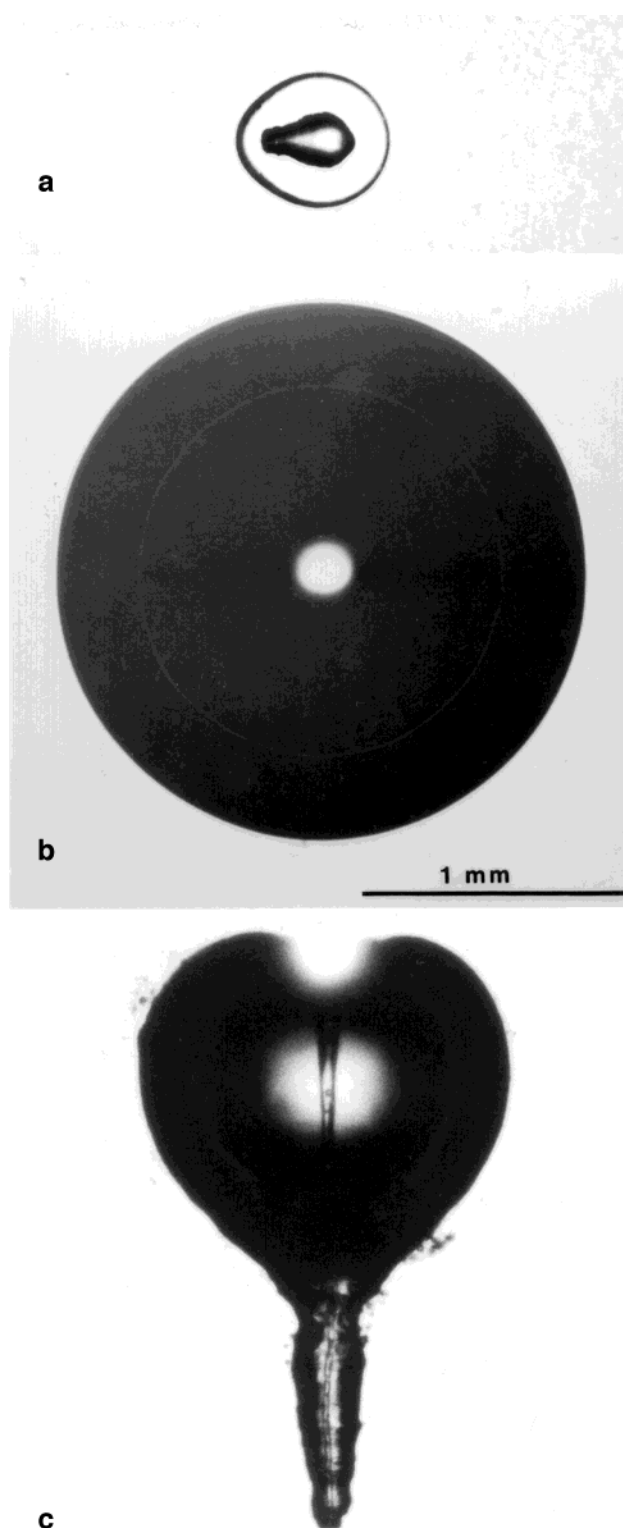


**Figure 55.** Cavitation bubble dynamics produced by focusing a 5-mJ, 6-ns Nd:YAG laser pulse into water. The laser light was incident from the right. (a) Shows the self-luminous plasma, and the bubble and the shock wave 90 ns after the laser pulse. (b) Shows the cavitation bubble when it reached its maximal size 130  $\mu\text{s}$  after the laser pulse. (c) Shows the formation of a high-speed liquid jet that forms during the collapse phase and was taken 50- $\mu\text{s}$  after the bubble collapse in the vicinity of a solid boundary (located just below the bottom of the picture). Jet formation concentrates energy at some distance from the optical breakdown site and is thus a potential source of collateral damage. (Reprinted with permission from ref 29. Copyright 1997 IOP Publishing Ltd.)

**Table 5. Dependence of Shock Wave Pressure and Cavitation Bubble Energy on the Laser Pulse Duration (Data from Refs 30 and 387)**

pulse duration	wavelength (nm)	$E/E_{th}$	pressure at plasma boundary (GPa)	pressure at 12-mm distance (MPa)	degree of conversion of absorbed light energy into bubble energy (%)
76 ns	750	6	10	4.0	22.0
6 ns	1 064	60	7–30	3.0	22.5
30 ps	532	60	1.7–10	0.65	13.5
3 ps	580	60	2.2	0.23	11.0
300 fs	580	60	1.8	0.11	3.0
100 fs	580	60	0.9	0.06	3.0

As shown in Table 5, the pressure of the shock waves emitted from the optical breakdown site decreases with decreasing pulse duration,<sup>30,387,448,452,453</sup> but not as strongly as the reduction in plasma energy density. The reason for this phenomenon is that picosecond and femtosecond plasmas are always produced under stress confinement. While the pressure induced by a phase transition in the plasma volume is small for low energy densities, the thermoelastic stresses are still very high. Numerical simulations for plasmas with a free-electron density of  $\rho = 10^{21} \text{ cm}^{-3}$  predicted a temperature rise of 274 °C that is accompanied by the generation of a thermoelastic pressure wave of 240 MPa compressive amplitude outside the laser focus.<sup>428</sup> This pressure is much higher than the saturated vapor pressure for this temperature (8.5 MPa). The tensile component of the thermoelastic stress wave determines whether the threshold for bubble formation is surpassed at the laser focus. We can conclude that the mechanical effects at the threshold for plasma-mediated soft-tissue ablation with femtosecond pulses are comparable to those accompanying stress-confined linear absorption.

Although high temperatures of several thousand Kelvin are reached within nanosecond and picosecond plasmas,<sup>460–462</sup> a thermally modified zone less than 0.2  $\mu\text{m}$  thick was found at the rim of ablation craters in corneal tissue, regardless of pulse duration.<sup>381,463</sup> The sharp delineation of the heated zone is due to the sharpness of the plasma boundary, owing to the nonlinearity of its formation and to the short time available for heat diffusion that is limited by rapid adiabatic cooling during the cavitation bubble expansion.<sup>381</sup>

Within the plasma, thermal degradation of the tissue is accompanied by chemical dissociation induced by the interaction of the free electrons with the biomolecules and water. Electrons with energies below 15 eV can initiate fragmentation of biomolecules via attachment of the incident electron. The electron attachment leads to the formation of a resonance, namely a transient molecular anionic state.<sup>428,464,465</sup> For a molecule XY, this process corresponds to  $XY + e^- \rightarrow XY^{*-}$ , where the  $XY^{*-}$  has a repulsive potential along the X–Y bond coordinate. The molecular anionic state can decay by electron detachment (leaving a vibrationally excited molecule) or by molecular dissociation along one or several specific bonds, such as  $XY^{*-} \rightarrow X^* + Y^-$ . Another chemical interaction mechanism was described by Nikogosyan and co-workers,<sup>466</sup> who analyzed the formation of  $\text{OH}^*$  and  $\text{H}_2\text{O}_2$  through various path-

ways following ionization and dissociation of water molecules. Both oxygen species are highly reactive and known to cause cell damage.<sup>467</sup> The dissociation of water molecules during femtosecond laser-induced plasma formation was confirmed by chemical analysis of the gas content of the bubbles produced at energies above the optical breakdown threshold.<sup>248</sup> The chemical processes within the breakdown region have little practical relevance for large radiant exposures that produce a high plasma energy density, because in such cases the tissue effects are dominated by disruptive thermomechanical effects. However, these chemical processes are of major importance for femtosecond plasmas with energy densities below the threshold for bubble formation. They enable highly localized chemically mediated ablation or dissection processes with little or no thermomechanical contribution.<sup>428</sup>

## G. Implications for Tissue Ablation

The use of plasma-mediated ablation and disruption that are based on nonlinear absorption makes it possible to perform surgery inside of transparent biological structures.<sup>30,410–416,456</sup>

Owing to the high energy density at nanosecond and picosecond durations and the inertial confinement inside of transparent structures, the precision of plasma-mediated effects is generally compromised by cavitation effects (section X.F). Therefore, plasma-mediated effects in bulk tissue are better suited for cutting and disruption than for ablation of large tissue volumes with sharply delineated boundaries.<sup>455</sup> The precision of plasma-mediated cutting can be optimized by various means: (a) use of a clean beam profile that provides the minimal possible spot size at any given focusing angle; (b) use of the largest possible focusing angle for each application, because it guarantees a small focal spot in both lateral and axial direction; (c) minimization of aberrations in the optical delivery system, including the contact lenses used for intraocular applications;<sup>468,469</sup> (d) use of ultrashort pulse durations to exploit the decrease of the optical breakdown threshold and the minimization of mechanical side effects observed with decreasing pulse duration; and (e) separation of subsequent application sites during pulse series such that the plasma production is not hindered by cavitation bubbles produced by previous pulses.<sup>414,470</sup>

The refinement of tissue effects with decreasing pulse duration has been demonstrated in various experimental studies<sup>412,414,419,458,471</sup> and is illustrated in Figure 56. When ultrashort laser pulses are



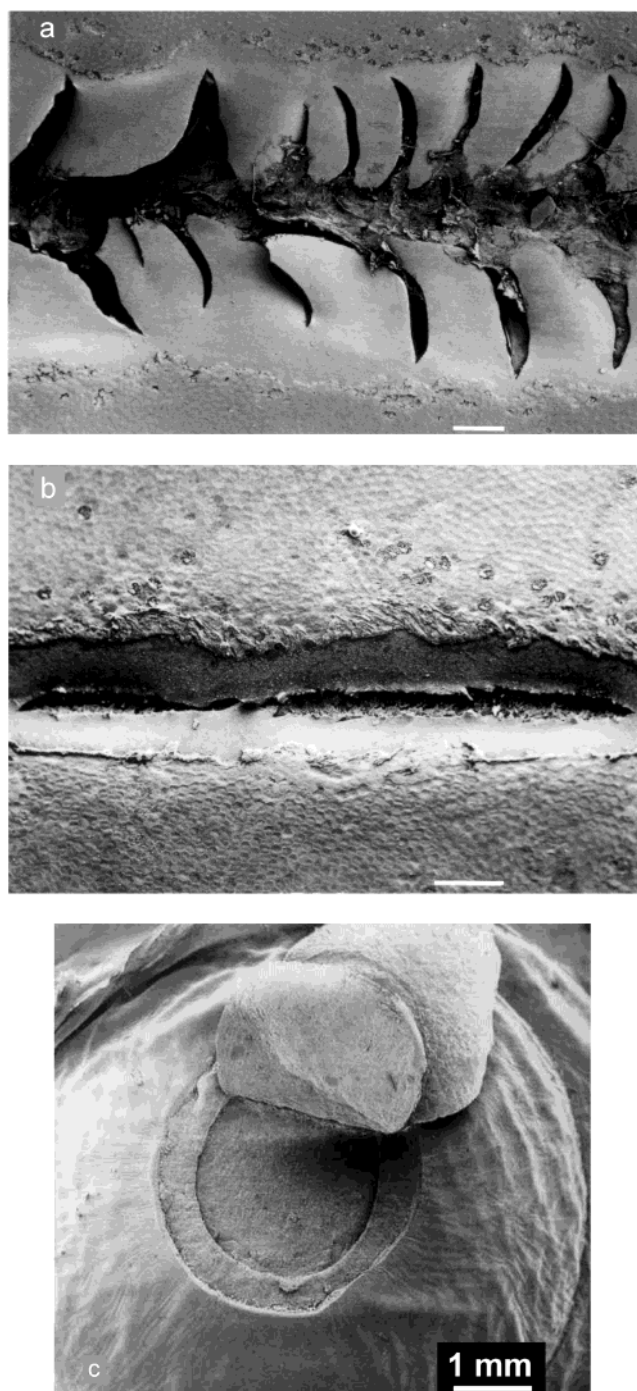


**Figure 56.** Refinement of plasma-mediated tissue effects using shorter laser pulses. (a) Cut in Descemet's membrane in the cornea produced by 6-ns laser pulses of 1064-nm wavelength. (b) Cut produced by 30-ps laser pulses. The scale bars are 100  $\mu\text{m}$  in length (Reprinted with permission from ref 419. Copyright 1994 Association for Research in Vision and Ophthalmology.) (c) Lenticule dissected out of the corneal stroma using 110-fs pulses at  $\lambda = 780$  nm wavelength. (Reprinted with permission from ref 414. Copyright 2002 SPIE.)

applied at a very large numerical aperture, it is possible to perform intranuclear chromosome dissection in living cells.<sup>415</sup> In this procedure, the material removal per pulse is less than  $0.1 \mu\text{m}^3$ . On the other hand, standard ophthalmic applications, such as iridotomies and capsulotomies, often take advantage of the disruptive mechanical effects accompanying

optical breakdown that are best achieved using nanosecond pulses.<sup>411</sup>

Plasma-mediated processes have also been applied for material removal at soft and hard tissue surfaces in air.<sup>10,414,463,472–474</sup> We showed in section X.D that the plasma absorption coefficients in bulk aqueous media are 2 orders of magnitude smaller than the linear tissue absorption coefficients for ArF excimer or Er:YAG laser radiation that are often used for surface ablation. Therefore, the desired precision of plasma-mediated ablation must be controlled by an appropriate choice of the focusing angle and pulse energy. Both parameters determine the growth of the plasma from the beam waist into the cone angle of the incoming laser beam. The ablation depth for femtosecond ablation of soft tissues was found to be relatively large (1.5–200  $\mu\text{m}$ ) when the laser radiation was focused to a spot size on the order of 20  $\mu\text{m}$ .<sup>454,463,473–475</sup> While the ablation depth could be reduced through the use of smaller spot sizes (i.e., a larger focusing angle) and very small pulse energies, the process would then involve a considerably longer processing time. Moreover, such a procedure would require a very precise tracking of the tissue surface in the axial direction of the laser beam, because the focal spot must be located exactly at the tissue surface to achieve precise ablation.

When the laser beam is only moderately focused, a tissue layer of up to 200  $\mu\text{m}$  thickness is ejected by the expansion of the plasma formed in the beam waist.<sup>454,474,475</sup> Because mechanical ejection is involved in the ablation process, the ablation depth depends on the ultimate tensile strength of the tissue. At equal radiant exposure and pulse duration, much smaller ablation rates have been observed for the mechanically resistant corneal stroma (1.5–10  $\mu\text{m}$  using 30-ps pulses<sup>463</sup> and 3–16  $\mu\text{m}$  using 140-fs pulses<sup>473</sup>) than for the much weaker neural tissue (50–200  $\mu\text{m}$  using 30-ps pulses<sup>475</sup> and 20–200  $\mu\text{m}$  using 140-fs-pulses.<sup>474</sup>

The strong nonlinear dependence of plasma electron density with irradiance, shown in Figures 51b and 52b, enables localized energy deposition in sharply delineated volumes. Therefore, large ablation depths can be achieved with little thermal damage in the residual tissue. Thermal side effects are almost negligible with single laser exposures, regardless of the laser pulse duration.<sup>381,463,474</sup> Even with nanosecond pulses, the thickness of the thermally damaged layer in corneal tissue remains  $<1 \mu\text{m}$ .<sup>381</sup> However, when ultrashort laser pulses are applied at high repetition rates, residual heat remaining in the nonablated tissue may accumulate and lead to larger zones of thermal damage if the laser beam is applied to a large spot and not laterally scanned during ablation.<sup>447,472,476</sup> This phenomenon is due to the continuous variation of free-electron density and thus energy density with irradiance for femtosecond pulse durations (Figure 52b). Thus, when femtosecond pulses are used, the target is heated in regions where the ablation threshold is not exceeded. When nanosecond pulses are used, the sharp drop of the electron density for irradiances below the optical breakdown threshold prevents heating of the non-

ablated tissue (Figure 51b).

The dependence of the ablation depth on radiant exposure was found to be logarithmic for corneal tissue.<sup>463</sup> The ablation efficiency for corneal tissue is thus highest close to the ablation threshold and decreases for higher radiant exposures.<sup>438,473</sup> This dependence is typical for a blow-off ablation process under conditions in which the spatial energy density profile in the tissue corresponds to Beer's law (section VII.A.1). Similar conditions may arise in plasma-mediated ablation due to the shielding of deeper tissue layers by the plasma produced at the surface. Remarkably, for neural tissue that is mechanically very weak, the variation of ablation depth with radiant exposure is not logarithmic but linear, and it is much larger than that for cornea.<sup>474</sup> An explanation is that the shielding-induced reduction of energy density in the depth of the tissue is, to a certain degree, counteracted by self-focusing and self-channeling, leading to filament formation beyond the location of the laser focus. This phenomenon was described theoretically first for laser beam propagation in air<sup>434,435</sup> but was also observed in fused silica,<sup>477</sup> water,<sup>30,379</sup> gelatin,<sup>478</sup> and in TEM pictures of femtosecond laser-irradiated cornea.<sup>414</sup> Because the filaments are much thinner than the diameter of the irradiated spot, they will be able to remove only tissue that is mechanically very weak. This could be responsible for the large ablation depth for neural tissue and the different scaling law with radiant exposure as compared to that for corneal tissue.

The most outstanding feature of plasma-mediated ablation is its ability to create ablation effects inside of tissues that are transparent at low irradiance. Plasma-mediated surface ablation of soft tissues, on the other hand, achieves relatively large etch depths with minimal thermal damage, which is an additional unique feature. For both applications, a minimization of mechanical collateral effects can be achieved by employing ultrashort laser pulses. However, if disruptive laser effects are desired, the use of nanosecond pulses is more effective.

## ***XI. Control of Precision, Thermal and Mechanical Damage, and Ablated Mass***

### **A. Control of Precision**

High precision of pulsed laser ablation implies a small ablation depth per pulse, together with minimal thermal and mechanical side effects. When linear absorption is utilized to deposit laser energy, high precision can be achieved by selecting a laser wavelength with a very small optical penetration depth, combined with a short pulse duration sufficient to provide thermal confinement (section IV.C). Moreover, irradiation under stress-confined conditions can further enhance precision, as the action of the thermoelastic stresses catalyzes the ablation process and lowers the ablation threshold and enthalpy (section V.G). This enables the removal of thinner tissue layers.

Precise ablation based on nonlinear absorption (plasma mediated ablation) requires the use of small pulse energies to minimize disruptive mechanical

effects. The lowest threshold energies for plasma formation are achieved by using ultrashort laser pulses focused at large numerical apertures. The use of ultrashort laser pulses also permits the creation of plasmas with low energy densities that produce minimal mechanical side effects. The combination of short pulse durations with large numerical apertures enables the production of tissue effects as small as  $0.1 \mu\text{m}^3$  (section X.G).

Energy deposition based on linear absorption is suitable only for surface ablation, whereas plasma-mediated processes enable the deposition of energy within materials that are transparent at low irradiances. Plasma-mediated surface ablation also offers large ablation depths with little collateral thermal damage. However, it requires focusing of the laser pulses exactly on the target surface, while linear absorption automatically restricts the laser-tissue interaction to the surface layer. Furthermore, when large areas or volumes are to be ablated, the use of plasma-mediated ablation would require a time-consuming scanning of the laser beam. By contrast, ablation based on linear absorption can be done over the entire area using a large laser beam with a sufficiently pulse energy.

### **B. Control of Thermal Side Effects**

The most direct strategy to control thermal side effects involves the selection of a pulse duration that is sufficiently short to minimize heat diffusion during the laser pulse from the volume of energy deposition into the nonablated tissue (eq 5). However, similar results may also be obtained when using longer pulses if the velocity of the ablation front during the laser pulse is comparable to or faster than the heat diffusion into the residual tissue. A theoretical analysis of this strategy was performed by Venugopalan and co-workers,<sup>176</sup> and experimental evidence for its validity was presented by various authors.<sup>196,313,314,479</sup>

Thermal side effects can be diminished further by selecting laser pulse durations that are sufficiently short to provide both stress and thermal confinement, because the lowering of the ablation enthalpy in the stress confinement regime reduces the residual heat in the tissue.<sup>394,406</sup> This is shown in Figure 57, where the thermal damage of ablation with free-running thulium laser pulses (thermally confined energy deposition) is compared to the damage zone produced by ablation using Q-switched thulium laser pulses (stress-confined and thermally confined energy deposition).

When multiple pulses are delivered to a single location, both the extent of the thermal damage zone and the degree of thermal damage are influenced by heat accumulation. The pulse repetition rate must be sufficiently low to avoid progressive accumulation of the residual heat within the tissue.<sup>24,314,472,480</sup> An alternative strategy to avoid heat accumulation involves scanning the laser beam in order to lengthen the time interval between subsequent exposures at each location within the ablated area.

On the other hand, the heat accumulation occurring when series of laser pulses are applied can be used intentionally to create a coagulation effect in



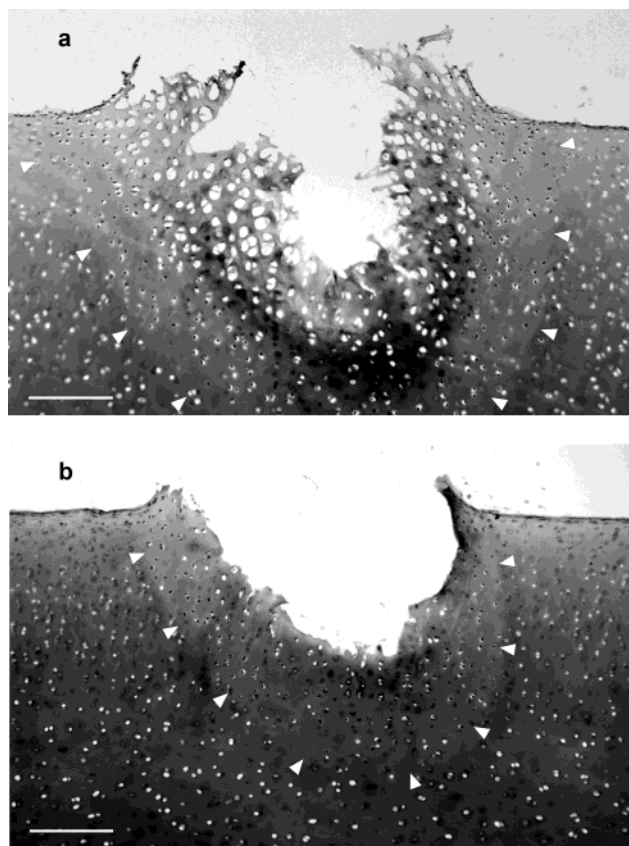


**Figure 57.** Histological sections through ablation craters produced in cartilage using (a) free-running thulium pulses ( $t_p = 200 \mu\text{s}$ ,  $E = 1000 \text{ mJ}$ ) and (b) multiply Q-switched thulium pulses ( $t_p = 100 \text{ ns}$ ,  $40 \text{ mJ} + 3 \times 100 \text{ mJ}$ ). Scale bars are  $200 \mu\text{m}$  in length. When compared to the multiply Q-switched pulses, the free-running laser pulse produces both a much larger thermal damage zone (arrows) and a more severe degree of damage. Bursts of Q-switched pulses create much smoother ablation craters than free-running pulses. (Reprinted with permission from ref 406. Copyright 2002 SPIE.)

conjunction with precise laser ablation. Since precise tissue ablation requires a short optical penetration depth and a short pulse duration, hemostasis is often not produced at the tissue surface. Hemostasis can be achieved by applying a series of sub-ablation threshold pulses with sufficiently high repetition rate.<sup>481</sup>

### C. Control of Mechanical Side Effects

For the range of radiant exposures that are used clinically, mechanical side effects are usually not a limiting factor for surface ablation in a gaseous environment (section VI.B). However, the situation is quite different for pulsed laser ablation in a liquid environment, where the confinement of the ablation products creates pressure transients with large amplitudes and cavitation effects that may result in large structural tissue deformation (section IX.B). One option to minimize cavitation effects without reducing the rate of mass removal is to use longer laser pulses, as this reduces the transduction of the laser pulse energy into cavitation bubble energy. However, the use of long laser pulses usually results in a smaller ablation efficiency than that obtained

using nanosecond pulses and also in a larger thermal damage zone. To avoid this limitation, Vogel and co-workers introduced a technique for the reduction of cavitation effects produced by short laser pulses.<sup>397,405,406</sup> A prepulse with small energy is followed by one or several ablation pulses with larger energy, separated by time intervals of  $50\text{--}100 \mu\text{s}$ . The prepulse produces a small cavitation bubble, which is then filled by the ablation products produced by the main pulses. In this manner, no additional cavitation effects are induced, and tissue tearing and other mechanical side effects are minimal. The reduction of the cavitation bubble size by a prepulse is shown in Figure 58. In addition, the transiently empty space created by the prepulse between the fiber tip and the tissue surface improves the optical transmission to the target and thus increases the ablation efficiency.

### D. Maximizing the Ablated Mass

The ablation models described in section VII.A predict that steady-state ablation will be more suitable for a removal of large amounts of material than ablation based on a blow-off process. This arises because the ablated mass scales linearly with radiant exposure in a steady-state ablation processes but logarithmically in a blow-off process. However, the difference between the two types of ablation process becomes less pronounced if shielding is considered. A steady-state process is most advantageous under conditions in which the absorption of the incident laser beam in the ablation plume is markedly smaller than the absorption in the corresponding layer of target tissue present in the blow-off situation. Very high ablation rates, such as that required for myocardial laser revascularization (TMR), in which a deep hole is drilled into the myocardium during one fraction of the systolic cycle, have been achieved using IR laser pulses with millisecond duration.<sup>400,408</sup>

The highest ablation efficiency for a given average laser power can be achieved by using a series of short pulses with high peak power instead of continuous or long-pulsed irradiation with pulse durations of hundreds of microseconds to milliseconds. When short pulses are employed, disruptive mechanical effects contribute to ablation, especially in a liquid environment, due to the high peak powers involved (sections VI.B.2 and IX.B). The generation of disruptive effects is particularly suitable for dissection procedures, in which precision and smoothness of the cut are less important than cutting efficiency.

### E. Selective Ablation

When the removal of tissue layers that exhibit pathologic changes from underlying healthy tissue (for example, burn eschar versus normal tissue; plaque versus artery wall) is desired, or when a sensitive tissue structure adjacent to the target structure must be protected (for example, neural tissue in microspinal surgery), it is necessary to confine the ablation to the target structure. Researchers first sought to achieve selective ablation by making use of intrinsic differences in the optical



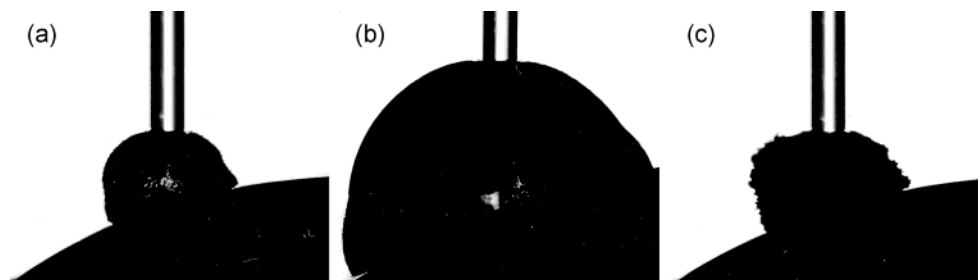


**Figure 58.** Use of a prepulse to reduce cavitation effects and ensure maximal light transmission to the tissue target. (a) Cavitation bubble produced by a single 40-mJ Q-switched thulium laser pulse. (b) Bubble produced by a 100-mJ pulse. (c) Bubble resulting from a 40-mJ prepulse, followed by a 100-mJ ablation pulse delivered after a time delay of 120  $\mu$ s. The use of a prepulse produces a bubble whose size is only one-ninth the volume produced when only a single ablation pulse is applied. (Reprinted with permission from ref 405. Copyright 2001 SPIE.)

properties of the tissues involved.<sup>482–484</sup> Later, online monitoring and active feedback techniques were introduced to discriminate between different tissue types and to automatically stop the ablation procedure when the transition between the layers is reached. Such techniques include the analysis of the acoustic transients in air generated during ablation,<sup>276,485–487</sup> fluorescence spectroscopy for discrimination between plaque and vessel wall,<sup>370</sup> plasma spectroscopy to distinguish between bone and nerve tissue,<sup>488</sup> and analysis of the cavitation bubble dynamics at the fiber tip for controlled sclera perforation in glaucoma surgery.<sup>374, 388</sup>

## XII. Outlook and Challenges

In this review, we have collected and organized information on the mechanisms of pulsed laser tissue ablation that until now was widely scattered in the scientific literature. We developed a framework to identify relevant mechanisms governing various laser ablation techniques that facilitates a rational selection of appropriate irradiation strategies for specific tasks. Nevertheless, much work remains to further improve the mechanistic understanding of pulsed laser ablation processes.

On the experimental side, further investigations are needed to better characterize both the changes of tissue properties during pulsed laser irradiation and the dynamics of tissue deformation, fracture, and material ejection. In our opinion, four points deserve particular attention. First, the strain rates that tissue is subject to during the ablation process approach  $10^5$ – $10^7$  s<sup>−1</sup>. Data that characterize the elastic and fracture properties under dynamic conditions have been obtained only on time scales that are longer by a minimum of 3 orders of magnitude. The knowledge of tissue mechanical properties on the appropriate time scales is essential for an accurate representation of the fracture dynamics and the phase change kinetics during ablation. Second, further work is necessary to characterize the denaturation kinetics of collagen and other structural tissue proteins on the nanosecond and microsecond time scales, as it influences the mechanical properties of the tissue matrix. Third, although both photoacoustic measurements and fast-frame photography have provided valuable qualitative and quantitative information regarding the dynamics of tissue deformation, frac-

ture, and material ejection, significant uncertainties remain regarding the timing of gaseous and particulate material ejection for both pulsed UV and IR laser ablation. Careful comparative studies are necessary to resolve apparent inconsistencies in the results obtained using photoacoustic and photographic techniques and to further clarify the reasons for the observed differences in pulsed UV and IR laser ablation. Fourth, investigators have performed tissue ablation using laser wavelengths at the amide I ( $\lambda = 6.1$   $\mu$ m) and amide II ( $\lambda = 6.45$   $\mu$ m) bands where the radiation is absorbed by *both* water *and* protein.<sup>489</sup> The simultaneous targeting of tissue water and the ECM may allow for both efficient and relatively damage-free ablation. Moreover, compact solid-state sources in this wavelength region are emerging. Much work remains to investigate both the dynamic optical properties and the detailed ablation dynamics using laser sources in the 6  $\mu$ m region.

On the modeling and computational side, work is necessary to integrate the present knowledge on the thermodynamics, kinetics, and hydrodynamics of pulsed laser ablation to build a functioning model of the entire process dynamics. The challenge is to devise models that link material removal with both the complex phase change processes (e.g., phase explosion, confined boiling, etc.) known to initiate material removal and the tissue mechanical properties that modulate the temperatures and pressures generated within the tissue prior to fracture. Moreover, once material removal is initiated, such models must consider that the recoil forces associated with ablation and the flow of the plume can themselves influence material removal. Such forces can be accurately modeled only if a full 3D model of the plume dynamics is implemented.

It is likely that the construction of a model that accommodates the considerations mentioned above necessitates a computational rather than an analytical approach. The validity of results obtained through such an approach depends critically upon the accuracy with which the computational model represents tissue properties and considers the possible photothermal, photomechanical, and photochemical pathways for phase change and material failure. Sophisticated computational codes that have already been developed<sup>490</sup> must be re-evaluated and modified to faithfully represent the composite structure of biological tissues and accommodate the changes in

the mechanical and optical tissue properties that are altered during the course of the ablation process.

Molecular dynamics (MD) simulations offer a promising alternate approach that may provide valuable insights into the pulsed laser ablation process. MD simulations relieve the investigator from having to develop realistic macroscopic equations that govern the dynamics of the various processes. Instead, the burden is shifted to developing relationships that accurately represent intermolecular interactions, molecular excitation, and intermolecular energy transfer within a given system. By tracking the equations of motion of this system, MD simulations have revealed much of the complex behavior involved in pulsed laser ablation with subnanosecond resolution.

However, many compromises have been made in the construction of such simulations. First, to make the computation tractable, the MD simulations of laser ablation do not model the material on an atomic level but instead adopt a "breathing sphere" model in which a group of atoms is treated as a unit.<sup>339</sup> This simplification provides a realistic rate of vibrational relaxation of excited molecules but only approximately treats internal atomic motions. While this simplification enables the MD simulations to simulate the time evolution of much larger groups of molecules over longer time scales, the effects of such a simplification on the accuracy of the predicted ablation dynamics remains an open question. Second, the organic solids modeled thus far possess extremely simple properties and are far from representing the molecular diversity and complexity of molecular interactions present in a composite biological tissue. Third, MD simulations have thus far only considered the case of instantaneous energy deposition and have not simulated the more common case of laser energy deposition during the laser ablation process. In this regard, these simulations must accommodate the dynamic changes in the optical and mechanical properties of the tissue as well as possible shielding of the incoming laser energy by the ablation products. Once such requirements are met, one must be able to relate the predictions of MD simulations that are applicable on a microscopic scale to those given by more macroscopic thermodynamic and hydrodynamic codes. If such capabilities could be developed, analytic modeling combined with hydrodynamic codes and MD simulations may be able to provide the information necessary to characterize the dynamics of pulsed laser tissue ablation with high spatial ( $\sim 10$  nm) and temporal ( $< 1$  ns) resolutions and may enable direct comparison with time-resolved experimental investigations.

### XIII. Acknowledgment

We thank our mentors, collaborators, colleagues, and students who have contributed to our activities and have made research in this area enjoyable and stimulating. For support of our research, we thank the Deutsche Forschungsgemeinschaft, the German Bundesministerium für Bildung und Forschung, the U.S. Department of Defense, Medical Free Electron Laser Program, and the National Center for Research Resources of the U.S. National Institutes of Health.

### XIV. References

- (1) Solon, L. R.; Aronson, R.; Gould, G. *Science* **1961**, *134*, 1506.
- (2) Zaret, M.; Breinin, G. M.; Schmidt, H.; Rippes, H.; Siegel, I. M.; Solon, L. R. *Science* **1961**, *134*, 1525.
- (3) Campbell, C. J.; Noyori, K. S.; Koester, C. J.; Rittler, M. C. *Acta Ophthalmol.* **1962**, *S76*, 22.
- (4) Goldman, L.; Blaney, D. J.; Kindel, D. J.; Franke, E. A. *J. Invest. Dermatol.* **1963**, *40*, 122.
- (5) Zweng, H. C.; Flocks, M.; Peppers, N. A.; Kapany, N. S.; Silbert, R. N. *Am. J. Ophthalmol.* **1964**, *58*, 353.
- (6) L'Esperance, F. A. *Trans. Am. Ophthalmol. Soc.* **1968**, *66*, 827.
- (7) Krasnov, M. M. *Am. J. Ophthalmol.* **1973**, *75*, 674.
- (8) Krauss, J. M.; Puliafito, C. A.; Steinert, R. F. *Surv. Ophthalmol.* **1986**, *31*, 37.
- (9) Welch, A. J., van Gemert, M. J. C., Eds. *Optical-Thermal Response of Laser-Irradiated Tissue*; Plenum Press: New York, 1995.
- (10) Niemz, M. H. *Laser-Tissue Interactions. Fundamentals and Applications*, 2nd ed.; Springer: Berlin, 2002.
- (11) Waynant, R. W., Ed. *Lasers in Medicine*; CRC Press: Boca Raton, FL, 2002.
- (12) Ready, J. F. *Effects of High-Power Laser Radiation*; Academic Press: Orlando, 1971.
- (13) Bäuerle, D. *Laser Processing and Chemistry*; Springer: Berlin, 2000.
- (14) Hillenkamp, F. In *Lasers in Biology and Medicine*; Hillenkamp, F., Pratesi, R., Sacchi, C. A., Eds.; NATO Advanced Study Institutes Series A34; Plenum Press: New York, 1980; p 37.
- (15) Jacques, S. *Surg. Clin. N. Am.* **1992**, *72*, 531.
- (16) Srinivasan, R. *Science* **1986**, *234*, 559.
- (17) Srinivasan, R.; Braren, B. *Chem. Rev.* **1989**, *89*, 1303.
- (18) Pettit, G. H. In *Lasers in Medicine*; Waynant, R. W., Ed.; CRC Press: Boca Raton, FL, 2002; p 109.
- (19) Boulnois, J. L. *Lasers Med. Sci.* **1985**, *1*, 47.
- (20) McKenzie, A. L. *Phys. Med. Biol.* **1990**, *35*, 1175.
- (21) Verdaasdonk, R. M. In *Advances in Lasers and Applications*; Finlayson, D. M., Sinclair, B. D., Eds.; Institute of Physics Publishing: Bristol, UK, 1999; p 181.
- (22) Marshall, J. *Eye* **1988**, *2*, S98.
- (23) Krueger, R. R.; Binder, P. S.; McDonnell, P. J. In *Corneal Laser Surgery*; Salz, J. J. Ed.; Mosby: St. Louis, 1995; p 11.
- (24) Müller, G.; Dörschel, K.; Kar, H. *Lasers Med. Sci.* **1991**, *6*, 241.
- (25) Oraevsky, A. A.; Esenaliev, R. O.; Letokhov, V. S. In *Laser Ablation, Mechanism and Applications*; Miller, J. Ed.; Springer: New York, 1991; p 112.
- (26) van Leeuwen, T.; Jansen, E. D.; Motamedi, M.; Borst, C.; Welch, A. J. In *Optical-Thermal Response of Laser-Irradiated Tissue*; Welch, A. J., van Gemert, M. J. C., Eds.; Plenum Press: New York, 1995; p 709.
- (27) Walsh, J. T. Pulsed laser angioplasty: a paradigm for tissue ablation. In *Optical-Thermal Response of Laser-Irradiated Tissue*; Welch, A. J., van Gemert, M. J. C., Eds.; Plenum Press: New York, 1995; p 865.
- (28) Gitomer, S. J.; Jones, R. D. *IEEE Trans. Plasma Sci.* **1991**, *19*, 1209.
- (29) Vogel, A. *Phys. Med. Biol.* **1997**, *42*, 895.
- (30) Vogel, A. *Optical Breakdown in Water and Ocular Media, and its Use for Intraocular Photodisruption*; Shaker: Aachen, 2001.
- (31) Alberts, B.; Bray, D.; Lewis, J.; Raff, M.; Roberts, K.; Watson, J. D. *Molecular Biology of the Cell*; Garland Press: New York, 1994.
- (32) Parry, D. A. D.; Craig, A. S. In *Ultrastructure of the Connective Tissue Matrix*; Ruggeri, A., Motta, P. M. Eds.; Martinus Nijhoff Publishers: Boston, 1984; p 34.
- (33) Silver, F. H. *Biological materials: Structure, Mechanical Properties, and Modeling of Soft Tissue*; New York University Press: New York, 1987.
- (34) Yannas, I. V. *J. Macromol. Sci.-Rev. Macromol. Chem.* **1972**, *C7*, 49.
- (35) Nimni, M. E.; Harkness, R. D. In *Collagen. Vol. I, Biochemistry*; Nimni, M. E., Ed.; CRC Press: Boca Raton, FL, 1988; p 1.
- (36) Junquiera, L. C.; Carneiro, J. *Histologie*, 4th ed.; Springer: Heidelberg, 1996.
- (37) Thomsen, S. *Photochem. Photobiol.* **1991**, *53*, 825.
- (38) Berman, E. R. *Biochemistry of the Eye*; Plenum Press: New York, 1991; p 89.
- (39) Jacobovic, H. R.; Ackerman, A. B. In *Dermatology, Vol. 1*; Moschella, S. L., Hurley, H. J., Eds.; Saunders: Philadelphia, 1985; p 1.
- (40) Linsenmayer, T. F. In *Cell Biology of Extracellular Matrix*, 2nd ed.; Hay, E. D., Ed.; Plenum Press: New York, 1991; p 7.
- (41) Eady, R. A. J.; Leigh, I. M.; Pope, F. M. In *Rook/Wilkinson/Ebling Textbook of Dermatology*, 6th ed.; Champion, R. H., Burton, J. L., Burns, D. A., Breathnach, S. M., Eds.; Blackwell Science: Oxford, 1998; p 37.
- (42) Claire, K.; Pecora, R. *J. Phys. Chem.* **1997**, *101*, 746.



- (43) Stryer, L. *Biochemistry*; W. H. Freeman and Co.: San Francisco, 1987.
- (44) Smith, L. T.; Holbrook, K. A.; Byers, P. H. *J. Invest. Dermatol.* **1982**, *79*, 93s.
- (45) Zimmermann, D. R.; Fischer, R. W.; Winterhalter, K. H.; Witmer, R.; Vaughan, L. *Exp. Eye Res.* **1988**, *46*, 431.
- (46) Birk, D. E.; Silver, F. H.; Trelstad, R. L.; Matrix Assembly. In *Cell Biology of Extracellular Matrix*, 2nd ed.; Hay, E. D., Ed.; Plenum Press: New York, 1991; p 221.
- (47) Cintron, C.; Burrows, R. *Invest. Ophthalmol. Vis. Sci.* **1997**, *38*, S682.
- (48) Daxer, A.; Misof, K.; Grabner, B.; Ettl, A.; Fratzl, P. *Invest. Ophthalmol. Vis. Sci.* **1998**, *39*, 644.
- (49) Maurice, D. M. In *The Eye*, Vol. 1; Davson, H., Ed.; Academic Press: New York, 1962; p 289.
- (50) Benedek, G. B. *Appl. Opt.* **1971**, *10*, 459.
- (51) Nomura, S.; Hiltner, A.; Lando, J. B.; Baer, E. *Biopolymers*. **1977**, *16*, 231.
- (52) Walsh, J. T.; Deutsch, T. F. *IEEE Trans. Biomed. Eng.* **1989**, *36*, 1195.
- (53) Yamada, H. *Strength of Biological Materials*; Robert E. Krieger Publishing Co.: Huntington, NY, 1970.
- (54) Duck, F. A. *Physical Properties of Tissue*; Academic Press: London, 1990.
- (55) Vogel, H. G. *Biophys. Acta* **1972**, *286*, 79.
- (56) Haut, R. C. *Trans. ASME Biomed. Eng.* **1989**, *111*, 136.
- (57) Dombi, G. W.; Haut, R. C.; Sullivan, W. G. *J. Surg. Res.* **1993**, *54*, 21.
- (58) Allain, J. C.; Le Lous, M.; Cohen-Solal, L.; Bazin, S.; Maroteaux, P. *Connect. Tissue Res.* **1980**, *7*, 127.
- (59) Kampmeier, J.; Radd, B.; Birngruber, R.; Brinkmann, R. *Cornea* **2000**, *19*, 355.
- (60) Burdzhanaadze, T. V.; Tiktupulo, E. I.; Privalov, P. L. *Dokl. Akad. Nauk. SSSR* **1987**, *293*, 720.
- (61) Burdzhanaadze, T. V.; Bezhitadze, M. O. *Biofizika* **1988**, *33*, 220.
- (62) McLain, P. E.; Wiley, E. R. *J. Biol. Chem.* **1972**, *247*, 692.
- (63) Asiy-Vogel, M. N.; Brinkmann, R.; Notbohm, H.; Eggers, R.; Lubatschowski, H.; Laqua, H.; Vogel, A. *J. Cataract Refract. Surg.* **1997**, *23*, 515.
- (64) Le Lous, M.; Allain, J. C.; Bazin, S.; Maroteaux, P. *Ann. Biol. Clin.* **1981**, *39*, 165.
- (65) Le Lous, M.; Flandin, F.; Herbage, D.; Allain, J. C. *Biophys. Acta* **1982**, *717*, 295.
- (66) Le Lous, M.; Allain, J. C.; Cohen-Solal, L.; Maroteaux, P. *Connect. Tissue Res.* **1983**, *11*, 199.
- (67) Henriques, F. C. *Arch. Pathol.* **1947**, *43*, 489.
- (68) Joly, M. A. *Physico-chemical Approach to the Denaturation of Proteins*; Academic Press: London, 1965.
- (69) Johnson, F. H.; Eyring, H.; Stover, B. J. *The Theory of Rate Processes in Biology and Medicine*; Wiley: New York, 1974.
- (70) Pearce, J.; Thomsen, S. In *Optical-Thermal Response of Laser-Irradiated Tissue*; Welch, A. J., Van Gemert, M., Eds.; Plenum Press: New York, 1995; p 561.
- (71) Birngruber, R.; Hillenkamp, F.; Gabel, V. P. *Health Phys.* **1985**, *48*, 781.
- (72) Brinkmann, R.; Kampmeier, J.; Grotehusmann, U.; Vogel, A.; Koop, N.; Asiy-Vogel, M.; Birngruber, R. *Proc. SPIE* **1996**, *2681*, 56.
- (73) Chang, J.; Söderberg, P. G.; Denham, D.; Nose, I.; Lee, W.; Parel, J. M. *Proc. SPIE* **1996**, *2673*, 70.
- (74) Flory, P. J.; Garret, R. R. *J. Am. Chem. Soc.* **1958**, *80*, 4836.
- (75) Diamant, J.; Keller, A.; Baer, E.; Litt, M.; Arbridge, R. G. C. *Proc. R. Soc. London B* **1972**, *180*, 293.
- (76) Harris, D. M.; Fried, D.; Reinisch, L.; Bell, T.; Schlichter, D.; From, L.; Burkart, J. *Lasers Surg. Med.* **1999**, *25*, 107.
- (77) Coohill, T. P. In *Lasers in Medicine*; Waynant, R. W., Ed.; CRC Press: Boca Raton, FL, 2002; p 85.
- (78) Dyer, P. E.; Al-Dhahir, R. K. *Proc. SPIE* **1990**, *1202*, 46.
- (79) Prael, S. A.; Vitkin, I. A.; Brüggemann, U.; Wilson, B. C.; Anderson, R. R. *Phys. Med. Biol.* **1992**, *37*, 1203.
- (80) Oraevsky, A. A.; Jacques, S. L.; Tittel, F. K. *Appl. Opt.* **1997**, *36*, 402.
- (81) Yablon, A. D.; Nishioka, N. S.; Mikić, B. B.; Venugopalan, V. *Appl. Opt.* **1999**, *38*, 1259.
- (82) Dark, M. L.; Perelman, L. T.; Itzkan, I.; Schaffer, J. L.; Feld, M. S. *Phys. Med. Biol.* **2000**, *45*, 529.
- (83) Cheong, W.-F. In *Optical-Thermal Response of Laser-Irradiated Tissue*; Welch, A. J., van Gemert, M. J. C., Eds.; Plenum Press: New York, 1995; p 275.
- (84) Jagger, J. *Introduction to Research in Ultraviolet Photobiology*; Prentice-Hall: Englewood Cliffs, NJ, 1967.
- (85) Grand, D.; Bernas, A.; Amouyal, E. *Chem Phys.* **1979**, *44*, 73.
- (86) Painter, L. R.; Hamm, R. N.; Arakawa, E. T.; Birkhoff, R. D. *Phys. Rev. Lett.* **1968**, *21*, 282.
- (87) Williams, F.; Varama, S. P.; Hillenius, S. *J. Chem. Phys.* **1976**, *64*, 1549.
- (88) Wetlaufer, D. B. In *Advances in Protein Chemistry*, Vol. 17; Anfinsen, C. B., Jr.; Anson, M. L.; Bailey, K., Eds.; Academic Press: New York, 1962; p 304.
- (89) Pettit, G. H.; Ediger, M. N. *Appl. Opt.* **1996**, *35*, 3386.
- (90) Kollias, N.; Baqer, A. *J. Soc. Cosmet. Chem.* **1988**, *39*, 347.
- (91) Jacques, S. L.; Glickman, R. D.; Schwartz, J. A. *Proc. SPIE* **1996**, *2681*, 468.
- (92) Glickman, R. D.; Jacques, S. L.; Hall, R. M.; Kumar, N. *Proc. SPIE* **2001**, *4257*, 134.
- (93) Prael, S. A., <http://omlc.ogi.edu/spectra/hemoglobin/> (1999).
- (94) Wray, S.; Cope, M.; Delpy, D. T.; Wyatt, J. S.; Reynolds, E. O. R. *Biophys. Acta* **1988**, *933*, 184.
- (95) Kollias, N.; Baqer, A. *J. Invest. Derm.* **1985**, *85*, 38.
- (96) Wolbarsht, M. L.; Walsh, A. W.; George, G. *Appl. Opt.* **1981**, *20*, 2184.
- (97) Kollias, N.; Sayre, R. M.; Zeise, L.; Chedekel, M. R. *J. Photochem. Photobiol. B: Biol.* **1991**, *9*, 135.
- (98) Sardar, D. K.; Mayo, M. L.; Glickman, R. D. *J. Biomed. Opt.* **2001**, *6*, 404.
- (99) Wilson, E. B., Jr.; Decius, J. C.; Cross, P. C. *Molecular Vibrations: The Theory of Infrared and Raman Vibrational Spectra*; Dover Publications: New York, 1980.
- (100) Downing, H. D.; Williams, D. J. *Geophys. Res.* **1975**, *80*, 1656.
- (101) Hale, G. M.; Querry, M. R. *Appl. Opt.* **1973**, *12*, 555.
- (102) Harris, D. C.; Bertolucci, M. D. *Symmetry and Spectroscopy: An Introduction to Vibrational and Electronic Spectroscopy*; Dover Publications: New York, 1990.
- (103) Jacques, S. *Appl. Opt.* **1993**, *32*, 2447.
- (104) Saidi, I. S.; Jacques, S. L.; Tittel, F. K. *Appl. Opt.* **1995**, *34*, 7410.
- (105) Dunn, A. K.; Richards-Kortum, R. *IEEE J. Sel. Top. Quantum Electron.* **1996**, *2*, 898.
- (106) Schmitt, J. M.; Kumar, G. *Opt. Lett.* **1996**, *21*, 1310.
- (107) Schmitt, J. M.; Kumar, G. *Appl. Opt.* **1998**, *21*, 2788.
- (108) Wang, R. K. *J. Mod. Opt.* **2000**, *47*, 103.
- (109) Mourant, J. R.; Johnson, T. M.; Guerra, A.; Aida, T.; Freyer, J. P. *J. Biomed. Opt.* **2002**, *7*, 378.
- (110) Goldman, J. N.; Benedek, G. B. *Invest. Ophthalmol.* **1967**, *6*, 574.
- (111) Doornbos, R. M. P.; Lang, R.; Aalders, M. C.; Cross, F. W.; Sterenborg, H. J. C. M. *Phys. Med. Biol.* **1999**, *44*, 967.
- (112) Troy, T. L.; Thennadil, S. N. *J. Biomed. Opt.* **2001**, *6*, 167.
- (113) Hielscher, A. H.; Alcouffe, R. E.; Barbour, R. L. *Phys. Med. Biol.* **1998**, *43*, 1285.
- (114) Star, W. M. *Phys. Med. Biol.* **1997**, *42*, 763.
- (115) Jaywant, S.; Wilson, B.; Patterson, M. S.; Lilge, L.; Flotte, T. J.; Woolsey, J.; McColloch, C. *Proc. SPIE* **1993**, *1882*, 218.
- (116) Nau, W. H.; Roselli, R. J.; Milam, D. F. *Lasers Surg. Med.* **1999**, *24*, 38.
- (117) Ritz, J.-P.; Roggan, A.; Isbert, C.; Müller, G.; Buhr, H. J.; Germer, C.-T. *Lasers Surg. Med.* **2001**, *29*, 205.
- (118) Walsh, J. T.; Flotte, T. J.; Deutsch, T. F. *Lasers Surg. Med.* **1989**, *9*, 314.
- (119) Walsh, J. T.; Deutsch, T. F. *Lasers Surg. Med.* **1989**, *9*, 327.
- (120) Nishioka, N. S.; Domankevitz, Y. *Lasers Surg. Med.* **1989**, *9*, 375.
- (121) Ren, Q.; Venugopalan, V.; Schomacker, K.; Deutsch, T. F.; Flotte, T. J.; Puliafito, C. A.; Birngruber, R. *Lasers Surg. Med.* **1992**, *12*, 274.
- (122) Schomacker, K. T.; Domankevitz, Y.; Flotte, T. J.; Deutsch, T. F. *Lasers Surg. Med.* **1991**, *11*, 141.
- (123) Fishman, E. *Appl. Opt.* **1962**, *1*, 493.
- (124) Vodopyanov, K. L. *J. Chem. Phys.* **1991**, *94*, 5389.
- (125) Cummings, J. P.; Walsh, J. T. *Appl. Phys. Lett.* **1993**, *62*, 1988.
- (126) Furzikov, N. P. *Proc. SPIE* **1992**, *1646*, 172.
- (127) Jansen, E. D.; van Leeuwen, T. G.; Motamedi, M.; Borst, C.; Welch, A. J. *Lasers Surg. Med.* **1994**, *14*, 258.
- (128) Walsh, J. T.; Cummings, J. P. *Lasers Surg. Med.* **1994**, *15*, 295.
- (129) Shori, R.; Walston, A. A.; Stafsudd, O. M.; Fried, D.; Walsh, J. T. *IEEE J. Sel. Top. Quantum Electron.* **2002**, *7*, 959.
- (130) Lange, B. I.; Brendel, T.; Hüttmann, G. *Appl. Opt.* **2002**, *41*, 5797.
- (131) Ediger, M. N.; Pettit, G. H.; Weiblinger, R. P.; Chen, C. H. *Lasers Surg. Med.* **1993**, *13*, 204.
- (132) Ediger, M. N.; Pettit, G. H.; Hahn, D. W. *Lasers Surg. Med.* **1994**, *15*, 107.
- (133) Staveteig, P. T.; Walsh, J. T. *Appl. Opt.* **1996**, *35*, 3392.
- (134) Carslaw, H. S.; Jaeger, J. C. *Conduction of Heat in Solids*, 2nd ed.; Oxford University Press: Oxford, 1959.
- (135) Anderson, R. R.; Parrish, J. A. *Science* **1983**, *220*, 524.
- (136) Venugopalan, V. *Proc. SPIE* **1995**, *2391*, 184.
- (137) Venugopalan, V.; Nishioka, N. S.; Mikić, B. B. *Biophys. J.* **1996**, *70*, 2981.
- (138) Carome, E. F.; Clark, N. A.; Moeller, C. E. *Appl. Phys. Lett.* **1964**, *4*, 95.
- (139) Bushnell, J. C.; McCloskey, D. J. *J. Appl. Phys.* **1968**, *39*, 5541.
- (140) Sigrist, M. W. *J. Appl. Phys.* **1986**, *60*, R83.
- (141) Dingus, R. S.; Scammon, R. J. *Proc. SPIE* **1991**, *1427*, 45.
- (142) Gusev, V. E.; Karabutov, A. A. *Laser Optoacoustics*; American Institute of Physics: New York, 1993.
- (143) Paltauf, G.; Schmidt-Kloiber, H. *Appl. Phys. A* **1996**, *62*, 303.
- (144) Callen, H. B. *Thermodynamics and an Introduction to Thermostatistics*; John Wiley & Sons: New York, 1985.
- (145) Venugopalan, V.; Zweig, A. D.; Deutsch, T. F.; Nishioka, N. S.; Mikić, B. B. *Proc. SPIE* **1993**, *1886*, 102.



- (146) Cross, F. W.; Al-Dhahir, R. K.; Dyer, P. E.; MacRobert, A. J. *Appl. Phys. Lett.* **1987**, *50*, 1019.
- (147) Burmistrova, L. V.; Karabutov, A. A.; Rudenko, O. V.; Cherepet-skaya, E. B. *Sov. Phys. Acoust.* **1979**, *25*, 348.
- (148) Lyamshev, L. M.; Naugol'nykh, K. A. *Sov. Phys. Acoust.* **1981**, *27*, 357.
- (149) Schuele, G.; Huettmann, G.; Brinkmann, R. *Proc. SPIE* **2002**, *4611*, 64.
- (150) Venugopalan, V.; Nishioka, N. S.; Mikić, B. B. *Biophys. J.* **1995**, *69*, 1259.
- (151) Frenz, M.; Paltauf, G.; Schmidt-Kloiber, H. *Phys. Rev. Lett.* **1996**, *76*, 3546.
- (152) Paltauf, G.; Schmidt-Kloiber, H.; Frenz, M. *J. Acoust. Soc. Am.* **1998**, *104*, 890.
- (153) Paltauf, G.; Schmidt-Kloiber, H. *Appl. Phys. A* **1999**, *68*, 525.
- (154) Albagli, D.; Dark, M.; Perelman, L. T.; von Rosenberg, C.; Itzkan, I.; Feld, M. S. *Opt. Lett.* **1994**, *19*, 1684.
- (155) Albagli, D.; Dark, M.; von Rosenberg, C.; Perelman, L.; Itzkan, I.; Feld, M. S. *Med. Phys.* **1994**, *21*, 1323.
- (156) Itzkan, I.; Albagli, D.; Dark, M. L.; Perelman, L. T.; von Rosenberg, C.; Feld, M. *Proc. Natl. Acad. Sci. U.S.A.* **1995**, *92*, 1960.
- (157) Pini, R.; Rossi, F.; Salimbeni, S.; Siano, S.; Vannini, M.; Carones, F.; Trabucchi, G.; Brancato, R.; Gobbi, P. G. *Proc. SPIE* **1996**, *2632*, 25.
- (158) Debenedetti, P. *Metastable Liquids: Concepts and Principles*; Princeton University Press: Princeton, NJ, 1996.
- (159) Skripov, V. P. *Metastable Liquids*; Wiley: New York, 1974.
- (160) Skripov, V. P.; Sinityn, E. N.; Pavlov, P. A.; Ermakov, G. V.; Muratov, G. N.; Bulanov, N. V.; Baidakov, V. G. *Thermophysical properties of liquids in the metastable (superheated) state*; Gordon and Breach Science Publishers: New York, 1988.
- (161) Beegle, B. L.; Modell, M.; Reid, R. C. *Am. Inst. Chem. Eng. J.* **1974**, *20*, 1200.
- (162) Blander, M.; Katz, J. L. *AIChE J.* **1975**, *21*, 833.
- (163) Reid, S. C. *Am. Sci.* **1976**, *64*, 146.
- (164) Miotello, A.; Kelly, R. *Appl. Phys. Lett.* **1995**, *67*, 3535.
- (165) Miotello, A.; Kelly, R. *Appl. Phys. A* **1999**, *69*, S67.
- (166) Afanas'ev, Yu. V.; Krokhin, O. N. *Sov. Phys. JETP* **1967**, *25*, 639.
- (167) Krokhin, O. N. In *Physics of High Energy Density*; Caldirola, P., Knoefel, H., Eds.; Academic Press: New York, 1971; p 278.
- (168) Krokhin, O. N. In *Laser Handbook*; Arecchi, F. T., Schulz-DuBois, E. O., Eds.; North-Holland Pub. Co.: New York, 1972; p 1371.
- (169) Knight, C. J. *AIAA J.* **1979**, *17*, 519.
- (170) Knight, C. J. *AIAA J.* **1982**, *20*, 950.
- (171) Kelly, R.; Braren, B. *Appl. Phys. B* **1991**, *53*, 160.
- (172) Schrage, R. W. *A Theoretical Study of Interphase Mass Transfer*; Columbia University Press: New York, 1953.
- (173) Yablon, A. D.; Nishioka, N. S.; Mikić, B. B.; Venugopalan, V. *Proc. SPIE* **1998**, *3343*, 69.
- (174) Brennen, C. E. *Cavitation and Bubble Dynamics*; Oxford University Press: Oxford, 1995.
- (175) Frenkel, I. I. *Kinetic theory of liquids*; Dover Publications: New York, 1955.
- (176) Venugopalan, V.; Nishioka, N. S.; Mikić, B. B. *Trans. ASME J. Biomech. Eng.* **1994**, *116*, 62.
- (177) Olmes, A.; Franke, H. G.; Bänsch, E.; Lubatschowski, H.; Raible, M.; Dziuk, G.; Ertmer, W. *Appl. Phys. B* **1997**, *65*, 659.
- (178) Gibbs, J. W. *The Scientific Papers of J. Willard Gibbs, Volume I, Thermodynamics*; Dover Publications: New York, 1961.
- (179) Martynyuk, M. M. *Sov. Phys. Technol. Phys.* **1974**, *19*, 793.
- (180) Martynyuk, M. M. *Combust. Explos. Shock Waves* **1977**, *13*, 178.
- (181) Apfel, R. E. *Nature Phys. Sci.* **1972**, *238*, 63.
- (182) aus der Wiesche, S.; Rembe, C.; Hofer, E. P. *Heat Mass Transfer* **1999**, *35*, 143.
- (183) Lienhard, J. H. A. *Heat Transfer Textbook*, 2nd ed.; Prentice-Hall: Englewood Cliffs, NJ, 1987.
- (184) Briggs, L. J. *J. Appl. Phys.* **1950**, *21*, 721.
- (185) Roedder, E. *Science* **1967**, *155*, 1413.
- (186) Zheng, Q.; Durben, D. J.; Wolf, G. H.; Angell, C. A. *Science* **1991**, *254*, 829.
- (187) Temperley, H. N. V. *Proc. Phys. Soc. London* **1947**, *59*, 199.
- (188) Speedy, R. J. *Phys. Chem.* **1982**, *86*, 3002.
- (189) Kwak, H.-Y.; Panton, R. L. *J. Phys. D: Appl. Phys.* **1985**, *18*, 647.
- (190) Dmitriev, A. C.; Furzikov, N. P. *Nuovo Cimento D* **1988**, *10D*, 1511.
- (191) Dmitriev, A. K.; Furzikov, N. P. *Izv. Akad. Nauk Ser. Fiz.* **1989**, *53*, 1105.
- (192) Dmitriev, A. K.; Furzikov, N. P. *Sov. Phys. Acoust. USSR* **1990**, *36*, 568.
- (193) Mikić, B. B.; Rohsenow, W. M.; Griffith, P. *Int. J. Heat Mass Transfer* **1970**, *13*, 657.
- (194) Venugopalan, V.; Nishioka, N. S.; Mikić, B. B. *Biophys. J.* **1996**, *71*, 3530.
- (195) Esenaliev, R. O.; Karabutov, A. A.; Podymova, N. B.; Letokhov, V. S. *Appl. Phys. B* **1994**, *59*, 73.
- (196) Hibst, R.; Kaufmann, R. *Lasers Med. Sci.* **1991**, *6*, 391.
- (197) Majaron, B.; Plestenjak, P.; Lukac, M. *Appl. Phys. B* **1999**, *69*, 71.
- (198) Verdaasdonk, R. M.; Borst, C.; van Germert, M. J. C. *Phys. Med. Biol.* **1990**, *35*, 1129.
- (199) LeCarpentier, G. L.; Motamedi, M.; McMath L. P.; Rastegar, S.; Welch, A. J. *IEEE Trans. Biomed. Eng.* **1993**, *40*, 188.
- (200) Kim, D.; Ye, M.; Grigoropoulos, C. P. *Appl. Phys. A* **1998**, *67*, 169.
- (201) Curran, D. R.; Seaman, L.; Shockey, D. A. *Phys. Rep.* **1987**, *147*, 254.
- (202) Grady, D. E. *J. Mech. Phys. Solids* **1988**, *36*, 353.
- (203) Oraevsky, A. A.; Jacques, S. L.; Tittel, F. K. *J. Appl. Phys.* **1995**, *78*, 1281.
- (204) Oraevsky, A. A.; Jacques, S. L.; Esenaliev, R. O.; Tittel, F. K. *Lasers Surg. Med.* **1996**, *18*, 231.
- (205) Paltauf, G.; Reichel, E.; Schmidt-Kloiber, H. *Proc. SPIE* **1992**, *1646*, 343.
- (206) Paltauf, G.; Schmidt-Kloiber, H. *Lasers Surg. Med.* **1995**, *16*, 277.
- (207) Cross, F. W.; Al-Dhahir, R. K.; Dyer, P. E. *J. Appl. Phys.* **1988**, *64*, 2194.
- (208) Esenaliev, R. O.; Oraevsky, A. A.; Letokhov, V. S.; Karabutov, A. A.; Malinsky, T. V. *Lasers Surg. Med.* **1993**, *13*, 470.
- (209) Dingus, R. S.; Curran, D. R.; Oraevsky, A. A.; Jacques, S. L. *Proc. SPIE* **1994**, *2134A*, 434.
- (210) Albagli, D.; Perelman, L. T.; Janes, G. S.; von Rosenberg, C.; Itzkan, I.; Feld, M. *Lasers Life Sci.* **1994**, *6*, 55.
- (211) Comninou, M.; Yannas, I. V. *J. Biomech.* **1976**, *9*, 427.
- (212) Kawamura, Y.; Toyoda, K.; Namba, S. *Appl. Phys. Lett.* **1982**, *40*, 374.
- (213) Srinivasan, R.; Mayne-Barton, V. *Appl. Phys. Lett.* **1982**, *41*, 576.
- (214) Trokel, S. L.; Srinivasan, R.; Braren, B. *Am. J. Ophthalmol.* **1983**, *96*, 710.
- (215) Srinivasan, R.; Leigh, W. *Am. J. Chem. Soc.* **1982**, *104*, 6784.
- (216) Jellinek, H. H. G.; Srinivasan, R. *J. Phys. Chem.* **1984**, *88*, 3048.
- (217) Palmer, B. J.; Keyes, T.; Clarke, R. H.; Isner, J. M. *J. Phys. Chem.* **1989**, *93*, 7509.
- (218) Garrison, B. J.; Srinivasan, R. *J. Appl. Phys.* **1985**, *57*, 2909.
- (219) Wayne, C. E.; Wayne, R. P. *Photochemistry*; Oxford University Press: Oxford, 1996.
- (220) Schmidt, H.; Ihlemann, J.; Wolff-Rottke, B.; Luther, K.; Troe, J. *J. Appl. Phys.* **1998**, *83*, 5458.
- (221) Ashfold, M. N. R.; Cook, P. A. In *Encyclopedia of Physical Science and Technology*, 3rd ed.; Meyers R. A., Ed.; Academic Press: San Diego, 2002.
- (222) Yeh, Y. C. *J. Vac. Sci. Technol.* **1986**, *A4*, 653.
- (223) Davis, G. M.; Gower, M. C.; Fotakis, C.; Efthimiopoulos, T.; Argyrakos, P. *Appl. Phys. A* **1985**, *36*, 27.
- (224) Dyer, P. E.; Sidhu, J. *J. Appl. Phys.* **1985**, *57*, 1420.
- (225) Gorodetsky, G.; Kazyaka, T. G.; Melcher, R. L.; Srinivasan, R. *Appl. Phys. Lett.* **1985**, *46*, 828.
- (226) Brunco, D. P.; Thompson, M. O.; Otis, C. E.; Goodwin, P. M. *J. Appl. Phys.* **1992**, *72*, 4344.
- (227) Otis, C. E.; Braren, B.; Thompson, M. O.; Brunco, D.; Goodwin, P. M. *Proc. SPIE* **1993**, *1856*, 132.
- (228) Sutcliffe, E.; Srinivasan, R. *J. Appl. Phys.* **1986**, *60*, 3315.
- (229) Srinivasan, R. *Appl. Phys. A* **1993**, *56*, 417.
- (230) Andrew, J. E.; Dyer, P. E.; Forster, D.; Key, P. H. *Appl. Phys. Lett.* **1983**, *43*, 717.
- (231) Küper, S.; Madaressi, S.; Stuke, M. *J. Phys. Chem.* **1990**, *94*, 7514.
- (232) Kitai, M. S.; Popkov, V. L.; Semchishen, V. A.; Kharizov, A. A. *IEEE J. Quantum Electron.* **1991**, *27*, 302.
- (233) Arnold, N.; Bityurin, N. *Appl. Phys. A* **1999**, *68*, 615.
- (234) Nikogosyan, D. N.; Görner, H. *IEEE J. Sel. Top. Quantum Electron.* **1999**, *5*, 1107.
- (235) Yingling, Y. G.; Zhigilei, L. V.; Garrison, B. J. *J. Photochem. Photobiol.* **2001**, *145*, 173.
- (236) Oraevsky, A. A.; Jacques, S. L.; Pettit, G. H.; Saidi, I. S.; Tittel, F. K.; Henry, P. D. *Lasers Surg. Med.* **1992**, *12*, 585.
- (237) Srinivasan, R.; Braren, B.; Casey, K. G.; Yeh, M. *Appl. Phys. Lett.* **1989**, *55*, 2790.
- (238) Walsh, J. T.; Deutsch, T. F. *Appl. Phys. B* **1991**, *52*, 217.
- (239) Bor, Z.; Hopp, B.; Rác, B.; Szabó, G.; Ratkay, I.; Süveges, I.; Füst, A.; Mohay, J. *Refract. Corneal Surg. (Suppl.)* **1993**, *9*, S111.
- (240) Nahen, K.; Vogel, A. J. *Biomed. Opt.* **2002**, *7*, 165.
- (241) Nahen, K. *Akustische Online-Kontrolle der Infrarot-Photoablation biologischer Gewebe*; Der Andere Verlag: Osnabrück, 2002.
- (242) Puliafito, C. A.; Stern, D.; Krueger, R. R.; Mandel, E. R. *Arch. Ophthalmol.* **1987**, *105*, 1255.
- (243) Noack, J.; Tönnies, R.; Hohla, C.; Birngruber, R.; Vogel, A. *Ophthalmology* **1997**, *104*, 823.
- (244) Frenz, M.; Zweig, A. D.; Romano, V.; Weber, H. P.; Chapliev, N. I.; Silenok, A. S. *Proc. SPIE* **1990**, *1202*, 22.
- (245) Hibst, R. *Technik, Wirkungsweise und medizinische Anwendungen von Holmium- und Erbium-Lasern*; Ecomed: Landsberg, 1996.

- (246) Ventzek, P. L. G.; Gilgenbach, R. M.; Ching, C. H.; Lindley, R. A. *J. Appl. Phys.* **1992**, *72*, 1696.
- (247) Kermani, O.; Koort, H. J.; Roth, E.; Dardenne, M. U. *J. Cataract Refract. Surg.* **1988**, *14*, 638.
- (248) Heisterkamp, A.; Ripken, T.; Mamom, T.; Drommer, W.; Welling, H.; Ertmer, W.; Lubatschowski, H. *Appl. Phys. B* **2002**, *74*, 419.
- (249) Apitz, I.; Vogel, A. *Proc. SPIE* **2003**, *4961*, in press.
- (250) Vogel, A.; Kersten, B.; Apitz, I. K. *Nahen. Proc. SPIE* **2003**, *4961*, in press.
- (251) Cummings, J. P.; Walsh, J. T. *Proc. SPIE* **1992**, *1646*, 242.
- (252) Sullivan, B.; Tam, A. C. *J. Acoust. Soc. Am.* **1984**, *75*, 437.
- (253) Sell, J. A.; Heffeling, D. M.; Ventzek, P. L.; Gilgenbach, R. M. *J. Appl. Phys.* **1991**, *69*, 1330.
- (254) Diaci, J.; Mozina, J. *Appl. Phys. A* **1992**, *55*, 352.
- (255) Emmony, D. C.; Geerken, B. M.; Straaijer, A. *Infrared Phys.* **1976**, *16*, 87.
- (256) Jacques, S. L.; Gofstein, G. *Proc. SPIE* **1991**, *1427*, 63.
- (257) Arnold, N.; Gruber, J.; Heitz, J. *Appl. Phys. A* **1999**, *69*, S87.
- (258) Brode, H. L. *Phys. Fluids* **1959**, *2*, 217.
- (259) Bulgakov, A. V.; Bulgakova, N. M. *J. Phys. D: Appl. Phys.* **1998**, *31*, 693.
- (260) Zhigilei, L. V.; Garrison, B. J. *J. Appl. Phys.* **2000**, *88*, 1281.
- (261) Krueger, R. R.; Trokel, S. L. *Arch. Ophthalmol.* **1985**, *103*, 1741.
- (262) Taylor, G. *Proc. R. Soc. A* **1950**, *201*, 159.
- (263) Sedov, L. I. *Similarity and Dimensional Methods in Mechanics*; Academic Press: New York, 1959.
- (264) Zel'dovich, Y. B.; Raizer, Y. P. *Physics of Shock Waves and High-Temperature Hydrodynamic Phenomena, Vols. I and II*; Academic Press: New York, 1966.
- (265) Landau, L. D.; Lifschitz, E. M. *Fluid Mechanics*, 2nd ed.; Pergamon Press: Oxford, 1987.
- (266) Sakurai, A. *J. Phys. Soc. Jpn.* **1953**, *8*, 662.
- (267) Sakurai, A. *J. Phys. Soc. Jpn.* **1954**, *9*, 256.
- (268) Freiwald, D. A. *J. Appl. Phys.* **1972**, *43*, 2224.
- (269) Freiwald, D. A.; Axford, R. A. *J. Appl. Phys.* **1975**, *46*, 1171.
- (270) Leonard, T. A.; Hammerling, P. *J. Appl. Phys.* **1980**, *51*, 6130.
- (271) Braren, B.; Casey, K. G.; Kelly, R. *Nucl. Instrum. Methods B* **1991**, *58*, 463.
- (272) Kelly, R.; Miotello, A. *Appl. Phys. B* **1993**, *57*, 145.
- (273) Dyer, P. E.; Sidhu, J. *J. Appl. Phys.* **1988**, *64*, 4657.
- (274) Jones, D. L. *Phys. Fluids* **1968**, *11*, 1664.
- (275) Stauter, C.; Gérard, P.; Fontaine, J.; Engel, T. *Appl. Surf. Sci.* **1997**, *109/110*, 174.
- (276) Nahen, K.; Vogel, A. *Lasers Surg. Med.* **1999**, *25*, 69.
- (277) Tam, A. C. *Rev. Mod. Phys.* **1986**, *58*, 381.
- (278) Morse, P. M.; Ingard, K. U. *Theoretical Acoustics*; McGrawHill Book Co.: New York, 1968; p 381.
- (279) Nahen, K.; Vogel, A. *Proc. SPIE* **2000**, *3914*, 166.
- (280) Zweig, A. D. *J. Appl. Phys.* **1991**, *70*, 1684.
- (281) Cummings, J. P.; Walsh, J. T. *Appl. Opt.* **1993**, *32*, 494.
- (282) Phipps, C. R.; Harrison, R. F.; Shimada, T.; York, G. W.; Turner, T. P.; Corlis, X. F.; Steele, H. S.; Haynes, L. C.; King, T. R. *Lasers Particle Beams* **1990**, *8*, 281.
- (283) Kőnz, F.; Frenz, M.; Pratisto, H.; Weber, H. P.; Lubatschowski, H.; Kermani, O.; Ertmer, W.; Altermatt, H. J.; Schaffner, T. *Proc. SPIE* **1994**, *2077*, 78.
- (284) Frenz, M.; Romano, V.; Zweig, A. D.; Weber, H. P.; Chapliev, N. I.; Silenok, A. V. *J. Appl. Phys.* **1989**, *66*, 4496.
- (285) Dingus, R. S. *Proc. SPIE* **1993**, *1882*, 399.
- (286) Konov, V. I.; Kulevsky, L. A.; Lukashev, A. V.; Pashinin, P. P.; Silenok, A. S. *Proc. SPIE* **1991**, *1427*, 232.
- (287) Domankevitz, Y.; Nishioka, N. S. *IEEE J. Quantum Electron.* **1990**, *26*, 2276.
- (288) Zweig, A. D.; Weber, H. P. *IEEE J. Quantum Electron.* **1987**, *23*, 1787.
- (289) Zweig, A. D.; Frenz, M.; Romano, V.; Weber, H. P. *Appl. Phys. B* **1988**, *47*, 259.
- (290) Zweig, A. D. *Proc. SPIE* **1991**, *1427*, 2.
- (291) Chapyak, E. J.; Godwin, R. P. *Proc. SPIE* **1999**, *3590*, 328.
- (292) Brujan, E. A.; Nahen, K.; Schmidt, P.; Vogel, A. *J. Fluid Mech.* **2001**, *433*, 251.
- (293) Brujan, E. A.; Nahen, K.; Schmidt, P.; Vogel, A. *J. Fluid Mech.* **2001**, *433*, 283.
- (294) Park, J. B. *Biomaterials. An Introduction*; Plenum Press: New York, 1979.
- (295) Bowden, F. P.; Brunton, J. H. *Proc. R. Soc. London A* **1961**, *263*, 433.
- (296) Watanabe, S.; Flotte, T. J.; McAuliffe, D. J.; Jacques, S. L. *J. Invest. Dermatol.* **1988**, *90*, 761.
- (297) Yashima, Y.; McAuliffe, D. J.; Flotte, T. J. *Lasers Surg. Med.* **1990**, *10*, 280.
- (298) Yashima, Y.; McAuliffe, D. J.; Jacques, S. L.; Flotte, T. J. *Lasers Surg. Med.* **1991**, *11*, 62.
- (299) Doukas, A. G.; McAuliffe, D. J.; Flotte, T. J. *Ultrasound Med. Biol.* **1993**, *19*, 137.
- (300) Doukas, A. G.; McAuliffe, D. J.; Lee, S.; Venugopalan, V.; Flotte, T. J. *Ultrasound Med. Biol.* **1995**, *21*, 961.
- (301) Hamrick, P. E.; Cleary, S. F. *J. Acoust. Soc. Am.* **1969**, *45*, 1.
- (302) Smith, R. J.; Cleary, S. F. *J. Acoust. Soc. Am.* **1975**, *56*, 1883.
- (303) Cleary, S. F. In *Laser Applications in Medicine and Biology*, Vol. 3; Wolbarsht, M. L., Ed.; Plenum Press: New York, 1977; p 175.
- (304) Lin, D. T. C. *Ophthalmology* **1994**, *101*, 1432.
- (305) Seiler, T.; McDonnell, P. J. *Surv. Ophthalmol.* **1995**, *40*, 89.
- (306) Shimmick, J. K.; Telfair, W. B.; Munnerlyn, C. R.; Bartlett, J. D.; Trokel, S. L. *J. Refract. Surg.* **1997**, *13*, 235.
- (307) Ghosh, A. P.; Hurst, J. E. *J. Appl. Phys.* **1988**, *64*, 287.
- (308) Izatt, J. A.; Sankrey, N. D.; Partovi, F.; Fitzmaurice, M.; Rava, R. P.; Itzkan, I.; Feld, M. S. *IEEE J. Quantum Electron.* **1990**, *26*, 2261.
- (309) Majaron, B.; Sustercic, D.; Lukac, M.; Skaleric, M.; Funduk, N. *Appl. Phys. B* **1998**, *66*, 479.
- (310) Hibst, R.; Kaufmann, R. *Lasers Med. Sci.* **1991b**, *6*, 391.
- (311) Hibst, R.; Kaufmann, R. *Lasermedizin* **1995**, *11*, 108.
- (312) Young, S. J. *J. Quant. Spectrosc. Radiat. Transfer* **1977**, *18*, 29.
- (313) Kaufmann, R.; Hibst, R. *Lasers Surg. Med.* **1996**, *19*, 324.
- (314) Venugopalan, V.; Nishioka, N. S.; Mikić, B. B. *IEEE Trans. Biomed. Eng.* **1991**, *38*, 1049.
- (315) Walsh, J. T.; Deutsch, T. F. *Lasers Surg. Med.* **1988**, *8*, 264.
- (316) Root, R. G. In *Laser-Induced Plasmas and Applications*; Radziemski, L. J., Cremers, D. A., Eds.; Marcel Dekker: New York, 1989; p 69.
- (317) Willmott, P. R.; Huber, J. R. *Rev. Mod. Phys.* **2000**, *72*, 315.
- (318) Green, H. A.; Domankevitz, Y.; Nishioka, N. *Lasers Surg. Med.* **1990**, *10*, 476.
- (319) Deutsch, T. F.; Geis, M. W. *J. Appl. Phys.* **1983**, *54*, 7201.
- (320) Zhigilei, L. V.; Garrison, B. J. *Appl. Phys. Lett.* **1999**, *74*, 1341.
- (321) Yingling, Y. G.; Zhigilei, L. V.; Garrison, B. J.; Koubenakis, A.; Labrakis, J.; Georgiou, S. *Appl. Phys. Lett.* **2001**, *78*, 1631.
- (322) Domankevitz, Y.; Lee, M. S.; Nishioka, N. S. *Appl. Opt.* **1993**, *32*, 569.
- (323) Nishioka, N. S.; Domankevitz, Y. *IEEE J. Quantum Electron.* **1990**, *26*, 2271.
- (324) Dabby, F. W.; Paek, U.-C. *IEEE J. Quantum Electron.* **1972**, *8*, 106.
- (325) Gagliano, F. P.; Paek, U.-C. *Appl. Opt.* **1974**, *13*, 274.
- (326) Kelly, R.; Miotello, A. *Appl. Surf. Sci.* **1996**, *96–98*, 205.
- (327) Langerholc, J. *Appl. Opt.* **1979**, *18*, 2286.
- (328) McKenzie, A. L. *Phys. Med. Biol.* **1983**, *28*, 905.
- (329) McKenzie, A. L. *Phys. Med. Biol.* **1986**, *31*, 967.
- (330) McKenzie, A. L. *Phys. Med. Biol.* **1989**, *34*, 107.
- (331) Partovi, F.; Izatt, J. A.; Cothren, R. M.; Kittrell, C.; Thomas, J. E.; Strikwerda, S.; Kramer, J. R.; Feld, M. S. *Lasers Surg. Med.* **1987**, *7*, 141.
- (332) Gerstmann, M.; Sagi, A.; Avidor-Zehavi, A.; Katzir, A.; Akselrod, S. *Opt. Eng.* **1993**, *32*, 291.
- (333) Sagi, A.; Avidor-Zehavi, A.; Shitzer, A.; Gerstmann, M.; Akselrod, S.; Katzir, A. *Opt. Eng.* **1992**, *31*, 1425.
- (334) Batanov, V.; Fedorov, V. B. *JETP Lett.* **1973**, *17*, 247.
- (335) Reilly, J. P.; Ballantyne, A.; Woodroffe, J. A. *AIAA J.* **1979**, *17*, 1098.
- (336) Woodroffe, J. A.; Hsia, J.; Ballantyne, A. *Appl. Phys. Lett.* **1980**, *36*, 14.
- (337) Rosen, D. I.; Mitteldorf, J.; Kothandaraman, G.; Pirri, A. N.; Pugh, E. R. *J. Appl. Phys.* **1982**, *53*, 3190.
- (338) Rosen, D. I.; Hastings, D. E.; Weyl, G. M. *J. Appl. Phys.* **1982**, *53*, 5882.
- (339) Zhigilei, L. V.; Kodali, P. B. S.; Garrison, B. J. *J. Phys. Chem. B* **1997**, *101*, 2028.
- (340) Zhigilei, L. V.; Kodali, P. B. S.; Garrison, B. J. *J. Phys. Chem. B* **1998**, *102*, 2845.
- (341) Zhigilei, L. V.; Garrison, B. J. *Proc. SPIE* **1998**, *3254*, 135.
- (342) Taboada, J.; Archibald, C. J. *Preprints of Annual Scientific Meeting—Aerospace Medical Association*; Aerospace Medical Association: Washington, DC, 1981; No. 1981 98–99, ISSN 0065-3764.
- (343) Puliafito, C. A.; Steinert, R. F.; Deutsch, T. F.; Hillenkamp, F.; Dehm, E. J.; Adler, C. M. *Ophthalmology* **1985**, *92*, 741.
- (344) Lane, R. J.; Linsker, R.; Wynne, J. J.; Torres, A.; Geronemus, R. G. *Arch. Dermatol.* **1985**, *121*, 609.
- (345) Puliafito, C. A.; Wong, K.; Steinert, R. F. *Lasers Surg. Med.* **1987**, *7*, 155.
- (346) Campos, M.; Wang, X. W.; Hertzog, L.; Lee, M.; Clapham, T.; Trokel, S. L.; McDonnell, P. *Invest. Ophthalmol. Vis. Sci.* **1993**, *34*, 2493.
- (347) Berns, M. W.; Chao, L.; Giebel, A. W.; Liaw, L.-H.; Andrews, J.; VerSteeg, B. *Invest. Ophthalmol. Vis. Sci.* **1999**, *40*, 826.
- (348) Seiler, T.; Marshall, J.; Rothery, S.; Wollensak, J. *Lasers Ophthalmol.* **1986**, *1*, 49.
- (349) Loertscher, H.; Mandelbaum, S.; Parrish, R. K., III; Parel, J. M. *Am. J. Ophthalmol.* **1986**, *102*, 217.
- (350) Bende, T.; Kriegerowski, M.; Seiler, T. *Lasers Light Ophthalmol.* **1989**, *2*, 263.
- (351) Wolbarsht, M. L. *IEEE J. Quantum Electron.* **1984**, *20*, 1427.
- (352) Lembares, A.; Hu, X.-H.; Kalmus, G. W. *Invest. Ophthalmol. Vis. Sci.* **1997**, *38*, 1283.
- (353) Pettit, G. H.; Ediger, M. N.; Weiblinger, R. P. *Appl. Opt.* **1993**, *32*, 488.



- (354) Landry, R. J.; Pettit, G. H.; Hahn, D. W.; Ediger, M. N.; Yang, G. C. *Lasers Light Ophthalmol.* **1994**, *6*, 87.
- (355) Pettit, G. H.; Ediger, M. N.; Weiblinger, R. P. *Opt. Eng.* **1995**, *34*, 661.
- (356) Tuft, S.; Al-Dahir, R.; Dyer, P.; Zehao, Z. *Invest. Ophthalmol. Vis. Sci.* **1990**, *31*, 1512.
- (357) Lubatschowski, H.; Kermani, O.; Otten, C.; Haller, A.; Schmiedt, K. C.; Ertmer, W. *Lasers Surg. Med.* **1994**, *14*, 168.
- (358) Cohen, D.; Chuck, R.; Bearman, G.; McDonnell, P.; Grundfest, W. J. *Biomed. Opt.* **2001**, *6*, 339.
- (359) Srinivasan, R.; Dyer, P. E.; Braren, B. *Lasers Surg. Med.* **1987**, *6*, 514.
- (360) Ishihara, M.; Arai, T.; Sato, S.; Morimoto, Y.; Obara, M.; Kikuchi, M. *Lasers Surg. Med.* **2002**, *30*, 54.
- (361) Ishihara, M.; Arai, T.; Sato, S.; Morimoto, Y.; Obara, M.; Kikuchi, M. *Proc. SPIE* **2001**, *4257*, 298.
- (362) Dyer, P. E.; Srinivasan, R. *Appl. Phys. Lett.* **1986**, *48*, 445.
- (363) Hahn, D. W.; Ediger, M. N.; Pettit, G. H. *Lasers Surg. Med.* **1995**, *16*, 384.
- (364) Pettit, G. H.; Ediger, M. N. *Lasers Surg. Med.* **1993**, *13*, 363.
- (365) Telfair, W. B.; Hoffman, H. J.; Nordquist, R. E.; Eiferman, R. A. *Proc. SPIE* **1998**, *3246*, 97.
- (366) Hoffmann, H. J.; Telfair, W. B. *J. Biomed. Opt.* **1999**, *4*, 465.
- (367) Telfair, W. B.; Bekker, C.; Hoffman, H. J.; Yoder, P. R., Jr.; Norquist, R. E.; Eiferman, R. A.; Zenzie, H. H. *J. Refract. Surg.* **2000**, *16*, 40.
- (368) Hoffman, H. J.; Telfair, W. B. *J. Refract. Surg.* **2000**, *16*, 90.
- (369) Stern, D.; Puliafito, C. A.; Dobi, E. T.; Reidy, W. T. *Ophthalmology* **1987**, *95*, 1434.
- (370) Deckelbaum, L. I. *Lasers Surg. Med.* **1994**, *14*, 101–110.
- (371) Köstli, K. P.; Frenz, M.; Weber, H. P.; Paltauf, G.; Schmidt-Kloiber, H. *Proc. SPIE* **1999**, *3601*, 310.
- (372) Dyer, P. E.; Khosroshahi, M. E.; Tuft, S. J. *Appl. Phys. B* **1993**, *56*, 84.
- (373) Jansen, E. D.; van Leeuwen, T. G.; Motamedi, M.; Borst, C.; Welch, A. J. *J. Appl. Phys.* **1995**, *78*, 564.
- (374) Brinkmann, R.; Hansen, Ch.; Mohrenstecher, D.; Scheu, M.; Birngruber, R. *IEEE J. Sel. Top. Quantum Electron.* **1996**, *2*, 826.
- (375) Frenz, M.; Könz, F.; Pratisto, H.; Weber, H. P.; Silenok, A. S.; Konov, V. I. *J. Appl. Phys.* **1998**, *84*, 5905.
- (376) Skripov, V. P.; Pavlov, P. A. *Sov. Technol. Rev. B: Therm. Phys.* **1989**, *2*, 171.
- (377) Skripov, V. P. *Fluid Mech. Res.* **1992**, *21*, 43.
- (378) Dingus, R. S. *Proc. SPIE* **1992**, *1646*, 266.
- (379) Vogel, A.; Noack, J.; Nahen, K.; Theisen, D.; Busch, S.; Parlit, U.; Hammer, D. X.; Noojin, G. D.; Rockwell, B. A.; Birngruber, R. *Appl. Phys. B* **1999**, *68*, 271.
- (380) Vogel, A.; Hentschel, W.; Holzfuß, J.; Lauterborn, W. *Ophthalmology* **1986**, *93*, 1259.
- (381) Vogel, A.; Schweiger, P.; Frieser, A.; Asiyu, M.; Birngruber, R. *IEEE J. Quantum Electron.* **1990**, *26*, 2240.
- (382) Lin, C.; Stern, D.; Puliafito, C. A. *Invest. Ophthalmol. Vis. Sci.* **1990**, *31*, 2546.
- (383) Srinivasan, R.; Casey, K. G.; Haller, J. D. *IEEE J. Quantum Electron.* **1990**, *26*, 2279.
- (384) van Leeuwen, T. G.; van Erven, L.; Meertens, J. H.; Motamedi, M.; Post, M. J.; Borst, C. *J. Am. Coll. Cardiol.* **1992**, *19*, 1610.
- (385) van Leeuwen, T. G.; Meertens, J. H.; Velema, E.; Post, M. J.; Borst, C. *Circulation* **1993**, *87*, 1258.
- (386) Palanker, D.; Hemo, I.; Turovets, I.; Lewis, A. *Proc. SPIE* **1994**, *2134A*, 460.
- (387) Vogel, A.; Busch, S.; Parlit, U. *J. Acoust. Soc. Am.* **1996**, *100*, 148.
- (388) Brinkmann, R.; Dröge, G.; Schröer, F.; Scheu, M.; Birngruber, R. *Ophthalmol. Surg. Lasers* **1997**, *28*, 853.
- (389) Cole, R. H. *Underwater Explosions*; Princeton University Press: Princeton, NJ, 1948.
- (390) Young, F. R. *Cavitation*; McGraw-Hill: London, 1989.
- (391) Vogel, A.; Lauterborn, W.; Timm, R. *J. Fluid Mech.* **1989**, *206*, 299.
- (392) Ith, M.; Pratisto, H.; Altermatt, H. J.; Frenz, M.; Weber, H. P. *Appl. Phys. B* **1994**, *59*, 621.
- (393) Jansen, E. D.; Asshauer, T.; Frenz, M.; Motamedi, M.; Delacrétaz, G.; Welch, A. J. *Lasers Surg. Med.* **1996**, *18*, 278.
- (394) Frenz, M.; Pratisto, H.; Könz, F.; Jansen, E. D.; Welch, A. J.; Weber, H. P. *IEEE J. Quantum Electron.* **1996**, *32*, 2025.
- (395) Benjamin, T. B.; Ellis, A. T. *Philos. Trans. R. Soc. London* **1966**, *260*, 221.
- (396) Palanker, D.; Vankov, A.; Miller, J. *Proc. SPIE* **2002**, *4617A*, 112.
- (397) Vogel, A.; Engelhardt, R.; Behnle, U.; Parlit, U. *Appl. Phys. B* **1996**, *62*, 173.
- (398) Snyder, W. J.; Shi, W. Q.; Vari, S. G.; Grundfest, W. S. *Proc. SPIE* **1993**, *1882*, 153.
- (399) Jansen, E. D.; van Leeuwen, T. G.; Verdaasdonk, R. M.; Le, T. H.; Motamedi, M.; Welch, A. J.; Borst, C. *Proc. SPIE* **1993**, *1882*, 139.
- (400) Brinkmann, R.; Theisen, D.; Brendel, T.; Birngruber, R. *IEEE J. Sel. Top. Quantum Electron.* **1999**, *5*, 969.
- (401) Frenz, M.; Mischler, Ch.; Romano, V.; Forrer, M.; Müller, O. M.; Weber, H. P. *Appl. Phys. B* **1991**, *52*, 251.
- (402) Isner, J. M.; deJesus, S. R.; Clarke, R. H.; Gal, D.; Rongione, A. J.; Donaldson, R. F. *Lasers Surg. Med.* **1988**, *8*, 543.
- (403) van Leeuwen, T. G.; van der Veen, M. J.; Verdaasdonk, R.; Borst, C. *Lasers Surg. Med.* **1991**, *11*, 26.
- (404) Pratisto, H.; Frenz, M.; Ith, M.; Altermatt, H. J.; Jansen, E. D.; Weber, H. P. *Appl. Opt.* **1996**, *35*, 3328.
- (405) Vogel, A.; Schmidt, P.; Flucke, B. *Proc. SPIE* **2001**, *4257*, 184.
- (406) Vogel, A.; Schmidt, P.; Flucke, B. *Proc. SPIE* **2002**, *4617*, 105.
- (407) Kodama, T.; Tomita, Y. *Appl. Phys. B* **2000**, *70*, 139.
- (408) Jansen, E. D.; Frenz, M.; Kadipasaoglu, K. A.; Pfefer, T.; Altermatt, H. J.; Motamedi, M.; Welch, A. J. *Proc. SPIE* **1996**, *2671*, 49.
- (409) Shen, Y. R. *The Principles of Nonlinear Optics*; Wiley: New York, 1984.
- (410) Niemz, M. H.; Hoppeler, T. P.; Juhasz, T.; Bille, J. F. *Lasers Light Ophthalmol.* **1993**, *5*, 149.
- (411) Steinert, R. F.; Puliafito, C. A. *The Nd:YAG Laser in Ophthalmology. Principles and Clinical Practice of Photodisruption*; Saunders: Philadelphia, 1986.
- (412) Juhasz, T.; Loesel, F. H.; Kurtz, R. M.; Horvath, C.; Bille, J. F.; Mourou, G. *IEEE J. Sel. Top. Quantum Electron.* **1999**, *5*, 902.
- (413) Lubatschowski, H.; Maatz, G.; Heisterkamp, A.; Hetzel, U.; Drommer, W.; Welling, H.; Ertmer, W. *Graef's Arch. Clin. Exp. Ophthalmol.* **2000**, *238*, 33.
- (414) Lubatschowski, H.; Heisterkamp, A.; Will, F.; Serbin, J.; Bauer, T.; Fallnich, C.; Welling, H. *Proc. SPIE* **2002**, *4633*, 38.
- (415) König, K.; Riemann, I.; Fischer, P.; Halbhauer, K. *Cell. Mol. Biol. Lett.* **2002**, *88*, 078103.
- (416) Tuler, F. R.; Butcher, B. M. *Int. J. Fract. Mech.* **1968**, *4*, 431.
- (417) Venugopalan, V.; Guerra, A.; Nahen, K.; Vogel, A. *Phys. Rev. Lett.* **2002**, *88*, 078103.
- (418) Docchio, F.; Sacchi, C. A.; Marshall, J. *Lasers Ophthalmol.* **1986**, *1*, 83.
- (419) Vogel, A.; Capon, M. R. C.; Asiyu, M. N.; Birngruber, R. *Invest. Ophthalmol. Vis. Sci.* **1994**, *35*, 3033.
- (420) Sacchi, C. A. *J. Opt. Soc. Am. B* **1991**, *8*, 337.
- (421) Bloembergen, N. *IEEE J. Quantum Electron.* **1974**, *QE-10*, 375.
- (422) Kennedy, P. K. *IEEE J. Quantum Electron.* **1995**, *QE-31*, 2241.
- (423) Niemz, M. H. *Appl. Phys. Lett.* **1995**, *66*, 1181.
- (424) Stuart, B. C.; Feit, M. D.; Hermann, S.; Rubenchik, A. M.; Shore, B. W.; Perry, M. D. *Phys. Rev. B* **1996**, *53*, 1749.
- (425) Feng, Q.; Moloney, J. V.; Newell, A. C.; Wright, E. M.; Cook, K.; Kennedy, P. K.; Hammer, D. X.; Rockwell, B. A.; Thompson, C. R. *IEEE J. Quantum Electron.* **1997**, *33*, 127.
- (426) Lenzner, M.; Krüger, J.; Sartania, S.; Cheng, Z.; Spielmann, Ch.; Mourou, G.; Kautek, W.; Krausz, F. *Phys. Rev. Lett.* **1998**, *80*, 4076.
- (427) Noack, J.; Vogel, A. *IEEE J. Quantum Electron.* **1999**, *35*, 1156.
- (428) Vogel, A.; Noack, J.; Hüttmann, G.; Paltauf, G. *Proc. SPIE* **2002**, *4633*, 23.
- (429) Marburger, J. H. *Prog. Quantum Electron.* **1975**, *4*, 35.
- (430) Vogel, A.; Nahen, K.; Theisen, D. *IEEE J. Sel. Top. Quantum Electron.* **1996**, *2*, 847.
- (431) Hammer, D. X.; Noojin, G. D.; Thomas, R. J.; Hopkins, R. A.; Kennedy, P. K.; Druessel, J. J.; Rockwell, B. A.; Welch, A. J.; Cain, C. P. *SPIE Proc.* **1997**, *2975*, 163.
- (432) Schaffer, C. B.; Brodeur, A.; Garcia, J. F.; Mazur, E. *Opt. Lett.* **2001**, *26*, 93.
- (433) Yablonovitch, E.; Bloembergen, N. *Phys. Rev. Lett.* **1972**, *29*, 907.
- (434) Braun, A.; Korn, G.; Liu, X.; Du, D.; Siquier, J.; Mourou, G. *Opt. Lett.* **1995**, *20*, 73.
- (435) Couairon, A.; Tzortzakis, S.; Berge, L.; Franco, M.; Prade, B.; Mysyrowicz, A. *J. Opt. Soc. Am. B* **2002**, *19*, 1117.
- (436) Barnes, P. A.; Rieckhoff, K. E. *Appl. Phys. Lett.* **1968**, *13*, 282.
- (437) Hammer, D. X.; Thomas, R. J.; Noojin, G. D.; Rockwell, B. A.; Kennedy, P. A.; Roach, W. P. *IEEE J. Quantum Electron.* **1996**, *QE-3*, 670.
- (438) Oraevsky, A. A.; DaSilva, L. B.; Rubenchik, A. M.; Feit, M. D.; Glinzky, M. E.; Perry, M. D.; Mammini, B. M.; Small, W., IV; Stuart, B. C. *IEEE J. Sel. Top. Quantum Electron.* **1996**, *2*, 801.
- (439) Docchio, F.; Regondi, P.; Capon, M. R. C.; Mellerio, J. *Appl. Opt.* **1988**, *27*, 3661.
- (440) Docchio, F.; Regondi, P.; Capon, M. R. C.; Mellerio, J. *Appl. Opt.* **1988**, *27*, 3669.
- (441) Nahen, K.; Vogel, A. *IEEE J. Sel. Top. Quantum Electron.* **1996**, *2*, 861.
- (442) Raizer, Y. P. *Sov. Phys. JETP* **1965**, *48*, 1508–1519.
- (443) Kennedy, P. K.; Hammer, D. X.; Rockwell, B. A. *Prog. Quantum Electron.* **1997**, *21*, 155.
- (444) Hughes, T. P. *Plasmas and Laser Light*; Adam Hilger: Bristol, UK, 1975.
- (445) Godwin, R. P.; van Kessel, C. G. M.; Olsen, J. N.; Sachsenmaier, P.; Sigel, R. Z. *Naturforsch.* **1977**, *32a*, 1100.
- (446) Rubenchik, A. M.; Feit, M. D.; Perry, M. D.; Larsen, J. T. *Appl. Surf. Sci.* **1998**, *127–129*, 193.



- (447) Feit, M. D.; Rubenchik, A. M.; Kim, B. M.; Da Silva, L. B.; Perry, M. D. *Appl. Surf. Sci.* **1998**, 127–129, 869.
- (448) Noack, J.; Hammer, D. X.; Noojin, G. D.; Rockwell, B. A.; Vogel, A. *J. Appl. Phys.* **1998**, 83, 7488.
- (449) Zysset, B.; Fujimoto, J. G.; Deutsch, T. F. *Appl. Phys. B* **1989**, 48, 139.
- (450) Doukas, A. G.; Zweig, A. D.; Frisoli, J. K.; Birngruber, R.; Deutsch, T. F. *Appl. Phys. B* **1991**, 53, 237.
- (451) Vogel, A.; Busch, S.; Jungnickel, K.; Birngruber, R. *Lasers Surg. Med.* **1994**, 15, 32.
- (452) Juhasz, T.; Hu, X. H.; Turi, L.; Bor, Z. *Lasers Surg. Med.* **1994**, 15, 91.
- (453) Juhasz, T.; Kastis, G. A.; Suarez, C.; Bor, Z.; Bron, W. E. *Lasers Surg. Med.* **1996**, 19, 23.
- (454) Fischer, J. P.; Juhasz, T.; Bille, J. F. *Appl. Phys. A* **1997**, 64, 181.
- (455) Vogel, A.; Günther, T.; Asiyo-Vogel, M.; Birngruber, R. *J. Cataract Refract. Surg.* **1997**, 23, 1301.
- (456) Juhasz, T.; Kurtz, R.; Horvath, C.; Suarez, C.; Nordan, L. T.; Slade, S. G. *Proc. SPIE* **2002**, 4633, 1.
- (457) Teng, P.; Nishioka, N. S.; Anderson, R. R.; Deutsch, T. F. *IEEE J. Quantum Electron.* **1987**, QE-23, 1845.
- (458) Stern, D.; Schoenlein, R. W.; Puliafito, C. A.; Dobi, E. T.; Birngruber, R.; Fujimoto, J. G. *Arch. Ophthalmol.* **1989**, 107, 587.
- (459) Fabbro, R.; Fournier, J.; Ballard, P.; Devaux, D.; Virmont, J. *J. Appl. Phys.* **1990**, 68, 775.
- (460) Stolarski, D. J.; Hardman, J.; Bramlette, C. G.; Noojin, G. D.; Thomas, R. J.; Rockwell, B. A.; Roach, W. P. *Proc. SPIE* **1995**, 2391, 100.
- (461) Thomas, R. J.; Hammer, D. X.; Noojin, G. J.; Stolarski, D. J.; Rockwell, B. A.; Roach, W. P. *Proc. SPIE* **1996**, 2681, 402.
- (462) Chapyak, E. J.; Godwin, R. P.; Vogel, A. *Proc. SPIE* **1997**, 2975, 335.
- (463) Niemz, M. H.; Klancnik, E. G.; Bille, J. F. *Lasers Surg. Med.* **1991**, 11, 426.
- (464) Boudaiffa, B.; Cloutier, P.; Hunting, D.; Huels, M. A.; Sanche, L. *Science* **2000**, 287, 1658.
- (465) Hotop, H. In *Gaseous Dielectrics IX*, Proceedings of the 9th International Symposium on Gaseous Dielectrics, Ellicott City, MD, 22–25 May, 2001; Christophorou, L. G., Olthoff, J. K., Eds.; Kluwer Academic/Plenum Press: New York, 2001; p 3.
- (466) Nikogosyan, D. N.; Oraevsky, A. A.; Rupasov, V. *Chem. Phys.* **1983**, 77, 131.
- (467) Tirlapur, U.K.; König, K.; Peuckert, C.; Krieg, R.; Halbhauer, K.-J. *Exp. Cell Res.* **2001**, 263, 88.
- (468) Röl, P.; Fankhauser, F.; Kwasniewska, S. *Lasers Ophthalmol.* **1986**, 1, 1.
- (469) Vogel, A.; Nahen, K.; Theisen, D.; Birngruber, R.; Thomas, R. J.; Rockwell, B. A. *Appl. Opt.* **1999**, 38, 3636.
- (470) Jungnickel, K.; Vogel, A. *Lasers Light Ophthalmol.* **1992**, 5, 95.
- (471) Zysset, B.; Fujimoto, J. G.; Puliafito, C. A.; Birngruber, R.; Deutsch, T. F. *Lasers Surg. Med.* **1989**, 9, 183.
- (472) Neev, J.; Da Silva, L. B.; Feit, M. D.; Perry, M. D.; Rubenchik, A. M.; Stuart, B. C. *IEEE J. Sel. Top. Quantum Electron.* **1996**, 2, 790.
- (473) Kurtz, R. M.; Elner, V.; Liu, X.; Juhasz, T. *J. Refract. Surg.* **1997**, 13, 653.
- (474) Loesel, F. H.; Fischer, J. P.; Götz, M. H.; Horvath, C.; Juhasz, T.; Noack, F.; Suhm, N.; Bille, J. F. *Appl. Phys. B* **1998**, 66, 121.
- (475) Fischer, J. P.; Dams, J.; Götz, M. H.; Kerker, E.; Loesel, F. H.; Messer, C. J.; Niemz, M. H.; Suhm, N.; Bille, J. F. *Appl. Phys. B* **1994**, 58, 493.
- (476) Kim, B. M.; Feit, M. D.; Rubenchik, A. M.; Joslin, E. J.; Eichler, J.; Stoller, P.; Da Silva, L. B. *Appl. Phys. Lett.* **2000**, 76, 4001.
- (477) Wu, Z.; Jiang, H.; Luo, L.; Gou, H.; Yang, H.; Gong, Q. *Opt. Lett.* **2002**, 27, 448.
- (478) Maatz, G.; Heisterkamp, A.; Lubatschowski, H.; Barcikowski, S.; Fallnich, C.; Welling, H.; Ertmer, W. *J. Opt. A: Pure Appl. Opt.* **2000**, 2, 59.
- (479) Schomacker, K. T.; Walsh, J. T.; Flotte, T. J.; Deutsch, T. F. *Lasers Surg. Med.* **1990**, 10, 74.
- (480) Choi, B.; Barton, J. K.; Chan, E. K.; Welch, A. J. *Lasers Surg. Med.* **1998**, 23, 185.
- (481) Majaron, B.; Srinivas, S. M.; Huang, H. L.; Nelson, J. S. *Lasers Surg. Med.* **2000**, 26, 215.
- (482) Prince, M. R.; Deutsch, T. F.; Shapiro, A. H.; Margolis, R. J.; Oseroff, A. R.; Fallon, J. T.; Parrish, J. A.; Anderson, R. R. *Proc. Natl. Acad. Sci. U.S.A.* **1986**, 83, 7064.
- (483) Prince, M. R.; LaMuraglia, G. M.; Teng, P.; Deutsch, T. F.; Anderson, R. R. *IEEE J. Quantum Electron.* **1987**, 23, 1783.
- (484) Al-Dhahir, R. K.; Dyer, P. E.; Zhu, Z. *Appl. Phys. B* **1990**, 51, 81.
- (485) Jean, B.; Bende, T.; Matallana, M. *German J. Ophthalmol.* **1993**, 2, 404.
- (486) Nahen, K.; Eisenbeiss, W.; Vogel, A. *Proc. SPIE* **2000**, 3916, 218.
- (487) Specht, H.; Bende, T.; Jean, B.; Fruehauf, W. *Proc. SPIE* **1999**, 3591, 33.
- (488) Kim, B. M.; Da Silva, L. B.; Feit, M. D.; Rubenchik, A. M. *Appl. Surf. Sci.* **1998**, 127–129, 857.
- (489) Edwards, G.; Logan, R.; Copeland, M.; Reinisch, L.; Davidson, J.; Johnson, B.; Maciunas, R.; Mendenhall, M.; Ossoff, R.; Tribble, J.; Werkhaven, J.; O'Day, D. *Nature* **1994**, 371, 416.
- (490) London, R. A.; Glinsky, M. E.; Zimmerman, G. B.; Bailey, D. S.; Eder, D. C.; Jacques, S. L. *Appl. Opt.* **1997**, 36, 9068.

CR010379N